INVESTIGATION OF CORROSION BEHAVIOUR OF NiCoAlTa SHAPE MEMORY ALLOY

A Thesis submitted to the College of Graduate and Postdoctoral Studies in Partial Fulfillment of the Requirements for the Degree of Doctor of Philosophy in the Department of Mechanical Engineering

University of Saskatchewan

Saskatoon

By

HANAN FARHAT

PERMISSION TO USE

In presenting this thesis/dissertation in partial fulfillment of the requirements for a Postgraduate degree from the University of Saskatchewan, I agree that the Libraries of this University may make it freely available for inspection. I further agree that permission for copying of this thesis/dissertation in any manner, in whole or in part, for scholarly purposes may be granted by Dr. Ikechukwuka Oguocha and Dr. Richard Evitts, who supervised my thesis/dissertation work or, in their absence, by the Head of the Department or the Dean of the College in which my thesis work was done. It is understood that any copying or publication or use of this thesis/dissertation or parts thereof for financial gain shall not be allowed without my written permission. It is also understood that due recognition shall be given to me and to the University of Saskatchewan in any scholarly use which may be made of any material in my thesis/dissertation.

Requests for permission to copy or to make other uses of materials in this thesis/dissertation in whole or part should be addressed to:

Head of the Department of Mechanical Engineering
57 Campus Drive
University of Saskatchewan
Saskatoon, Saskatchewan S7N 5A9
Canada

OR

Dean
College of Graduate and Postdoctoral Studies
University of Saskatchewan
116 Thorvaldson Building, 110 Science Place
Saskatoon, Saskatchewan S7N 5C9
Canada

ABSTRACT

FeNiCoAlTa shape memory alloy (SMA) possesses both large superelastic strain and high yield strength. This makes it a potential candidate for industrial applications, such as actuators and pipe couplings. The corrosion behaviour of this alloy since is mostly unknown. The SMA was tested by means of electrochemical methods in 0.6 molar (M) NaCl solution at four different temperatures (25 ^{o}C, 40 ^{o}C, 60 ^{o}C, and 80 ^{o}C) and three levels of solution pH (3, 6, and 10). At 80 ^{o}C, the corrosion resistance of the alloy was lower than that at the lower temperatures. This was indicated by higher corrosion rates and lower open circuit potentials. Low corrosion resistance in acidic solutions, good corrosion resistance in alkaline solutions in comparison to near neutral 0.6 M NaCl solution were observed. The SMA did not passivate in the 0.6 M NaCl solution, but suffered localized corrosion in the form of corrosion pits.

The effect of heat treatment on corrosion properties of the alloy and its microstructure was also investigated. It was found that aging heat treatment caused β - Ni_3Al phase to precipitate at the grain boundaries, resulting in chemical segregation between the grains and grain boundaries. The segregation degraded the corrosion resistance of the alloy, and caused intergranular corrosion in 0.6 M NaCl solution at 25 ^{o}C. Furthermore, the corrosion resistance of the alloy was determined in 0.5 M NaOH and 0.5 M H_2SO_4 solutions at 25 ^{o}C. It showed good corrosion resistance to the NaOH solution, but suffered severe corrosion in the H_2SO_4 solution.

The alloy was coupled to UNS G10180 (AISI 1018), UNS S30400 (AISI 304), UNS S31603 (AISI 316L), and UNS S32750 (AISI 2507), and its galvanic corrosion behaviour was investigated electrochemically. The test was conducted in 0.6 M NaCl solution at 25 ^{o}C, 40 ^{o}C, and 60 ^{o}C. For each couple, the specimen tested at 60 ^{o}C showed increased localized and pitting corrosion, an increase in galvanic current density, and a lower galvanic potential compared to couples tested at the other temperatures. The results show that when the alloy was coupled to UNS G10180, it acted as the cathode, whereas when coupled to stainless steels, it acted as the anode, and suffered localized corrosion attack with the formation of large pits and its overall corrosion increased.

ACKNOWLEDGMENTS

I would like to express my gratitude to my supervisors, Professors I. Oguocha and R. Evitts, for their support, encouragement, and collaboration. I also would like to thank my advisory committee members, Professors C. Zhang, A. Odeshi, V. Meda and R. Fotouhi, for their helpful suggestions and discussions.

I especially thank Professor R. Griffin from Texas A & M University at Qatar for his guidance in the early stages of this research project, where he acted as one of my supervisors. It is sad that his current circumstances prevent his continuing involvement in this research. Technical support from Mr. Abubaker Abdulmajid and Tariq Mohamed of the College of the North Atlantic-Qatar (CNAQ) in using the electrochemical testing equipment and optical microscope is highly appreciated. Technical support from Professor B. Palmer, who allowed me to use the corrosion laboratory facility and engaged in several fruitful discussions with me on interpreting the electrochemical test results, is also very much appreciated. I am thankful to Professor R. Johnsen from the Norwegian University of Science and Technology for technical support in using the X-Ray Diffraction (XRD), advice in interpreting electrochemical test results, and for proofreading my journal paper. Thanks as well to Mr. Philip Connolly and Dr. Myrto Georgakopoulou from University College of London- Qatar for giving me access to their SEM, and to Professor I. Karaman and Dr. L.W. Tseng of Texas A & M for providing the testing material and performing the heat treatment on the material. I would like to express my appreciation to Mr. Li. Gang for allowing me to analyze my potentiodynamic scan data using his customized Python module. Thanks to the Libyan Government for providing a scholarship that supported this research study. I would like to express my gratitude to Mr. Patrick Flanagan for editorial reading of this thesis. And finally, I wish to extend my deep thanks to my family and friends for their support during my academic program. Their continuous encouragement enabled me to reach this stage.

DEDICATION

To my husband and children, who bring me joy every day, and to my baby daughter, who witnessed most of this work, but did not live to see it completed. To Dan, Jasmine, Camille, and baby Yarib.

TABLE OF CONTENTS

LIST OF TABLES

LIST OF FIGURES

LIST OF SYMBOLS

English Letters

a	Area (cm^2)
A	Constant for Each Chemical Reaction Used in Arrhenius Equation
CR	Corrosion Rate (mm/y)
E	Electrode Potential (mV)
E_a	Molar Activation Energy (J/mol)
E_{oc}	Open Circuit Potential (mV)
E_{corr}	Corrosion Potential (mV)
E_g	Galvanic Potential (mV)
E_{gm}	Mean Value of the Galvanic Potential (mV)
E_p	Pitting Potential (mV)
E_{pp}	Passivation Potential (mV)
EW	Equivalent Weight (grams/equivalent)
I	Measured Cell Current (µA)
I_{corr}	Corrosion Current (µA)
i_{corr}	Corrosion Current Density ($\mu A/cm^2$)
I_{crit}	Critical Current Required for Passivation (µA)
i_g	Galvanic Current Density ($\mu A/cm^2$)
i_{gm}	Mean values of the Galvanic Current Density
I_{pass}	Passivation Current (µA)
I_{rms}	Root Square Mean of the Galvanic Current Density ($\mu A/cm^2$)
K	Constant Defines the Units for the Corrosion Rate
LI	Localisation Index
R	The Gas Constant (8.314 J/K.mol)
R_p	Polarization Resistance (ohms)

Greek Letters

α	Austenite Phase (bcc)
α'	Martensite Phase (bcc / bct)
β	Ni_3Al Precipitates
β_a	Anodic Tafel Constant (volts / decade)
β_c	Cathodic Tafel Constant (volts / decade)
γ	Austenite Phase (fcc)
γ’	Martensite Phase (fcc)
ε	Austenite Phase (hcp)
ε’	Martensite Phase (hcp)
ρ	Density (grams/cm^3)
σ_{Eg}	Standard Deviation of the Galvanic Potential Values
σ_i	Standard Deviation of the Mean Current Density Values
σ_{ig}	Standard Deviation of the Galvanic Current Density Values

LIST OF ABBREVIATIONS AND ACRONYMS

A_f	Austenite-finish-Temperature
A_s	Austenite-Start-Temperature
at. %	Atomic %
BCC	Body-Centered Cubic
BCT	Bocy-Centered Tetragonal
BSE	Backscattered Electron
CSCC	Chloride Stress Corrosion Cracking
EDS	X-Ray Energy Dispersive Spectrometry
Eh	Hydrogen Electrode
EIS	Electrochemical Impedance Spectroscopy
FCC	Face-Centered Cubic
GBP	Grain Boundary Precipitates
HCP	Hexagonal Close-Packed
IGC	Intergranular Corrosion
K	Kelvin
LPR	Linear Polarization Resistance Measurements
M_f	Martensite-finish-Temperature
M_s	Martetesite-Start-Temperature
MT	Martensitic Transformation
M	Molar
NCAT	FeNiCoAlTa Alloy
NCATB	FeNiCoAlTaB Alloy
^oC	Degrees Centigrade
RE	Rare Earth Element
RT	Room Temperature

SE	Superelasticity
SCE	Saturated Calomel Reference Electrode
SCC	Stress Corrosion Cracking
SEM	Scanning Electron Microscope
SMA	Shape Memory Alloy
SMAS	Shape Memory Alloys
SME	Shape Memory Effect
SMSS	Shape Memory Stainless Steel
SMSSs	Shape Memory Stainless Steels
T	Temperature
wt. %	Weight %
ZRA	Zero Resistance Ammeter

1. INTRODUCTION

Shape memory alloys (SMAs) are engineering materials that are able to remember their shape before deformation, and return to it, when the stimulus that caused this deformation is removed [1-7]. They are also known as smart alloys. They go through reversible solid-to-solid martensitic phase transformation, when a temperature, load, or magnetic field is applied to them. [1-7]. Nickel–titanium (Ni-Ti) alloys are the most commercially available SMAs, and are used mainly in medical applications [6, 8].

When Sato *et al.* [9] discovered the shape memory effect in Fe-30Mn-1Si in the early 1980s [9], iron-based SMAs have become more attractive due to their appealing mechanical properties, lower cost, high temperature range of application, and workability compared to the Ni-Ti SMAs [9-11]. This makes them potential candidates in applications such as solid-state actuators, fasteners and pipe couplings [12, 13]. Recently, researchers reported possible uses of these SMAs in civil engineering applications [14, 15]. However, almost all of the available Fe-based SMAs show non-thermoelastic martensitic transformation, resulting in poor superelasticity at room temperature [10, 16 - 19], which in turn reduces their applications. Maki *et al.* [20] were able to produce a thermoelastic martensitic transformation in Fe-Ni-Co-Ti SMA [20]. Nevertheless, the alloy exhibited only 0.7% elastic strain, which limits its practical applications [21]. Tanaka *et al*. [17], on the other hand, made a significant discovery when they introduced the Fe-28Ni-17Co-11.5Al-2.5Ta (NCAT) and Fe-28Ni-17Co-11.5Al-2.5Ta-0.05B (NCATB) SMAs. The addition of the tantalum (Ta), which is a strong martensite (γ') phase stabilizer, was found to increase the volume fraction of the γ' phase, resulting in a high hardness, and changing the transformation behaviour from non-thermoelastic to thermoelastic [17]. High transformation strains were observed in both NCAT and NCATB SMAs [17, 22, 23]. The NCAT and NCATB SMAs discovery opened a new era of room temperature (RT) applications of these alloys. The shape memory behaviour and the superelastic properties of the NCAT were documented [16, 21, 23 -27]. The corrosion properties

were, however, not studied. In order to use the NCAT as a pipe coupler or an actuator, it is important to investigate its corrosion properties.

1.1 Rationale and Knowledge Gap

Shape memory alloys (SMAs) are increasingly being used as alternatives to conventional engineering materials, except for Fe-based SMAs, which still have limited engineering applications due to their non-thermoelastic martensitic transformation. The development of NCAT SMA has opened the door for possible commercial applications of Fe-based SMAs. Although its shape memory properties have been well studied, currently, there is no documented study in the open literature that investigated the corrosion properties of NCAT SMA, which leaves a considerable knowledge gap regarding its practical applications. Therefore, there is a need to develop new scientific understanding of the corrosion characteristics of the NCAT SMA, which will help in determining how it might be used in commercial applications.

In this study, the corrosion properties of the alloy in different electrolytes and at different temperatures and levels of solution pH were documented. In addition, the galvanic corrosion of the alloy when coupled with commercial alloys was investigated. To the author's best knowledge, there is no study in the open literature that investigated the galvanic corrosion properties of Fe-based SMAs. This makes the results of this research an original scientific contribution, to NCAT SMA, and Fe-based shape memory alloys in general.

This research focused on addressing the corrosion knowledge gap regarding this alloy by answering the following questions:

1- What are the forms of corrosion and corrosion properties of NCAT SMA in 0.6 M NaCl, 0.5 M H_2SO_4, and 0.5 M NaOH at room temperature?
2- How is the corrosion resistance of the NCAT SMA compared to some other commercial alloys in 0.6 M NaCl solution?
3- What is the effect of heat treatment on the corrosion behaviour of NCAT SMA?
4- What is the effect of temperature and solution pH on corrosion properties of the alloy in 0.6 M NaCl solution?
5- How does the alloy behave when coupled to other commercial alloys?

1.2 Objectives

NCAT shape memory alloy has excellent shape memory properties including thermoelastic martensitic transformation ability. This makes it a potential material for a wide range of industrial applications. One of these is the use of this alloy as a pipe coupler. Pipe couplers are very desirable as they can be used to replace welding in pipeline construction. Welding and its associate heat affected zone are considered the weakest part of pipelines, where failures usually occur. Pipelines that carry oil and natural gas are distributed all over the world. The failure and leakage of these pipelines at welded sections will have significant negative impact on the environment and personnel health and safety. Since most of the oil and gas installations are located near the sea, and seawater is used in cooling systems in many plants, pipe couplers are subject to external and internal corrosion by salt water. This makes it crucial to investigate the corrosion behaviour of this SMA in marine environments.

This research study is based on the hypothesis that NCAT SMA is going to be used as a pipe coupler. This means that it will come into close contact with water, seawater, acid and alkaline solutions [5]. It will encounter OH^- ions in the alkaline fluids, and H_2S in oil and gas pipelines that would expose it to corrosion. Determining if the alloy is corrosion resistant to such solutions is important in order to determine whether it can be used as a pipe coupler for pipelines. In addition, pipe couplers join different types of alloys, which may expose them to galvanic corrosion attack. This makes it necessary to explore the effect of galvanic coupling on the corrosion resistance of NCAT SMA. Furthermore, aging heat treatment, which is necessary to achieve shape memory effect (SME) in NCAT SMA, could enhance or reduce the corrosion resistance of the alloy in corrosive environments. Investigating the effect of this heat treatment on the alloy's corrosion resistance in the studied solutions is crucial.

Based on the above hypothesis, the specific objectives of this research study are:

(i) To determine the corrosion behaviour of NCAT alloy in 0.6 M NaCl solution under different conditions of temperature and pH using electrochemical corrosion measurement methods.

(ii) To determine the galvanic corrosion properties of NCAT alloy when coupled to commercial alloys in 0.6 M NaCl solution at three different temperatures.

(iii) To determine the effect of aging heat treatment on microstructure and corrosion properties of the alloy in 0.6 M NaCl, 0.5 M H_2SO_4, and 0.5 M NaOH.

1.3 Research Impact

This research succeeded in creation of new knowledge about the corrosion behaviour of NCAT SMA in three corrosive environments. The new corrosion data generated can be used as a reference for materials selection of this alloy in 0.6 M NaCl solution, 0.5 M H_2SO_4, and 0.5 M NaOH. It also resulted in the development of a new, safe, and easy-to-prepare etching solution that reveals grain boundaries and grain boundary precipitates. Furthermore, this study gave new insights into the galvanic corrosion behaviour of the NCAT alloy when coupled to four commercially available steels. To the author's best knowledge, there is no documented study that explores the galvanic corrosion of Fe-based SMA. The results of this study will be beneficial to any future use of the NCAT SMA in applications such as pipe couplers.

1.4 Arrangement of Thesis Chapters

This dissertation is divided into five main chapters. In Chapter 1, background information on shape memory alloys and the rationale for the present study is presented. The objectives of the research project are outlined, the knowledge gap is identified, and the impact of this study is stated. In Chapter 2, a detailed review of SMAs, their properties, and applications is presented. A review of the corrosion studies that were conducted on Fe-based SMAs is also presented. In Chapter 3, details of the test materials, heat treatment procedures, and experimental techniques utilized for electrochemical testing, microstructural studies, and corrosion scale characterizations are described. The results of experiments carried out in Chapter 3 are presented and discussed in Chapter 4. The conclusions of the present research and recommendations for future research are presented in Chapter 5.

2. LITERATURE REVIEW

In this chapter, shape memory alloys with more focus on iron (Fe)-based shape memory alloys are discussed. It provides in-depth information on shape memory alloy properties and applications. In addition, the corrosion research studies on Fe-based shape memory alloys are summarized.

2.1 Shape Memory Alloys

Shape memory effect was first discovered by Arne Olander in a gold-cadmium (Au-Cd) alloy in 1932 [2, 28]. However, the breakthrough of their engineering significance did not take place until 1962 when Buehler and co-workers accidentally discovered the shape memory effect (SME) in a nickel-titanium (Ni-Ti) alloy [29]. Later, the alloy became known as NiTiNOL, a combination of the alloy composition (NiTi) and its place of discovery (the Naval Ordnance Laboratory) [30]. NiTi SMAs have been intensively investigated for several applications, and unto this day they are still the most important commercial SMAs due to their excellent recoverable strain, mechanical properties, superior corrosion, abrasion resistance, and biocompatibility [31- 34]. These attractive properties led to their use in a wide range of applications, mainly in orthodontic and other medical applications. However, they are expensive, used in limited range of temperature, and are challenging to process for large-scale applications [6, 8]. This made it necessary to research alternative alloys that display shape memory effect such as copper-based SMAs (e.g., Cu-Zn-Al, Cu-Al-Ni, and Cu-Al-Mn) and Fe-based SMAs (e.g., Fe-Mn-Si, Fe-Ni-Co (Ti, Al), Fe-Mn-Si-Ni-Cr, and Fe-Ni-Co-Al-Ta-B) [6, 8, 17]. Copper-based SMAs have the advantage of being less expensive, having high electrical conductivity, and possessing better ductility and machinability compared to NiTi SMAs [1, 4, 35]. They are most often used as actuator materials and in high temperature applications with nearly no degradation under thermal cycles [1, 8, 36, 37]. Fe-based SMAs have low cost, high strength, and good workability and weldability [5, 38-43]. They have shown a potential to be used in many applications [5, 8, 12, 36, 38, 41, 44-46]. This makes them the most attractive SMAs to many researchers.

2.2 Properties of Shape Memory Alloys

Shape memory alloys have two distinct properties: superelasticity (pseudoelasticity) and shape memory effect (SME) [1-7, 30, 47]. Superelasticity (SE) takes place when an alloy that has been deformed by an external load in a certain temperature range returns to its original shape and the deformation disappears after removing the load [2, 4, 30, 48, 49]. Shape memory effect, on the other hand, is the capability of remembering the alloy's shape before deformation and returning to it with full strain recovery when the alloy is heated above its austenite transformation temperature [30].

Shape memory alloys can exist in two different phases (austenite and martensite), with three different crystal structures (twinned martensite, detwinned martensite, and austenite). The unique properties of SMAs lies in their solid-to-solid phase transformation, also known as martensitic transformation (MT). The austenite phase structure is stable at high temperature, while the martensite phase structure is stable at lower temperatures. When SMAs are heated, they begin to transform from martensite to austenite at the austenite-start-temperature (A_s). This transformation ends when the austenite-finish-temperature (A_f) is reached. On cooling, they start transforming back to martensite at the martensite-start-temperature (M_s). This transformation ends when the martensite-finish-temperature (M_f) is reached. [1-7, 29, 30]. This type of phase transformation can be activated by stress, temperature, or magnetic field. A schematic of such a transformation is shown in Figure 2.1, in which a shape memory spring was deformed by the application of an external load in martensitic condition. When the applied load is removed, the deformed shape is recovered but not to the original undeformed condition. When the spring is heated over the reverse-transformation temperature, after removing the load, the undeformed original shape was recovered [7]. This behaviour consists of a number of different processes that depend on the applied stress and temperature [2, 7].

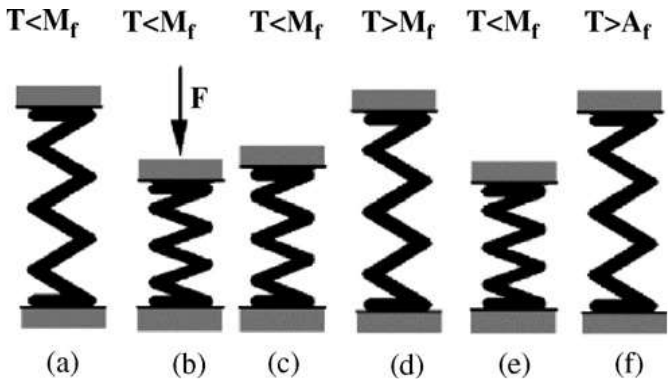

Figure 2.1. Cycles of a Cu-based shape memory spring: (a) original shape; (b) deformation; (c) removal of stress in martensitic condition; (d) heating over the martensite finish temperature; (e) cooling below the martensite finish temperature; (f) heating [7].

The mechanism by which the crystalline structure of the austenite phase transforms to martensite does not occur by diffusion of atoms but, rather, by shear lattice distortion. During martensitic transformation, atoms in the unit cell undergo a shear movement while maintaining their close relationships. Because the crystal structure of austenite is different than that of martensite, a macroscopic shape change occurs during the martensitic transformation, which is associated with local strains. These local strains are self-accommodated through the formation of twins in the martensite structure (twinned martensite) under stress-free conditions, resulting in no shape change in the SMA. When an external stress is applied on the twinned martensite, some martensite may detwin or reorient, resulting in a macroscopic shape change and an increase in the shape memory effect and superelasticity [30, 31]. Figure 2.2 illustrates this type of transformation.

The MT in Fe-based SMAs depends on the austenite and martensite crystal structure and can be categorized to three groups: (i) transformation between face-centered cubic (fcc) γ – austenite phase and body-centered cubic (bcc) or body-centered tetragonal (bct) α'- martensite phase. This type of transformation was observed in FePt, Fe-Ni-Co-Ti, Fe-Ni-Co-Al [20] and Fe-Ni-Co-Al-Ta [17]. (ii) transformation between (fcc) γ – austenite phase and hexagonal close-packed (hcp) ε – martensite phase. This type of transformation was recorded in Fe-Ni-Cr [33]. (iii) MT between (bcc) α – austenite phase and (fcc) γ' – martensite phase (not common). This type of transformation was reported in Fe-Mn-Al [16], Fe-Mn-Ga [50, 51] and Fe-Mn-Al-Ni [52] SMAs.

Shape memory effect and superelasticity of SMAs result from MT that is characterized by a small thermal hysteresis [10]. Most Fe-based alloys show poor or no SME due to their non-thermoelastic MT with a large thermal hysteresis [10, 15]. Many attempts have been made to

change the MT to a thermoelastic one by reducing the thermal hysteresis [20, 53, 54]. One of the effective methods is aging heat treatment that produces coherent-ordered precipitates [20, 53]. The tetragonality of martensite and the hardness of austenite are the controlling factors of thermoelastic MT. Both were found to increase in the presence of coherent-ordered precipitates [10, 20]. It was found that precipitation of LI_2 type ordered γ' phase and the resulting stress field created in the surrounding matrix changed the MT from non-thermoelastic to thermoelastic [17, 55].

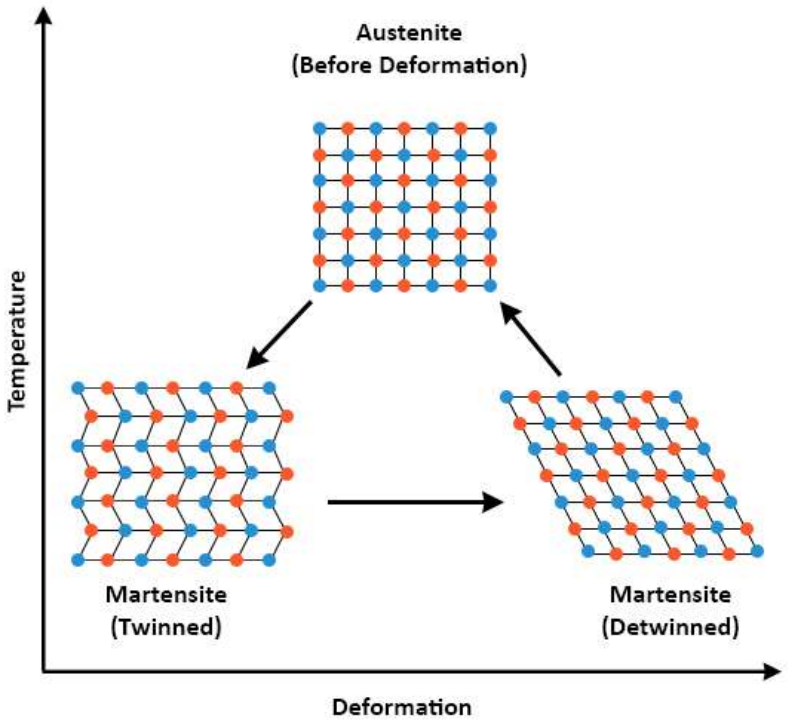

Figure 2.2. Demonstration of the martensitic transformation in SMAs, in which a change in temperature or a mechanical deformation results in shear lattice distortion.

2.3 Applications of Shape Memory Alloys

Shape memory alloys are unique due to their superelasticity and SME properties. These properties made them attractive to use in several applications such as those listed in the subsections below.

2.3.1 Aerospace Application

In aerospace application, SMAs are used mostly in actuation and vibration damping systems [30]. Actuators fabricated from SMAs have higher power-to-weight ratios than

conventional electro-mechanical actuators. In addition, they can act as both sensors and actuators [56-60]. There is high demand for SMAs actuators in aerospace applications [58-60]. One of the well-known applications is the DARPA/AFRL/NASA Smart Wing in which NiTi SMAs were used “as wire tendons to actuate hingeless ailerons and were also formed into torque tubes that initiated spanwise wing twist of a scaled-down F-18 aircraft wing.” [30]

2.3.2 Medical Applications

The SME and biocombatibility of NiTi SMAs made them suitable for use in medical applications such as stents, filters, orthodontic archwires, implants, bone fracture fixation plates and nails, and in devices for minimally invasive surgery [1-3, 30, 61-65].

2.3.3 Transportation Applications

SMAs have been used in several applications in automobiles, including impact absorption, sensing, and actuation. In addition, they are used in trains as actuators [30, 58-60].

2.3.4 Civil Engineering Applications

SMAs have recently been used in civil engineering field in such applications as passive vibration dampers, active vibration control, and actuators [66, 67]. The pre-stressing or tensioning of structures using fixed SMAs is one of the promising applications [68-70]. When SMAs are employed, the pre-stressing force is achieved by the SME, which eliminates the need for anchoring systems or hydraulic devices [68-70].

2.3.5 Pipe Couplers

The use of SMAs as pipe couplers was reported by several researchers [9,10, 12, 13, 20, 33, 38, 41, 44, 47, 71]. The most attractive SMAs for this application are the Fe-based SMAs due to their low cost and good mechanical properties.

2.4 Iron-based Shape Memory Alloys

When Sato *et al.* [9] encountered the SME in Fe-30Mn-1Si, Fe-based SMAs have become more attractive because of their appealing mechanical properties, their use in high range of temperature, workability, and lower cost compared to the NiTi SMAs [9-11, 72]. At the beginning, two groups of Fe-Mn-Si SMAs were developed, namely: Fe-28Mn-6Si-5Cr SMA and Fe-14Mn-

5Si-9Cr-5Ni SMA [9, 10]. Unfortunately, they showed poor shape recovery, resulting a need to enhance their SME by performing cycles of thermo-mechanical treatment known as "training" [5, 39-41]. The training consisted of several cycles of stress-induced γ (fcc) → ε (hcp) MT by deformation and then reversion of ε → γ by heating [5, 9, 39-41]. However, training requires high-energy consumption, thereby raising production cost. In addition, it is difficult to apply on parts with complex geometries [5, 40, 56]. This costly treatment dampened interest in using Fe-based SMAs in commercial applications. Hence, reduction of the number of training cycles to achieve significant SME became a notable research challenge [5, 40, 56, 73-75].

Kajiwara and his colleagues [10, 32, 76-80] made a significant contribution by developing a new method of manufacturing Fe-Mn-Si SMAs, which led to a significant reduction in the manufacturing cost [32, 76]. This method involved adding small amounts of niobium (Nb) and carbon (C) to the alloy, pre-deforming it either at elevated or room temperature, and then adjusting the aging treatment temperature and time to ensure that very small precipitates of Niobium carbides (NbC) were formed in the austenite. This improved the SME and made the training treatment redundant [32, 76]. Later, in other studies, Kajiwara et al. investigated the effect of aging time, temperature, and pre-rolling on the SME of Fe-Mn-Si SMAs at both RT and elevated temperatures [77, 78, 80]. They reported that cold/hot rolling or tensile deformation at room temperature before aging might refine NbC precipitates, which could act as nucleation sites for ε martensite and help in forming the very thin ε martensite of single variants, which could enhance the SME [79, 81]. They found that pre-rolling before aging at either elevated temperature or room temperature increased shape recovery, as well as shape recovery stress in Fe-Mn-Si alloys [80]. They attributed the improvement in shape memory properties to the uniform distribution of fine martensite plates that were mostly reversed to austenite when heated [39]. On the other hand, Stanford *et al.* [82] argued that rolling or tensile deformation at room temperature, followed by aging, should be considered as one cycle of thermo-mechanical treatment [82].

Most of the studies on the Fe-based SMAs focused on improving their properties by adding additional alloying elements to the alloy. Wen *et al.* [83] reported that $Cr_{23}C_6$ precipitates enhanced SME in Fe-Mn-Si-Cr-Ni-C SMAs [83], while Dong *et al.* [84] improved SME by precipitation of vanadium carbide (VC) [84]. In another study, shape recovery was improved with the precipitation of vanadium nitride (VN) [85, 86]. Kubo *et al.* [85] also developed an Fe–28Mn–6Si–5Cr SMA containing VN coherent precipitates. They managed to produce a large amount of shape recovery

strain in the SMA containing high-density formation of VN precipitates [85]. Cladera *et al.* [15] stated that if the amount of Cr exceeds 7% in Fe-based SMAs, brittle α phase will be introduced into the alloy which will impede the SME [15]. Maji *et al.* [87] reported the addition of Co to Fe-Mn-Si alloys up to 5 wt.% deteriorated shape recovery of the alloy. Co content greater than 5 wt.% improved shape recovery by forming precipitates within two-phase microstructures and resulted in high amounts of stress-induced ε martensite [87]. Lin *et al.* [88] added rhenium (Re) to Fe-30Mn-6Si-5Cr SMAs to improve their SME and concluded that properly combined treatments of pre-strain, aging, and training have to be applied to optimize shape memory performance [88]. Furthermore, Zhou [89] reported addition of rare earth elements (REs) to Fe-Mn-Si SMAs improved their shape memory properties significantly [89]. In another study, Bliznuk *et al.* [90] investigated the effect of nitrogen (N) and carbon (C) on the shape memory properties of a Fe–Mn–Si base SMA. They recorded larger recovered strain in the nitrogen-containing alloys in comparison to the carbon containing ones [90]. Their finding agreed with that of Jiang *et al.* [74] who reported that addition of a small amount of N to Fe-Mn-Si SMA increased the degree of shape recovery [74]. Koyama *et al.* [91] looked into the effect of adding 8 wt.% Si to Fe-17Mn-8Si-0.3C SMAs on the shape memory properties and found that it changed the microstructure from an austenite to an austenite/ferrite dual phase structure. The formation of ferrite was found to improve the yield strength and shape recovery stress of the alloy [91]. Maji and Krishnan [92] recommended limiting Si content in Fe-Mn-Si-Cr-Ni SMAs to 4-6 wt.%. They recorded poor shape recovery in alloys with Si <4% and >6% as a result of formation of α' martensite and δ-ferrite, respectively [92]. In another study, Shakoor *et al.* [93] found the addition of samarium (Sm) to Fe-Mn-Si-Cr-Ni SMA improved its strength and SME. Omori *et al.* [18] added Nb and B to Fe-Ni-Co-Al SMAs. They found the addition of Nb to change the MT from non-thermoelastic to thermoelastic, while the addition of B suppressed the formation of brittle grain boundary precipitates [18]. They reported 5% recoverable strain in the polycrystalline alloy [18].

Some studies investigated the effect of heat treatment on the shape memory behaviour of Fe-based SMAs. For example, increasing the aging time and temperature in Fe-Co-Ni-Ti SMAs was found to reduce the martensitic transformation temperature [94], increased transformation strain [95], increased the strength of austenite [95, 96], and increased the temperature range in which superelasticity was observed [95]. Liu *et al.* [97] increased the shape recovery ratio to 72% by increasing the aging time of Fe-Mn-Si-Cr-Ni SMA containing C, N, and V [97].

2.4.1 Applications of Iron-based SMAs

In addition to the superelasticity and SME, Fe-based SMAs have many attractive mechanical properties and are relatively low cost, which makes them suitable for several applications. Their primary use is as fasteners and pipe couplers [9, 10, 12, 13, 17, 20, 33, 38, 41, 44-47, 71]. Fe-Mn-Si SMAs were used as pipe couplings because they exhibited a thermally activated shape memory effect [9, 10, 20, 33, 71], while Fe-Mn-Si-Cr-Ni-(Co) SMAs, also known as shape memory stainless steels, were reported to be used in joints for oil pipes [12]. Yamauchi *et al.* [98] reported that Fe-Mn-Si-Cr SMAs have good formability, SME, and lower cost when compared to NiTi SMAs, which makes them ideal candidates for pipe coupling and fishplates [98]. Kubo *et al.* [85] developed a Fe–28Mn–6Si–5Cr SMA containing vanadium nitride (VN) coherent precipitates. To use this alloy for steel pipe joining in civil engineering applications, a proof stress over 350MPa and 3% of shape recovery are required. They achieved a proof stress of over 400MPa and 3.4% of recovery strain, which makes this alloy a suitable candidate for this application [85]. Li *et al.* [12] stated that alloy Fe-14Mn-6Si-9Cr-5Ni SMA exhibited good creep and stress relaxation resistance, high corrosion resistance in alkaline solutions, and tensile and sealing properties that fulfill the usual requirements for pipe joining in general industrial applications [12]. Nitrogen-alloyed Fe-Mn-Si-based SMAs were recommended for use as fasteners and actuator materials [8]. In addition, Fe-based SMAs were reported to be used in fishplates [17, 98]. Furthermore, a large number of Fe-based SMAs exhibit magnetic shape memory behaviour [33, 94, 99] which allows them to be used in sensing and energy harvesting [100, 101]. Another commercial use of Fe-based SMAs is in solid-state actuators [8, 12, 13, 36].

Recently, researchers reported the possible use of SMAs in civil engineering applications [14, 15]. Their desirable low-cycle fatigue resistance makes their use as vibration dampers very popular. These dampers can absorb vibration energy resulting from the external environment such as wind and earthquakes [47]. They were reported to be used in pre-stressing devices [8]. Cladera *et al.* [15] have conducted an extensive review of the use of Fe-based SMAs in civil engineering applications. They concluded that the use of Fe-based SMA tendons for repairing existing structures and reinforcing new structures is very promising due to their low cost and attractive properties such as good workability, weldability, and corrosion resistance. In addition, the alloys have higher elastic stiffness and a wider range of temperature application when compared to NiTi

SMAs. Furthermore, they exhibit no friction losses, and do not need hydraulic devices to apply the force.

2.4.2 The limitations of the Fe-based SMAs Applications

The main limitation in the use of Fe-based SMAs is that most of them show non-thermoelastic martensitic transformation, resulting in poor superelasticity at room temperature [10, 16-19] which, in turn, reduces their application. Maki *et al.* [20] were able to produce a thermoelastic γ [face-centered cubic (fcc)] / α′ [body-centered tetragonal (bct)] transformation in Fe-Ni-Co-Ti SMAs by precipitation of the γ′–$(Ni,Fe,Co)_3Ti$ phase with $L1_2$ structure. However, the alloy exhibited only 0.7% elastic strain, which limits its practical application [21]. It was not until 2010 that Tanaka *et al*. [17] made the biggest breakthrough in the Fe-based SMAs research when they found the best combination of alloy chemistry and microstructure suitable for obtaining a high level of superelasticity at room temperature [17], thereby widening the door of potential applications of the Fe-based SMAs. They introduced two grades of FE-based SMAs, namely: Fe-28Ni-17Co-11.5Al-2.5Ta (NCAT) and Fe-28Ni-17Co-11.5Al-2.5Ta-0.05B (NCATB) SMAs. The addition of tantalum (Ta), was found to increase the volume fraction of fine and coherent γ′ $(Ni,Fe,Co)_3(Al,Ta)$ precipitates with the $L1_2$ structure which led to a partial atomic ordering of the parent phase and high hardness, which changed the transformation behaviour from non-thermoelastic to thermoelastic [17]. High strength, great resistance to plastic deformation, and high transformation strains were observed in both NCAT and NCATB SMAs, with NCATB showing much larger values of superelastic strain (13.5%) — almost twice that of the commercial NiTi SMAs [17, 22, 23] — whereas the NCAT alloy showed 6.8 % superelastic strains for a single crystal specimen [102, 23]. Tanaka and co-researchers [53] also achieved excellent superelasticity in Fe43.5-Mn34-Al15-Ni7.5 polycrystalline SMAs by adding Ni to the Fe-Mn-Al alloy and producing nano-sized hard precipitates with B2 structure in the matrix of the alloy. The hard precipitates suppressed the dislocation plasticity during martensitic transformation, resulting in thermoelastic martensitic transformation [52].

2.5 NCAT and NCATB SMAs

The excellent shape memory behaviour of the NCAT and NCATB SMAs generated great interest among researchers to study their properties [16, 21, 23-27, 102 - 104]. Many of these

studies focused on improving the level of recoverable strains by using different aging heat treatments [17, 22, 25, 102, 103, 105-109]. Geng *et al.* [19] found that increasing aging time of NCATB SMAs resulted in the coarsening of precipitates, which changed the martensitic transformation from thermoelastic type to non-thermoelastic [19]. Ma *et al.* [103] also found that increase in aging time of NCAT SMAs increased their transformation temperature (martensite start temperature) [103].

Several studies investigated the effect of γ′ precipitates on the shape memory behaviour and superelastic properties of NCAT SMAs when different aging heat treatments were applied [22-24, 26, 102, 103, 105, 106]. Kroob *et al.* [106] observed substantial dependency of the cyclic transformation behaviour of the NCAT SMAs on the variation in the size of precipitates. Fine dispersed precipitates were found to improve cyclic stability [106]. In another study, Kroob *et al.* [26] found that the morphology of the precipitates greatly influenced the strain-temperature response during thermal cycling [26]. A high precipitates density was found to require low stress to activate martensitic transformation [26]. Evirgen *et al.* [24], in one such study, investigated the effect of aging heat treatment on superelastic response of a single crystal NCAT alloy in tension [24]. They reported a smaller γ′ precipitate size (3-4 nm) and lower transformation temperatures for samples aged at 700 ^{o}C for 7 h, as compared to samples aged at 600 ^{o}C for 90 h. The latter showed higher transformation temperatures and larger precipitate size of around 5 nm [24]. They reported high superelastic strains of up to 3.4%; however, this was still lower than the superelastic strains obtained for NCATB SMAs [17]. They attributed the difference in the superelastic strain to higher volume fraction of non-transforming γ′ precipitates and the lower volume fraction of transformation matrix [24]. Ma *et al.* [103] reported that γ′ precipitates have a large influence on the superelastic properties of the NCAT SMAs [103]. They explained that increasing the size of the precipitates results in more barriers to the MT (and thus more energy dissipation during transformation), and more irrecoverable strain [103]. In a different study, Ma *et al.* [22] found that experimentally observed transformation strain levels were lower than theoretically predicted levels. They attributed this to the presence of large volume fraction of non-transforming precipitates and incomplete martensite reorientation [22, 103]. Depending on the heat treatment performed, the volume fractions of these precipitates could reach 20-38% in NCAT SMAs [102, 103]. Chumlyakov *et al.* [25] reported differences between experimental and theoretical reversible strain values in single crystals of NCAT SMAs, with the latter having higher values [25]. They

attributed these differences to the presence of TaC particles that resulted in limiting the plasticity of the alloy. These particles were formed during the smelting of polycrystalline ingots and did not dissolve during subsequent homogenization [25]. Although the theoretical and experimental strain values of the NCAT SMA were different, the experimentally observed transformation strains are still much larger than the ones reported in other SMAs, such as Fe-Ni-Co-Ti SMAs [22]. In addition, the alloy shows considerable magnetic properties [22]. The magnetic properties of the NCAT SMAs, combined with their large transformation strain levels and relative low cost, make these alloys potential candidates for a wide range of engineering applications such as actuators and pipe couplers.

2.6 Corrosion Behaviour of Fe-based SMAs

This section summarizes the corrosion research study that was conducted on Fe-based based SMAs. An introduction to the concept of corrosion engineering and its basics is presented in Appendix A.

Much research on Fe-based SMAs focused on improving the corrosion resistance by alloying methods [5, 8, 38, 40, 41, 46, 75, 85, 90, 110 - 112]. Almost all of the studies were focused on Fe-Mn-Si SMAs [5, 8, 38, 40-42, 45, 75, 110, 111, 113-121]. For example, Ullakko *et al.* [8, 122] found that the addition of nitrogen (N) to Fe-Mn-Si and Fe-Mn-Si-Cr- Ni SMAs enhanced the SME, mechanical, and corrosion properties of these alloys [8, 122]. Wan *et al.* [5] reported similar findings. In another study, Charfi *et al.* [42] investigated the effect of Zn electroplated coating followed by chromate conversion treatment on the corrosion resistance of Fe-32Mn-6Si SMA [42]. They reported an improvement in the polarization resistance of the alloy. They noticed that the chromium layer passivated the zinc coating layer, thereby enhancing the corrosion resistance.

The corrosion behaviour of Fe-Mn-Si SMAs in 3.5 wt. % NaCl solution was studied by several researchers. Huang *et al.* [113] investigated the effect of the addition of a rare earth element (RE) on the corrosion behaviour of Fe-25Mn-6Si-5Cr SMAs in 3.5 % NaCl solution [113]. They found that such an addition enhanced the corrosion resistance of the alloy. They also observed the best corrosion resistance in the alloy containing 0.16 wt. % RE [113]. Soderberg *et al.* [41] and Maji *et al.* [45] did not observe any passivity or pitting in Fe-Mn-Si-Cr-Ni SMAs containing 9-12 wt.% Cr in 3.5% NaCl solution [41, 45], whereas Lin *et al.* [38] observed both passivity and pitting

in a similar alloy that contained more than 5 wt.% Cr [38]. Zhang *et al.* [114, 115] also observed pitting in Fe-Mn-based SMAs that were tested in 3.5 wt.% NaCl solution. These alloys had Al or Cr additions or a combination of both [114, 115].

Furthermore, the corrosion behaviour of Fe-Mn-based SMAs was investigated in other solutions. Zhang *et al.* [114, 115] reported passivity in neutral solutions (1M Na_2SO_4), basic solutions (10-50% NaOH), and in oxidizing acids (50% HNO_3). They didn't observe any passivity in reducing acids (10% HCl) and 3.5 % NaCl solutions [114, 115]. Li and Dunne [116] developed Fe-Mn-Si-Al-Cu and Fe-Mn-Si-Cr-Cu SMAs. The alloys showed better SME and corrosion resistance in HCl, H_2SO_4, and 3.5 wt. % NaCl solutions than the conventional Fe-Mn-Si SMAs. Alloying with Cu improved the corrosion resistance and passivation in acidic solutions, but did not seem to have any impact on the corrosion resistance of the alloy in 3.5 wt. % NaCl solution [116]. In another study, high Si content in Fe-Mn-Si SMAs (>14.5 wt.%) was found to enhance the corrosion resistance in acidic environments [110], but, at the same time, it promoted the formation of brittle sigma phase [110]. For this reason, the Si content in Fe-Mn-Si SMAs is recommended not to exceed 5-6 wt. %, and Mn is added to these alloys to control the MT temperature [75]. However, it was found that this latter addition could decrease the corrosion resistance of the alloy. Therefore, the addition of Cr or Al was recommended to improve the alloy's corrosion resistance [117]. Moriya *et al.* [118] reported that adding Cr to Fe-Mn-Si SMAs improved their corrosion resistance [118]. Furthermore, Fukai *et al.* [119] reported Cr had a large effect on the oxidation resistance of Fe-Mn-Si-Cr SMAs [119]. Balo *et al.* [120] found the addition of Cr to Fe-Mn-Si SMAs improved their corrosion resistance [120]. Peng *et al.* [40] and Otsuka *et al.* [75] reported similar findings, whereas Uhlig [110] argued that Cr content > 7 wt. % in a binary Fe-based SMA caused more brittle sigma phase to form. He recommended that Ni be added to impede sigma phase formation [110]. Wang *et al.* [111] and Otsuka *et al.* [75, 121] found that simultaneous addition of Cr and Ni to Fe-Mn-Si based SMAs enhanced both their corrosion resistance and SME. Fe-Mn-Si-Cr-Ni SMAs are also known as shape memory stainless steels (SMSSs). Wan *et al.* [5] compared the corrosion behaviour of three different Fe-Mn-Si-based SMAs (Fe-25Mn-6Si, Fe-25Mn-6Si-5Cr, and Fe-25Mn-6Si-5Cr-(0.12-0.14)N) in NaCl, NaOH, and HCl aqueous solutions. The best corrosion resistance was observed in the alloy that was microalloyed with nitrogen (N) intentionally added (i.e. Fe-Mn-Si-Cr-N) SMA [5]. In their research, Lin *et al.* [38] investigated the corrosion behaviour of three different Fe-Mn-Si SMAs

(Fe-30Mn-6Si, Fe-30Mn-6Si-5Cr, and Fe-13Mn-5Si-12Cr-5Ni) in 3.5 wt. % NaCl solution. Alloy Fe-13Mn-5Si-12Cr-5Ni, which is an SMSS alloy, showed the best corrosion resistance as shown in Figure 2.3, while alloy Fe-30Mn-6Si-5Cr suffered from severe localized corrosion in the form of pitting when it was immersed in the NaCl solution for 20 days [38]. Alloy Fe-30Mn-6Si was protected by a corrosion scale, but as soon as the scale was detached, the corrosion rate increased rapidly [38]. Additionally, Lin *et al.* [38] investigated the stress corrosion cracking (SCC) resistance of the three SMAs. The SMSS exhibited the highest fracture stress in atmospheric environment compared to the other two SMAs. When tested in saturated H_2S aqueous solution, its fracture stress showed the largest drop compared to the other two alloys. The authors attributed this behaviour to its elongated grain structure and the presence of α –martensite that contained high dislocation density. These two microstructural features usually facilitate surface cracking. In the presence of Ni, hydrogen atoms tended to accumulate on the surface, where cracks were located, resulting in hydrogen embrittlement of the alloy, which in turn reduced its fracture stress. Furthermore, Lin *et al.* [38] investigated the effect of annealing on the corrosion behaviour of the three SMAs. They reported the annealing at 1000 ^{o}C for 2 h increased the corrosion potential of Fe-30Mn-6Si SMA due to the formation of α-ferrite [38]. In contrast, Fe-30Mn-6Si-5Cr SMA became more active after annealing, whereas SMSS showed an increase in the corrosion current and no change in the corrosion potential [38]. It appears from all these studies that the SMSS alloy has a better corrosion resistance than the other Fe-Mn-Si SMAs studied. The literature review did not come across any study that investigated the galvanic corrosion resistance of Fe-based SMAs.

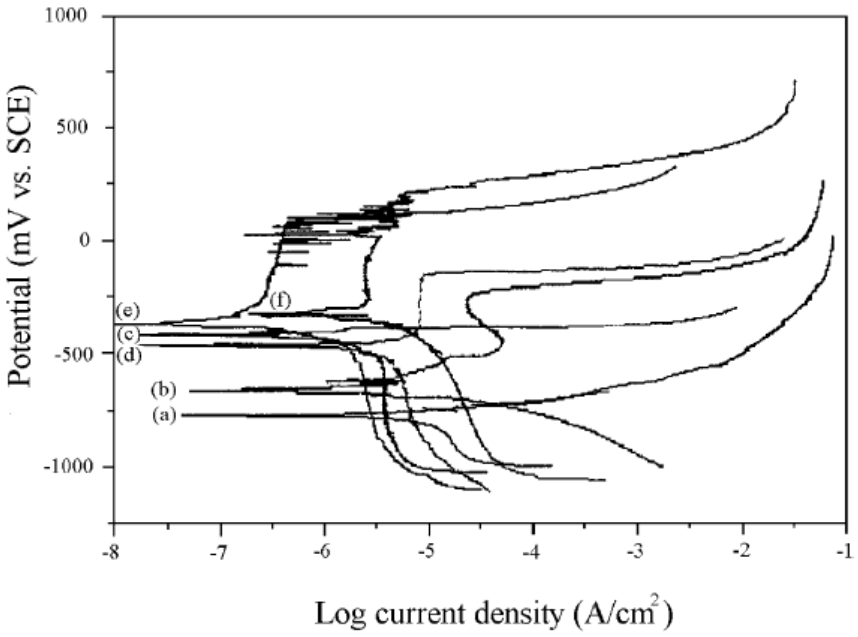

Figure 2.3. Polarization curves of various Fe-based SMAs: (a) as-rolled Fe-30Mn-6Si, (b) annealed Fe-30Mn-6Si, (c) as-rolled Fe-30Mn-6Si-5Cr, (d) annealed Fe-30Mn-6Si-5Cr, (e) as-rolled Fe-13Mn-6Si-12Cr-5Ni, and (f) annealed Fe-13Mn-6Si-12Cr-5Ni [38].

2.6.1 Corrosion Behaviour of Shape Memory Stainless Steels (SMSSs)

Several efforts have been made to improve the corrosion resistance of Fe-Mn-Si SMAs through alloying with corrosion resistant elements such as Cr and Ni [75, 121, 123] and/or interstitial atoms such as N [5] to produce what is generally known as shape memory stainless steels (SMSSs). SMSSs have been the subject of several corrosion studies to determine the effect of alloy chemistry on their corrosion behaviour and to evaluate their corrosion resistance in several solutions [38, 41, 45, 124]. Li *et al.* [12] reported high corrosion resistance and passivation for Fe-14Mn-6Si-9Cr-5Ni in alkaline solutions. The corrosion resistance was four to five times better than that of 304 and 316 stainless steels [12]. Della Rovere *et al.* [124] investigated the corrosion behaviour of three grades of Fe-Mn-Si-Cr-Ni-(Co) SMA in 0.5 M H_2SO_4 solution [124] and reported that the passive current density in the SMSS was similar to that of type 304 austenitic stainless steel [124]. They observed that the amount of Cr and Mn played a significant role in the corrosion behaviour of the alloy in H_2SO_4 solution [124]. They also observed the best corrosion behaviour in the alloy containing high amounts of Cr and low amounts of Mn. The characteristics of the passive film formed on Fe-Mn-Si-Cr-Ni-(Co) SMA that was tested in 0.5 M H_2SO_4 solution was investigated in more than one study [124-126]. It was found that the protectiveness of the

passive film on the SMA is similar to that of the passive film on the 304 stainless steel. Furthermore, Si was found to play an important role in the protectiveness of the passive film by forming an iron-chromium-mixed silicate film [125, 126]. When the alloy was tested in 3.5% NaCl solution, poor corrosion resistance compared to 304 stainless steel was reported [126]. The addition of Cu was found to improve the corrosion resistance of Fe-14Mn-5Si-9Cr-5Ni SMA in Cl^--containing solutions [46]. In another study [39], the addition of Nb was found to improve the corrosion resistance of SMSSs [39].

Heat treatment and shape memory training affect the corrosion resistance of SMSSs. Liu *et al.* [97] found that aging heat treatment reduced the corrosion resistance of Fe-Mn-Si-Cr-Ni SMA containing C, N, and V. The reported corrosion rate of the aged alloy was nearly three times higher than that of the unaged alloy in 0.5 M H_2SO_4 solution [97]. The alloy exhibited passivation in H_2SO_4 solution, whereas when tested in 3.5% NaCl solution, it did not show any passivation and suffered from localized corrosion (pitting) [97]. Figure 2.4 shows the potentiodynamic polarization curves obtained from samples with various aging times. The samples were tested in 0.5 M H_2SO_4 and 3.5% NaCl solution. Soderberg *et al.* [41] examined the effect of the shape memory training on the corrosion behaviour of Fe–Mn–Si–Cr–Ni SMAs. They reasoned that deformation during the shape memory training by cold rolling decreased the corrosion resistance of the alloy, and recovery heating further reduced the corrosion resistance. They also found that Cr and Mn had a significant influence on the shape memory effect and corrosion behaviour of the alloy. They observed that increasing Mn and decreasing Cr contents improved the shape memory effect but reduced the corrosion resistance of the alloy. On the other hand, Ni, N and V were found to enhance the corrosion resistance of the alloys. Maji *et al.* [45] heat treated several Fe-15Mn-7Si-9Cr-5Ni SMA samples to produce three different microstructures and investigated the corrosion behaviour of the samples in 0.5 M H_2SO_4 and 3.5% NaCl solutions. They found the corrosion behaviour in H_2SO_4 solution to be almost the same for all the tested samples, with very slight variation in the passivation range [45]. They also found that the passivation current density was nearly the same as that of 304 stainless steel [45]. In the NaCl solution, no passivation was observed. The three microstructures showed general dissolution without passivity or pitting [45]. They observed the best corrosion resistance in the alloy with a single-phase austenite microstructure [45].

In a study that was conducted by Nishimura [127, 128], the atmospheric corrosion resistance of Fe-Mn-Si-Cr-Ni SMAs was investigated using the wet and dry corrosion test containing NaCl solution. In addition, he conducted electrochemical impedance spectroscopy testing (EIS) as part of the study in order to understand the electrochemical behaviour of the alloy. He compared the corrosion behaviour of the alloy with that of carbon steel. His test results showed much higher corrosion resistance for the SMSS compared to carbon steel, which was due to the formation of a passive film on the surface of SMSS [128]. Nishimura [127, 128] analyzed the passive film and observed that it contained Fe, Mn, Cr, Si, and Ni, and oxygen. He found that the passive film consisted of three layers of Fe oxides, namely: (i) a Mn-rich outer layer, (ii) a Cr-Si-rich inner layer, and (iii) an interface layer. The corrosion resistance was primarily dependent on the Cr-Si layer, and was further supported by the Mn enriched layer. Another study by Lee *et al.* [66] compared the corrosion behaviour of Fe-17Mn-6Si-10Cr-4Ni-1(V, C) SMA with a reference structural steel material (EN 10149 PT2) to determine if the SMSS was suitable to use as a reinforcing element in pre-stressed concrete structures [66]. The SMSS was tested in simulated concrete pore solutions. They observed superior corrosion resistance of the SMSS alloy over the reference structural steel. They concluded that the SMSS could be used as a pre-stressed reinforcing element in concrete without any corrosion issues [66].

Although the SMSS showed an improved corrosion behaviour in different solutions and corrosion environments compared to other Fe-based SMAs, its commercial application is still very limited due to its non-thermoelastic MT, which makes it difficult to use. The thermoelastic MT, excellent shape memory properties, and high strength of the NCAT and NCATB SMAs make them appropriate for commercial applications. Although shape memory behaviour and the superelastic properties of NCAT and NCATB have been well studied [16, 17, 21, 23-27, 103, 104, 105], surprisingly, not a single study investigated their corrosion behaviour in the open literature. In order to use these alloys as pipe couplers or actuators, it is important to fill the knowledge gap in their corrosion behaviour in a variety of solutions and environmental conditions.

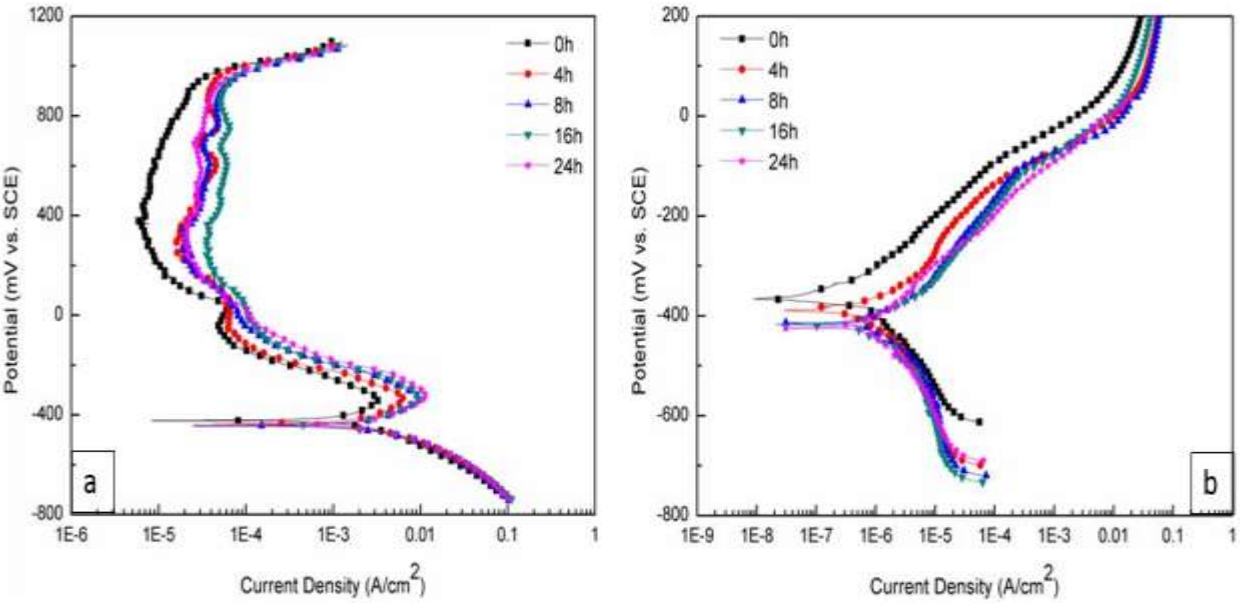

Figure 2.4. Potentiodynamic polarization curves acquired from Fe-Mn-Si-Cr-Ni SMA containing C, N, and V elements that were aged using various aging times in (a) 0.5 M H_2SO_4 solution, (b) 3.5% NaCl solution [97].

3. METHODS AND MATERIALS

The use of NCAT SMA is very promising in several applications such as pipe couplings and actuators and in several industries including oil and gas industry. The fact that pipe couplings are exposed to different solutions with different pH and at different temperatures makes it necessary to investigate the corrosion behaviour of this alloy in such environments. In this chapter, details of the tested alloys and the corrosion and materials characterization tests that were conducted to understand the behaviour of the NCAT SMA in corrosive environments are presented.

3.1 Materials

The main alloy investigated in this study is Fe-28Ni-17Co-11.5Al-2.5Ta (at%) (NCAT) SMA. It was extruded at 950 ^{o}C to make cylindrical-shaped specimens with a diameter of 10.08 mm and length of 13 mm. The specimens were supplied in the heat treated condition. The heat treatment was conducted in a high purity argon atmosphere in Thermo Scientific Lindberg blue M box BF Furnace in Texas A & M Laboratory in College Station, USA. The heat treatment was conducted following the procedures that were found in the literature [24, 26, 102, 103, 106]. Two sets of specimens were produced after the heat treatment: (i) Specimens that were solution-treated at 1300 ^{o}C for 24 h. The specimens do not exhibit any shape memory effect. These specimens were compared with aged specimens to study the effect of the aging on the alloy's corrosion properties. (ii) Specimens that were solution-treated at 1300 ^{o}C for 24 h to obtain a γ-single phase structure, and then aged at 600 ^{o}C for 90 h to allow the γ'-$(Ni,Fe,Co)_3(Al,Ta)$ phase to precipitate. These specimens exhibit shape memory effect (SME) and superelasticity [24, 26, 102, 103, 106]. The focus on this study will be mostly on these aged NCAT SMAs.

Shape memory alloys' composition is usually determined in at%. The composition of NCAT in at% was found to be 41.4 (±0.05) Fe, 27.4 (±0.04) Ni, 17.3 (±0.02) Co, 11.1 (±0.04) Al and 2.6 (±0.02) Ta. Table 3.1 shows the chemical composition (in wt%) of NCAT alloy and those

of four commercially available alloys with which its performance in corrosive environments was studiedThe tests that were conducted are presented in the experiment chart in Figure 3.1.

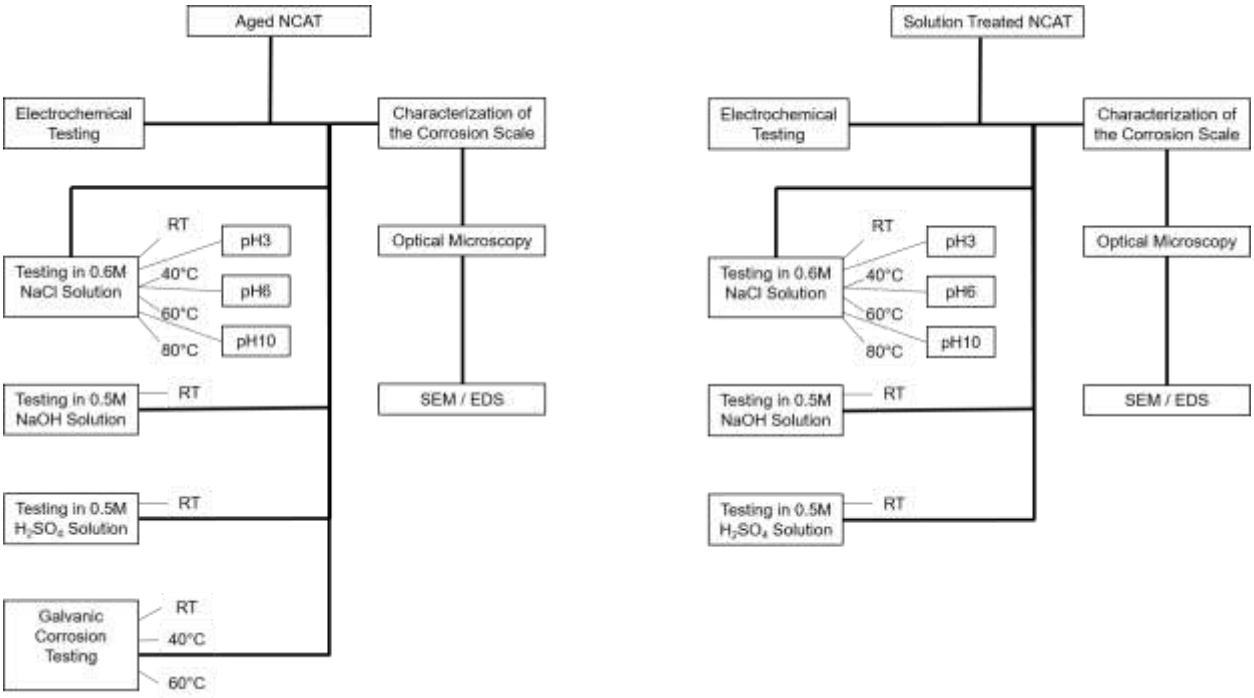

Figure 3.1. Flow chart of tests conducted in this study.

3.2 Electrochemical Testing

Several electrochemical tests were conducted to understand the corrosion behaviour of NCAT SMA. Tests were carried out to determine: the effect of heat treatment; coupling with other alloys; and change in temperature, pH, and electrolyte. The tests included:

(i) electrochemical corrosion testing at room temperature (RT) of aged and solution treated NCAT SMA in a 0.6 M NaCl solution with different pH (3, 6, and 10), 0.5 M H_2SO_4 solution, and 0.5 M NaOH; (ii) electrochemical corrosion testing of aged and solution treated NCAT SMA in a 0.6 M NaCl solution at 40 °C, 60 °C, and 80 °C; (iii) electrochemical corrosion testing the commercial alloys in 0.6 M NaCl solution at RT and 60 ^{o}C; and (iv) galvanic corrosion testing of NCAT SMA and commercial alloys in 0.6 M NaCl at different temperatures (RT, 40 °C, and 60 °C). Each test was repeated until three identical curves were acquired. During the electrochemical testing, the temperature and humidity was monitored and adjusted when needed.

Details of these tests are presented in the following sections.

Table 3.1. Chemical compositions (wt%) of NCAT and the commercial alloys used in this study.

Alloy	Fe	C	Si	Mn	P	S	Cr	Mo	Ni	Cu	N	Ti	Co	Al	Ta
NCAT FeNiCoAlTa	40.4	-	-	-	-	-	-	-	28.1	-	-	-	17.8	5.27	8.31
1018 UNS G10180	99.3	0.20		0.90	0.04	0.05	-	-	-	-	-	-	-	-	-
304 UNS S30400	71.2	0.03	0.33	1.45	0.03	0.03	18.25	0.22	8.1	0.28	0.06	0.002	-	-	-
316L UNS S31603	68.9	0.02	0.41	1.33	0.03	0.03	16.66	2.03	10.1	0.45	0.04	-	-	0.0001	-
2750 UNS S32750	62.2	0.02	0.41	0.80	0.02	0.001	25.15	3.90	6.9	0.30	0.25	-	-	-	-

3.2.1 Sample Preparation

Each specimen used in electrochemical corrosion tests was connected to a copper wire using a conductive silver epoxy. The specimens were then embedded in a non-conducting epoxy resin so that only the circular surface of the specimens was exposed to the electrolyte. Figure 3.2 shows an example of a typical test specimen. The specimens were wet ground with 240-grit SiC paper and wet polished with 600-grit SiC paper. Prior to immersion in the electrolyte, the specimens were cleaned with ethanol in an ultrasonic cleaner, rinsed with distilled water, and then dried. After testing, the specimens were wet ground to remove the corroded scale, and the epoxy resin was removed and replaced with a fresh one to reduce the possibility of crevice corrosion. The samples were then polished and reused in another electrochemical test.

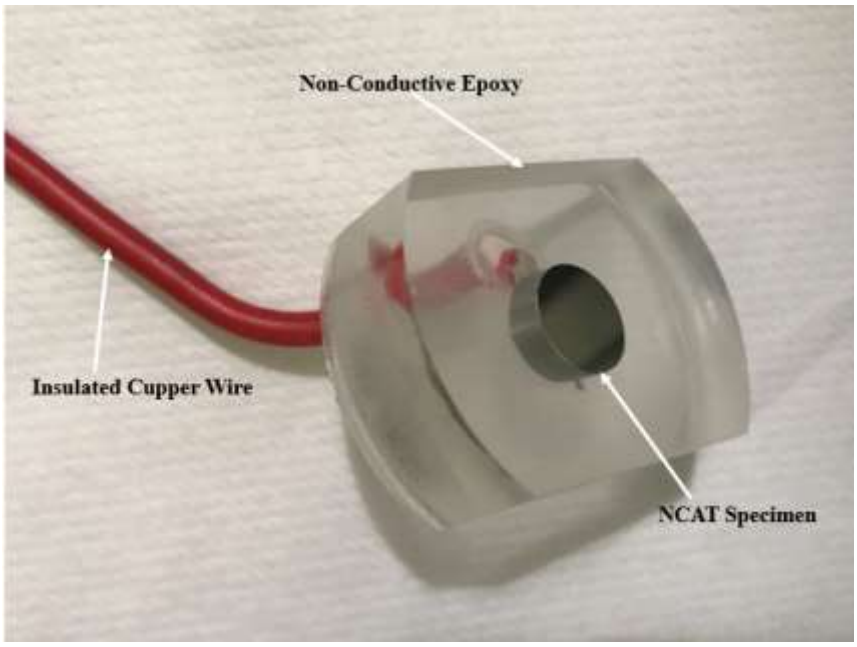

Figure 3.2. An image of a typical electrochemical test specimen that was used in this study.

All electrochemical measurements were carried out using a Gamry Reference 600 potentiostat/galvanostat and its accessories including the reference electrode. The equipment and accessories are manufactured in the USA. The testing was conducted with the test electrolyte exposed to the air. A three-electrode test cell — with a graphite counter electrode, a saturated calomel reference electrode (SCE), and the test specimen as a working electrode — was used in this study. The electrochemical test set-up is illustrated in Figure 3.3. All potentials were

referenced to SCE. All the solutions were made from distilled water and analytical grade chemicals manufactured in Germany by Millipore Sigma. When the test was conducted at temperatures higher than room temperature (RT), a Fisher Scientific ISOtemp digital control water bath model 220 that was made in the USA was used to heat the test solution within ±1 ^{o}C accuracy. In all the experiments, the tests were repeated at least three times until three curves were produced with similar electrochemical parameters. Appendix A shows examples of potentiodynamic polarization scans for aged and solution treated NCAT SMA in 0.6 NaCl at RT and pH of 6. The curves presented in this document are typical of the obtained results. The tests that were performed included the following:

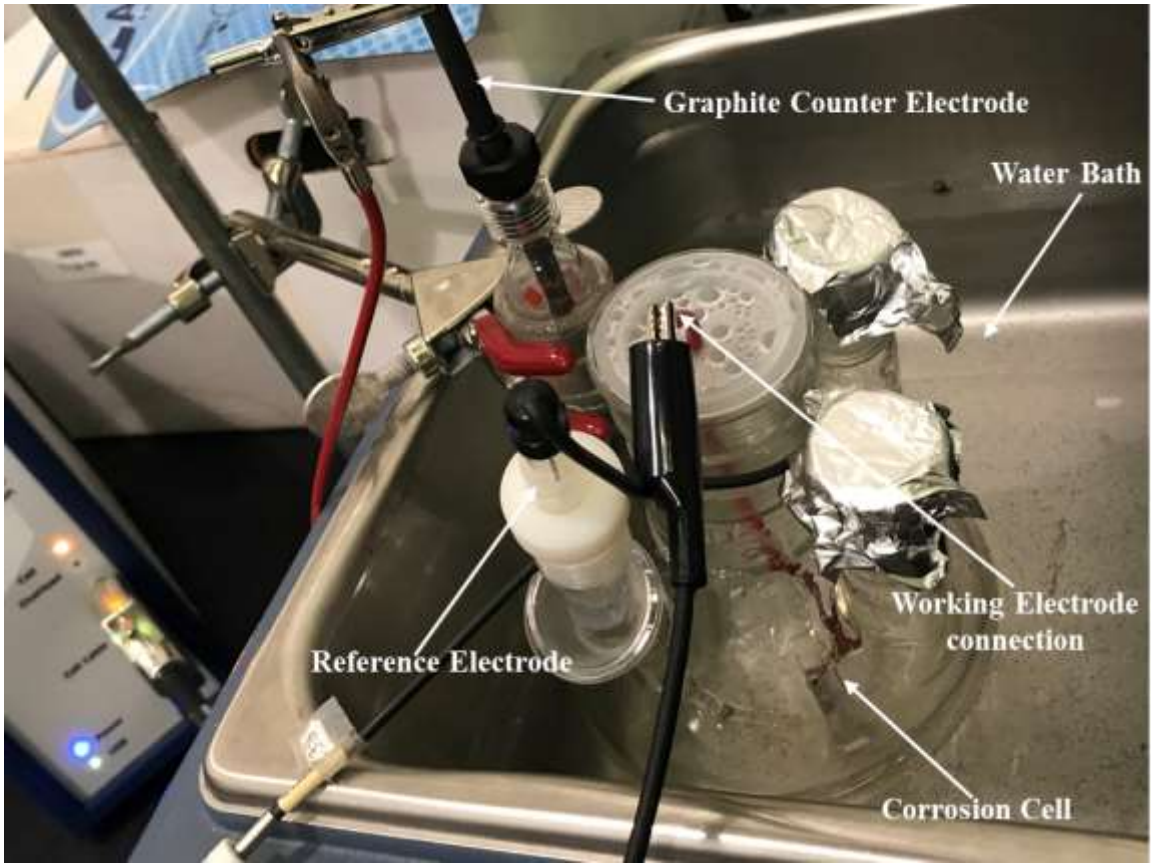

Figure 3.3. Image of the electrochemical test apparatus placed in a water bath showing the three electrodes and cell.

3.2.2 Open Circuit Potential Measurement

The open circuit potential (also known as rest potential) indicates the thermodynamic propensity of a material to corrode in a given solution. In this test, there is no current flow through the specimen. It just measures the open circuit potential (E_{oc}) of the specimen as it changes over time. This method is used to give a quick indication of the alloy's ability to corrode. The graphical result is a plot of potential-vs-time (Figure 3.4). The part of the curve that shows a stable potential can be used to determine the open circuit potential of the alloy. In this test, the specimens were immersed in the test solution for one hour, during which time the voltage between the reference electrode and the working electrode (specimen) was measured. Figure 3.3 shows a typical result obtained for an aged NCAT SMA in 0.6 M NaCl solution.

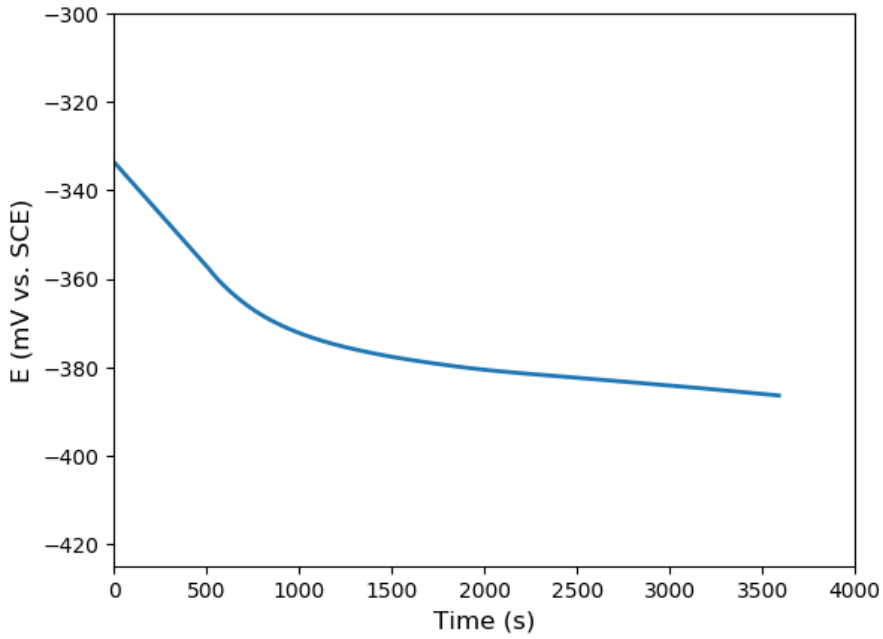

Figure 3.4. An example of the result obtained from open circuit potential (rest potential) measurement of an aged NCAT SMA in a 0.6 M NaCl solution at RT.

3.2.3 Linear Polarization Resistance Measurement (LPR)

This test was used to obtain the polarization resistance of the test specimen and provide an estimate of its corrosion rate in the test solution. During the test, a slow sweep of potentials from -20 to 20 mV versus the (E_{oc}) was conducted at a scan rate of 0.167 mV s^{-1} following ASTM G59-97 standard [129]. This method is very quick, and since the applied potential is small, the surface of the sample is not polarized and is not affected by the test. All the specimens were immersed

into the electrolyte at E_{oc} for 1 h before the test. As the applied voltage was small, the current response was roughly linear. The polarization resistance (R_p) was estimated from the slope of the current-vs-voltage curve. A schematic of a linear polarization scan is presented in Figure 3.5. The polarization resistance could be used to calculate the corrosion current density (i_{corr}) and the corrosion rate (CR) if the Tafel slopes are known, as described in section 3.2.5.

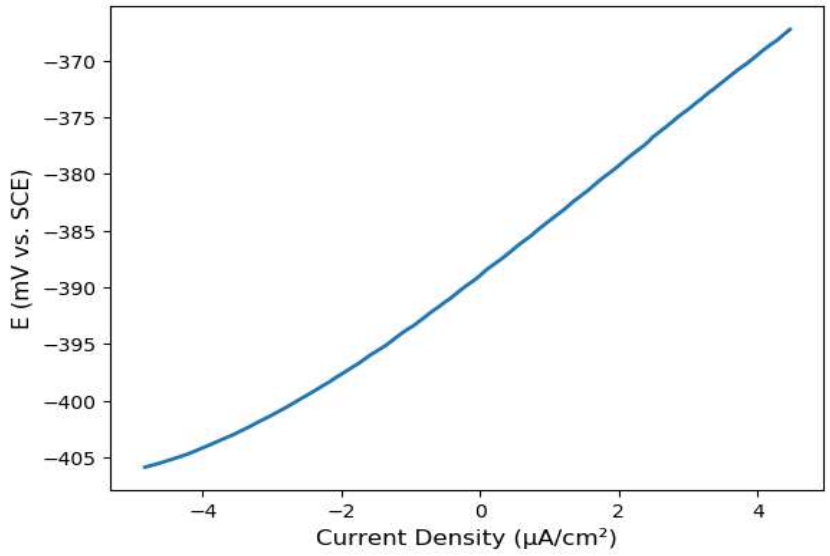

Figure 3.5. An example of a typical linear polarization resistance curve obtained for an aged NCAT SMA in 0.6 M NaCl solution at RT.

3.2.4 Potentiodynamic Polarization Measurement

This technique was used to characterize the overall corrosion behaviour of the test specimens and estimate their corrosion current densities (i_{corr}). It measures the current during a large potential sweep from the cathodic to the anodic region of the working electrode. During this sweep, the specimen undergoes different electrochemical reactions. ASTM G5-14 test standard was used in this test [130]. The data obtained were displayed in potential-vs-logarithm of the current density plots as shown in Figure 3.6. Analysis of the resulting curves yields the following information: (i) corrosion potential (E_{corr}), (ii) corrosion current (I_{corr}) and corrosion current density (i_{corr}); (iii) anodic and cathodic Tafel slopes (obtained from the linear extrapolation of the anodic and cathodic regions of the polarization curve); and (iv) corrosion rate (CR) that can be calculated using the above parameters, as will be described later in section 3.2.5.

The potentiodynamic polarization scans were carried out immediately following the linear polarization resistance tests. The specimens were not removed from the solution after the LPR test, since the test does not polarize or affect the specimens' surfaces. The scans were conducted from -200 mV with respect to E_{oc} to the anodic direction with a scan rate of 0.167mV/s. Corrosion current density (i_{corr}) and corrosion potential (E_{corr}) were obtained from the potential-vs-current density curves, whereas Tafel constants (β_a and β_c) were estimated from linear fits to the curve as illustrated in Figure 3.5.

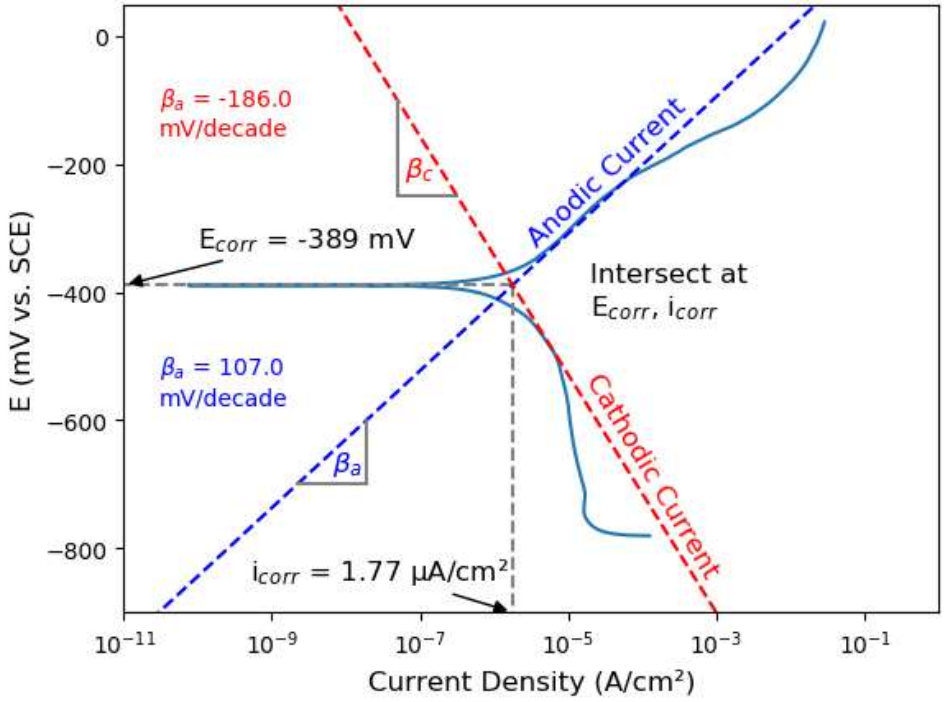

Figure 3.6. An example of the potentiodynamic polarization curve of aged NCAT in a 0.6 M NaCl solution at RT, showing how the corrosion parameters are identified.

3.2.5 Corrosion Rate Determination

The corrosion rate can be calculated from the parameters obtained in linear polarization resistance measurements or from the potentiodynamic polarization scans as follows:

I. Corrosion Rate Produced from Potentiodynamic Anodic Polarization Measurements

Tafel analysis is performed to estimate E_{corr}, i_{corr}, β_a, and β_c using Gamry Instruments' DC105 DC Corrosion Techniques software. The obtained parameters are then used in Butler-Volmer equation (3.1) to determine the corrosion current.

$$I = I_{corr}\left(e^{\left(\frac{2.3(E-E_{oc})}{\beta_a}\right)} - e^{\left(\frac{(-2.3(E-E_{oc})}{\beta_c}\right)}\right) \quad (3.1)$$

where, I = the measured cell current in amps, I_{corr} = the corrosion current in amps, E = the electrode potential in Volts, E_{oc} = the corrosion potential in Volts, β_a = the anodic Tafel constant in volts / decade, and β_c = the cathodic Tafel constant in volts / decade.

The calculated I_{corr} was then used to calculate CR from equation (3.2),

$$CR = \frac{i_{corr}\, K\, EW}{\rho a} \quad 3.2$$

where K = a constant that defines the units for the corrosion rate, EW = the equivalent weight of the specimen in grams/equivalent, ρ = density of the specimen in grams/cm^3, and A = cross-sectional area of the specimen in cm^2. EW is calculated by dividing the sum of the molecular weight of the dissolved substance in the solution (in grams) by the valence of these dissolved substances. The values of EW, ρ, and A in 0.6 M NaCl solution are provided in Table 3.2, while constant K values are given in Table 3.3. The corrosion rate units depend on the choice of the constant K as illustrated in Table 3.2.

Table 3.2. The values of density, equivalent weight, and surface area for the samples that were used in the electrochemical testing.

Material	ρ **(g/cm^3)**	*EW*	*A* **(cm^2*)**
304	8	25.204	0.509
316L	7.158	25.648	0.509
2750	5.788	24.623	0.509
NCAT 1	7.76	23.23	0.759
NCAT 2	7.72	23.23	0.759
1018	7.87	27.46	0.68

* In galvanic corrosion testing, all the tested samples had the same surface area (0.759 cm^2).

Table 3.3. K constant values that can be used for different corrosion units.

Units for Corrosion Rate	K
mm/year	3272 (mm/(amp.cm.year))
µm/year	3.272×10^6 (µm / (A.cm.year))
mils/year	1.288×10^5 (Milli inches / (amp.cm.year))

II. Corrosion Rate Produced from Linear Polarization Resistance Measurements

The R_p resulting from linear polarization resistance measurement is used to calculate the corrosion current (I_{corr}) using the Stern-Geary equation (3.3) and β_a and β_c values that were estimated from the potentiodynamic polarization curve.

$$I_{corr} = \frac{\beta_a \beta_C}{2.3 R_p (\beta_a + \beta_c)} \quad (3.3)$$

The calculated I_{corr} was then used to calculate CR from equation 3.2.

In this study, only one value of corrosion rate was reported, and that is the corrosion rate that was calculated using the potentiodynamic polarization results. At least, three matching potentiodynamic polarization curves and three linear polarization measurements were conducted for each test. The electrochemical testing parameters were taken from one of these curves. Figure 3.7 shows an example of three matching potentiodynamic polarization curves for aged NCAT that is typically used to determine the corrosion properties of the ally.

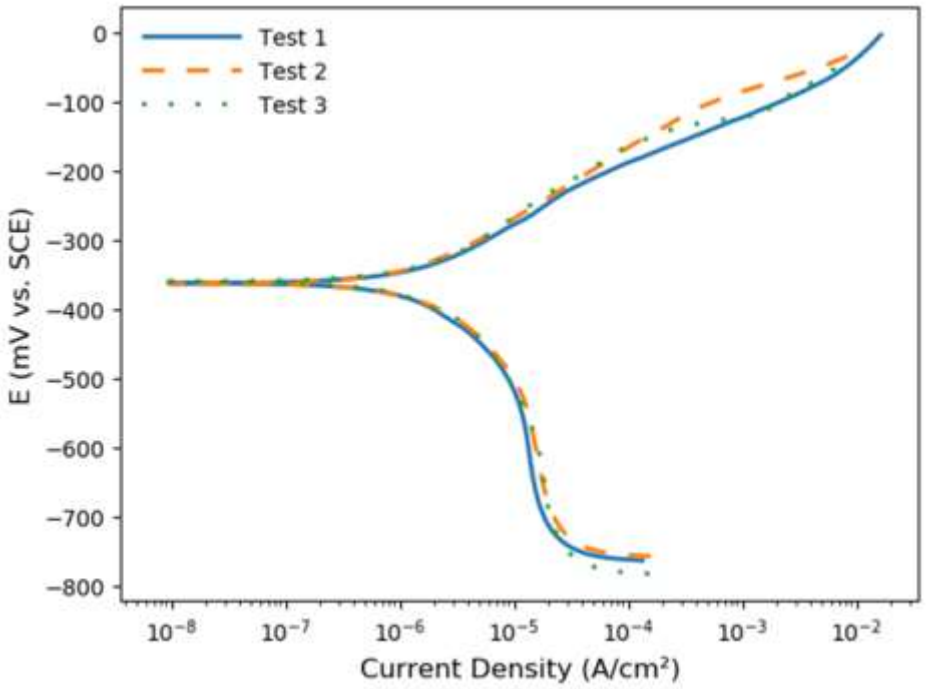

Figure 3.7. Three matching results of a potnetiodynamic polarization tests of aged NCAT that is typically used to determine the corrosion parameters of the alloy.

3.2.6 Galvanic Corrosion Test

In this test, the effects of galvanic interactions between NCAT SMA and four commercially available alloys (1018, 304, 316L, and 2750) in a 0.6 M NaCl solution with a pH of 6 were investigated at three different temperatures (25 ºC (RT), 40 ºC and 60 ºC). A zero resistance ammeter (ZRA) was used to measure the galvanic current flowing between the coupled alloys following ASTM F3044 standard [131]. The cathode to anode surface area ratio was identical (each having an area of 0.759 cm^2). The E_{oc} of each alloy was measured before the test to determine the cathode and anode in the coupling before connecting the specimens electrically through the ZRA. The cathode was connected as the counter electrode and the anode was connected as the working electrode. Immediately after immersing the electrodes in the solution, the galvanic corrosion test began. The test ran for a minimum of 24 h, during which time the galvanic current and galvanic potential established between the alloys were measured every 1 second. The mean values of galvanic current density (i_g) and galvanic potential (E_g) in the final 15 minutes of the ZRA test were used to determine the galvanic current density and galvanic potential of the couplings, as per ASTM F3044 standard [135]. After the test, the surfaces of the corroded

specimens were examined using an optical microscope and a scanning electron microscope (SEM) to determine the severity of the corrosion attack.

3.3 Microstructural Examination

The microstructure of the alloy was studied using a Nikon Eclipse MA100L inverted microscope manufactured in Japan. The microscope is equipped with a Nikon DS-Ri2 digital camera. A JEOL JSM-IT 500 scanning electron microscope (SEM) equipped with Oxford X-ray energy dispersive spectrometry (EDS) was used to study the microstructure of the alloy and determine the chemical composition of the corrosion scale. The SEM was manufactured in Japan, and the EDS software was developed in the United Kingdom. Figure 3.8 shows a picture of the SEM that was used in this study. At least three specimens from each set of samples were tested to give representative results. The specimens were prepared as per the standard metallographic techniques of ASTM E3-11[132].

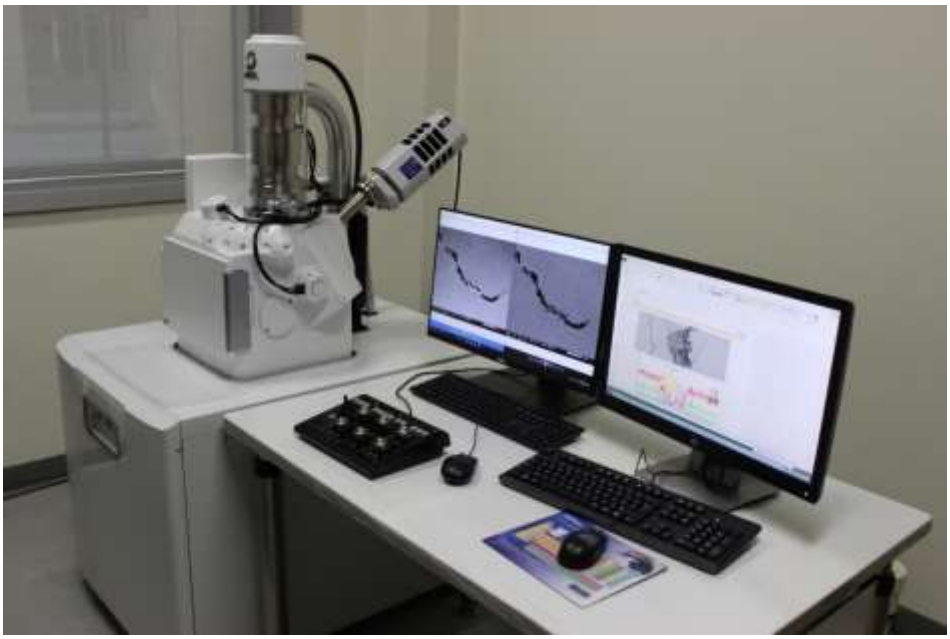

Figure 3.8. A picture of the JEOL JSM-IT 500 SEM that was used to characterize the microstructure of the alloy and the corrosion scales produced after exposure of the specimens to corrosive solutions.

3.3.1 Metallographic Sample Preparation Procedures

The metallographic specimen preparation procedures included the following steps:

(i) Mounting

First, the specimens were compression mounted using a Buehler Simplimet 1000 Automatic Mounting Press manufactured in the USA and a Buehler EPoMet F mounting resin. The specimens were placed in the mounting press and surrounded by the resin. The resin was heated to 60 ^{o}C for 3 minutes. Then it was cooled for 6 minutes while applying a pressure of 280 bars. Mounting was performed to make it easy to hold the specimen during grinding and polishing.

(ii) Grinding

Grinding of mounted specimens was performed, first using a Buehler Handimet II roll grinder manufactured in the USA and 240 grit silicon carbide papers. Automatic grinding using a Buehler EcoMet 250 grinding / polishing machine manufactured in the USA followed. Different grades of abrasive papers ranging from coarse to fine (240, 320, 400, 600, 800, 1000, and 1200 grit) were utilized. Between each grinding step, the specimens were rinsed with distilled water. The grinding was done so that all the scratches on the samples disappeared after the grinding process to make it easy to observe the microstructure of the alloy. Figure 3.9 shows the Buehler Handimet II manual roll grinder and Buehler EcoMet 250 automatic grinding- polishing machine.

Figure 3.9. Manual and automatic grinders used to grind the metallographic specimens.

(iii) Polishing

Polishing of the ground specimens was performed using a Buehler EcoMet 250 grinding / polishing machine manufactured in the USA (Figure 3.10). The samples were polished to a very fine mirror-like finish, using polishing cloths and four different polishing suspensions. The polishing was done in four steps using the following suspension in each step: (1) A 6µm Buehler MetaDi Supreme Polycrystaline Diamond Suspension was used in the first step; (2) A 3µm Buehler MetaDi Supreme Polycrystaline Diamond Suspension was used in the second step; (3) A 1 µm Buehler MetaDi Supreme Polycrystaline Diamond Suspension was used in the third step; and (4) A 0.06 µm Buehler MasterMet Colloidal Silica Polishing Suspension was used in the fourth step.

Between each polishing step the specimens were rinsed with distilled water followed by ethanol. After the last polishing step, they were washed thoroughly using a detergent and water, and rinsed with distilled water. The samples were then cleaned with ethanol in an ultrasonic cleaner for 5 minutes and subsequently dried using a low-heat drier.

Figure 3.10. Automatic polishing machines used to polish the metallographic specimens.

(iv) Etching

Etching involves the application of a chemical reagent on the surface of the alloy to highlight features of the alloy at microscopic level. Such features include grains, grain boundaries, second-phase structures, precipitates and inclusions.

NCAT SMA is usually etched using one of the following etching solutions:

1. A formulation based on hydrofluoric acid (10% hydrofluoric acid with distilled water). This is the most commonly used etching solution for this alloy. It reveals the grains and grain boundary precipitates clearly; however, it is dangerous to use and requires a special chemical hood, which is not available in the laboratories where this study was conducted.
2. A formulation composed of a 15 g sodium bisulfate + 10 g potassium meta-bisulfate + distilled water. This etching solution is safe to use. It can clearly reveal the grains and grain boundaries, but it doesn't show the grain boundary precipitates. Examples of the micrographs produced using this etchant is provided in Appendix B. Since the grain boundary precipitates could contribute to the alloy's corrosion behaviour, it was essential to use a different etching solution that can reveal these precipitates. The development of etching solution that was (i) easy to apply, (ii) safe to use, and (iii) that can reveal the grain boundary precipitates was one of the challenges faced in this study.

Several etching solutions were used in an attempt to reveal the grain boundary precipitates in this alloy, but failed to produce the desired images. Examples of the micrographs obtained are summarized in Appendix B. Different concentrations of nitric acid were explored Eventually, an etchant consisting of 6 vol% nitric acid mixed with 94 vol% distilled water was successful to reveal both grain boundaries and grain boundary precipitates of the alloy. It was applied by dripping the solution on the sample for 5 to 7 seconds. [Examples of the microstructures that were acquired using different etchants are illustrated in Appendix B.] After etching, the specimen was quickly rinsed with distilled water and then dried using a low-heat dryer, before observation using an optical microscope or an SEM.

3.4 Characterization of the Corrosion Product

The surface morphology of the corroded specimens was examined using a Nikon Eclipse MA100L inverted microscope equipped with a Nikon DS-Ri2 digital camera manufactured in Japan, as well as a JEOL JSM-IT 500 SEM manufactured in Japan. The SEM is equipped with a UK made Oxford EDS system that was used to determine the chemical composition of the NCAT specimens before and after corrosion. The chemical composition was determined at different locations on the specimens, including the grains, grain boundaries, inclusions, and pits.

4. RESULTS AND DISCUSSION

The test results from experiments conducted in Chapter 3 are presented and discussed in this chapter. It is divided into several sections and sub-sections to address the results obtained from specific experiments. The microstructure of the NCAT SMA and the predicted Eh-pH diagram of this alloy is discussed in the first part of this chapter. The results obtained from electrochemical corrosion testing and characterization of corrosion products are presented in the remaining parts.

4.1 Microstructure of NCAT SMA

A typical micrograph showing the microstructure of the tested aged NCAT alloy is presented in Figure 4.1. The microstructure consists of a single-phase austenite structure and precipitates can be observed at some of the grain boundaries. The precipitates are believed to be β-Ni_3Al-ordered bcc phase precipitates that have been reported by Tanaka *et al*. [17] and Omori *et al*. [18]. They can be seen inside the grains as well. Tanaka *et al*. [17] reported that the β phase is undesirable as it causes intergranular fracture that reduces the ductility of the alloy [17]. In their research, they added boron to NCAT alloy to supress the β phase in the NCATB alloy [17]. Figure 4.2 shows the output of a SEM line scan across a typical grain boundary with precipitates. Evidence of depletion of iron (Fe) and cobalt (Co) and enrichment of aluminum (Al), nickel (Ni) and tantalum (Ta) at the grain boundary is clearly observed. Carbon (C) was observed in very small amounts in some of these precipitates. The presence of carbon at the grain boundaries could be attributed to tantalum carbide (TaC) inclusions which were formed during solidification or cooling from the melt [22, 25]. Table 4.1 shows the elemental composition of typical grain boundary precipitates (GBPs) compared with that of the alloy matrix (i.e. within the grain). The composition was determined using EDS analysis at 28 different locations with an uncertainty of less than 0.1%. Approximately 44% and 27% reduction in Fe and Co contents, respectively, occurred at the GBP. In contrast, an increase of ~ 47%, 222% and 32% in Ni, Ta, and Al, respectively, was observed. This shows an evidence of solute segregation at grain boundaries with β phase precipitates. In other words, the

EDS analysis shows that grain boundary precipitates reported in this study consist of Ni, Al and Ta.

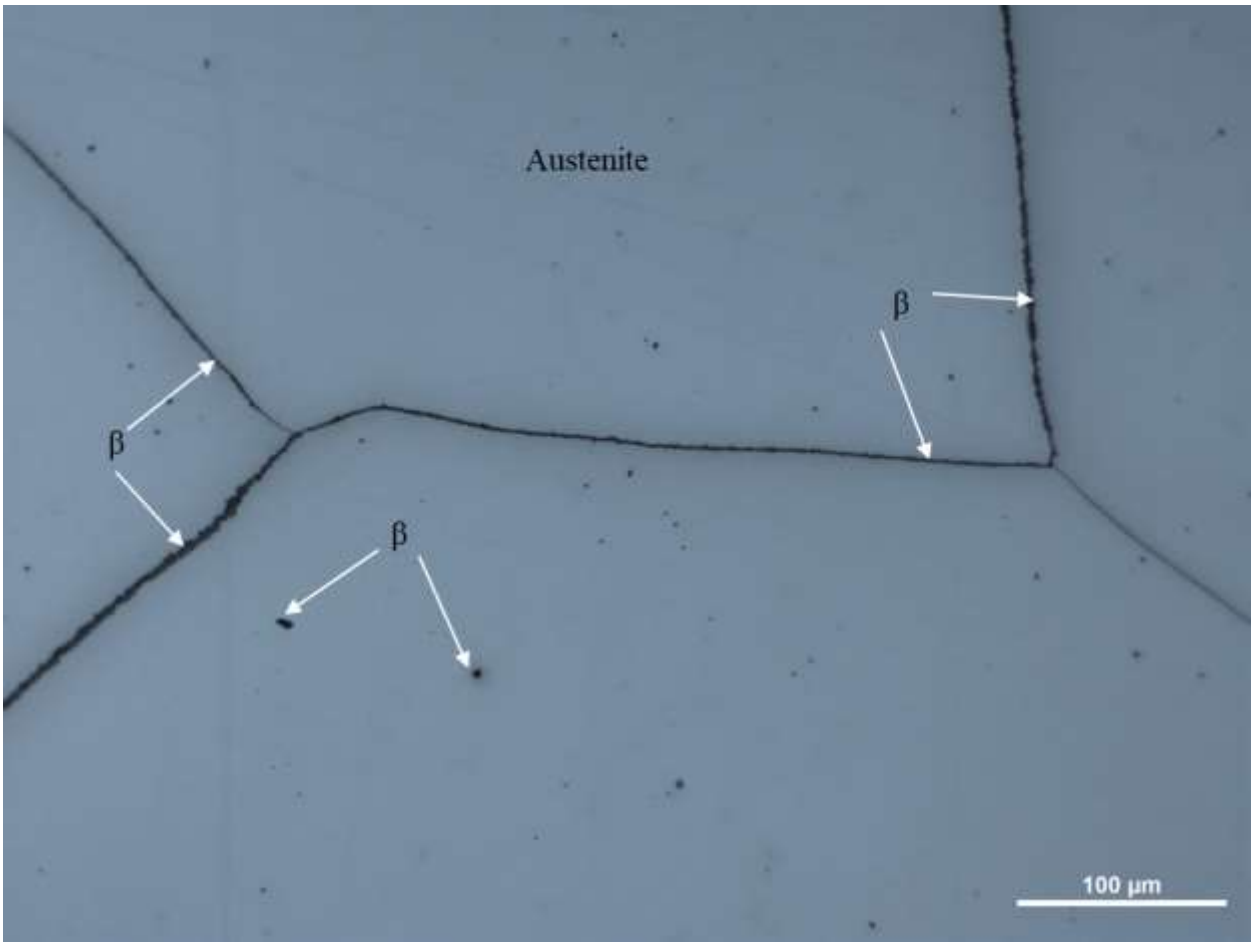

Figure 4.1. Typical optical micrograph of a polished and etched specimen of aged NCAT alloy showing its microstructure. β-phase precipitates can be seen at some of the grain boundaries and within the grains.

Table 4.1. Chemical composition of a typical grain boundary precipitate compared to that of the alloy matrix.

Alloying Element	**Fe**	**Ni**	**Co**	**Al**	**Ta**
Composition of the GBP*	23.31	40.44	12.64	14.74	8.47
(Confidence Interval in at%)	(±0.04)	(±0.02)	(±0.05)	(±0.03)	(±0.02)
Composition of the alloy*	41.43	27.45	17.31	11.14	2.63
(Confidence Interval in at%)	(±0.05)	(±0.04)	(±0.02)	(±0.04)	(±0.02)

* The values represent the mean of 27 measurements in at%.

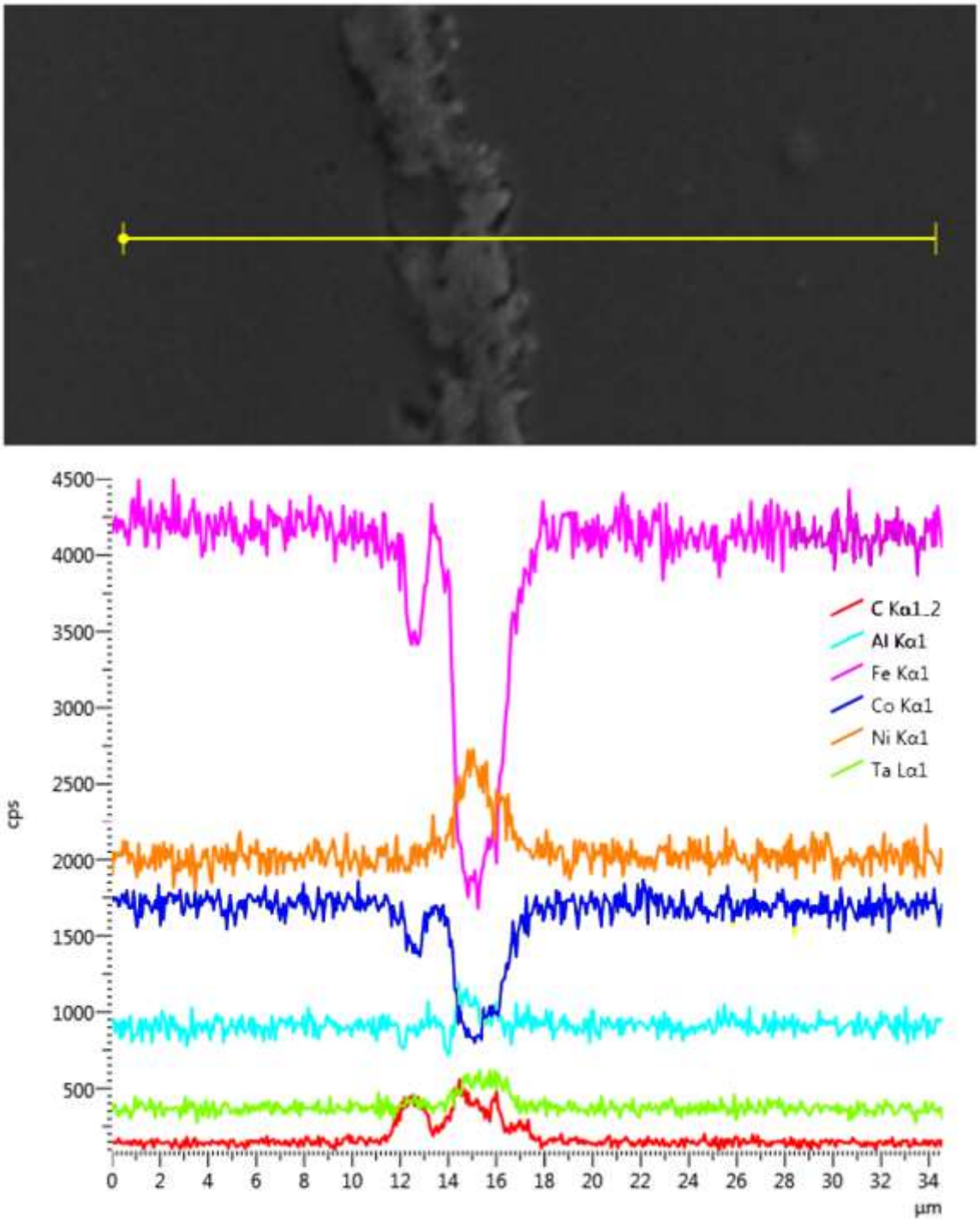

Figure 4.2. EDS line scans obtained for a NCAT specimen showing elemental distribution at a typical grain boundary with precipitates. Iron and cobalt are depleted from the precipitates.

4.2 Predicted Potential-pH Diagram of FeNiCoAlTa (NCAT) SMA

A potential (E) – pH diagram, also known as a Pourbaix diagram, shows a relationship between the oxidizing power (potential) of a solution and the solution acidity or alkalinity (pH). It presents the predicted reaction products that are present when thermodynamic equilibrium is reached [133]. The potential-pH diagram for the studied NCAT SMA in H_2O at 25 °C, determined using the Outotec HSC Chemistry Software for E-pH diagrams models (2012), is shown in Figure 4.3. The diagram shows that the potential shifts to lower values as the pH increases. It predicts that at positive potentials, Fe_2O_3 will be the favoured species to be formed on the surface of the alloy. At a potential of ~ -0.75 V or lower, corrosion of the alloy is reduced. Different oxide films are formed in alkaline solution (pH ≥ 8). It should be noted that this diagram will change when the alloy is tested in different solutions or in water at temperatures higher than 25 °C.

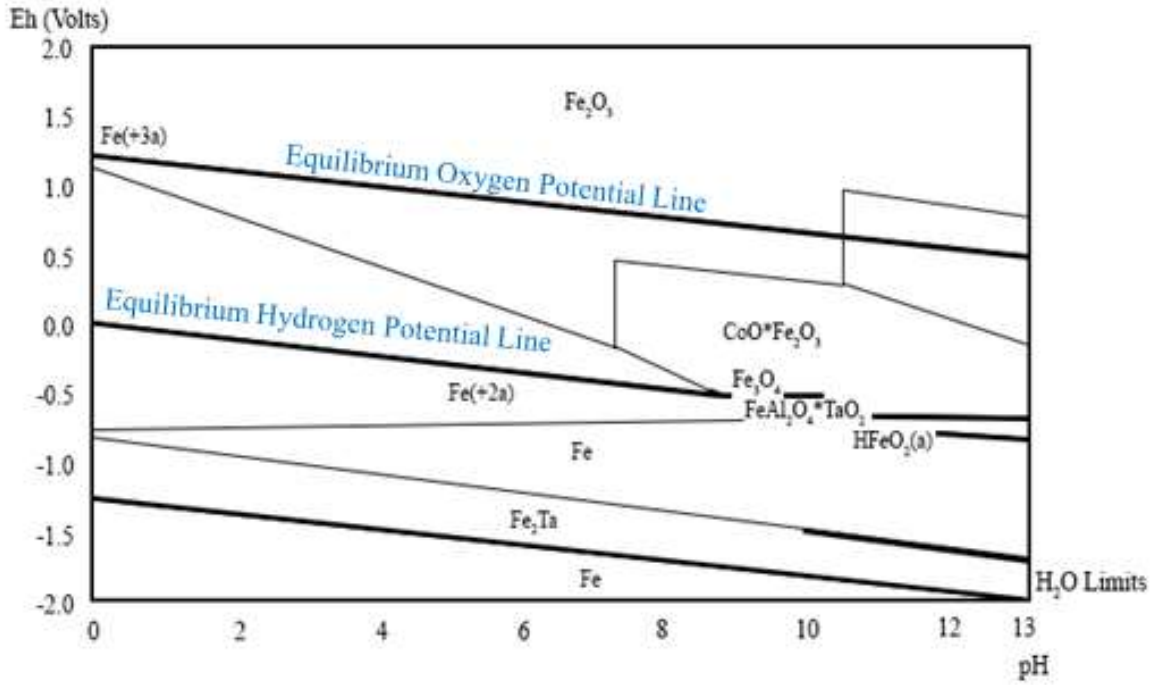

Figure 4.3. Predicted potential(E) – pH diagram for NCAT SMA in H_2O at 25 °C, produced using the Outotec HSC Chemistry Software for E-pH diagrams models (2012).

In the E – pH diagram, the anodic reaction is

$$Fe \rightarrow Fe^{2+} + 2e^{-} \quad (4.1)$$

The cathodic reduction reaction changes with the change in pH. In the pH range of 4 –10, a loose, porous ferrous oxide scale is formed on the surface [133]. The corrosion rate in this case is controlled by uniform diffusion of dissolved oxygen and is nearly constant [133]. Oxygen is reduced by the following reaction

$$O_2 + 2H_2O + 4e^- \rightarrow 4OH^- \quad (4.2)$$

In solutions with pH below 4, the formed oxide scale is soluble and the corrosion rate increases due to the presence of H^+ that is reduced by the following reaction

$$2H^+ + 2e^- \rightarrow H_2 \quad (4.3)$$

Dissolved oxygen can easily access the alloy surface when the oxide scale breaks down, which further increases the corrosion rate. Dissolved oxygen is cathodically reduced by

$$O_2 + 4H^+ + 4e^- \rightarrow H_2O \quad (4.4)$$

At pH above 10, ferric oxide film is formed in the presence of dissolved oxygen, and as a result, the corrosion rate is reduced to lower values.

4.3 Corrosion Rate and Open Circuit Potential of NCAT SMA in 0.6 M NaCl Solution

This section represents the results of the investigation of the electrochemical behaviour of NCAT in a 0.6 M NaCl solution at 25 ^oC. It presents the corrosion properties of the alloy in the solution and compares them with those of some commercially available alloys in the same solution.

4.3.1 Electrochemical Corrosion Behaviour

A comparison between the open circuit potential (E_{oc}) of aged NCAT SMA and four commercial alloys is presented in Figure 4.4. The open circuit potential of NCAT is approximately -386 mV (vs. SCE), which is more positive than that of 1018 carbon steel (-689 mV (vs. SCE)). This indicates that NCAT is less active than alloy 1018 in 0.6 M NaCl solution. On the other hand, alloy 304, 316L and 2750 are less active in the NaCl solution when compared to NCAT SMA. They have open circuit potential values of -145, -123 and -130 mV (vs. SCE), respectively.

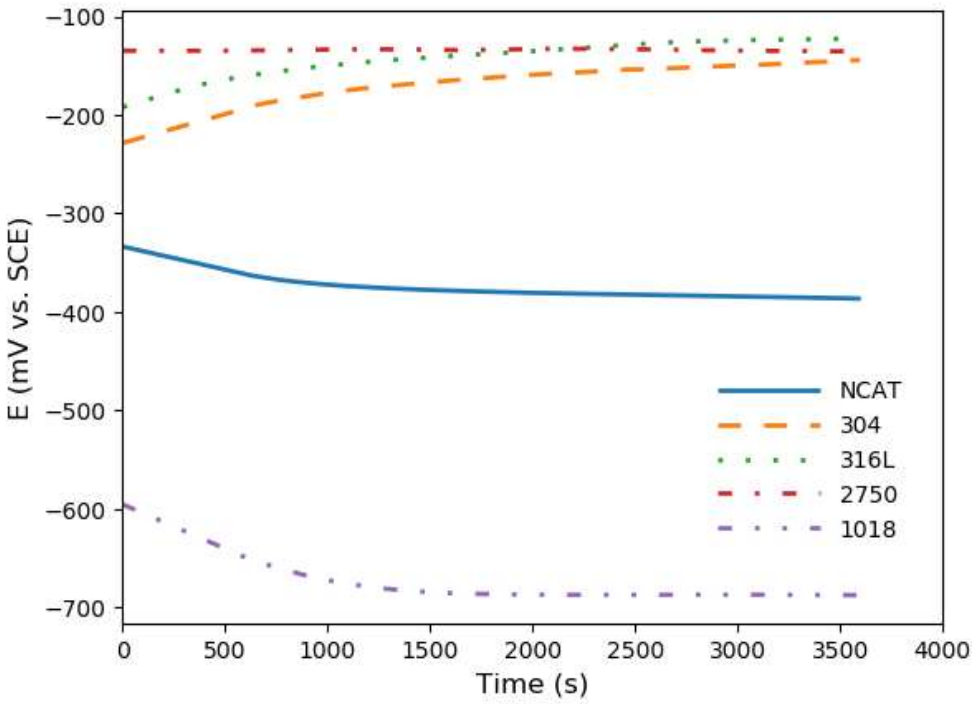

Figure 4.4. Open circuit potential (E_{oc}) of NCAT compared to those of four commercial alloys in a 0.6 M NaCl solution at RT and pH 6. Observe that NCAT alloy has higher E_{oc} than 1018 carbon steel.

The potentiodynamic polarization curves obtained for aged NCAT alloy and the four commercial alloys in a 0.6 M NaCl solution are shown in Figure 4.5. As can be seen, like alloy 1018, NCAT alloy does not passivate in NaCl solution, while 304, 316L and 2750 stainless steels show the expected active-passive corrosion behaviour in this solution. The different electrochemical corrosion parameters determined from these plots and from the LPR experiments are presented in Table 4.2. The corrosion behaviour of NCAT is characterized by general dissolution combined with localized attack in the form of pits, especially at grain boundaries. Its corrosion rate is 0.017 mm/y, which is lower than 0.071 mm/y of 1018 carbon steel. However, it is much higher than corrosion rates of 0.0007, 0.0007, and 0.0005 mm/y obtained for 304, 316L and 2750 stainless steels, respectively. The open circuit potential of NCAT alloy is also more negative than those of these three stainless steels.

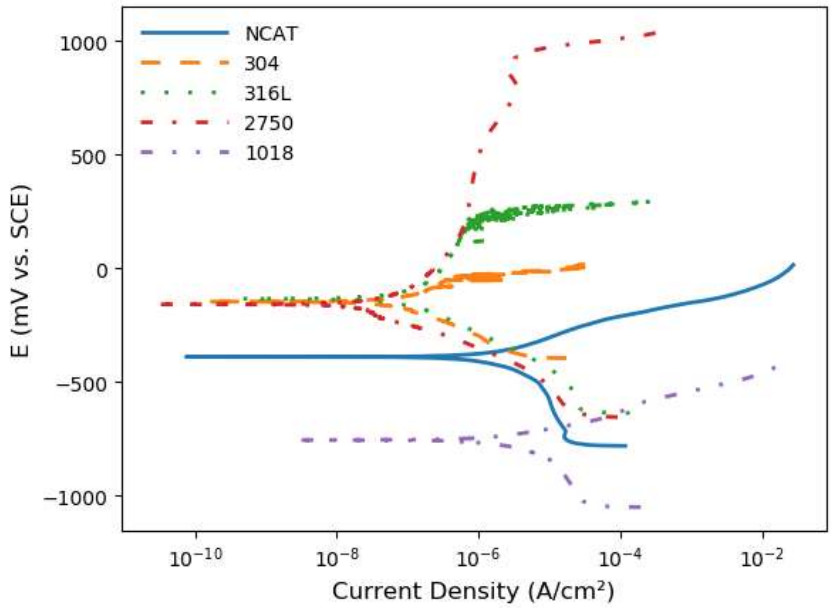

Figure 4.5. Potentiodynamic polarization curves obtained for NCAT alloy and four commercial alloys in a 0.6 M NaCl solution at RT and pH 6. NCAT shows similar behaviour to alloy 1018 in the solution.

Table 4.2. Summary of electrochemical corrosion parameters obtained from linear polarization resistance and potentiodynamic polarization tests in a 0.6 M NaCl solution at RT for NCAT alloy and the four commercial alloys.

Alloy	E_{oc}[1] mV	E_{corr}[1] mV	i_{corr} µA/cm²	β_a[1] V/decade	B_c[1] V/decade	Rp Ω.cm²	CR mm/y
304 (SD)[2]	-145 (±1.7)	-146 (±3.5)	0.13 (±0.02)	0.11 (±0.06)	-0.21 (±0.03)	$2.9x10^5$ ($±8.3x10^4$)	0.0007 (±0.0001)
316L (SD)[2]	-123 (±15.7)	-133 (±16.4)	0.12 (±0.03)	0.39 (±0.03)	-0.16 (±0.02)	$3.1x10^5$ ($±8.1x10^4$)	0.0007 (±0.0002)
2750 (SD)[2]	-130 (±9.1)	-129 (±13.2)	0.07 (±0.01)	0.22 (±0.01)	-0.15 (±0.02)	$4.3x10^5$ ($±2.1x10^5$)	0.0005 (±0.00008)
NCAT (SD)[2]	-386 (±16.4)	-389 (±13.5)	2.26 (±0.35)	0.12 (±0.01)	-0.22 (±0.03)	$1.6x10^4$ (±303.5)	0.017 (±0.002)
1018 (SD)[2]	-689 (±12.0)	-651 (±19.9)	8.80 (±1.09)	0.05 (±0.005)	-0.4 (±0.09)	$2.3x10^3$ (±660.8)	0.071 (±0.008)

[1] All the potential values are measured vs. SCE.

[2] Standard deviation (SD) values.

A survey of the literature shows that the corrosion properties of aged NCAT alloy in 0.6 M NaCl solution compare reasonably well with those of other Fe-based SMAs. For example, the corrosion current density of Fe-15Mn-7Si-9Cr-5Ni SMA was reported to be 1.76µA/cm² [45]

while that of NCAT alloy is 2.26μA/cm². Another Fe-Mn-Si-Cr-Ni SMA that underwent aging treatment for 24 h also showed a corrosion current density of 1.33 μA/cm² [97]. Nevertheless, the open circuit potential values varied in the reported alloys. Values of -425.3 mV (vs. SCE) and -358 mV (vs. SCE) were reported respectively for the alloys in references [97] and [45], while -386 mV (vs. SCE) was obtained for NCAT in this study, which lies between the reported open circuit potential values.

4.3.2 Observation and Analysis of Corrosion Scale Developed on NCAT Alloy

A typical SEM micrograph of the surface of a NCAT specimen that was subjected for potentiodynamic polarization test is shown in Figure 4.6. It can be seen that the corrosion attack is concentrated mainly at locations where precipitates decorated the grain boundary. The corrosion mode appears to be intergranular. There are a few pits within the matrix close to grain boundaries with precipitates. X-ray maps of the large pit highlighted in Figure 4.6 are shown in Figure 4.7. The absence of Fe and Co in the pit is quite noticeable. The corrosion products in the pit appear to be oxides of Ni, Ta and Al, which suggests that second-phase particles and/or inclusions containing these elements that occurred at these locations acted as preferred sites for pit formation.

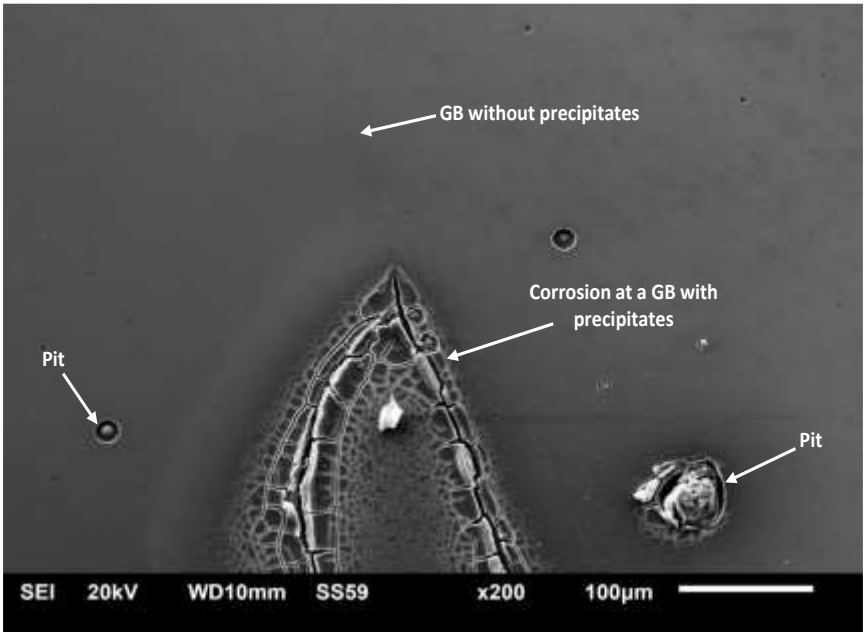

Figure 4.6. SEM micrograph of a NCAT alloy specimen subjected to potentiodynamic polarization test. Severe corrosion can be seen at the grain boundary with precipitates and pits located in the matrix near the corroded grain boundary.

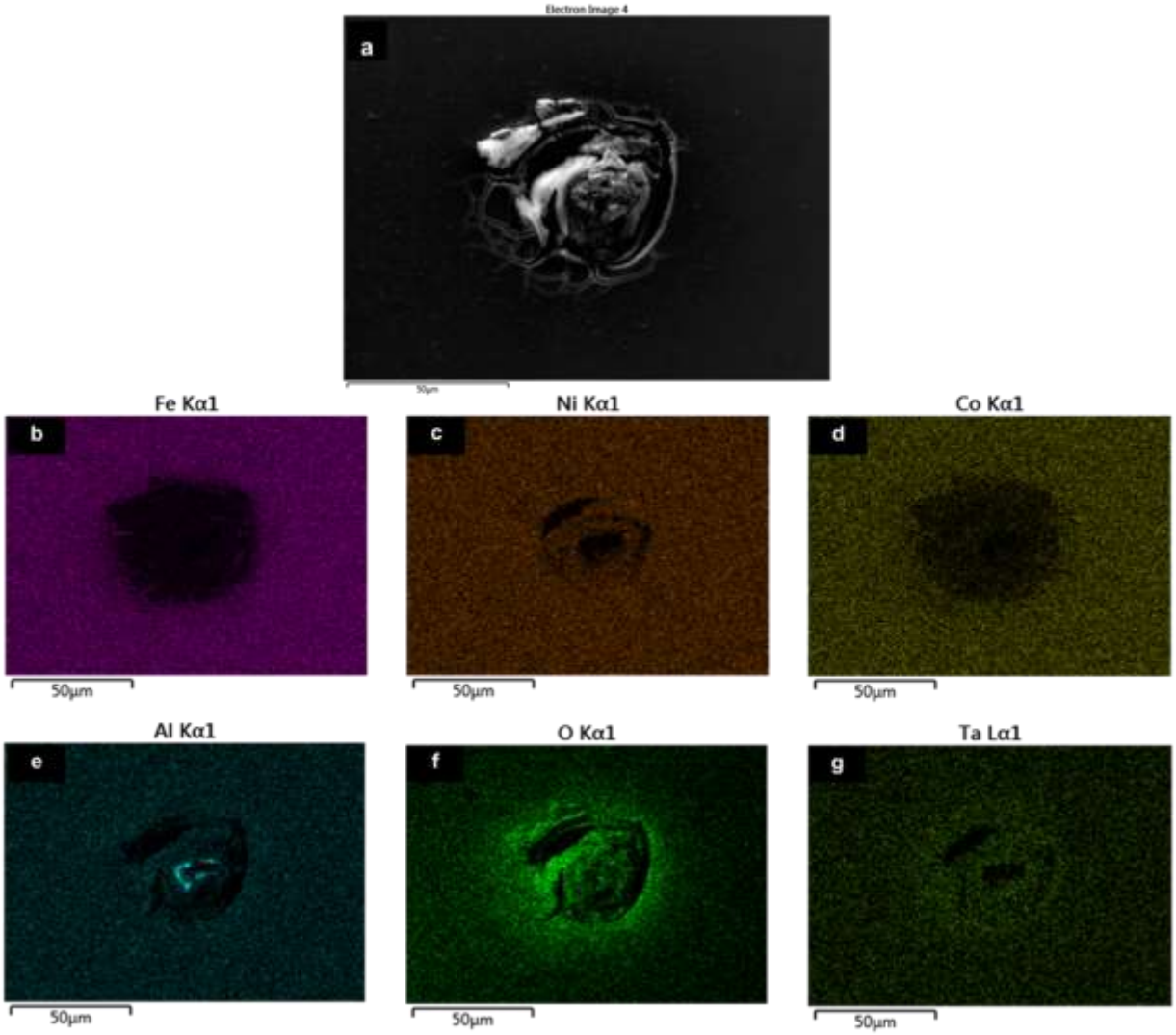

Figure 4.7. EDS X-ray maps obtained for the large pit in Figure 4.6. The absence of iron and cobalt is evident in the pit.

Figure 4.8 shows EDS X-ray maps acquired from another NCAT specimen that underwent potentiodynamic polarization testing. Once again, the corrosion attack is mainly concentrated around the grain boundary where precipitates exist. Figure 4.8 (b) and (d) show that Fe and Co are depleted at the grain boundary and nearby region. The high concentration of Ta and O at the grain boundary (Figure 4.8 (f) and (g)) is an indication that tantalum oxide film, probably Ta_2O_5, formed on the surface, but failed to provide protection for the alloy. Ni and Al appear to be distributed uniformly across the alloy (Figure 4.8 (c) and (e)).

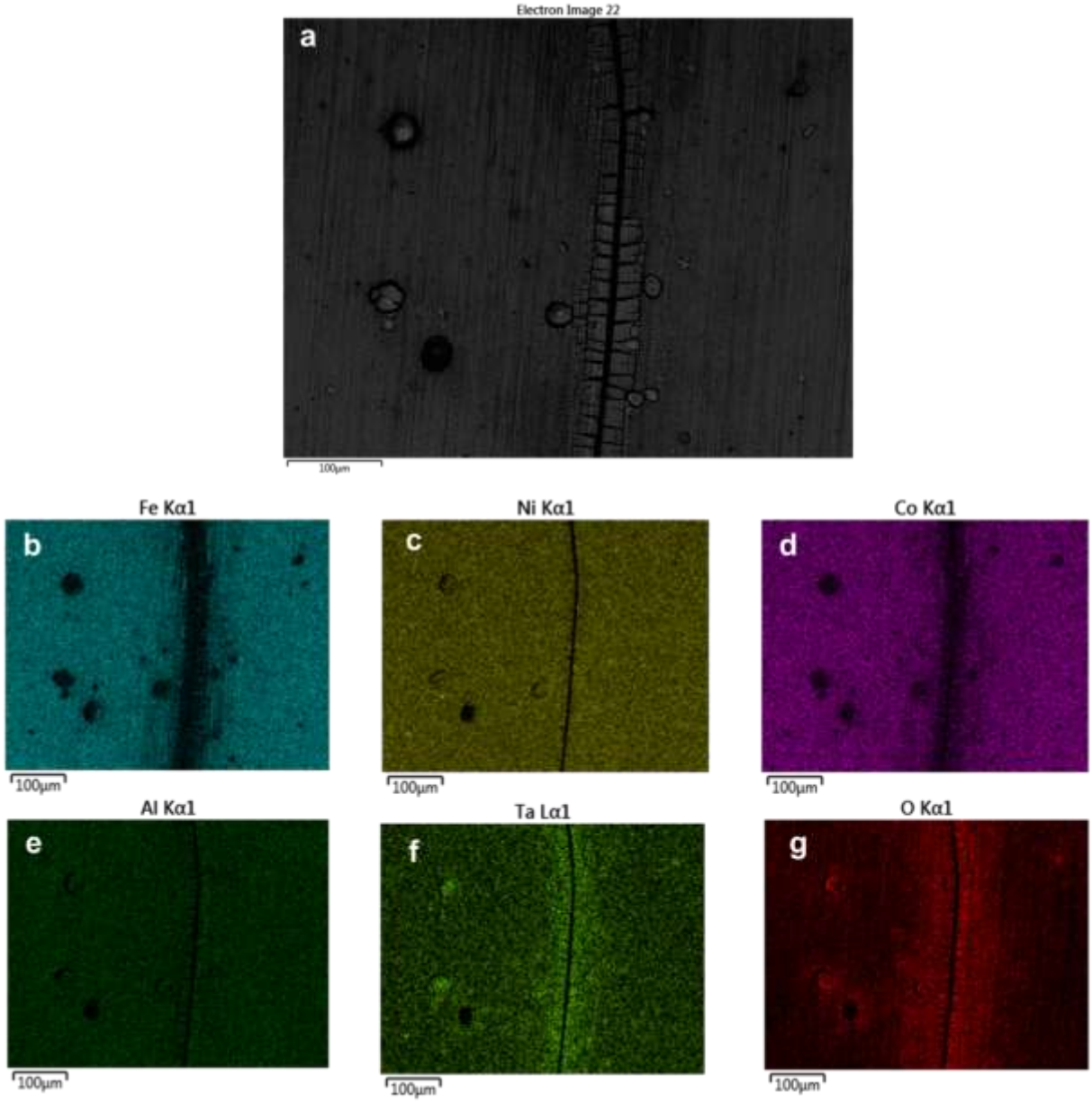

Figure 4.8. EDS X-ray maps showing elemental distribution around a typical grain boundary with precipitates in NCAT specimen after the potentiodynamic polarization test. The absence of Fe and Co at the grain boundary is evident.

Further EDS line scan analysis supporting this finding is shown in Figure 4.9. The line scan shows that corrosion is concentrated mainly on the grain boundaries and in areas close to them. There is almost no corrosion observed in the alloy matrix. Depletion of Fe and Co at grain boundaries and the surrounding area is evident from the line scans. There is an increase in Ta content; a slight increase in Ni content; and practically no change in Al content.

From the foregoing, it is quite obvious that grain boundary precipitates are the major cause of the intergranular corrosion (IGC) observed in the aged NCAT alloy. Precipitates usually form at grain boundaries because they are high-energy regions that can provide quick diffusion and segregation paths for solutes [134]. However, diffusion and segregation rates of alloying elements are slow in an austenitic matrix [135]. Grain boundary precipitation can produce zones of reduced corrosion resistance, resulting in an anodic grain boundary zone relative to the remainder of the alloy matrix [136, 137]. In the NCAT SMA, Fe and Co are depleted at grain boundaries where β-phase and TaC precipitation occurred. The measured corrosion potential (E_{corr}) value of - 389 mV (vs. SCE) for the alloy is very close to the corrosion potential value of -377 mV (vs. SCE) that was measured by Onyeachu *et al.* [138] for Ni_3Al, thereby indicating that the precipitates are the main driver for the corrosion by creating an anodic zone.

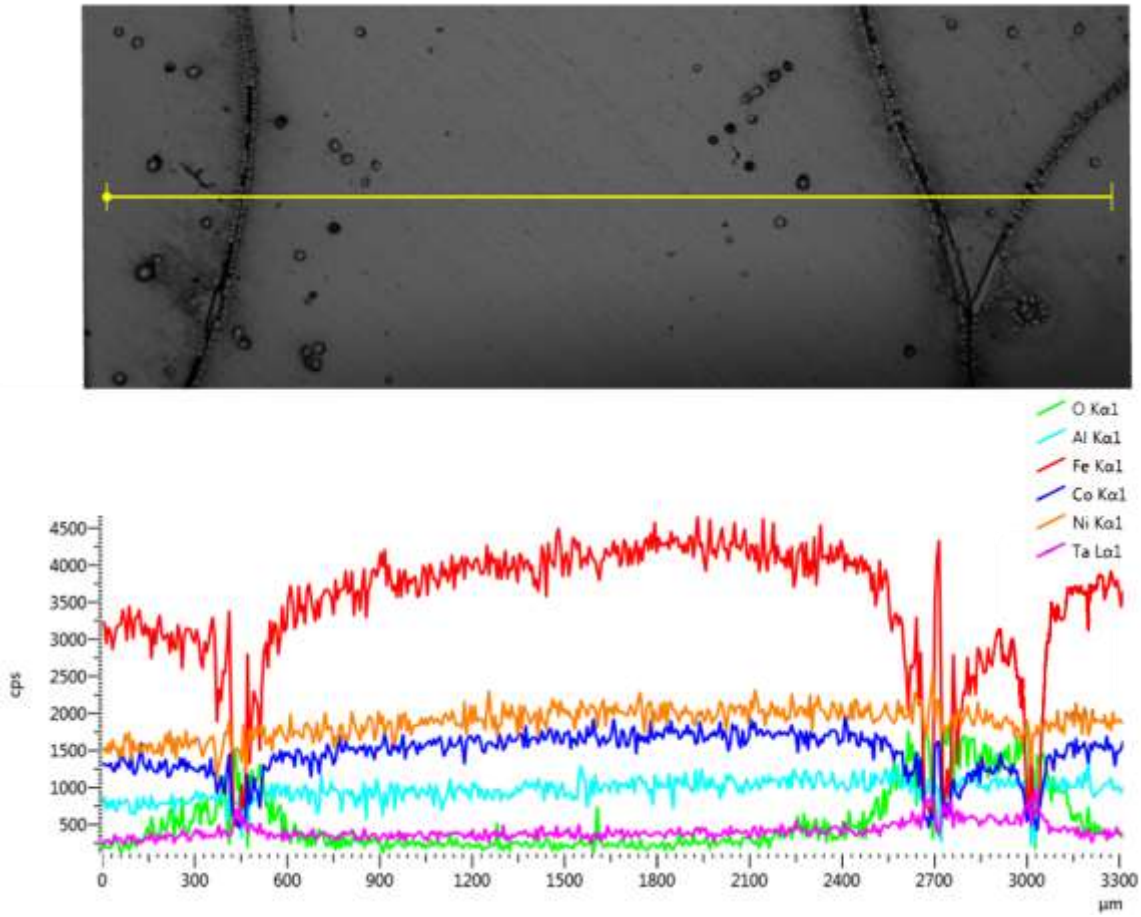

Figure 4.9. EDS line scan of a NCAT specimen used for potentiodynamic polarization test showing elemental distribution change at grain boundaries containing precipitates. Iron and cobalt are depleted in these precipitates.

The NCAT has a microstructure consisting of an austenite matrix with very fine, homogenously distributed γ′ precipitates (3-5 nm) [22, 24]. Ma *et al.* [103] observed a clear chemical partitioning between the matrix and the γ′ precipitates in the NCAT. They showed i) a change in the matrix composition with aging time, and ii) a reduction in iron and cobalt content, and a subsequent enrichment of nickel, tantalum, and aluminum content in the γ′ precipitates, when aging at 600 ^{o}C for 90 h [103]. These are the same aging conditions that the NCAT alloy went through in this study. Ma *et al.*'s [103] findings correlate with the data in Figure 4.2, and Figures 4.7 – 4.9. However, in this study, no chemical partitioning was observed in the alloy's matrix. Chemical partitioning was reported between the grains and the grain boundaries characterized by precipitates, indicating that β precipitates are the main contributor in the chemical partitioning in this case. The pitting around the GBP could also be attributed to the presence of β precipitates. These precipitates were observed inside the grains as can be seen in Figure 4.1.

The obvious relationship between the GBP and the alloy's corrosion behaviour makes it clear that the GBP are the main contributor to the alloy's corrosion behaviour. They were observed in the optical and SEM micrographs. These precipitates are very similar to the ones that were observed by Tanaka *et al.* [17] and Omori *et al.* [18], and are believed to be β-Ni_3Al-ordered bcc phase precipitates [17, 18]. Tanaka *et al*. [17] reported that the β phase is undesirable, as it causes intergranular fracture that results in reducing the alloy's ductility [17].

In spite of its austenitic microstructure, the aged NCAT alloy disappointedly showed very poor corrosion resistance in 0.6 M NaCl solution. This may be a concern if the alloy will be used in marine environment. The addition of Boron to this alloy (NCATB) was found to suppress the β phase precipitates, but did not completely eliminate them [17]. An investigation of the corrosion behaviour of the NCATB alloy for IGC in NaCl solutions could be a future consideration for this research project.

4.4 Effect of Heat Treatment on Microstructure, Corrosion Rate, and Open Circuit Potential of NCAT SMA

In this section, the microstructure and corrosion behaviour of NCAT alloy given only solution heat treatment (solution treated NCAT) and that which was solution heat treated and aged

at 600 ^{o}C for 90 h (aged NCAT) are compared. The additional aging treatment given to the alloy after solution heat treatment was to produce Ɣ'-$(Ni,Fe,Co)_3(Al,Ta)$ phase precipitates that contribute to the production of the shape memory effect in the alloy. Corrosion testing was performed in a 0.6 M NaCl solution at 25 ^{o}C.

4.4.1 Heat Treatment and Microstructure

Typical optical micrographs showing the microstructures of the two heat treated alloys are presented in Figure 4.10. Figure 4.10 (a) shows that the solution treated NCAT has an austenite single-phase structure, which is similar to that of the aged NCAT alloy (Fig. 4.10 (b). However, there is no visible trace of grain boundary precipitates in the solution treated alloy. An EDS line scan of a solution treated NCAT is shown in Figure 4.11. It can be seen that, unlike the EDS line scan of aged NCAT alloy shown in Fig. 4.2, there is uniform distribution of all the elements within the grains and at grain boundaries.

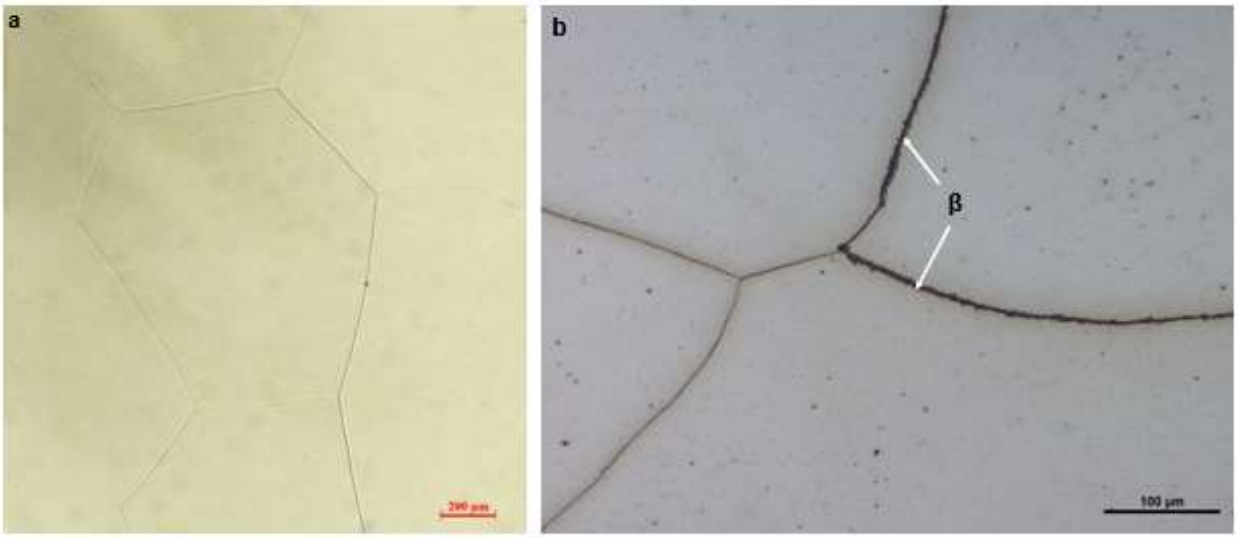

Figure 4.10. Comparison between the microstructures of (a) NCAT SMA given only solution heat treatment (solution treated NCAT) and (b) NCAT SMA given both solution heat treatment and age hardening (aged NCAT). Note the absence of the β phase at grain boundaries of solution treated NCAT.

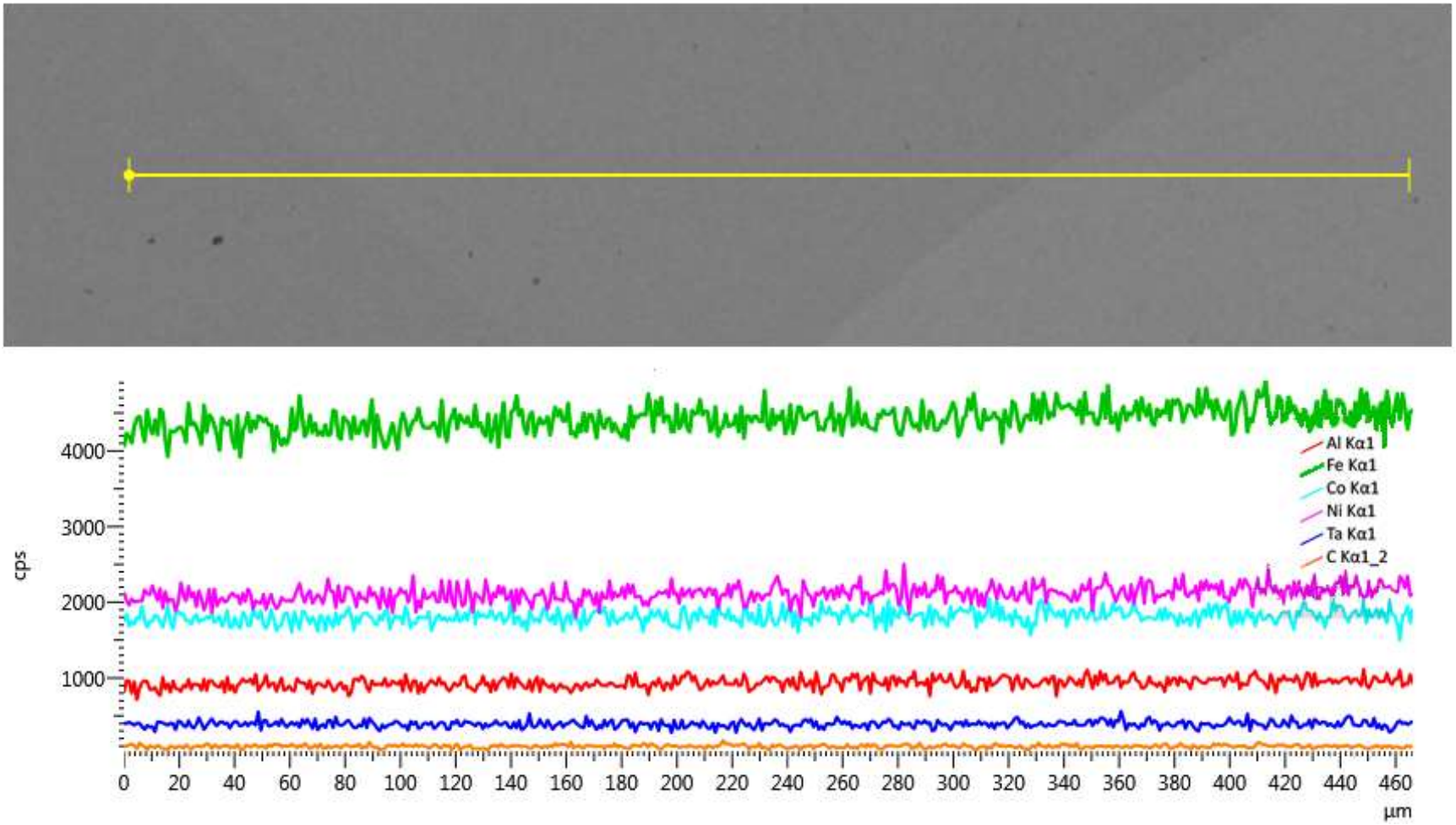

Figure 4.11. EDS line scans obtained for solution treated NCAT before the corrosion testing showing uniform distribution of all the elements within the grains and at grain boundaries.

4.4.2 Electrochemical Corrosion Behaviour

A comparison between the open circuit potential (E_{oc}) of solution treated NCAT and aged NCAT is shown in Figure 4.12. The E_{oc} of solution treated NCAT is -346 mV (vs. SCE), whereas that of aged NCAT is -386 mV (vs. SCE). Therefore, solution treated NCAT has more positive E_{oc} than aged NCAT, indicating that the aging heat treatment which followed solution heat treatment made the alloy more active. Similar behaviour after the aging heat treatment was reported for other Fe-based SMAs [45, 97].

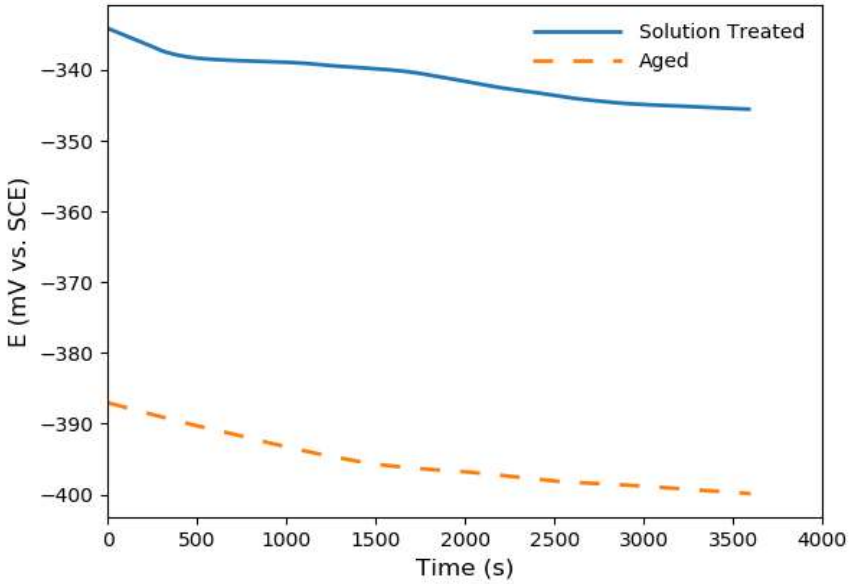

Figure 4.12. Comparison of open circuit potentials obtained for solution treated NCAT and aged NCAT in a 0.6 M NaCl solution at 25 °C and pH 6. Aged NCAT has a lower open circuit potential.

The potentiodynamic polarization curves obtained for solution treated NCAT and aged NCAT in a 0.6 M NaCl solution at 25 °C are compared in Figure 4.13, while the different electrochemical parameters determined for the alloys tested in this study are presented in Table 4.3. As can be seen, the two alloys did not passivate in 0.6 M NaCl solution. Solution treated NCAT has slightly better corrosion properties compared to aged NCAT. The corrosion current density and the corresponding corrosion rate for the solution treated NCAT are 1.75 µA/cm² and 0.013 mm/y, respectively, while those of aged NCAT alloy are respectively 2.26 µA/cm² and 0.017

mm/y. The higher corrosion rate obtained for aged NCAT could be attributed to the precipitates and chemical partitioning at the grain boundaries.

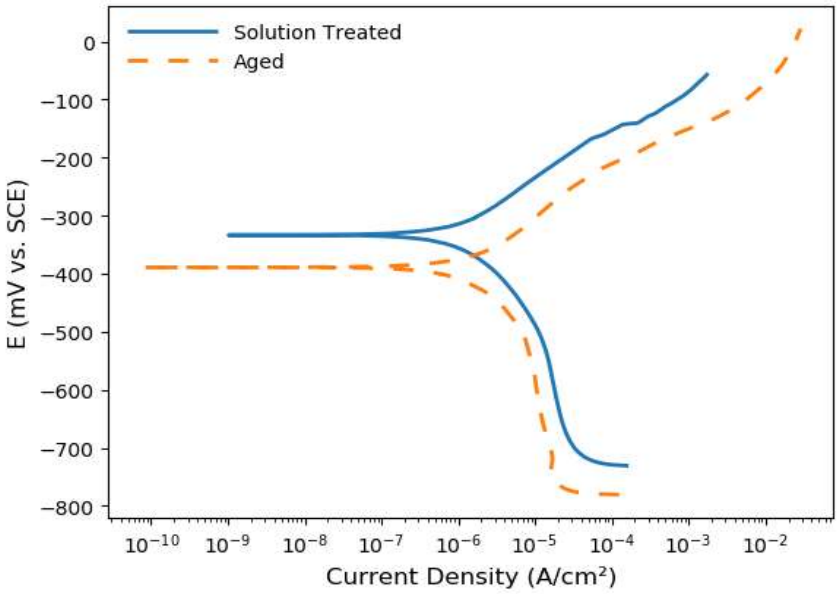

Figure 4.13. Potentiodynamic polarization curves obtained for solution treated NCAT and aged NCAT in a 0.6 M NaCl solution at 25 °C and pH 6. The solution treated alloy has a better corrosion resistance than the aged alloy.

Table 4.3. Electrochemical parameters obtained for the alloys tested in a 0.6 M NaCl solution at 25 °C and pH 6.

	E_{oc}[1] mV	E_{corr}[1] mV	i_{corr} µA/cm²	β_a[1] V/decade	β_c[1] V/decade	R_p Ω.cm²	CR Mm/y
Solution Treated NCAT	-346 (±10.8)	-334 (±35.4)	1.75 (±0.33)	0.06 (±0.02)	-0.16 (±0.06)	1.05x10⁴ (±5.8x10³)	0.013 (±0.002)
Aged NCAT (SD)[2]	-386 (±16.4)	-389 (±13.5)	2.26 (±0.35)	0.12 (±0.01)	-0.22 (±0.03)	1.6x10⁴ (±303.5)	0.017 (±0.002)
304 (SD)[2]	-145 (±1.7)	-146 (±3.5)	0.13 (±0.02)	0.11 (±0.06)	-0.21 (±0.03)	2.9x10⁵ (±8.3x10⁴)	0.0007 (±0.0001)
316L (SD)[2]	-123 (±15.7)	-133 (±16.4)	0.12 (±0.03)	0.39 (±0.03)	-0.16 (±0.02)	3.1x10⁵ (±8.1x10⁴)	0.0007 (±0.0002)
2750 (SD)[2]	-130 (±9.1)	-129 (±13.2)	0.07 (±0.01)	0.22 (±0.01)	-0.15 (±0.02)	4.3x10⁵ (±2.1x10⁵)	0.0005 (±0.00008)
1018 (SD)[2]	-689 (±12.0)	-651 (±19.9)	8.80 (±1.09)	0.05 (±0.005)	-0.4 (±0.09)	2.3x10³ (±660.8)	0.071 (±0.008)

[1] All the potential values are measured vs. SCE. [2] Standard deviation (SD) values.

4.4.3 Observation and Analysis of the Corrosion Scale

Optical micrographs of the surfaces of solution treated NCAT and aged NCAT after potentiodynamic polarization tests are compared in Figure 4.14, while equivalent SEM images of the alloys are compared in Figure 4.15. It can be seen that both solution treated NCAT and aged NCAT alloy suffered from pitting, whereas only the aged alloy suffered intergranular corrosion (IGC).

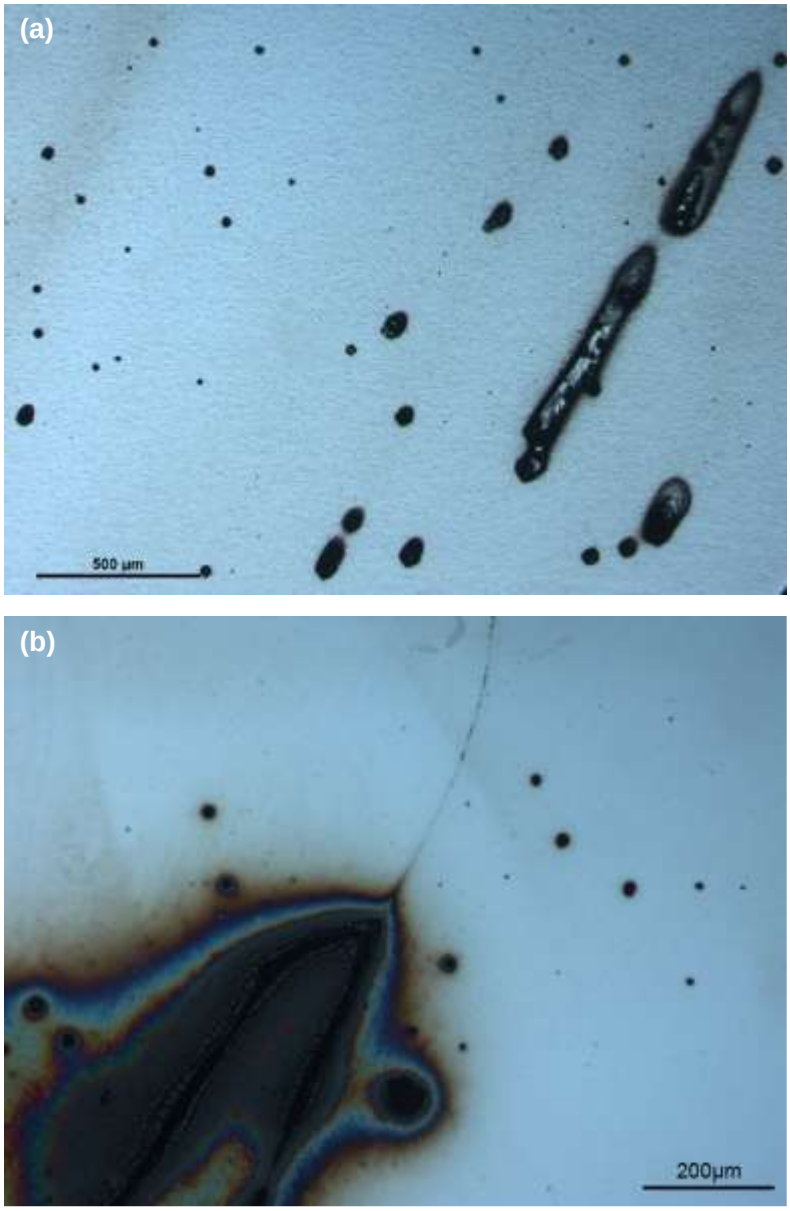

Figure 4.14. Optical micrographs of corroded (a) solution treated NCAT showing pits and clustered pits and (b) aged NCAT showing IGC. More corrosion was observed in aged NCAT compared to solution treated NCAT.

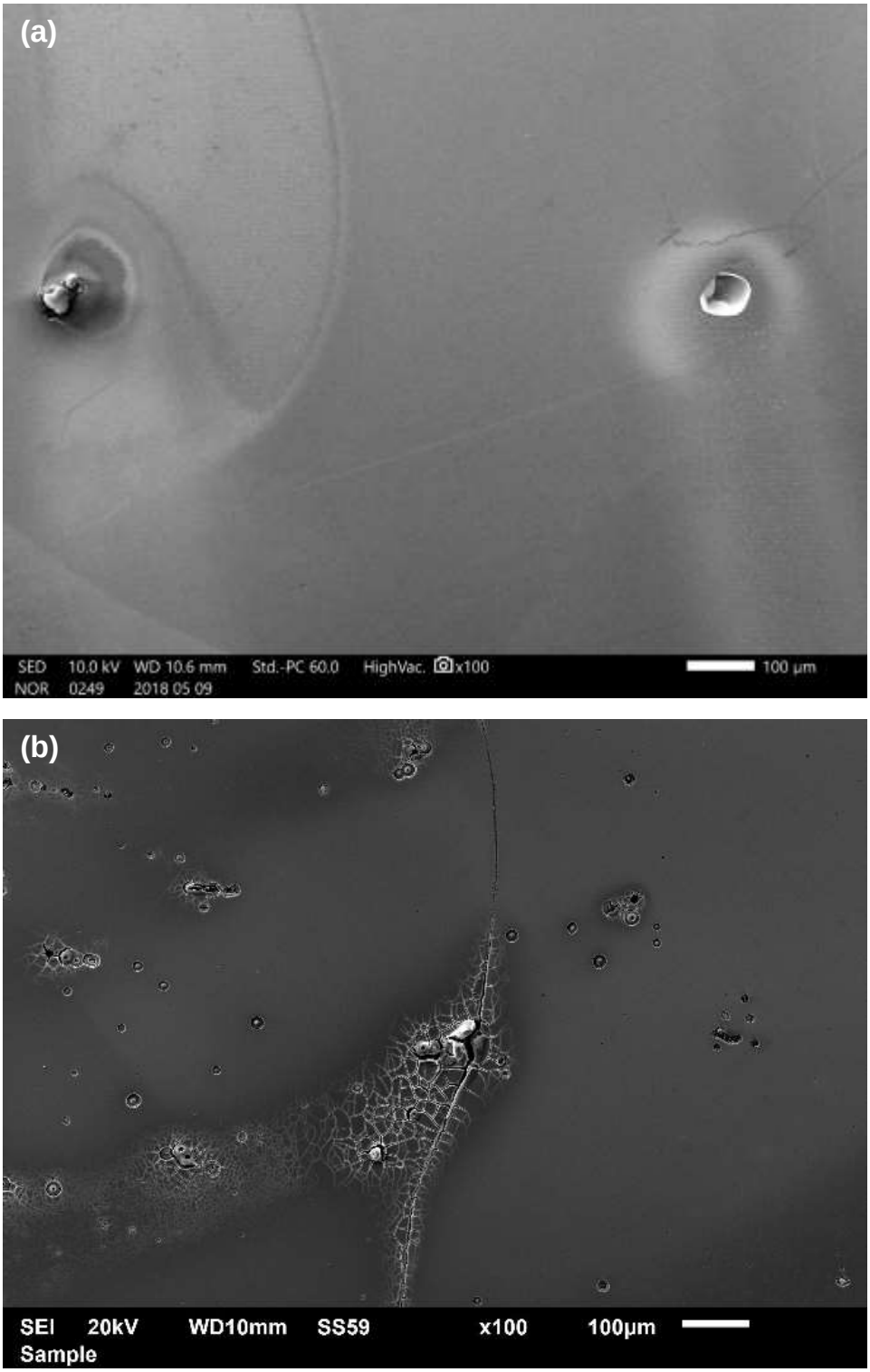

Figure 4.15. SEM micrographs of corroded (a) solution treated NCAT showing corrosion pits and (b) aged NCAT showing IGC and pitting near the grain boundaries. More corrosion and pitting is observed in the aged NCAT.

The analysis of the corrosion scale on the aged alloy was discussed in section 4.3.2. EDS line scans of the aged alloy before corrosion testing and after potentiodynamic polarization testing are given in Figure 4.2 and Figure 4.9, respectively. The line scan analysis shows depletion of Fe and Co, and enrichment of Ta, Al and Ni in the grain boundaries that are characterized with precipitates causing IGC when the alloy was subjected to potentiodynamic polarization test.

An EDS line scan was conducted on the solution treated NCAT that has been subjected to a potentiodynamic polarization test, and is provided in Figure 4.16. The scan was performed at the tip of a pit to determine the chemical composition of the corrosion scale around the pit. The scan showed that the elements distributed uniformly around the pit. At the tip of the pit, a slight reduction in iron, cobalt and nickel, and an increase in aluminum content was observed. Tantalum did not show any change, while high oxygen content in the corrosion scale is evident, indicating that the corrosion was caused by atmospheric oxygen. The increase in Al content in the corroded area indicates that Al could have contributed to the corrosion resistance of the alloy by forming an oxide scale. This scale protected the alloy for a while, but then it broke and pitting took place. Furthermore, an additional EDS spot and area analysis was conducted in a corroded solution treated NCAT to determine if there is any elemental composition change in the alloy. Spot analysis was conducted in the area surrounding a pit and at the edges of the pit, while an area analysis was performed in area away from the pit in Figure 4.17, where each spectrum indicates the location of the analysis. The analysis results are represented in Table 4.4, and compared to the analysis of a non-corroded solution treated NCAT. The results show a reduction in iron, cobalt, nickel, and tantalum, and an increase in aluminum content near the pits and in the corroded area. When comparing the results of the analysis of the area located away from the pit with the alloy's composition before the corrosion test, no remarkable difference in the chemical composition was observed (see spectrum 75 results in Table 4.4). The difference is probably because the chemical composition of the alloy before the corrosion test was determined from 27 measurements, and the results presented in the table are the mean values of these measurements. The reduction of the elemental composition in the corroded area and near the pits is not substantial, and is expected to take place when pitting occurs. It does not represent any elemental segregation similar to the one that was observed in the aged alloy.

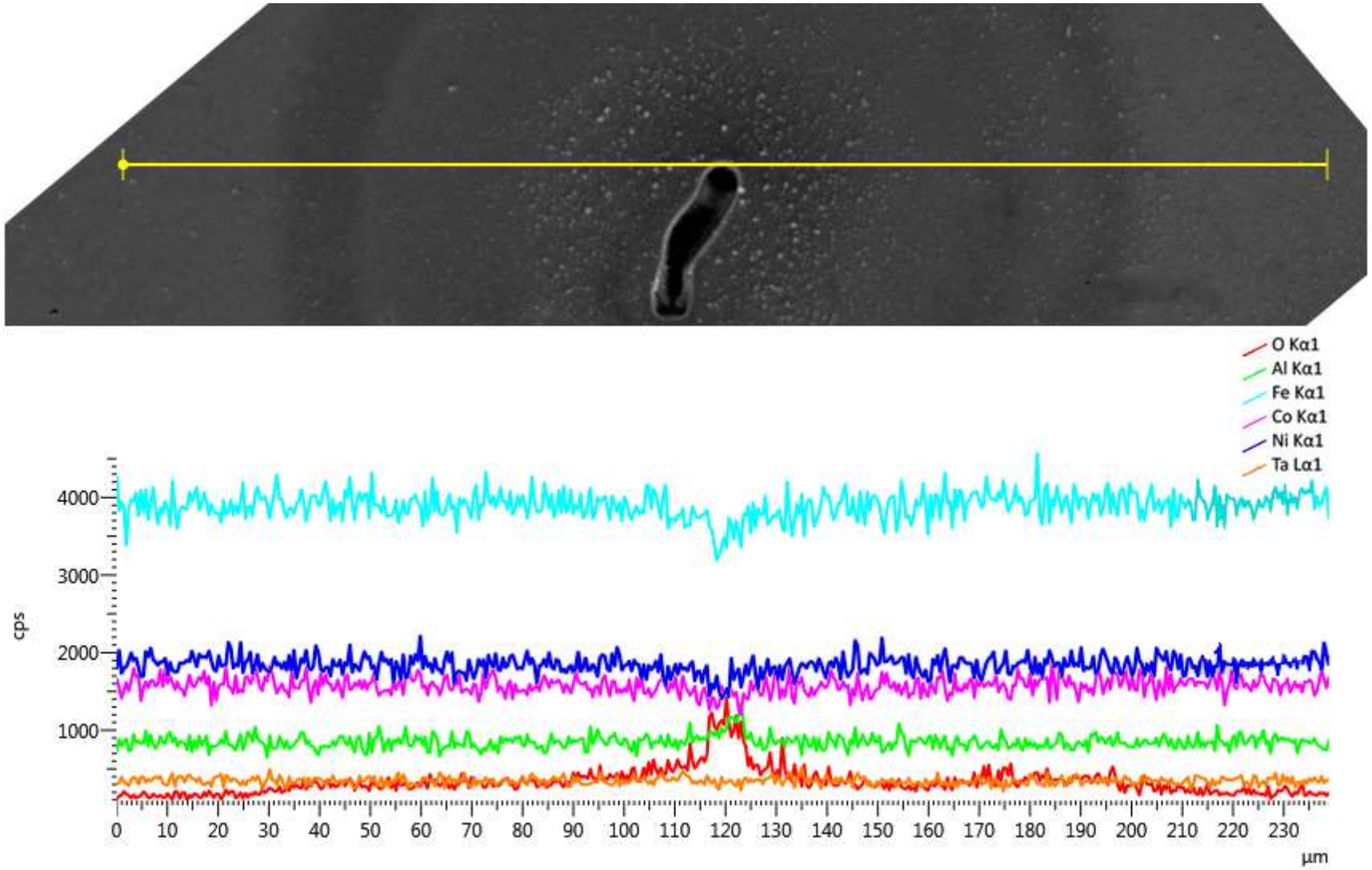

Figure 4.16. An EDS line scan at the tip of a pit in a corroded solution treated NCAT showing slight reduction in Fe, Ni and Co, an increase in oxygen, and slight increase in nickel in the corroded area near the pit. No change in Ta was observed.

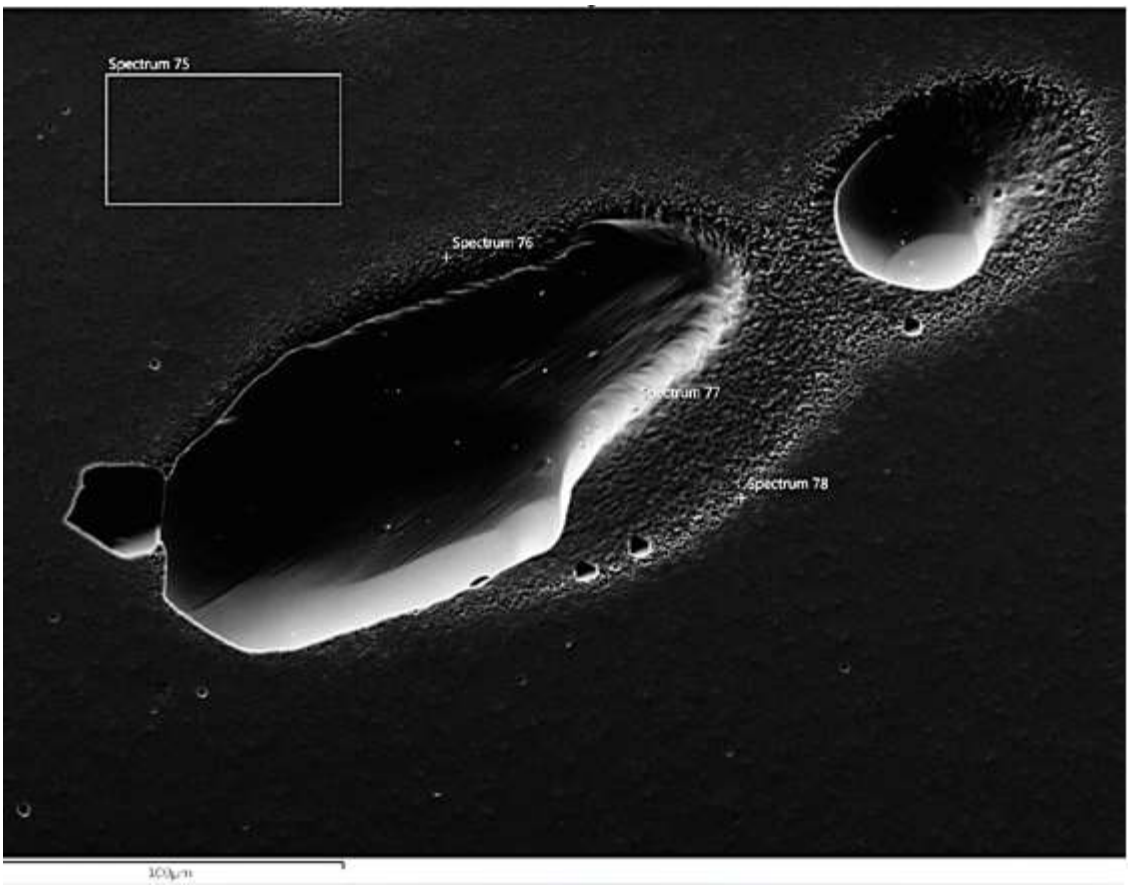

Figure 4.17. SEM micrographs of solution treated NCAT that has been subjected to a potentiodynamic polarization test. The labeled spectrum area and points show the locations of the EDS analysis.

Table 4.4. The EDS analysis conducted on the solution treated NCAT that has been subjected to a potentiodynamic polarization test (Figure 4.17). The analysis was conduced in different areas to cover corroded and non-corroded areas. Oxygen was detected, but was not included in the chemical analysis, as it can not be quantified using EDS analysis.

Elemental Composition	Before Corrosion (mean of 27 measurements) (at%)	Spectrum 75 (NC[1]) (at %)	Spectrum 76 (C[2]) (at %)	Spectrum 77 (C[2]) (at %)	Spectrum 78 (C[2]) (at %)
Al	11.22	11.30	12.66	15.93	13.90
Fe	41.45	41.47	40.78	39.13	40.10
Co	17.26	17.15	16.71	16.10	16.43
Ni	27.45	27.48	27.10	26.11	26.72
Ta	2.60	2.59	2.58	2.49	2.61

[1]NC: Non-corroded area. [2]C: Corroded area.

From the potentiodynamic polarization curves, open circuit potential curves, and images acquired from corroded surfaces of solution treated NCAT alloy and aged NCAT alloy, it is evident that the aging heat treatment of the NCAT alloy is detrimental to its corrosion resistance in NaCl solution. Similar findings in different Fe-based SMA were recorded [45, 97]. Liu *et al.* [97] found the aging treatment to reduce the corrosion resistance of Fe-Mn-Si-Cr-Ni SMA containing C, N, and V elements, while Maji *et al.* [45] tested Fe-15Mn-7Si-9Cr-5Ni SMAs that were heat treated differently in a 0.6 M NaCl solution. They obtained the best corrosion resistance in the alloy with single-phase austenite microstructure [45], which is a similar microstructure to that of solution treated NCAT. Liu *et al.* [97] found that prolonging the aging time produced better corrosion resistance in Fe-Mn-Si-Cr-Ni SMAs. They attributed this behaviour to the improved chemical homogeneity of the austenite matrix, and distribution of the precipitates during the longer aging periods [97]. As mentioned previously, the aging heat treatment results in the precipitation of γ' phase within the grains and β phase in the grain boundaries. The β phase appeared to be responsible for elemental segregation at grain boundaries, which resulted in an anodic grain boundary zone relative to the remainder of the alloy matrix [136, 137]. This caused IGC of the aged alloy in the 0.6 M NaCl solution. Therefore, aging heat treatment is harmful to the corrosion resistance of NCAT alloy. On the other hand, the aging treatment is essential to producing shape memory effect in the alloy. This is a dilemma, where one has to select between shape memory properties or better corrosion resistance. In order to use the NCAT alloy in marine environments, where corrosion resistance to chloride ions is essential, an improvement in the heat treatment to overcome the grain boundary precipitates is essential.

4.5 Corrosion of Heat Treated NCAT SMA in Three Different Solutions

In this section, the corrosion behaviour of solution treated NCAT alloy and aged NCAT alloy in three different solutions is presented and discussed. The alloys were tested at 25 ^{o}C in a 0.6 M NaCl solution, 0.5 M NaOH and 0.5 M H_2SO_4. Linear polarization resistance tests and potentiodynamic polarization scans were performed.

4.5.1 Electrochemical Corrosion behaviour

A comparison between the open circuit potentials of solution heat treated NCAT and aged NCAT in the three solutions is presented in Figure 4.18 and Table 4.5. The open circuit potentials of the two NCAT alloys are more negative in 0.5 M NaOH solution than in the other solutions, which is expected as a result of the increase in pH as per the predicted potential-pH diagram of the alloy shown previously in Figure 4.3. The corrosion potential in 0.6 M NaCl solution is more positive compared to the other two solutions. For example, when comparing the aged NCAT, the open circuit potential was -386 mV (vs. SCE) in NaCl solution compared to -415 mV (vs. SCE) in H_2SO_4 solution, and -454 mV (vs. SCE) in NaOH solution. It is evident from Table 4.5 that in all the test solutions, the solution treated NCAT alloy has more positive open circuit potential compared to the aged NCAT. As previously discussed, this is probably attributable to its single-phase structure (austenite) as compared to the structure (austenite and precipitates) of aged NCAT alloy.

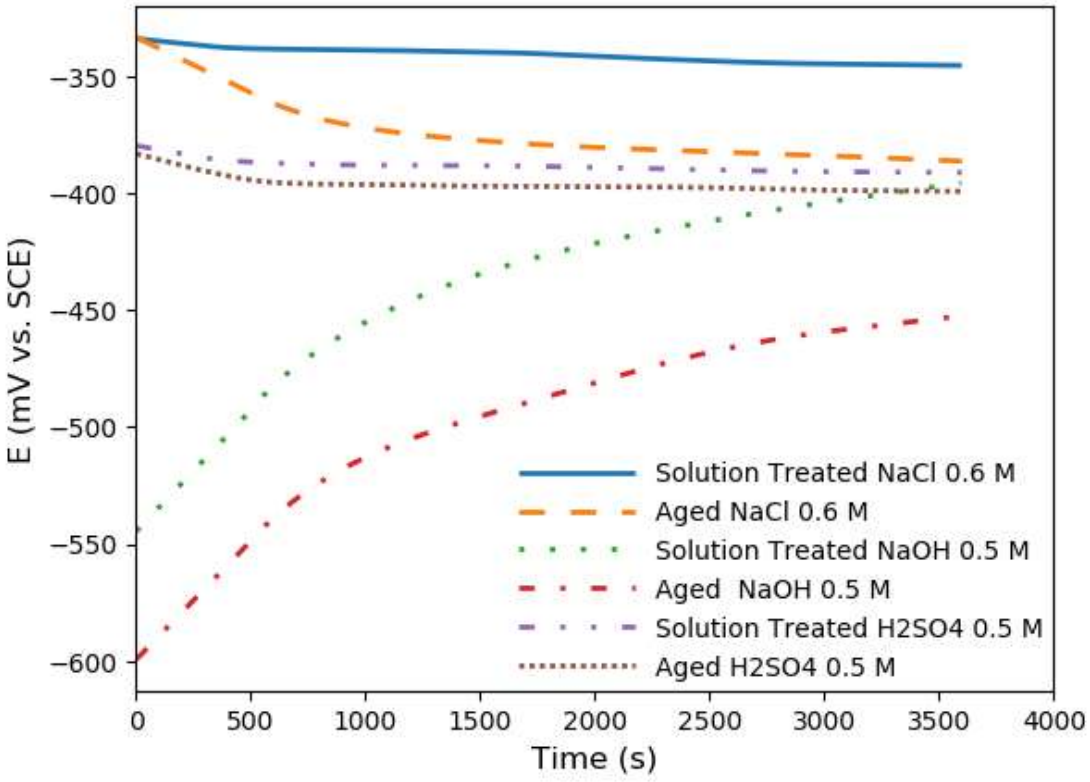

Figure 4.18. Open circuit potentials obtained for solution treated NCAT and aged NCAT tested in three different solutions at 25 ^{o}C. The aging heat treatment resulted in a reduction of the open circuit potential in all the solutions.

The potentiodynamic polarization behaviour of solution treated NCAT and aged NCAT in the three solutions at 25 ^{o}C is illustrated in Figure 4.19, while electrochemical parameters determined from potentiodynamic polarization and LPR plots are presented in Table 4.5. Figure 4.19 shows that the two heat treated NCAT alloys behave differently in the 0.5 M NaOH and 0.5 M H_2SO_4 solutions compared to their behaviour in 0.6 M NaCl solution. The alloys passivated in the two solutions, whereas they showed no passivation, and localized corrosion attack (pitting), when tested in the 0.6 M NaCl solution. Higher corrosion rates were obtained for the two alloys in the H_2SO_4 solution compared to the other two solutions as can be seen from Table 4.5. The lowest corrosion rates were obtained for the alloys in NaOH solution. Furthermore, with respect to the calculated corrosion rates (in mm/y), the aging heat treatment does not show a noteworthy effect on the corrosion rate of the alloy in NaOH solutions. A corrosion rate of 0.0012 mm/y was obtained for the solution treated alloy compared to 0.0015 mm/y for the aged alloy. Similarly, in NaCl solution, the difference in corrosion rate between the two heat treated alloys was not high, with the solution treated alloy showing a corrosion rate of 0.013 mm/y, whereas the aged alloy showed a corrosion rate of 0.017 mm/y. In H_2SO_4 solution, the difference in the corrosion rate was remarkable. The solution treated NCAT has a corrosion rate of 0.786 mm/y compared to 2.488 mm/y for the aged NCAT. In general, better corrosion resistance and more positive corrosion potentials were obtained for the solution treated NCAT compared to the aged NCAT in all the solutions.

The passivation parameters determined from the potentiodynamic polarization plots are presented in Table 4.6. In 0.5 M H_2SO_4 solution, passivation was observed clearly for both alloys. As the potential increased, the alloys reached the passivation potential (E_{pp}) at the critical current density that is required for passivation (i_{crit}), after which the current density started to drop until the passive current density (i_{pass}) was reached. The passivation potential of the solution treated NCAT alloy is -71 mV (vs. SCE) compared to 80 mV (vs. SCE) for the aged NCAT alloy, while the critical current density obtained for the solution treated NCAT is 24.2 mA/cm^2 compared to 41.9 mA/cm^2 for the aged NCAT. The passive current density, on the other hand, is 8.67 µA/cm^2 for the solution treated NCAT compared to 0.13 µA/cm^2 for the aged NCAT alloy. The pitting potential of the solution treated NCAT in 0.5 M H_2SO_4 solution is 1375 mV (vs. SCE), while that of the aged NCAT is 1330 mV (vs. SCE). All the tested samples in this solution show lower passive

current density and higher positive pitting potentials for the solution treated NCAT alloy compared to the aged NCAT alloy.

The behaviour of the alloys in 0.5 M NaOH solution did not show a similar active-passive behaviour to that obtained for the alloys in 0.5 M H_2SO_4 solution. The pitting potential values are more than three times lower than the values obtained in 0.5 M H_2SO_4 solution, with the solution treated NCAT showing a higher pitting potential value of 424 mV (vs. SCE) than 400 mV (vs. SCE) obtained for the aged NCAT.

The behaviour of the alloys in 0.5 M H_2SO_4 solution and 0.6 M NaCl solution is very similar to that reported by Liu *et al.* [97], and Maji *et al.* [45]. They both reported passivation of aged shape memory alloys in 0.5 M H_2SO_4 solution and no passivation when the alloys were tested in 0.6 M NaCl solution. Liu *et al.* [97] recorded corrosion rates of the aged alloys that were nearly three times higher than that of the unaged alloys when tested in 0.5 M H_2SO_4 solution [97]. When comparing the corrosion rates of the aged and solution treated NCAT alloys in the same solution (Table 4.5), a similar trend was observed. The corrosion rate of the aged alloy was nearly three times higher than that of the solution treated NCAT alloy.

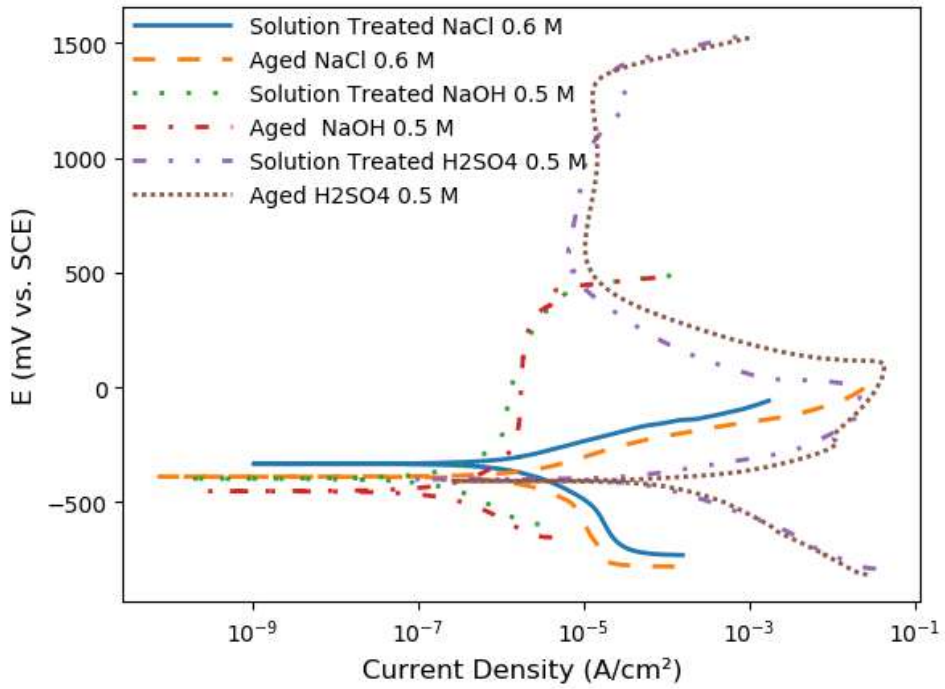

Figure 4.19. Potentiodynamic polarization curves obtained for solution treated NCAT and aged NCAT in three different solutions at 25 °C. The trans-passive behaviour is observed in the H_2SO_4 solution, and the lowest corrosion current density is seen in NaOH solution.

Table 4.5. Electrochemical parameters of solution treated NCAT and aged NCAT tested in three different solutions at 25 °C.

Alloy	**Solution**	**pH**	**E_{oc}[1] mV**	**E_{corr}[1] mV**	**i_{corr} µA/cm²**	**β_a[1] V/decade**	**β_c[1] V/decade**	**R_p Ω.cm²**	**CR mm/y**
Solution Treated NCAT (SD)[2]	0.6 M NaCl	6	-346 (±10.8)	-334 (±35.4)	1.75 (±0.33)	0.06 (±0.02)	-0.16 (±0.06)	$1.05x10^4$ ($±5.8x10^3$)	0.013 (±0.002)
Aged NCAT (SD)[2]	0.6 M NaCl	6	-386 (±16.4)	-389 (±13.5)	2.26 (±0.35)	0.12 (±0.01)	-0.22 (±0.03)	$1.6x10^4$ (±303.5)	0.017 (±0.002)
Solution Treated NCAT (SD)[2]	0.5 M NaOH	12.8	-396.4 (±6.3)	-398 (±2.7)	0.17 (±0.02)	0.21 (±0.10)	-0.16 (±0.05)	$1.8x10^5$ ($±1.9x10^4$)	0.0012 (±0.0002)
Aged NCAT (SD)[2]	0.5 M NaOH	12.8	-454 (±16.6)	-452 (±14.2)	0.2 (±0.04)	0.13 (±0.10)	-0.19 (±0.007)	$1.4x10^5$ ($±1.8x10^4$)	0.0015 (±0.0003)
Solution Treated NCAT (SD)[2]	0.5 M H_2SO_4	0.72	-391 (±3.9)	-401 (±6.8)	105.7 (±3.65)	0.09 (±0.009)	-0.16 (±0.11)	409.6 (±143.6)	0.786 (±0.03)
Aged NCAT (SD)[2]	0.5 M H_2SO_4	0.72	-415 (±12.6)	-409 (±13.9)	333 (±41.0)	0.09 (±0.01)	-0.35 (±0.09)	177.4 (±48.07)	2.488 (±0.31)

[1] All the potential values are measured vs. SCE. [2] Standard deviation (SD) values.

Table 4.6. Passivation parameters obtained from potentiodynamic polarization scans of solution treated NCAT and aged NCAT tested in 0.5 M NaOH and 0.5 M H_2SO_4 solutions at 25 °C.

Alloy	Solution	E_{corr}[1] mV	E_{pp}[1] mV	E_p[1] mV	i_{corr} µA/cm²	i_{crit} mA/cm²	i_{pass} µA/cm²
Solution Treated NCAT (SD)[2]	0.5 M NaOH	-398 (±2.7)	-	424 (±12)	0.17 (±0.02)	-	-
Aged NCAT (SD)[2]	0.5 M NaOH	-452 (±14.2)	-	400 (±17.5)	0.2 (±0.04)	-	-
Solution Treated NCAT (SD)[2]	0.5 M H_2SO_4	-401 (±6.8)	-71 (±17)	1375 (±16)	105.7 (±3.65)	24.2 (±0.30)	8.67 (±0.07)
Aged NCAT (SD)[2]	0.5 M H_2SO_4	-409 (±13.9)	80 (±23)	1330 (±35)	333 (±41.0)	41.9 (±6.21)	13.3 (±0.02)

[1] All the potential values are measured vs. SCE. [2] Standard deviation (SD) values.

4.5.2 Observation and Analysis of the Corrosion Scale

SEM micrographs showing the surface morphologies of the solution treated NCAT and aged NCAT after potentiodynamic polarization test in the three solutions are presented in Figures 4.20 – 4.22. The optical micrographs obtained for these samples can be found in Appendix C. As shown in Figure 4.20, the solution treated NCAT alloy showed some pitting, while the aged NCAT alloy suffered IGC and pitting in the area near grain boundaries with precipitates in 0.6 M NaCl solution. In Figure 4.21, it is seen that the two alloys did not display much corrosion attack when tested in 0.5 M NaOH. In fact, the solution treated alloy showed almost no corrosion, with very minor pitting. This is also evident from its corrosion rate of 0.0012 mm/y. The aged alloy showed only small sized pits with an average size of ~ 17 μm. On the other hand, when tested in 0.5 M H_2SO_4 solution (Figure 4.22), the alloys showed extensive general corrosion and pitting all over the grains. Large-sized pits are observed in the two heat treated alloys. Some of the clustered pits in the aged alloy have an average size of ~ 114 μm. More corrosion at the grain boundaries are observed in the aged NCAT alloy. No IGC is detected in the alloys tested in 0.5 M H_2SO_4 or 0.5 M NaOH solutions.

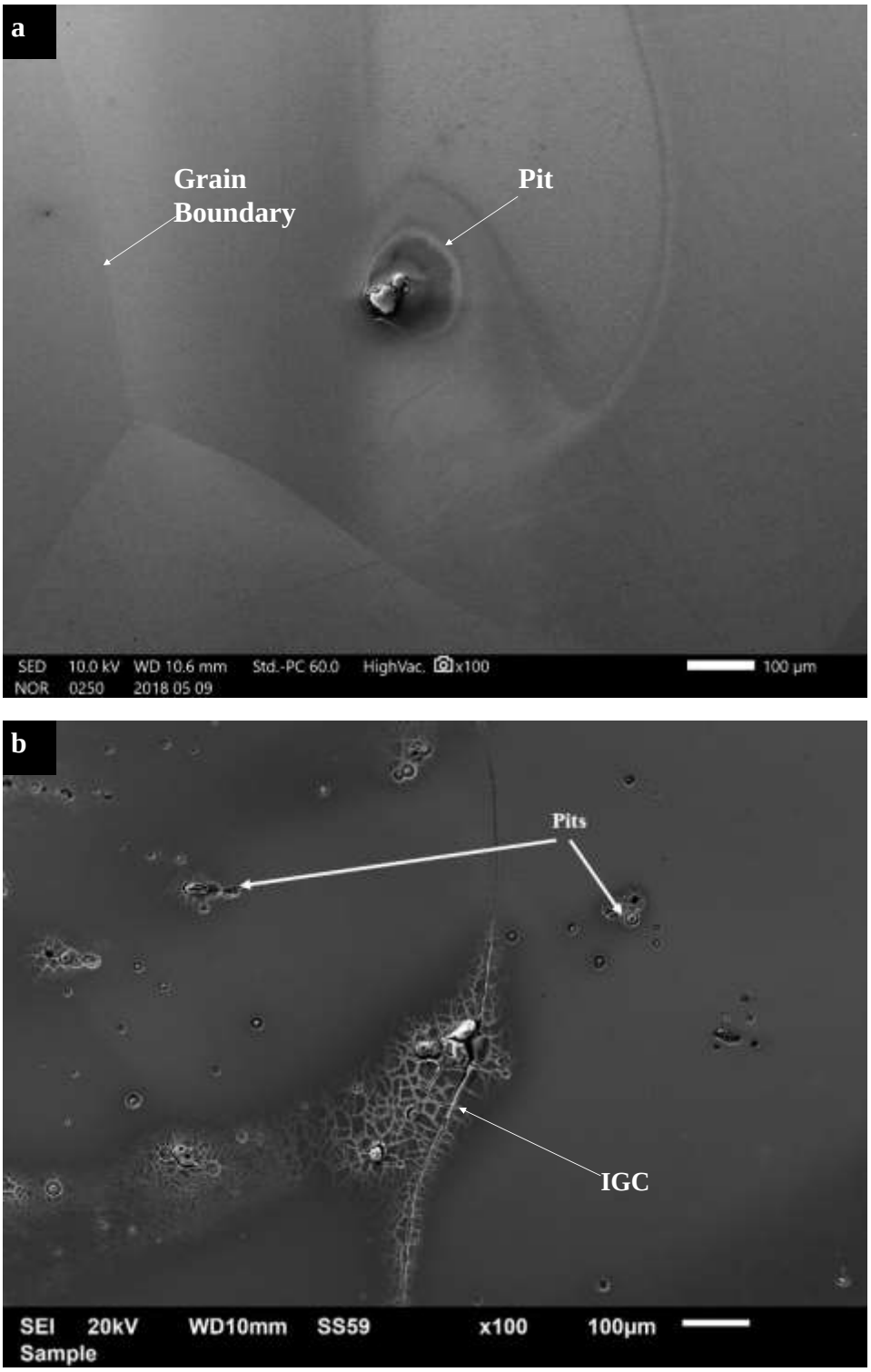

Figure 4.20. SEM micrographs of (a) solution treated and (b) aged NCAT samples that were subjected to potentiodynamic polarization scans in 0.6 M NaCl solution at 25 ^{o}C. Intergranular corrosion (IGC) is evident in the aged sample.

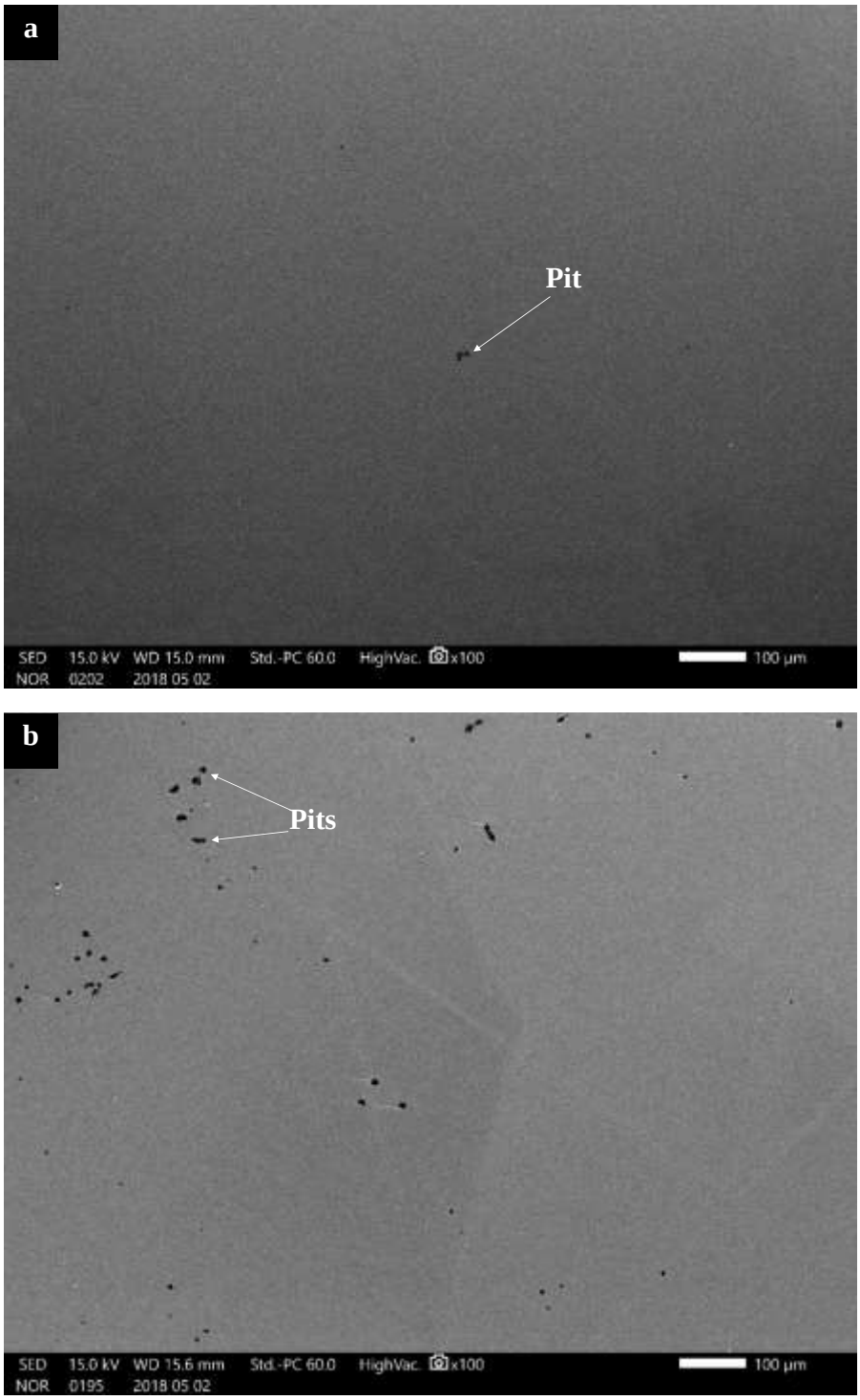

Figure 21. SEM micrographs of (a) solution treated and (b) aged NCAT samples that were subjected to potentiodynamic polarization scans in 0.5 M NaOH solution at 25 ^{o}C. Minor pitting and almost no signs of corrosion were observed in the solution treated NCAT sample, while small size pits are seen in the aged NCAT sample.

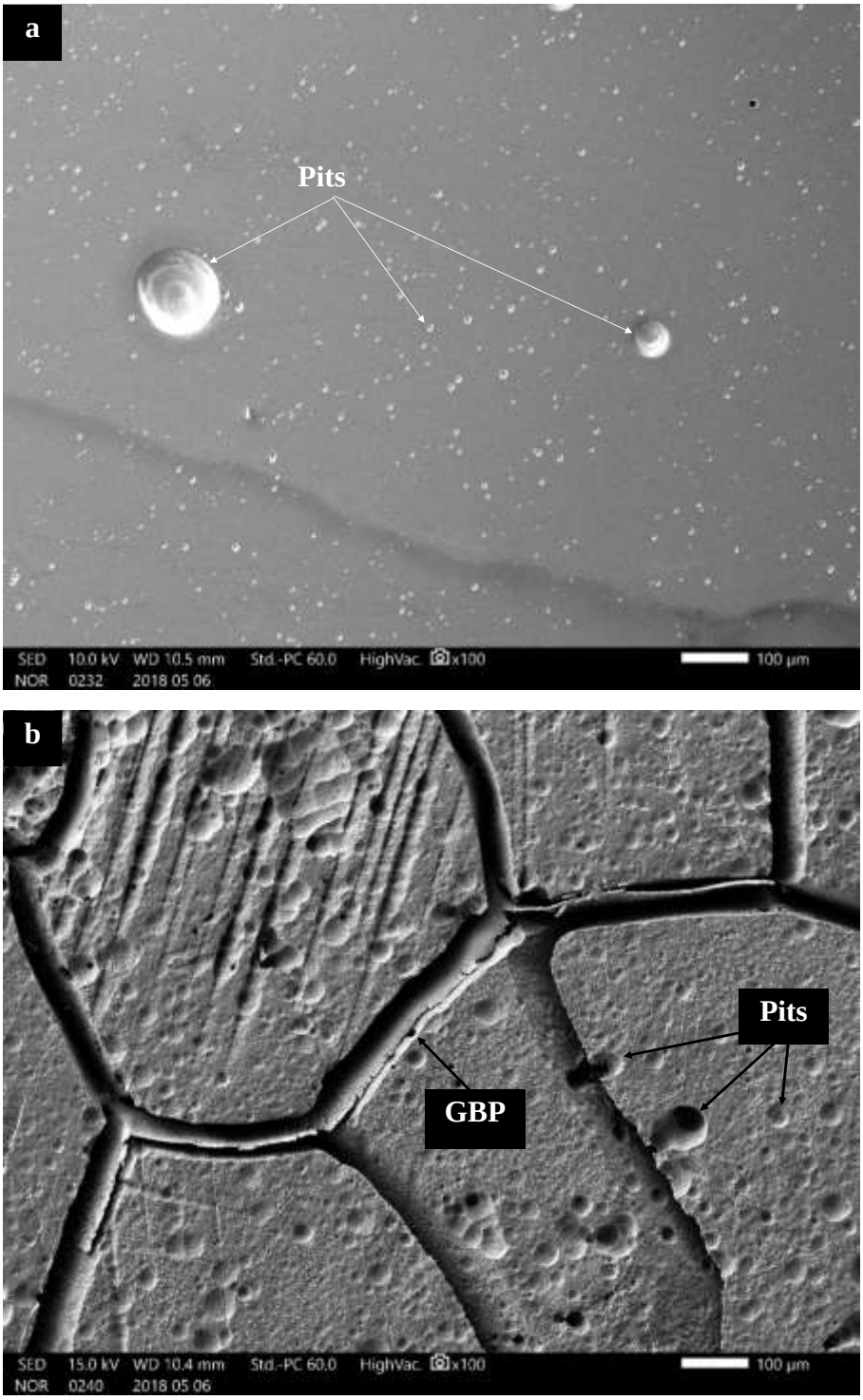

Figure 4.22. SEM micrographs of (a) solution treated NCAT and (b) aged NCAT samples that were subjected to potentiodynamic polarization scans in 0.5 M H_2SO_4 solution at 25 ^oC. Grain boundary corrosion and pitting in the matrix can be seen in the aged sample. No signs of grain boundary corrosion were observed in the solution treated NCAT.

Further analysis of the surface films of the alloys tested in NaOH and H_2SO_4 solutions was carried out using the X-ray mapping tool of the EDS system. The acquired maps are shown in Figures 4.23 – 4.26.

X-ray maps of solution treated NCAT alloy tested in 0.5 M H_2SO_4 are shown in Figure 4.23, while those of aged NCAT alloy are presented in Figure 4.24. The pit in the solution treated alloy is covered with a corrosion product that consists of aluminum and oxygen, which indicates that although aluminum oxide formed, it failed to protect the alloy. The distribution of the alloying elements and oxygen appears to be uniform all over the alloy, and no elemental segregation was observed. On the other hand, the aged NCAT alloy (Figure 4.24) showed severe pitting all over the alloy. The acidic solution etched the alloy and revealed grain boundary precipitates where elemental segregation occurred. An oxide layer appears to be distributed all over the alloy, and is pitting can be observed on the alloy matrix. The grain boundary precipitates were attacked by the acidic solution that caused their rupture as can be seen in Figure 4.22 (b). The grain boundary precipitates did not suffer IGC, which is different from the corrosion attack that was observed in the aged NCAT alloy in 0.6 NaCl solution. More corrosion attack was observed in the GBP in aged NCAT alloy in 0.5 M H_2SO_4 solution, which is expected. It can be seen that tantalum and nickel contents at grain boundaries are higher than that of any other element.

X-ray maps of solution treated NCAT alloy tested in 0.5 M NaOH solution are provided in Figure 4.25, while those of aged NCAT alloy are shown in Figure 4.26. The solution treated alloy shows a uniform distribution of the alloying elements all over the alloy structure. No oxygen was observed, indicating that the oxidation of the alloy was very minimal. This is consistent with the recorded corrosion rate of the alloy of 0.0012 mm/y. The aged alloy, on the other hand, showed similar uniform elemental distribution, except in the pit area where aluminum, tantalum and oxygen can be observed in the corrosion product in and around the pit. This indicates that oxide films of Al and Ta were formed, but were not able to protect the alloy from further pitting attack. It also indicates that possibly precipitates are located in this area that was a preferred site for pitting. Tantalum appears to be present in smaller content compared to the aluminum content, as can be seen by their colour and brightness in the maps in Figure 4.26, indicating that the oxide film consisted mostly of aluminum oxide and some tantalum oxide. Other EDS scan maps performed

away from the pitting area did not show the presence of oxygen in the alloy matrix. An example is provided in Figure 4.27, where oxygen was not found. No grain boundaries can be observed in the alloy, making it difficult to judge if the analysis covered any grain boundaries. The aged NCAT demonstrated low corrosion rate of 0.0015 mm/y in this solution.

The results of the EDS scan maps support the findings of potentiodynamic polarization test results, where the high corrosion rates were observed for the alloys tested in 0.5 M H_2SO_4 solution, and low corrosion rates for the alloys tested in 0.5 M NaOH solution. The results from electrochemical tests and EDS analysis of corrosion scales show that aging heat treatment reduced the corrosion resistance of the alloy. As previously discussed, this heat treatment is needed to impart shape memory effect to NCAT alloy. Therefore, it is very important to optimize this heat treatment to reduce its effect on the corrosion resistance of the alloy. Two options are available:

(i) Alloy modification: Tanaka *et al*. [17] encountered intergranular fracture that results in reducing the NCAT's ductility due to the presence of the β phase precipitates in the grain boundaries. β phase grain boundary precipitates were found to consist mostly of Ni_3Al [17]. Tanaka *et al*. [17] added boron to NCAT SMA to supress β phase grain boundary precipitates. The new alloy that contained boron showed better shape memory effect and superelasticity than NCAT alloy [17]. However, its corrosion behaviour has yet to be investigated. Testing this alloy in the three electrolytes that were used in this section will determine if the aging heat treatment will be an issue for the NCATB alloy's corrosion resistance.

(ii) Modification of age hardening parameters: Liu *et al*. [97] studied the influence of the length of aging time on the corrosion behaviour of a Fe-based alloy. They found the prolonged aging time (24 h) to result in higher corrosion potential and lower passive current density values than those of the alloys aged in shorter time. They concluded that prolonged aging treatment could result in improvement of the distribution of the precipitates and superior homogenization effect, which in turn, reversed the corrosion resistance of the alloy [97]. Increasing the length of the aging treatment time of NCAT alloy should be considered to determine if it could improve the corrosion resistance of the alloy.

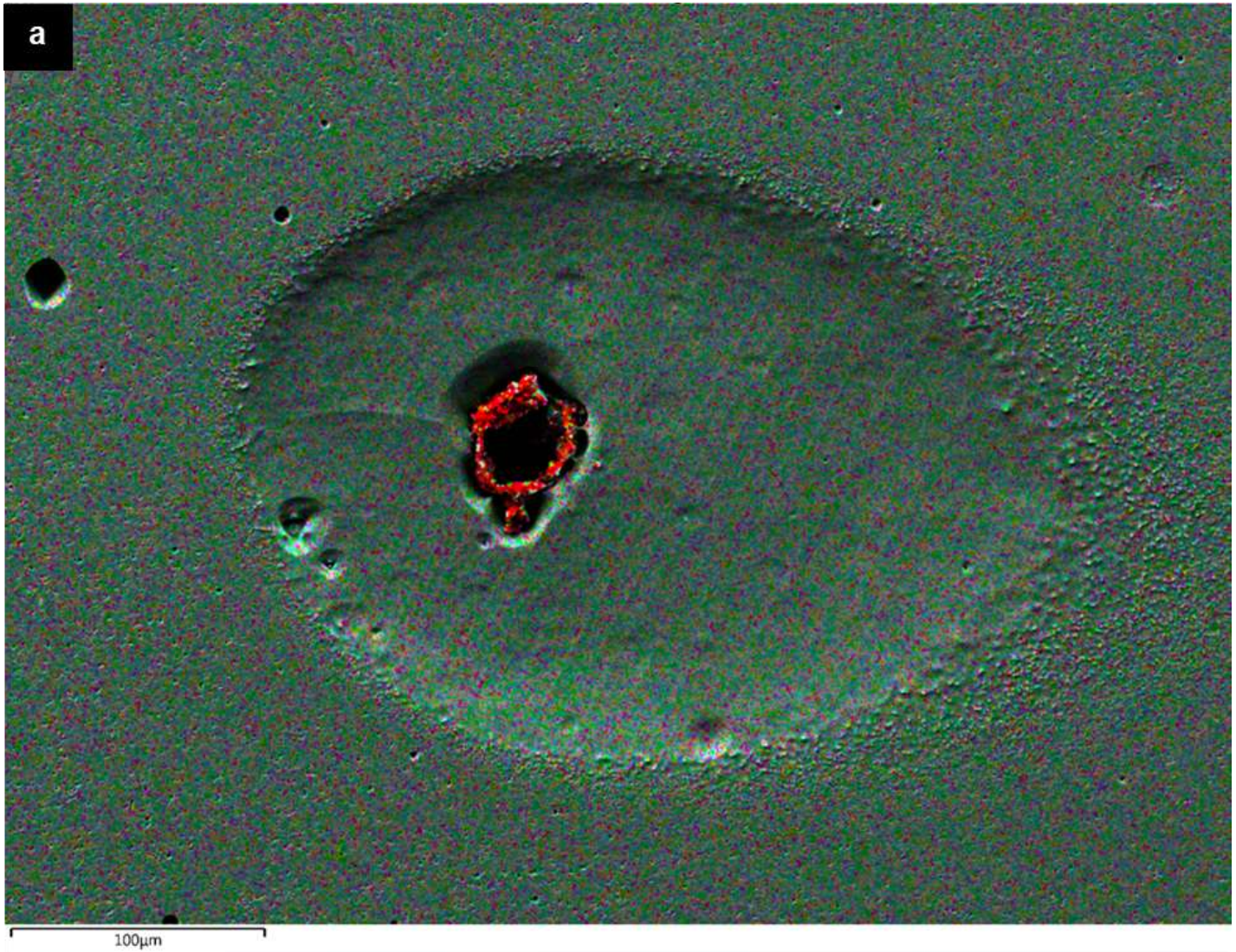

Figure 4.23. Typical EDS X-ray maps obtained for solution treated NCAT that was tested in H_2SO_4 solution at 25 ^oC. (a) analyzed area, (b) Fe $K\alpha_1$, (c) Ni $K\alpha_1$, (d) Co $K\alpha_1$, (e) Al $K\alpha_1$, (f) Ta $K\alpha_1$, and (g) O $K\alpha_1$. Note the elevated concentration of aluminum and oxygen in the corrosion product that surrounds the pit.

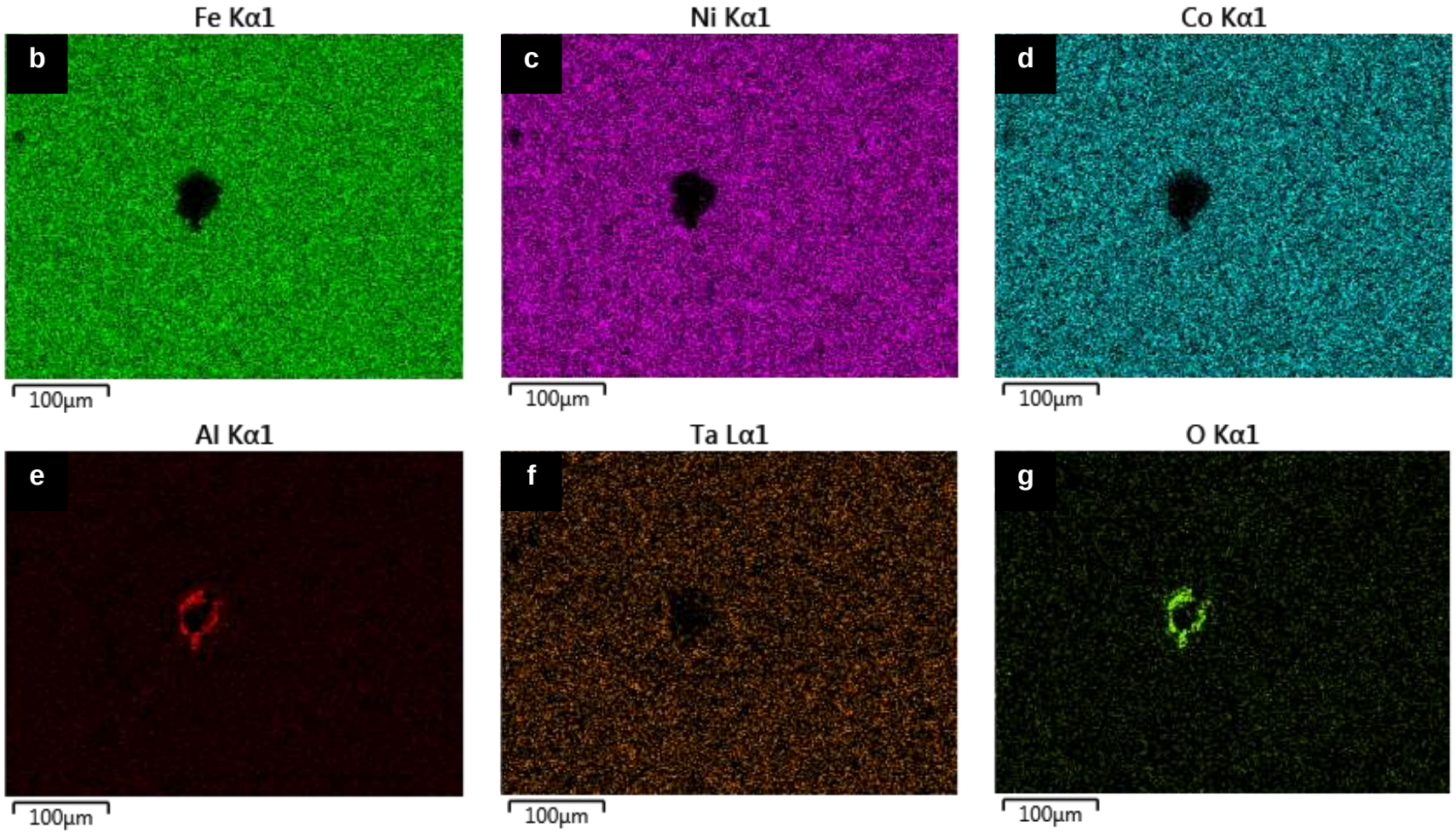

Figure 4.23. Continued.

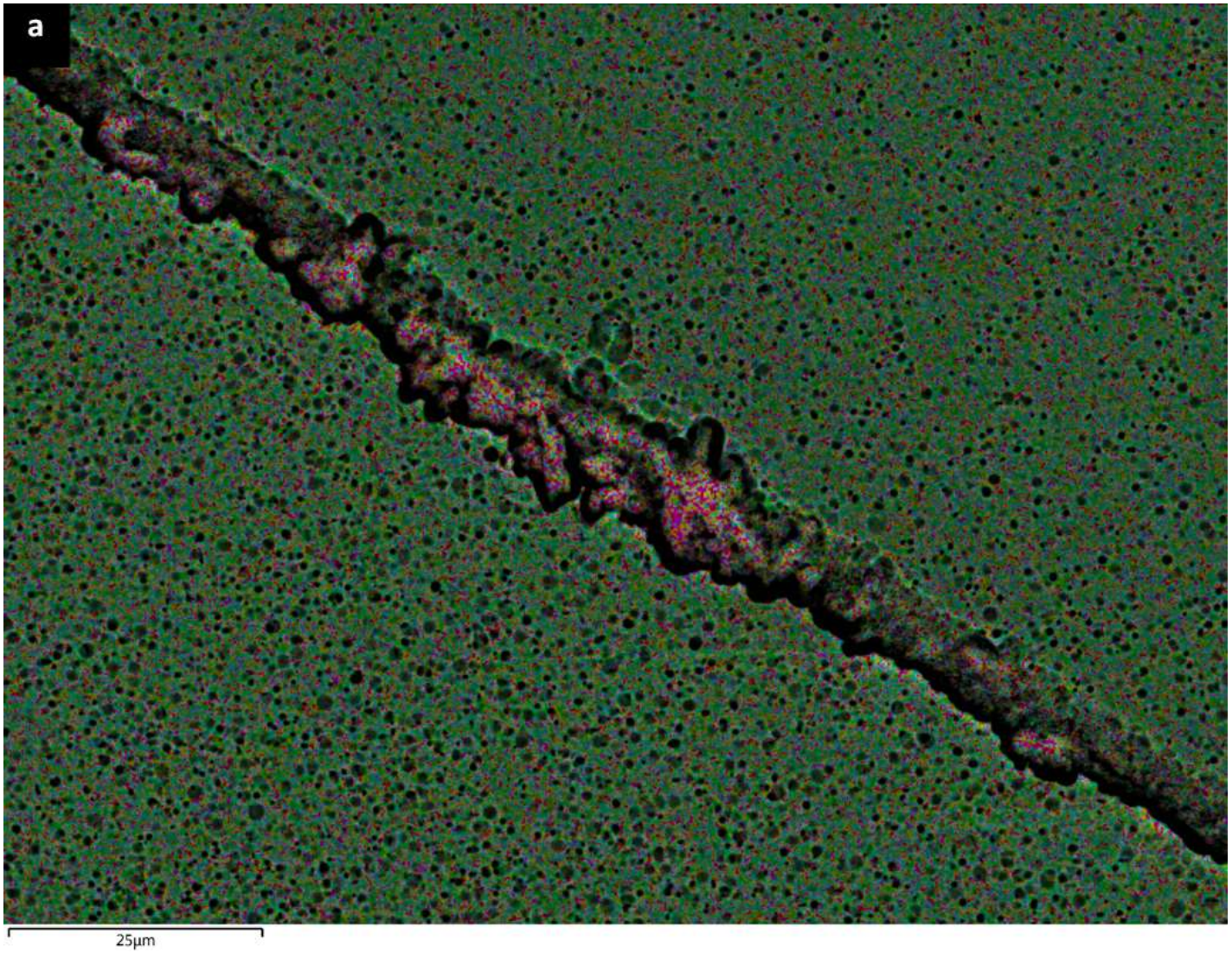

Figure 4.24. Typical EDS X-ray maps obtained for aged NCAT tested in H_2SO_4 solution at 25 ^oC. (a) analyzed area, (b) Fe $K\alpha_1$, (c) Ni $K\alpha_1$, (d) Co $K\alpha_1$, (e) Al $K\alpha_1$, (f) Ta $K\alpha_1$, and (g) O $K\alpha_1$.The oxidation is distributed all over the alloy with more oxidation in the grain boundary that has precipitates. The precipitates consist mostly of nickel and tantalum. Observe that iron and cobalt are depleted from the grain boundary.

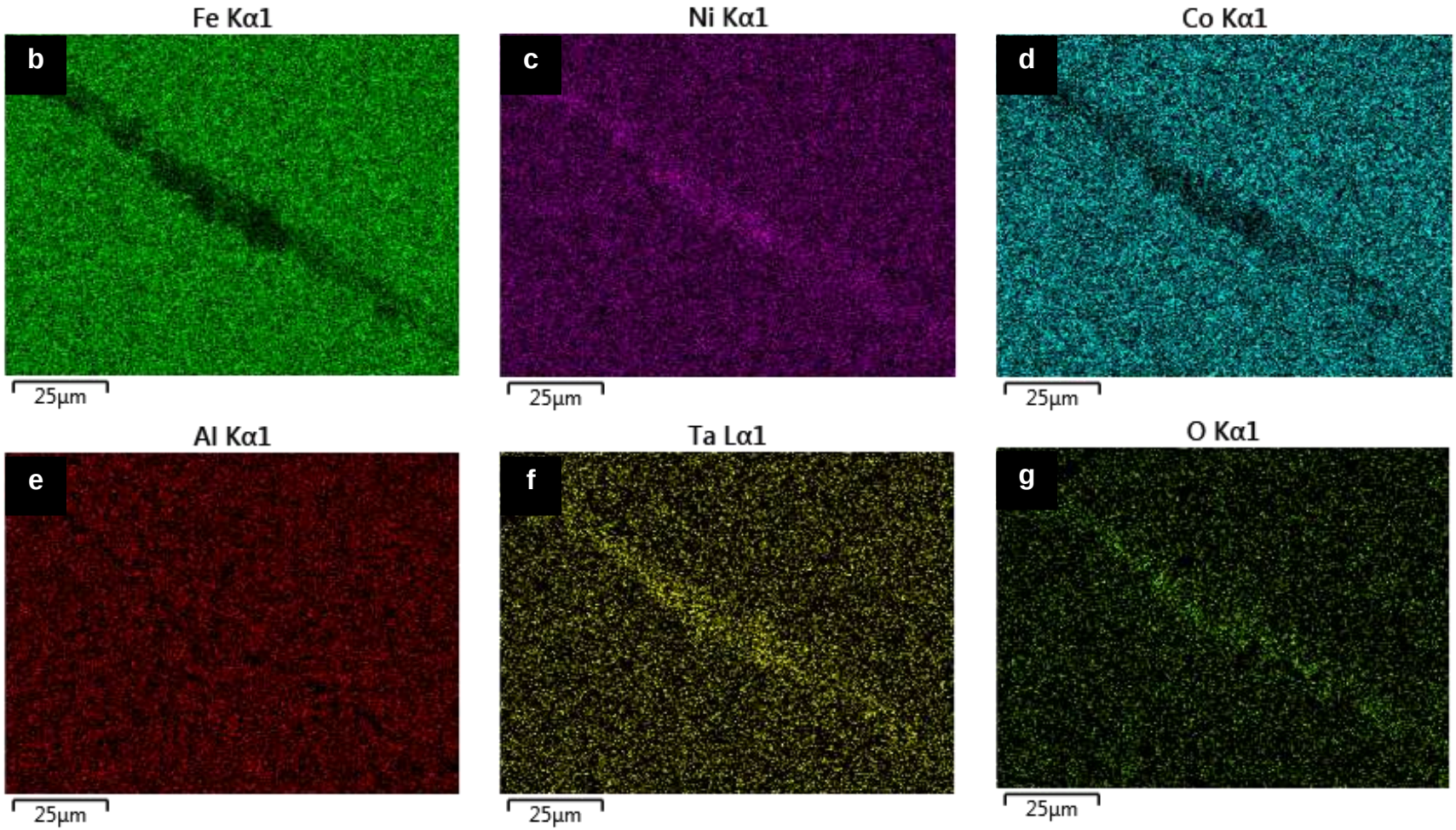

Figure 4.24. Continued.

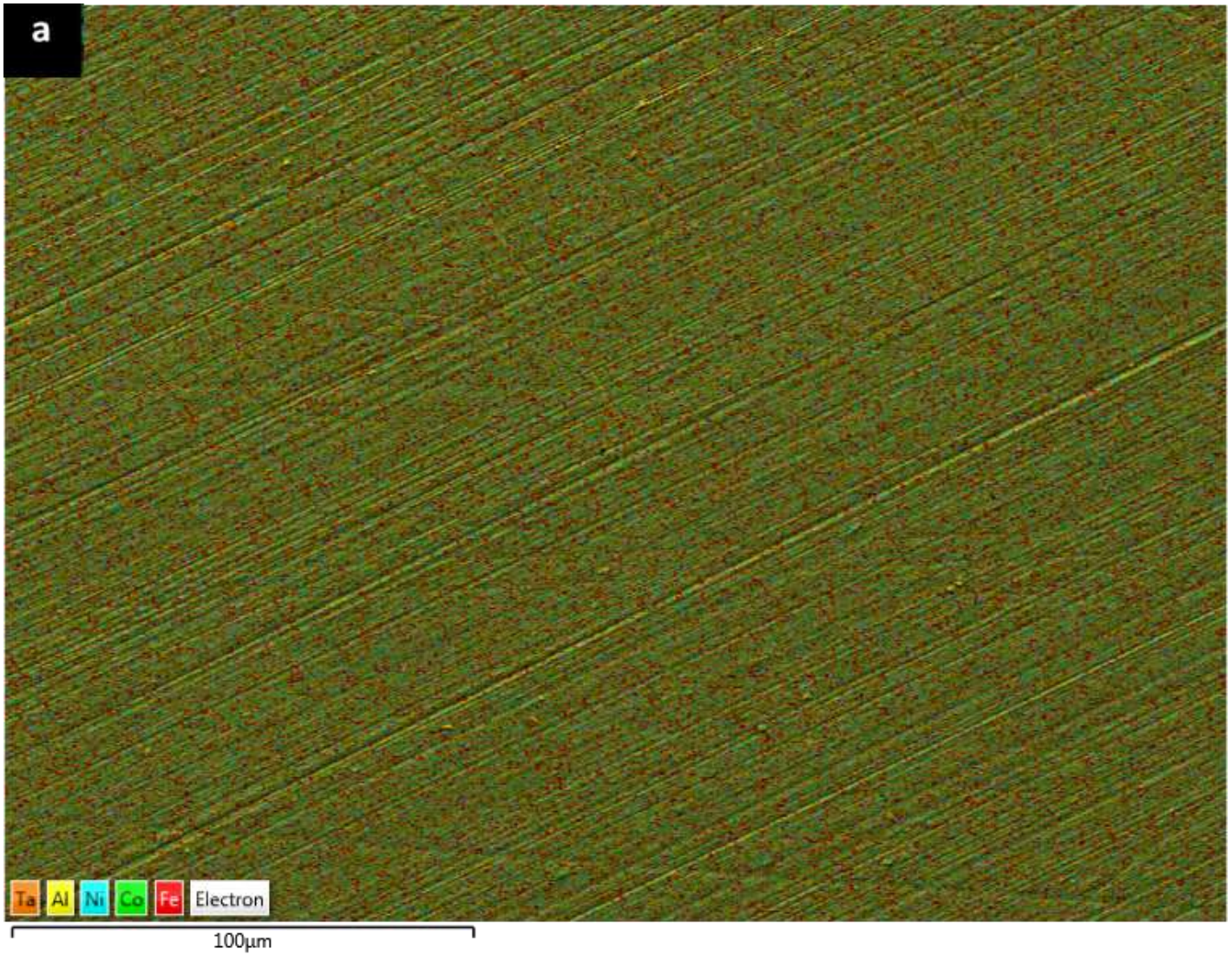

Figure 4.25. Typical EDS X-ray maps obtained for solution treated NCAT alloy that was tested in NaOH solution at 25 ^{o}C. (a) analyzed area, (b) Fe Kα_1, (c) Co Kα_1, (d) Ta Kα_1, (e) Ni Kα_1, and (f) Al Kα_1. No discernable signs of corrosion were observed in this sample.

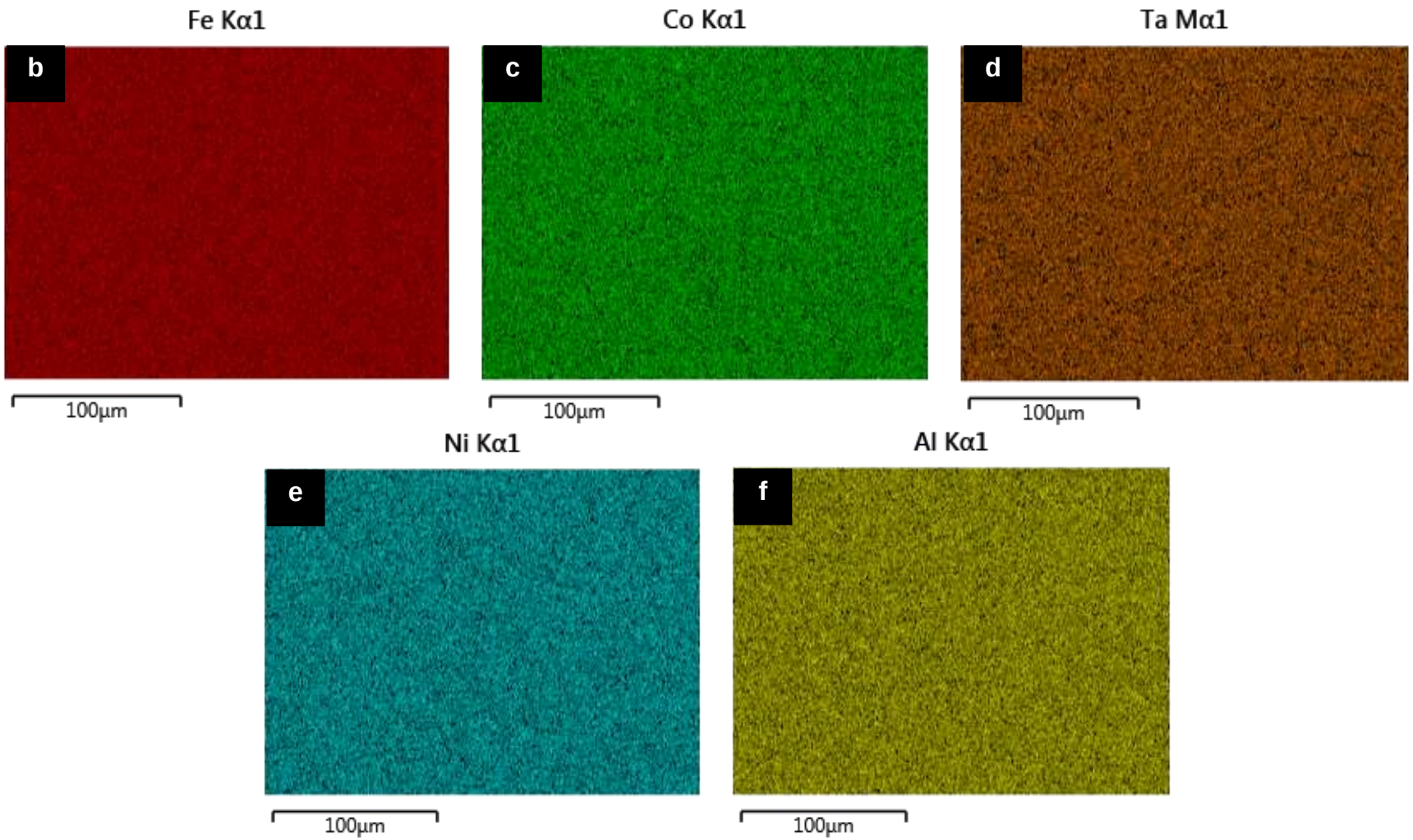

Figure 4.25. Continued.

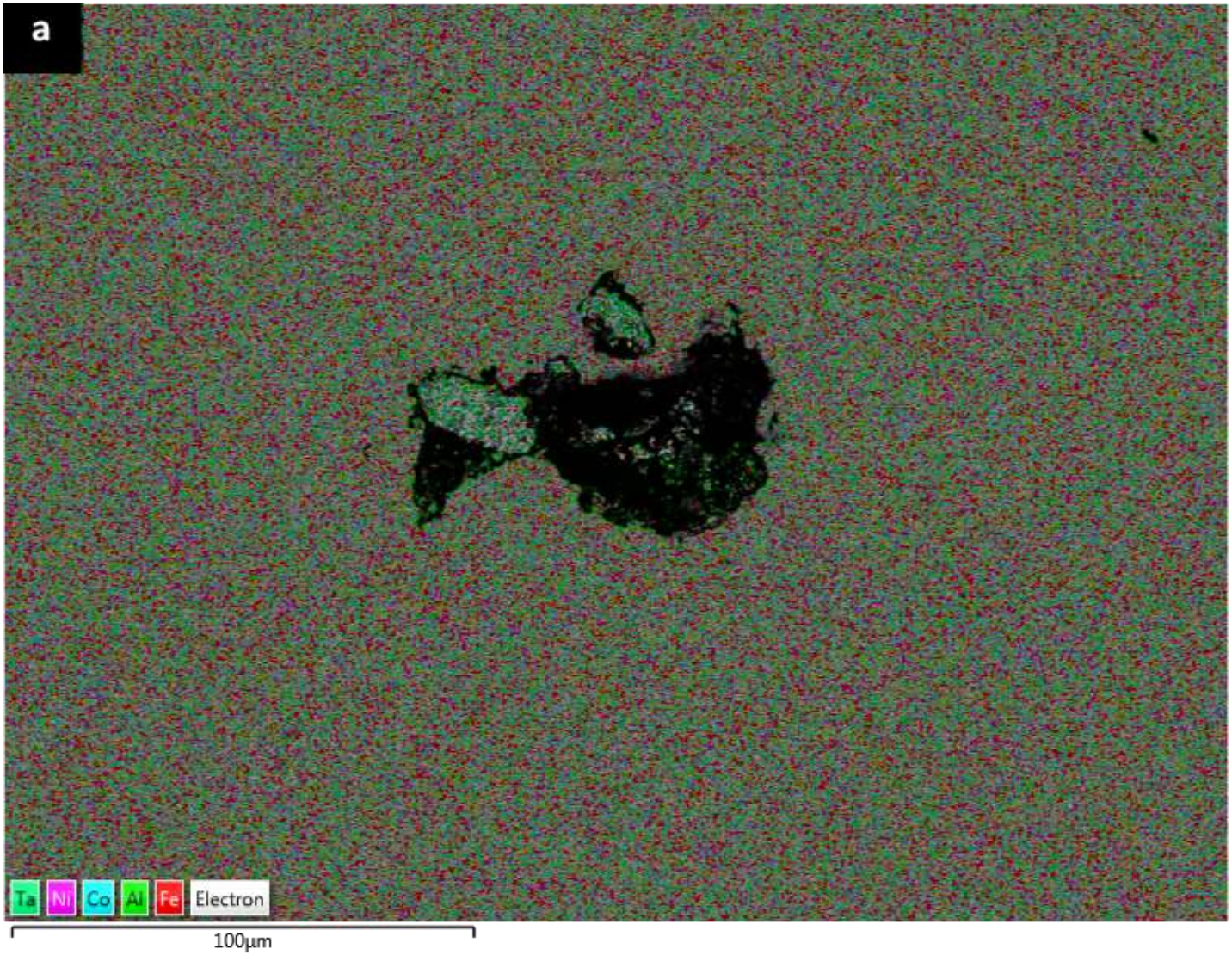

Figure 4.26. Typical EDS X-ray maps of aged NCAT alloy tested in 0.5 M NaOH solution at 25 ºC. (a) analyzed area, (b) Fe $K\alpha_1$, (c) Al $K\alpha_1$, (d) Ni $K\alpha_1$, (e) Co $K\alpha_1$, (f) Ta $K\alpha_1$, and (g) O $K\alpha_1$. The corrosion product surrounding the pit consists of aluminum, tantalum and high content of oxygen. More aluminum was observed in the corrosion product than tantalum.

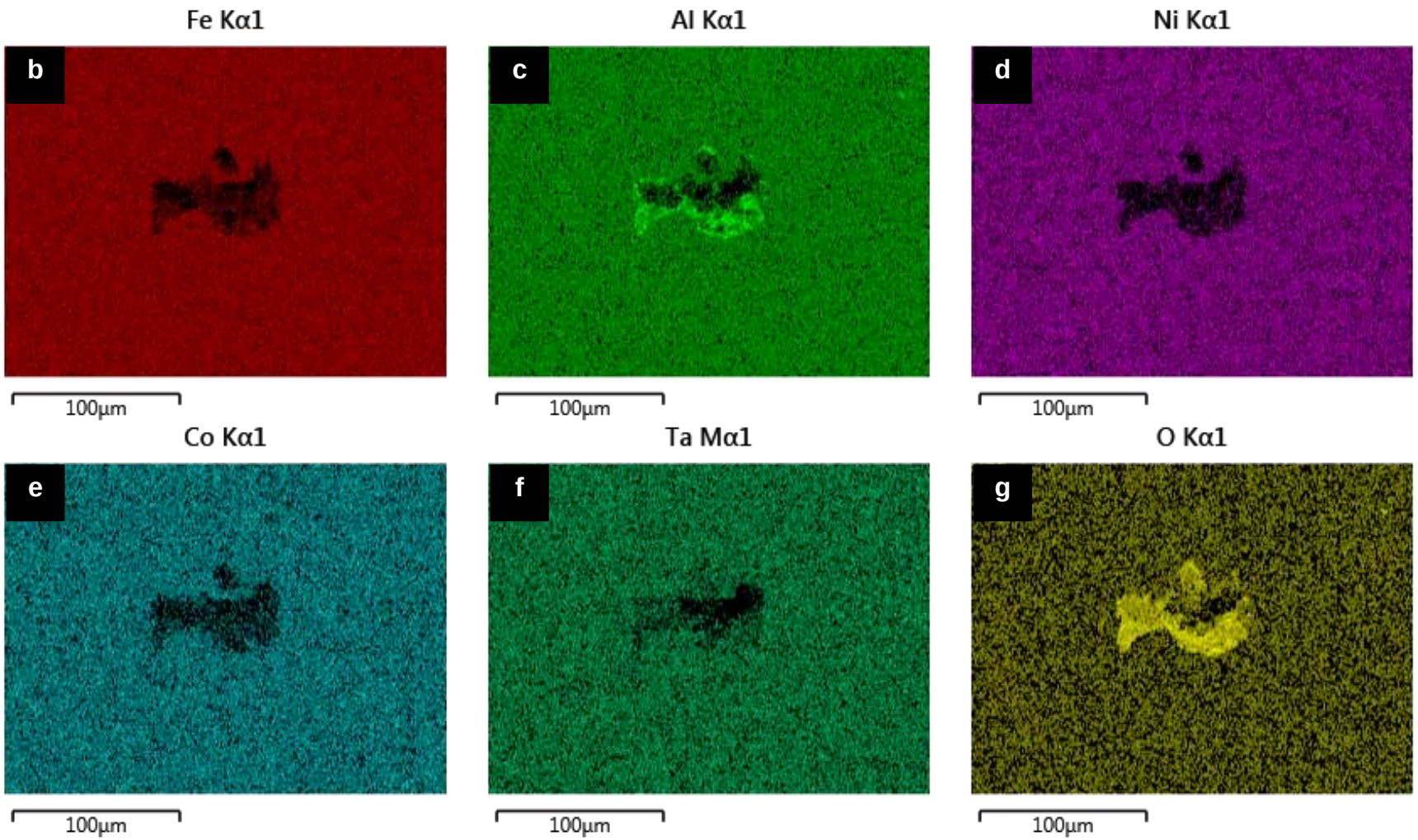

Figure 4.26. Continued.

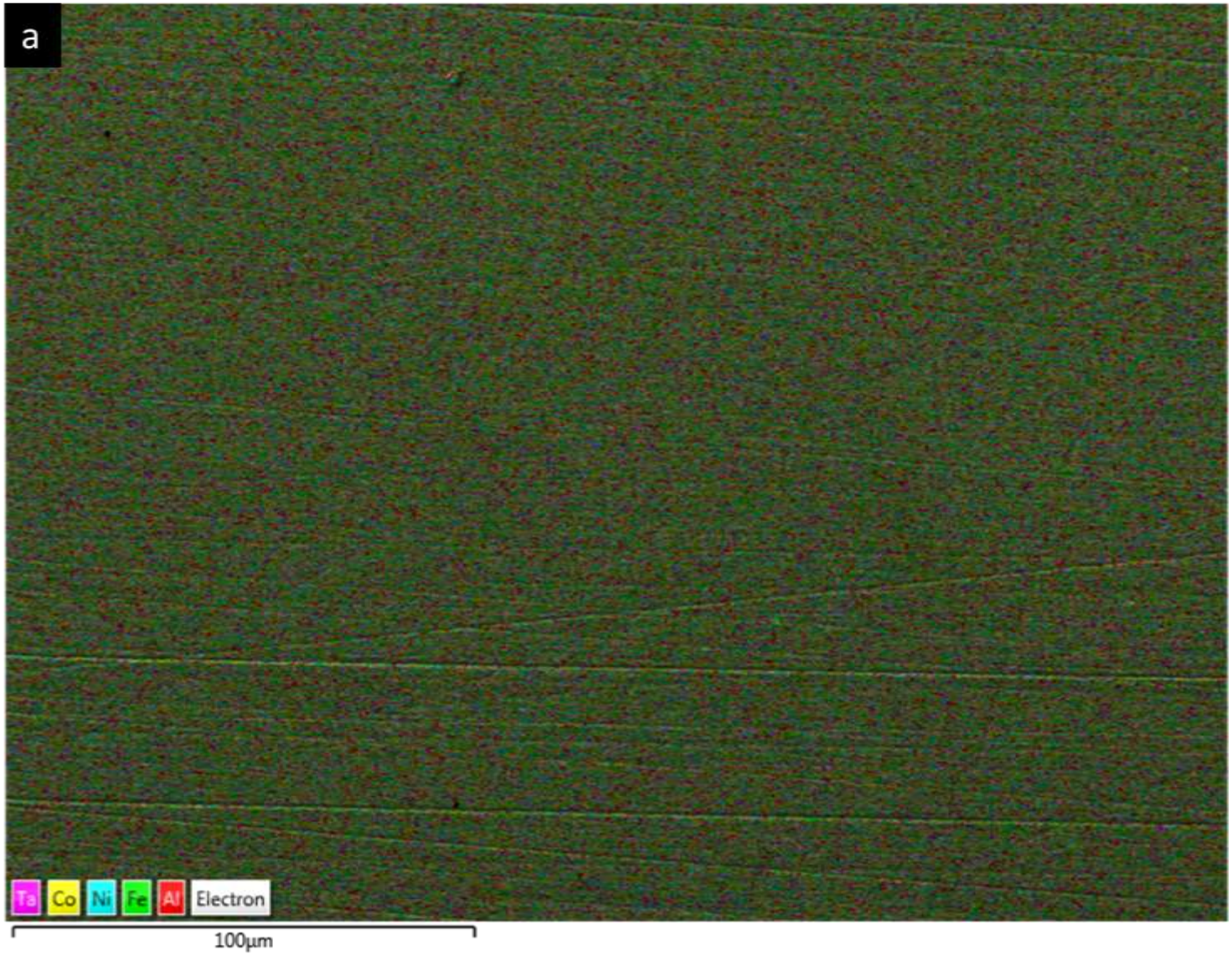

Figure 4.27. Typical EDS scan maps of aged NCAT sample that was tested in NaOH solution at 25 ºC and did not contain pits. (a) Analyzed area, (b) Fe Kα1, (c) Ni Kα1, (d) Al Kα1, (e) Co Kα1, and (f) Ta Kα1. No evidence of oxidation is found in this sample.

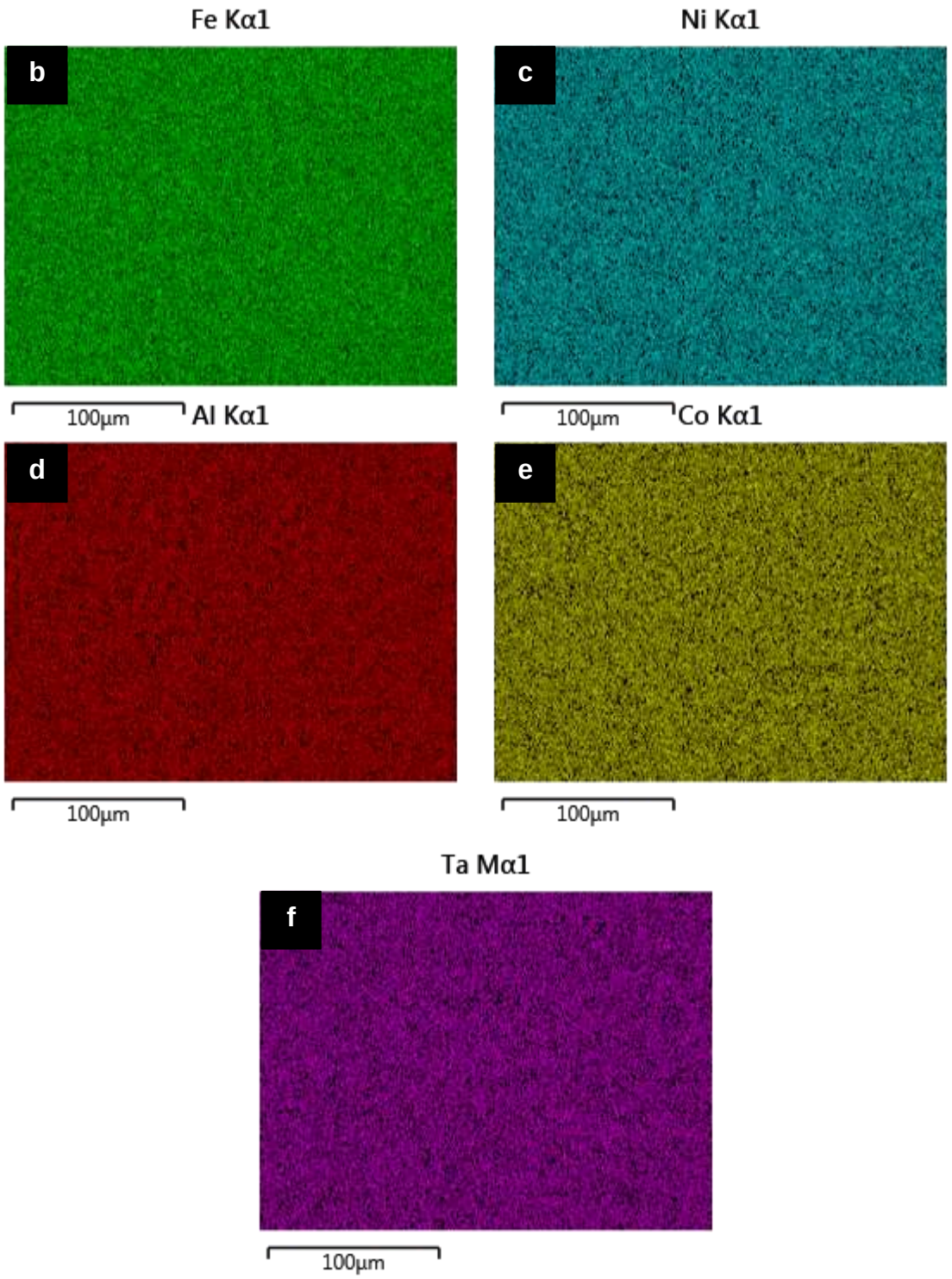

Figure 4.27. Continued.

4.6 Effect of Temperature and pH on Corrosion of Aged NCAT SMA in 0.6 M NaCl Solution

In this section, the results obtained for aged NCAT alloy tested in a 0.6 M NaCl solution at four different temperatures (RT, 40 ^{o}C, 60 ^{o}C and 80 ^{o}C) and three pH values (3, 6 and 10) are presented.

4.6.1 Effect of Temperature on of NCAT SMA at Different pH

Figure 4.28 presents the open circuit potentials obtained for aged NCAT alloy in 0.6 M NaCl solution having different pH and at different temperatures, while Figure 4.29 shows the potentiodynamic polarization curves obtained for the alloy under the same test conditions. Table 4.7 summarizes the electrochemical parameters obtained for the alloy.

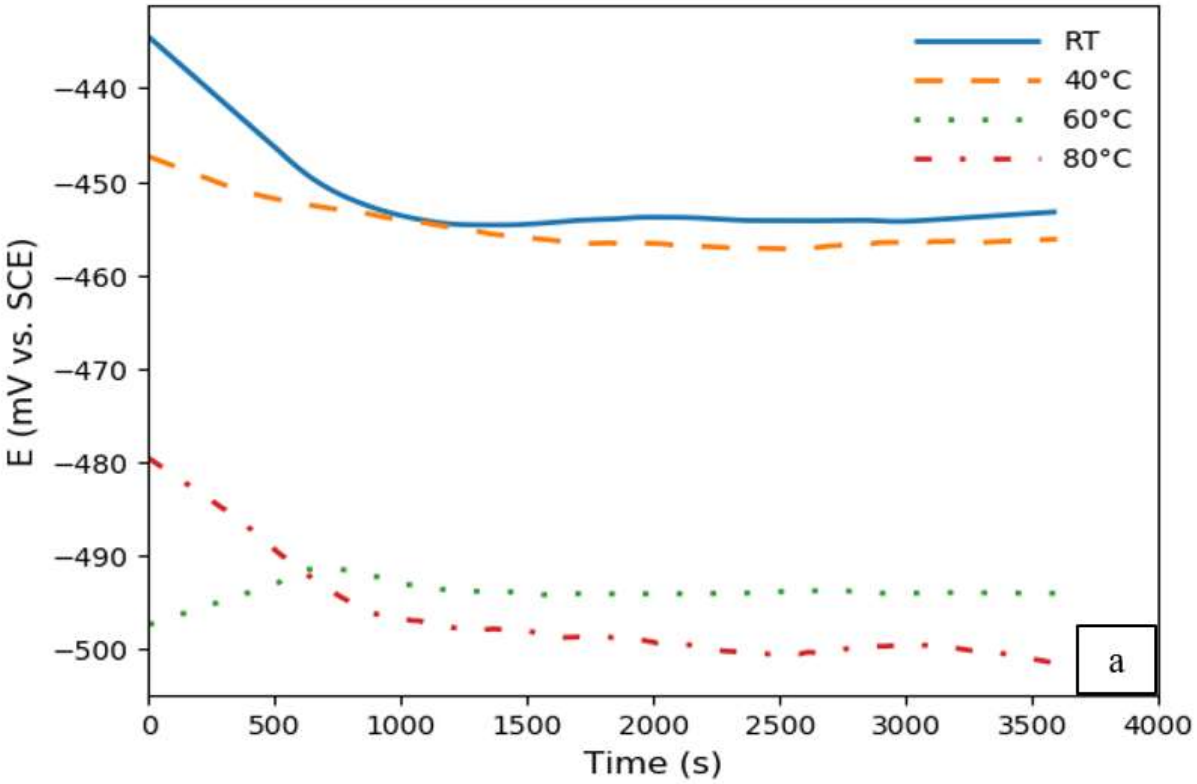

Figure 4.28. Typical open circuit potential obtained for aged NCAT alloy in a 0.6 M NaCl solution with a pH of (a) 3, (b) 6, and (c) 10 measured at different temperatures. The lowest open circuit potential is observed in solutions having a pH of 3 and at the highest temperature of 80 ^{o}C.

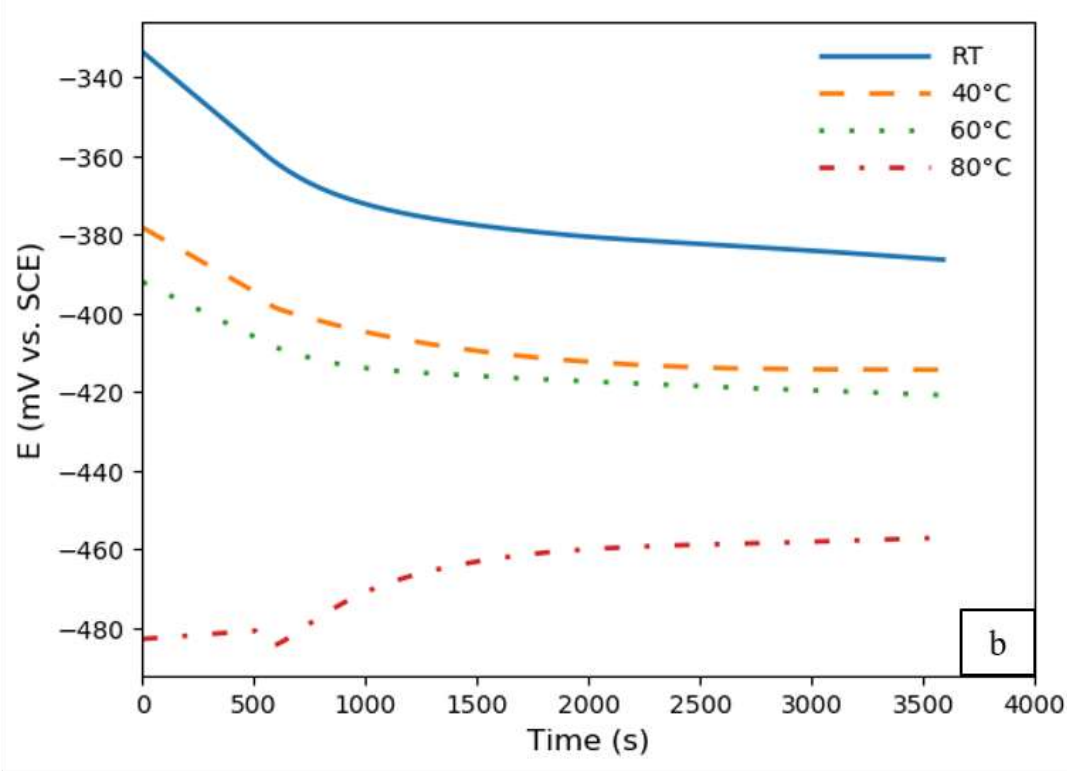

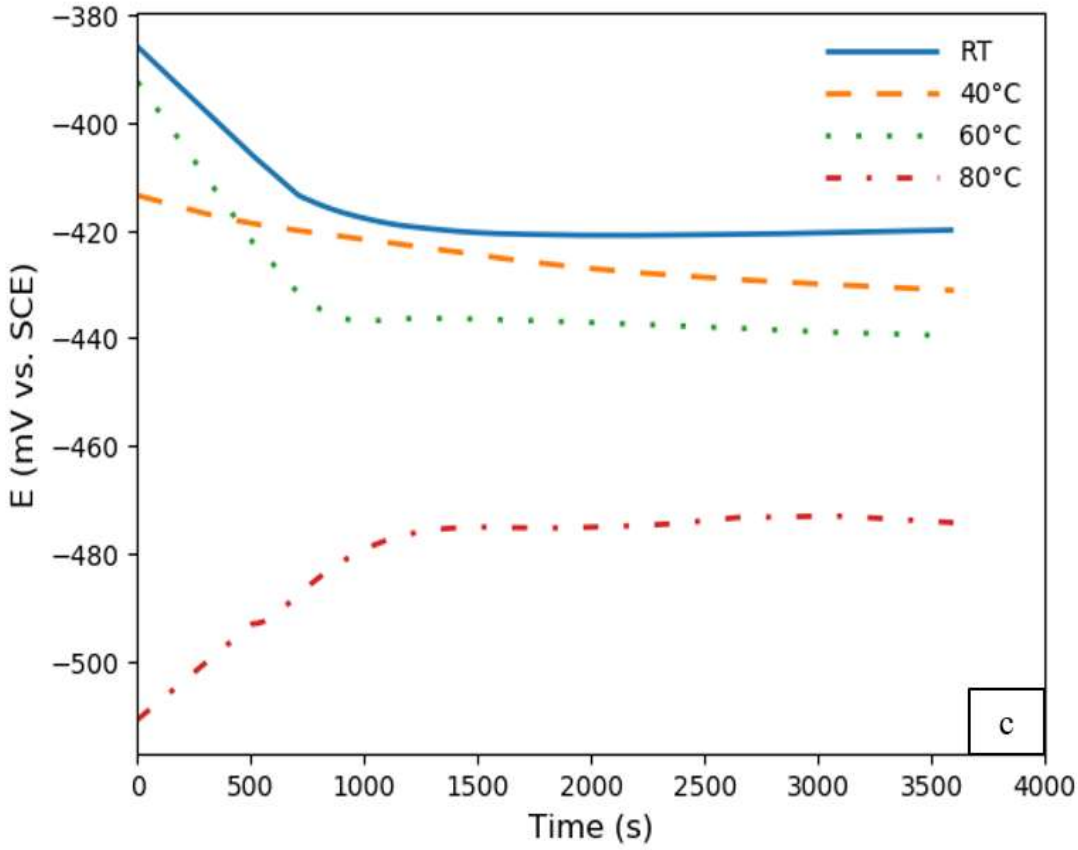

Figure 4.28. Continued.

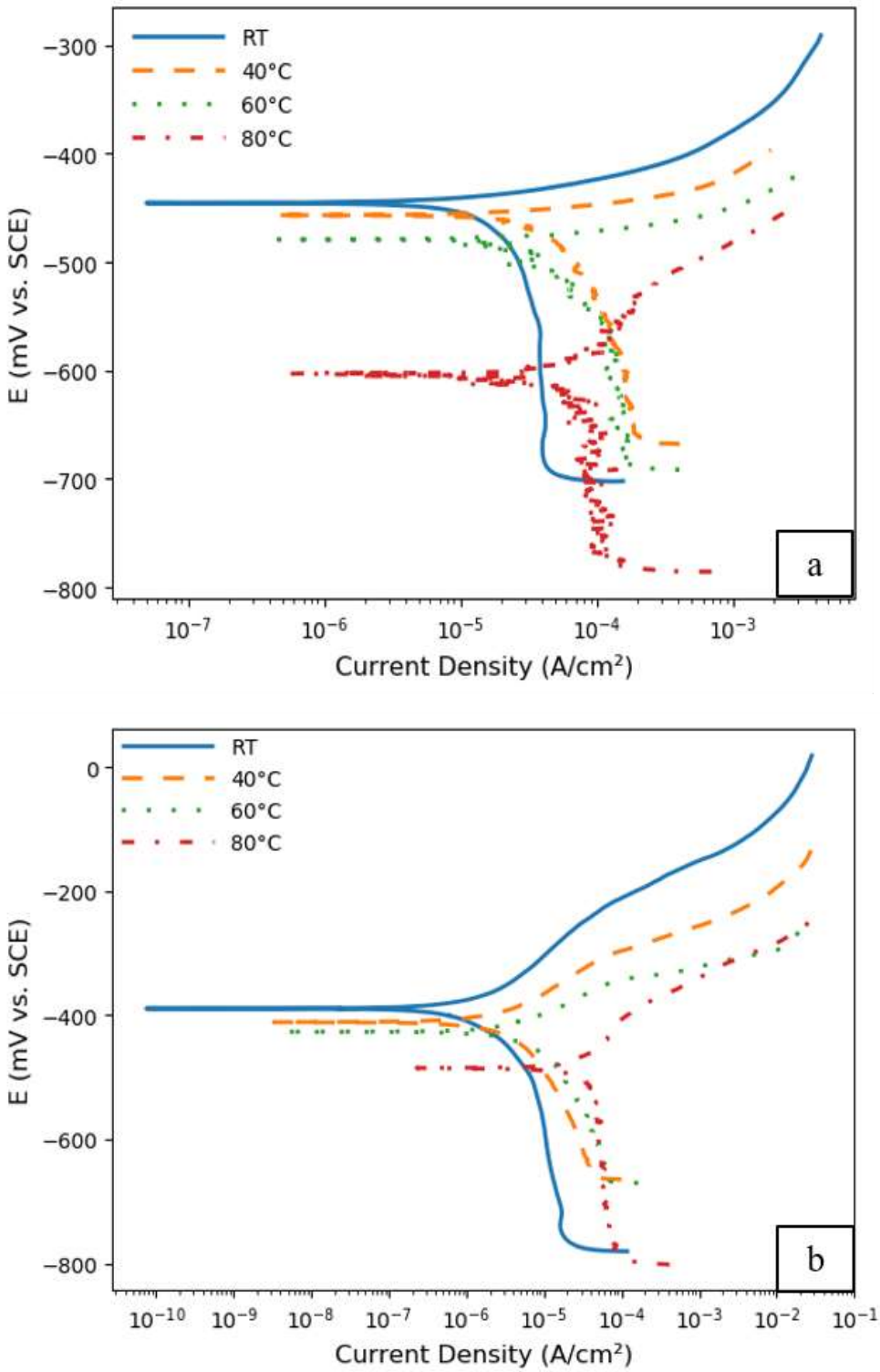

Figure 4.29. Potentiodynamic polarization curves obtained for aged NCAT alloy in a 0.6 M NaCl solution with a pH of (a) 3, (b) 6, and (c) 10 measured at different temperatures. The highest current density values are observed in solutions with pH of 3, and the lowest values are found in solutions with a pH of 10. At higher temperatures in all the solutions, the corrosion current density is greater.

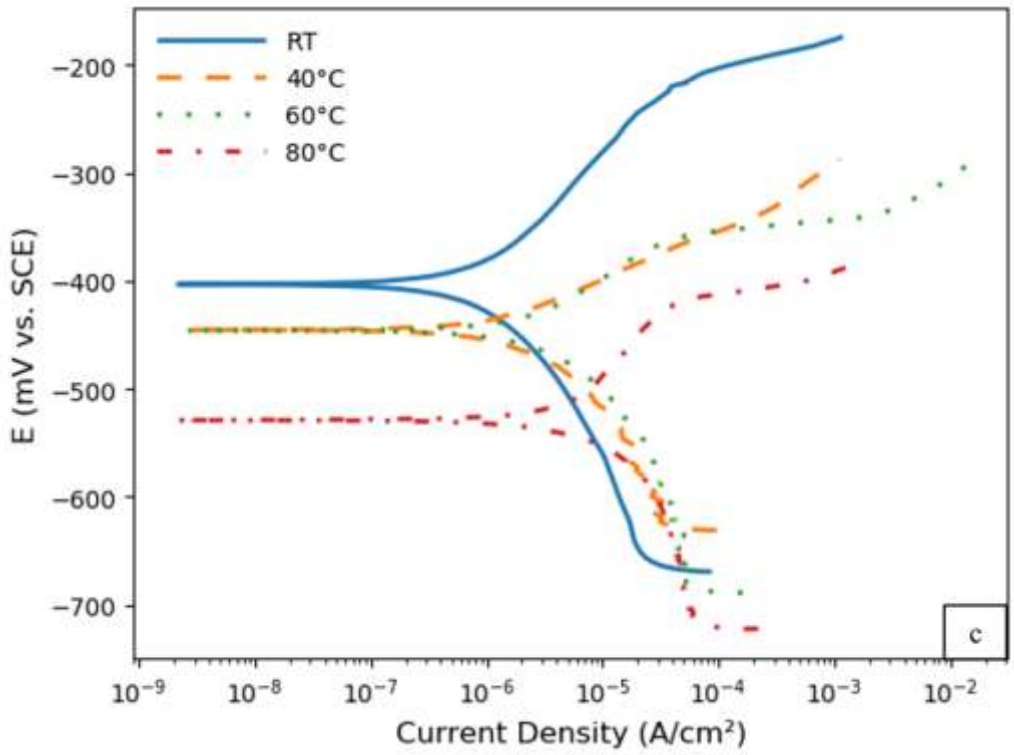

Figure 4.29. Continued.

It can be seen from Figures 4.28 and 4.29 as well as Table 4.7 that the open circuit potential and corrosion potential shifted to more negative values and the corrosion rate increased with increasing temperature for any given pH, thus indicating an increase in corrosion activity of the alloy in the solution when the temperature is high. For example, samples that were tested in solutions having a pH of 3 showed an increase in corrosion rate from 0.17 mm/y at RT to 0.70 mm/y at 80 ^{o}C. Similar behaviour was reported in other alloys in the literature [139, 140]. This is due to the acceleration of the kinetics of corrosion reaction with temperature [141]. The corrosion rate was found to increase with temperature regardless of the pH of the solution, as can be seen in Table 4.7. This can be ascribed to the increase in metal dissolution and oxidation-reduction reaction with temperature. The lowest corrosion rates were recorded in solutions having a pH of 10, while the highest corrosion rates were found in solutions with a pH of 3. The potentiodynamic polarization curve of the alloy that was tested at 80 ^{o}C in a solution having a pH of 10 displays a region, where no major change in potential and corrosion current density is observed at ~ - 420 mv (vs. SCE). This indicates that an oxide film is formed on the surface of the alloy to resist the corrosion at high temperatures.

Table 4.7. Electrochemical parameters obtained for aged NCAT alloy in 0.6 M NaCl solution with three different levels of pH at four different temperatures. The change of pH and temperature affects the corrosion properties of the alloy.

Alloy	Temp. °C	pH	E_{oc}[1] mV	E_{corr}[1] mV	i_{corr} µA/cm²	β_a[1] V/decade	β_c[1] V/decade	R_p Ω.cm²	CR mm/y
NCAT	RT	3	-453	-446	23.28	0.03	-0.53	959.6	0.17
(SD)[2]			(±13.8)	(±20.1)	(±1.05)	(±0.02)	(±0.04)	(±263.4)	(±0.008)
NCAT	RT	6	-386	-389	2.26	0.12	-0.22	$1.6x10^4$	0.017
(SD)[2]			(±16.4)	(±13.5)	(±0.35)	(±0.01)	(±0.03)	(±303.5)	(±0.002)
NCAT	RT	10	-420	-403	1.12	0.13	-0.16	$2.4x10^4$	0.008
(SD)[2]			(±33.4)	(±48.6)	(±0.92)	(±0.06)	(±0.02)	($\pm2.5x10^4$)	(±0.007)
NCAT	40	3	-455	-458	46.5	0.02	-0.24	331.5	0.35
(SD)[2]			(±9.2)	(±3.3)	(±7.11)	(±0.02)	(±0.15)	(±152.7)	(±0.05)
NCAT	40	6	-415	-411	3.91	0.09	-0.19	$6.1x10^3$	0.03
(SD)[2]			(±14.9)	(±17.0)	(±0.81)	(±0.02)	(±0.05)	($\pm1.9x10^3$)	(±0.006)
NCAT	40	10	-431	-445	1.6	0.06	-0.09	$8.7x10^3$	0.01
(SD)[2]			(±27.6)	(±48.8)	(±1.74)	(±0.03)	(±0.03)	($\pm1.8x10^3$)	(±0.01)
NCAT	60	3	-492	-480	60.4	0.023	-0.322	208.6	0.45
(SD)[2]			(±11.8)	(±14.2)	(±3.5)	(±0.019)	(±0.082)	(±53.2)	(±0.026)
NCAT	60	6	-421	-426	9.25	0.09	-0.23	$3.8x10^3$	0.07
(SD)[2]			(±31.6)	(±9.4)	(±4.70)	(±0.02)	(±0.03)	($\pm1.5x10^3$)	(±0.03)
NCAT	60	10	-439	-446	5.38	0.11	-0.17	$6.1x10^3$	0.04
(SD)[2]			(±44.9)	(±60.2)	(±5.5)	(±0.01)	(±0.01)	($\pm2.3x10^3$)	(±0.04)
NCAT	80	3	-536	-604	94.2	0.116	-0.207	207.0	0.70
(SD)[2]			(±64.4)	(±91.5)	(±2.2)	(±0.03)	(±0.38)	(±483.1)	(±0.017)
NCAT	80	6	-457	-511	35.13	0.26	-0.27	$1.2x10^3$	0.26
(SD)[2]			(±33.8)	(±36.1)	(±10.9)	(±0.08)	(±0.07)	(±624.01)	(±0.08)
NCAT	80	10	-473	-528	18.03	0.32	-0.25	$2.9x10^3$	0.13
(SD)[2]			(±41.8)	(±79.3)	(±1.4)	(±0.12)	(±0.07)	(±488.1)	(±0.01)

[1] All the potential values are measured vs. SCE. [2] Standard deviation (SD) values.

An Arrhenius plot obtained for the corrosion of aged NCAT alloy in 0.6 M NaCl solution at different temperatures is shown in Figure 4.30, where a relationship between log corrosion rate and temperature (in K) is given. Equation (4.1) [141] is a general formalization of the Arrhenius relationship between reaction rate and temperature. The equation shows that the kinetics of the electrochemical reactions are faster at elevated temperatures, that is, the anodic dissolution of the metals increases.

$$k = Ae^{\frac{-E_a}{RT}} \tag{4.1}$$

where k is the reaction rate, which is represented by corrosion rate (CR) in this study, A is a constant for each chemical reaction, R is the gas constant (8.314 J/mol. K), T is the temperature (K), and E_a (J/mol) is the molar activation energy. It represents the energy barrier that must be overcome by the electrons through the electrode/electrolyte interphase [141, 142].
Equation (4.1) can be recast as follows:

$$Log\left(k\right) = Log\left(A\right) - \frac{E_a}{2.303R}\left(\frac{1}{T}\right) \tag{4.2}$$

If the activation energy is expressed in kilojoules (kJ), then equation (4.2) will become:

$$log\left(k\right) = log\left(A\right) - \frac{E_a\left(kJ\right)}{2.303R}\left(\frac{1{,}000}{T}\right) \tag{4.3}$$

The Arrhenius plot is generated by plotting log (k) versus 1000/T. The slope of this plot is expressed as:

$$Slope = \frac{-E_a\left(kJ\right)}{2.303R} \tag{4.4}$$

The activation energy (E_a) is determined from the slope of the straight line obtained by plotting *log* (*k*) or *log* (corrosion rate) against 1000/*T*. The intercept of the generated plot with the Y axis gave the values of *A*. The values of E_a and *A* determined from the present work are summarized in Table 4.8. As can be seen, the activation energy seems to be dependent on the solution pH. It generally increased with increasing pH.

In Figure 4.30 all the curves showed an almost linear relationship. This indicates that only one process is controlling the kinetics of the electrochemical reactions. The relationship between corrosion rate and temperature in solutions that have a pH of 6 and pH of 10 show steeper slope compared to solutions with a pH of 3. The steeper the slope of the curves, the faster the dependence of the corrosion rate on temperature, and the higher the activation energy values. The recorded values of activation energy in solutions that have a pH of 6 and 10 were ~ 43 and 45 kJ/mol, respectively, compared to 21 kJ/mol for solutions with pH of 3. The higher the activation energy values, the more difficult it is to begin the corrosion process. In 0.6 M NaCl solutions that have pH of 6 and pH of 10, it is more difficult to corrode the NCAT alloy compared to solutions with pH of 3, where the activation energy is remarkably lower.

Figure 4.31 shows micrographs obtained for aged NCAT samples after potentiodynamic polarization scans in a 0.6 M NaCl solution with a pH of 6. The samples were tested at four different temperatures (RT, 40 ^{o}C, 60 ^{o}C, and 80 ^{o}C). Intergranular corrosion is evident at RT and, 40 ^{o}C. It is less obvious as the temperature increased. Instead, general corrosion of the alloy matrix is increased, as can be seen by the colour of the corroded samples in Figure 4.31 (c) and (d) that was caused by the corrosion. In addition, the pits and surrounded corroded area sizes are both increased in most of the cases. This is probably due to the acceleration of the dissolution of the NCAT SMA at higher temperatures [133]. In all the samples, pitting seems to occur very close to the grain boundaries that have precipitates.

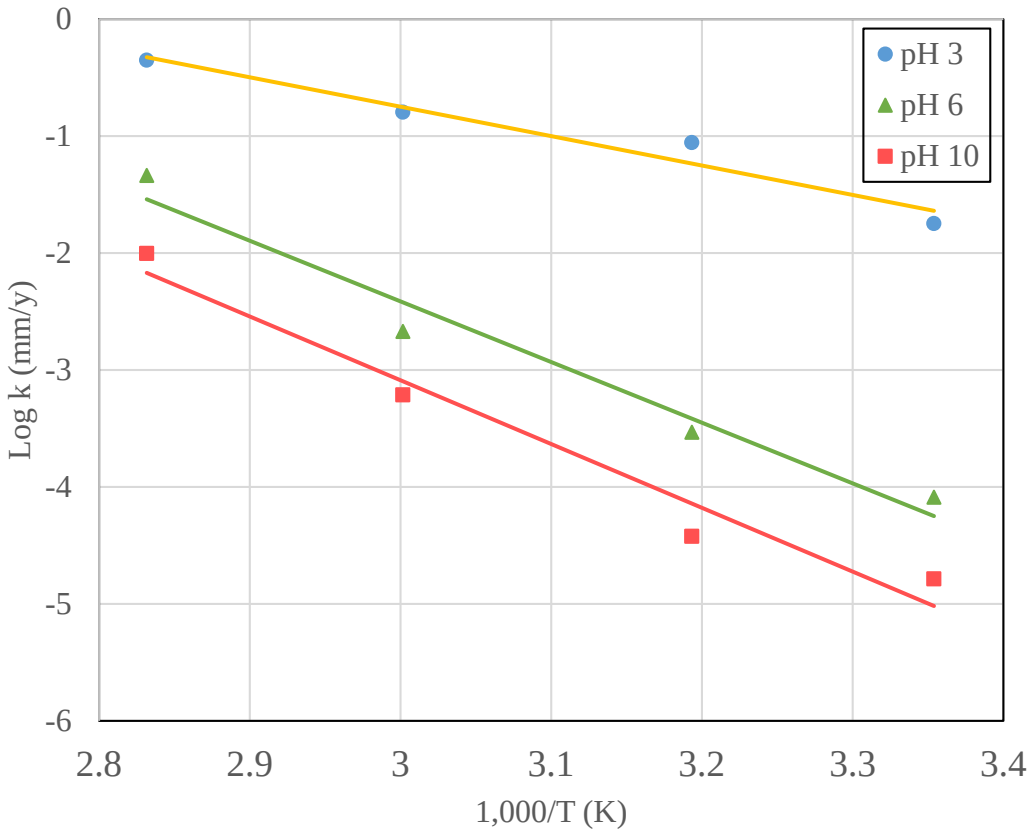

Figure 4.30. Arrhenius plot obtained for aged NCAT alloy tested in 0.6 M NaCl having three different pH. At higher tempertures, the corrosion rate is increased.

Table 4.8. Arrhenius parameters determined from the Arrhenius plot in Figure 4.30 for corrosion of aged NCAT alloy in 0.6 M NaCl solutions with differnet pH.

Parameter	pH 3	pH 6	pH 10
Activation Energy (E_a) (kJ/mol)	21.0	43.1	45.3
Constant A (mm/y.mol)	893.6	485,645.2	715,879.6

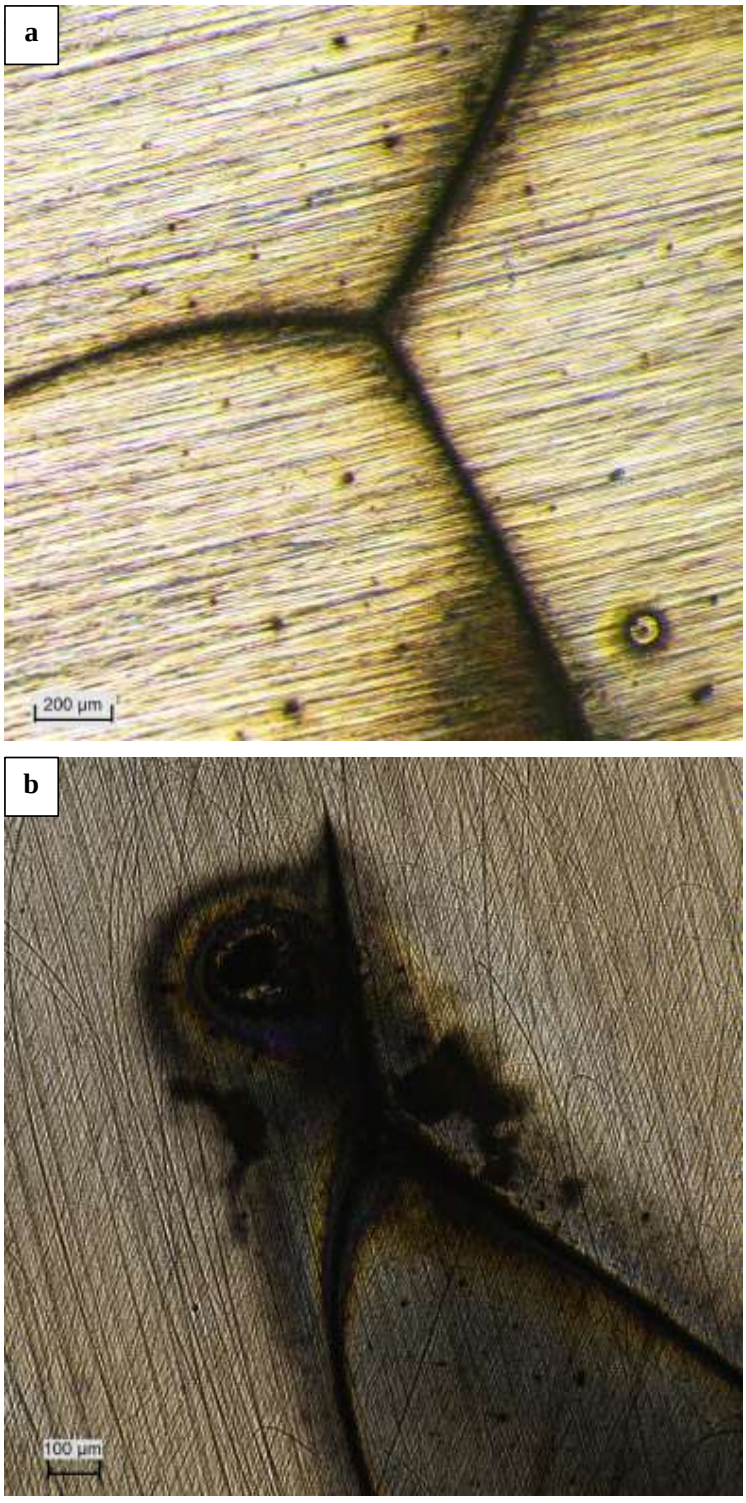

Figure 4.31. Optical micrographs of NCAT SMA after potentiodynamic polarization scans in a 0.6 M NaCl solution with a pH of 6 at (a) RT, (b) 40 ^{o}C, (c) 60 ^{o}C, and (d) 80 ^{o}C. The higher temperatures resulted in increasing the severity of the corrosion attack. IGC is observed, especially in RT and 40 ^{o}C, while corrosion of the alloy matrix is evident in the higher temperatures.

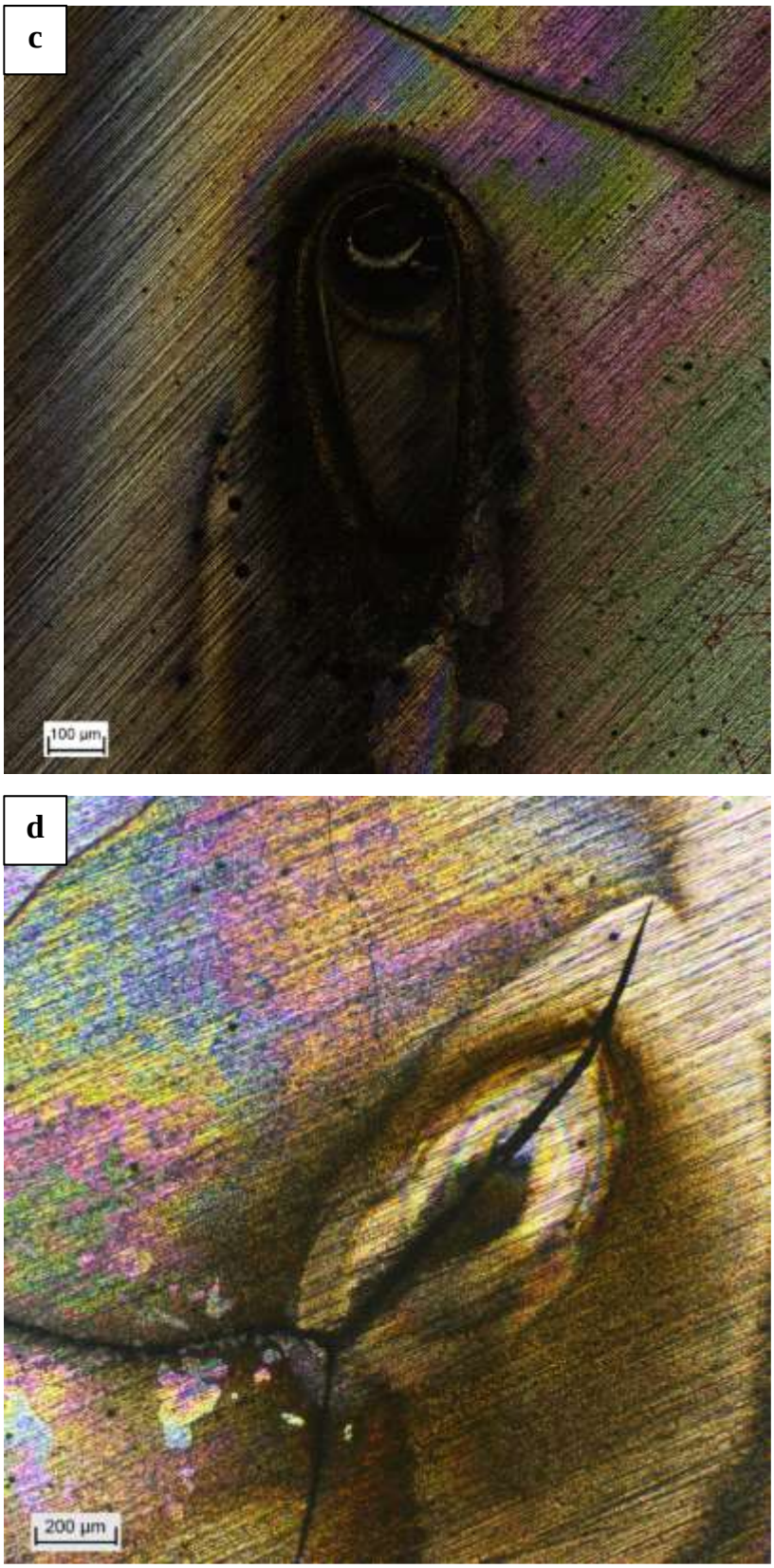

Figure 4.31. Continued.

4.6.2 Effect of pH on Corrosion of Aged NCAT SMA at Different Temperatures

Figure 4.32 presents the open circuit potentials obtained at four different temperatures for aged NCAT alloy tested in three 0.6 M NaCl solution having pH of 3, 6, and 10. The potentiodynamic polarization curves obtained for the alloy under the same test conditions are shown in Figure 4.33. The electrochemical parameters determined from the potentiodynamic polarization scans and linear polarization resistance experiments are summarized in Table 4.7 in section 4.6.1.

From the open circuit potential measurements in Figure 4.32, it is evident that the open circuit potential is shifted to more negative values as the solution becomes more alkaline (pH 10) or more acidic (pH 3). The lowest open circuit potential values were recorded in solutions with a pH of 3. As the temperature increased, the open circuit potential was decreased in all the tested solutions. The lowest open circuit potential values were recorded in solutions with a pH of 3 at 80 ^{o}C.

The potentiodynamic polarization curves of the alloy in Figure 4.33 show greater corrosion current density in solutions having a pH of 3. Solutions with a pH of 10, on the other hand, have the lowest corrosion current density. As previously discussed in section 4.6.1, the increase in temperature resulted in increasing the corrosion current density, hence, the corrosion rate in all the solutions.

In Table 4.7, the corrosion parameters that were measured during the electrochemical tests show that not only the change in temperature has an impact on the corrosion potential and corrosion rate of NCAT SMA, but also the change in pH is found to affect the corrosion potential and corrosion rate of the alloy. The samples that were tested in the more acidic pH solutions (pH 3) showed the lowest corrosion potential values and the highest corrosion rate values. The samples that were tested in more alkaline pH solutions (pH 10) showed the lowest corrosion rate values. These corrosion rate values were not very far from the values that were measured in samples tested in solutions with a pH of 6, especially at RT and 40 ^{o}C.

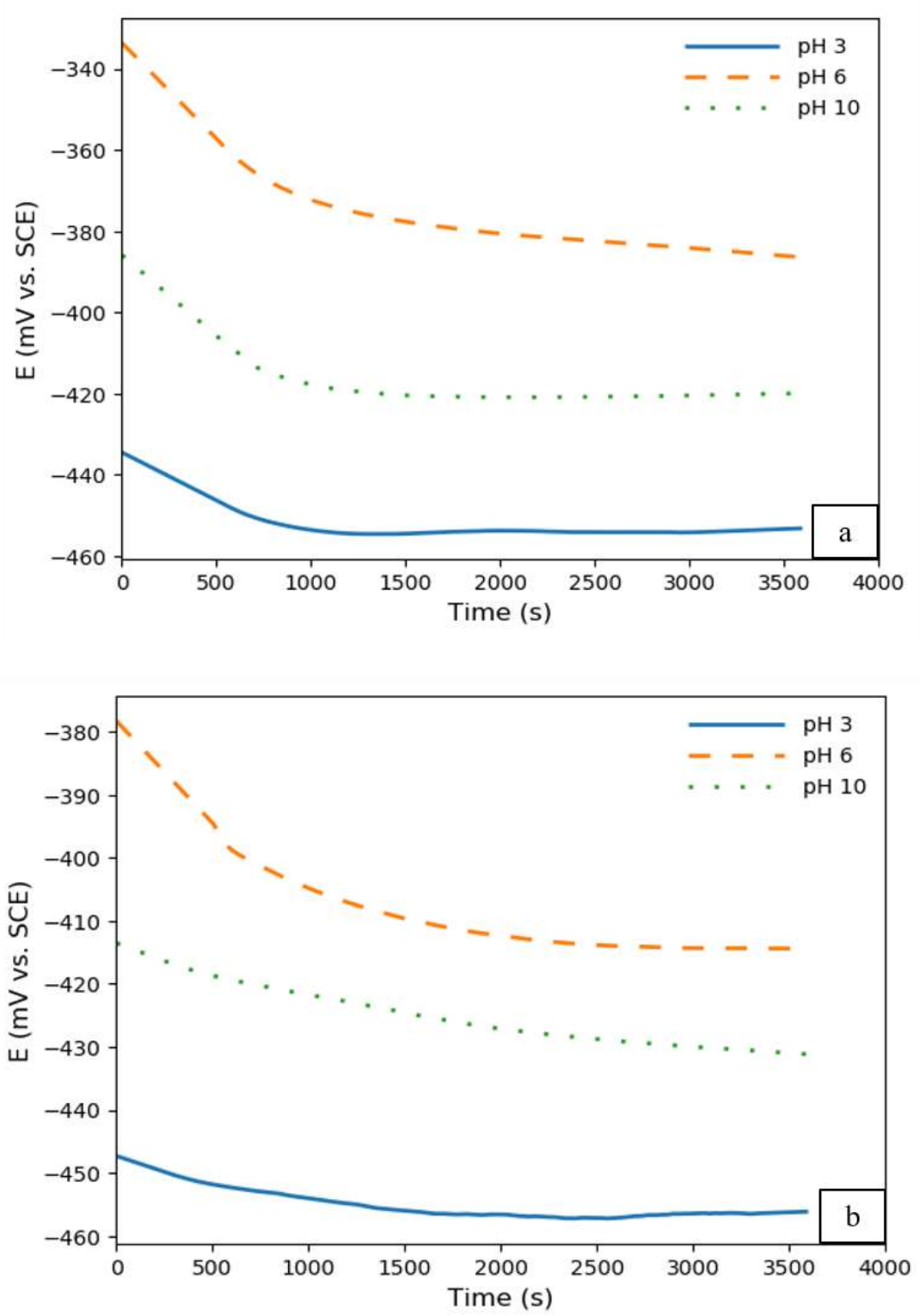

Figure 4.32. Typical open circuit potential curves obtained for NCAT alloy in 0.6 M NaCl solution with different pH at: (a) RT, (b) 40 °C, (c) 60 °C, and (d) 80 °C. The open circuit potential shifted to negative values at high temperatures. The lowest values are observed in solutions having a pH of 3.

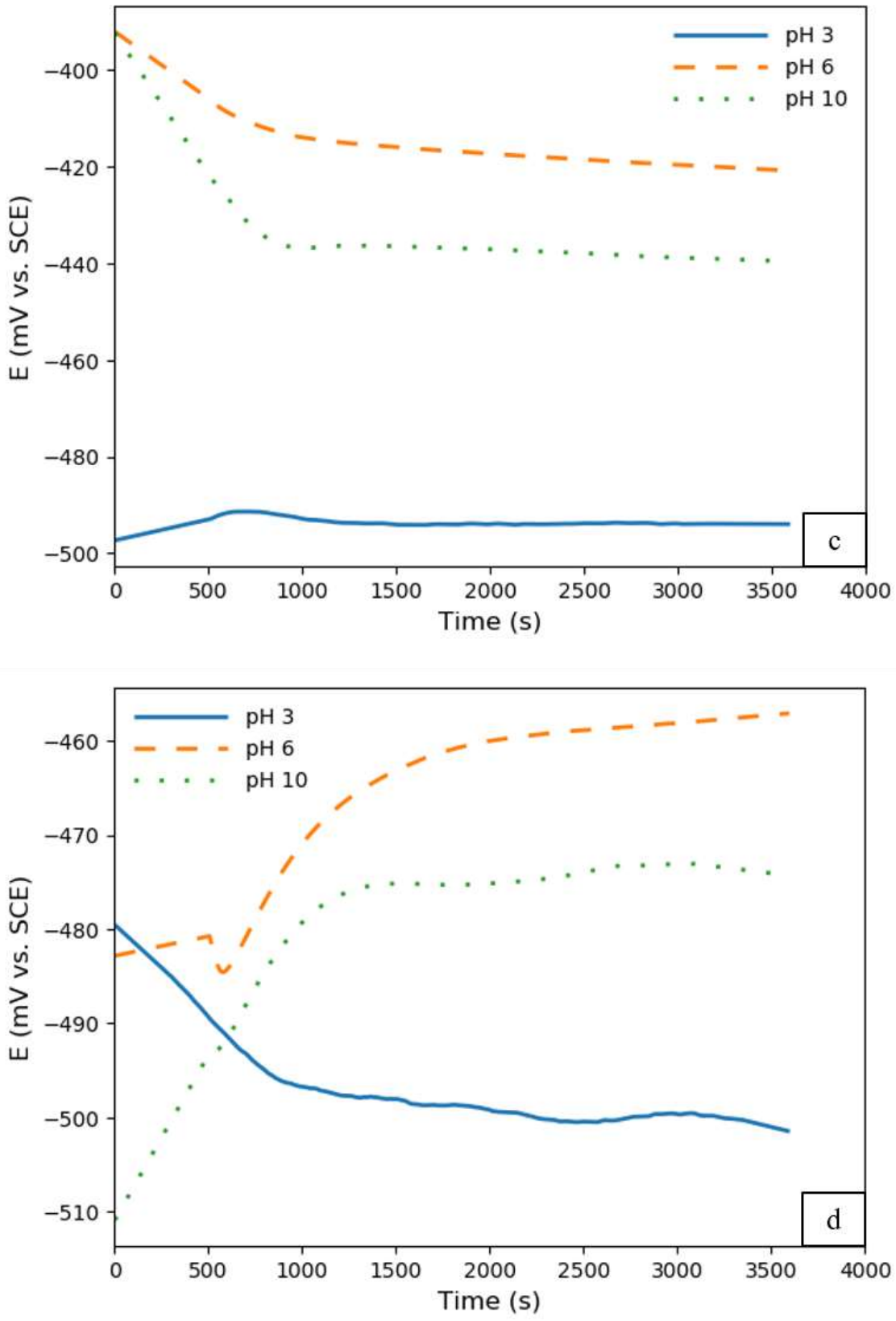

Figure 4.32. Continued.

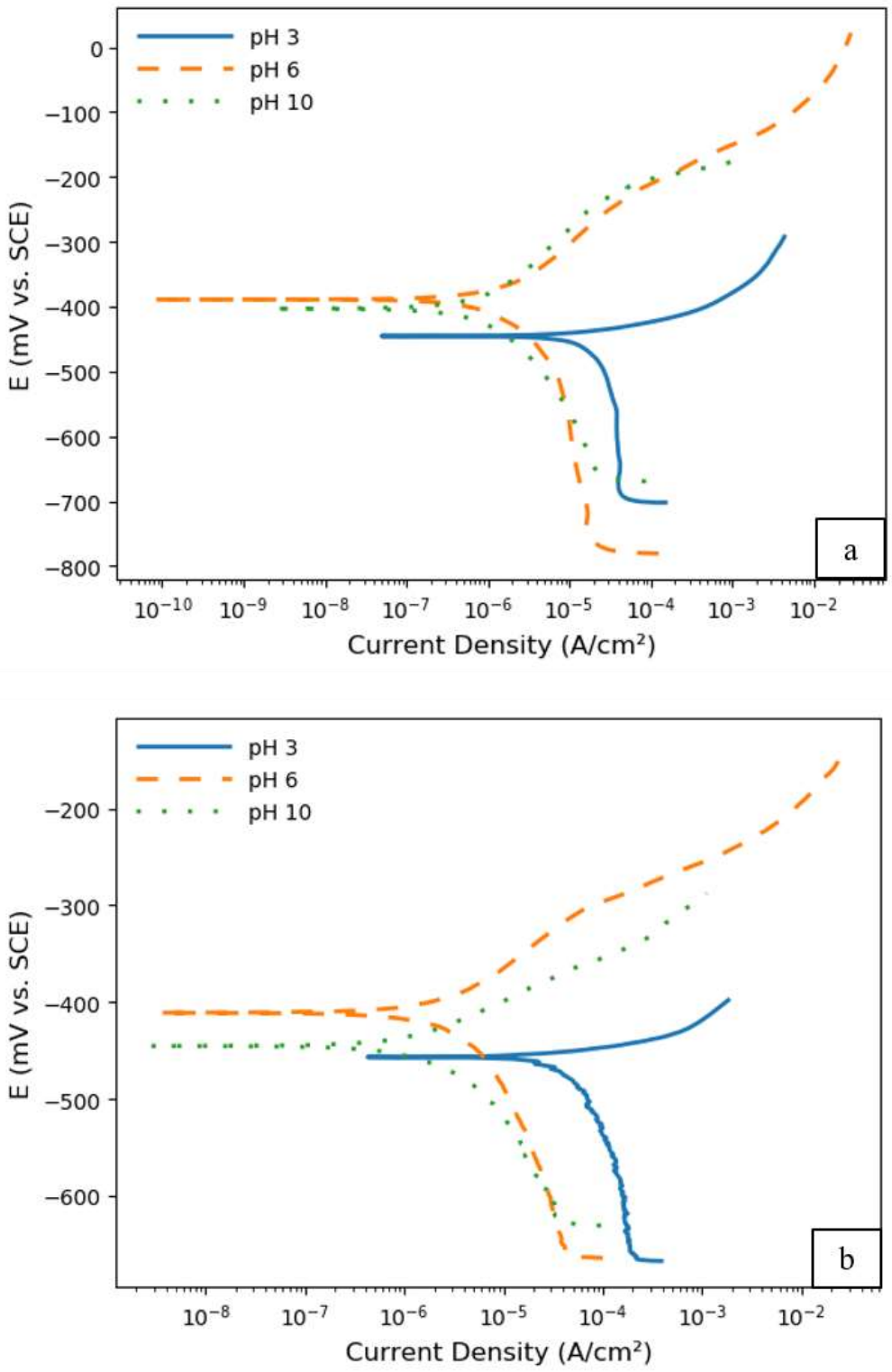

Figure 4.33. Potentiodynamic polarization curves obtained for NCAT alloy in 0.6 M NaCl solution with different pH at: (a) RT, (b) 40 °C, (c) 60 °C, and (d) 80 °C. The high temperature resulted in high corrosion current density and lower corrosion potentials. Solutions with a pH of 3 showed the highest current density and lowest corrosion potentials.

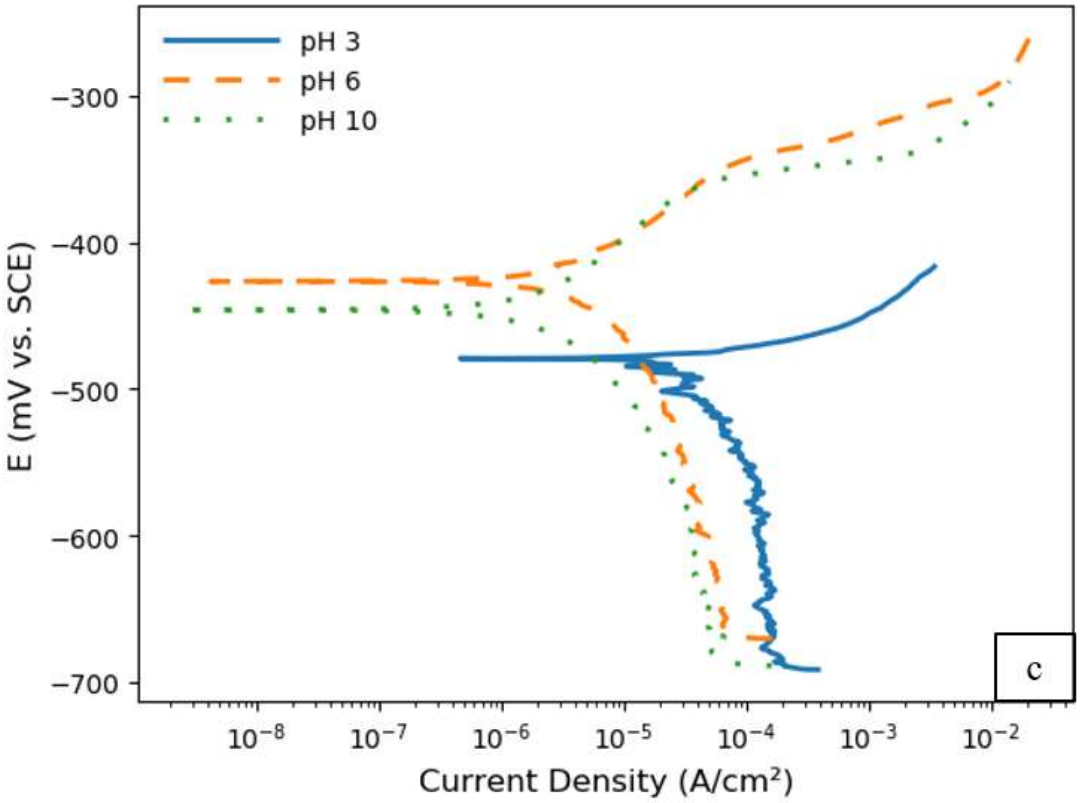

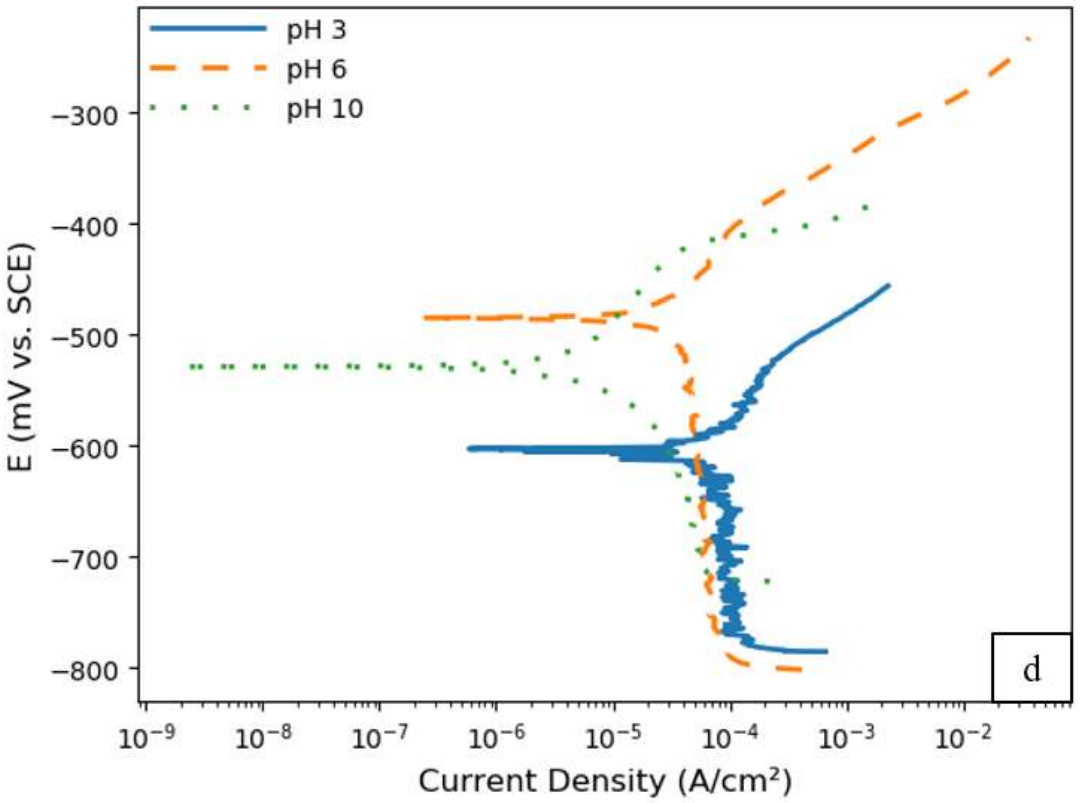

Figure 4.33. Continued.

To understand the relationship between the corrosion potential and solution pH, the predicted potential (Eh) – pH diagram of NCAT SMA in H_2O that is represented in Figure 4.3 in section 4.2 was used. In the Eh – pH diagram, the potential was represented on the hydrogen scale, while in the electrochemical tests, the measured potential was referenced to calomel electrode. The potential of the calomel electrode on the hydrogen scale is 0.241 volts. Therefore,

$$\text{The potential (Eh)} = \text{E (calomel)} + 0.241 \quad (4.9)$$

The equilibrium oxygen potential in Figure 4.3 is given by Nernst equation [133] as:

$$\text{E (oxygen)} = 1.23 - 0.0591\ \text{pH} \quad (4.10)$$

while the equilibrium potential of the hydrogen electrode [133] is given by:

$$\text{E (hydrogen)} = 0 - 0.0591\ \text{pH} \quad (4.11)$$

During the electrochemical open circuit potential measurements, the potential reaches a steady state value with time, where the potential is nearly constant. The steady state potential is the mixed potential between the anodic reaction (metal oxidation) and the cathodic reaction (reduction of oxygen or hydrogen ion, or both).

The steady state potential can be calculated for the different solutions that were used in this study as follows:

1. <u>In acidic solution of pH 3.0 (0.6 M NaCl with pH 3.0) at RT</u>

Using the open circuit potential values provided in Table 4.8, the steady state potential (open circuit potential) is E (calomel), which is found to be = - 0.453 volts. Using equation 4.9, Eh can be calculated as follows:

Eh = - 0.453 + 0.241 = - 0.212 volts.

The equilibrium potential of the hydrogen electrode at pH 3.0 is calculated using equation 4.11:

Eh = 0 – 0.0591(3.0) = -0.177 volts.

Since the steady state corrosion potential is below the hydrogen electrode equilibrium potential, corrosion in this case can occur through evolution of hydrogen gas on the surface of the metal.

2. <u>In acidic Solutions of pH 0.72 (0.5 M H_2SO_4 Solution) at RT</u>

The pH of this solution is 0.72. The steady state potential is given in Table 4.5 as E (calomel) = - 0.415 volts. Eh can be calculated as:

Eh = - 0.415 + 0.241 = - 0.174 volts.

The equilibrium potential of the hydrogen electrode at pH 0.72 is:

Eh = 0 – 0.0591(0.72) = - 0.0425 volts.

Since the corrosion potential is below the hydrogen electrode equilibrium potential, corrosion similar to the above case can occur by evolution of hydrogen gas on the surface of the metal.

3. <u>Non-Acidic Solutions</u>

The steady state potentials and equilibrium electrode potentials were calculated using potential values from Table 4.5 and Table 4.7, and equations 4.9, 4.10 and 4.11. The results are presented in Table 4.9.

In Table 4.9, all of the steady state potentials are above the hydrogen electrode potential, therefore, the corrosion in these solutions does not involve hydrogen gas evolution. Since all of the potentials are also below the potential of the oxygen electrode, atmospheric oxygen is capable of oxidizing the metals in each case. Accordingly, oxygen is likely the oxidizing agent in these four cases.

4.6.2.1 Steady State Potential vs. pH

In Table 4.9, the steady state potentials (Eh) appear to decrease as the pH values increase. This is due to the thermodynamics of the anodic corrosion reactions. This is consistent with Nernst equation, at which, the potential (Eh) is given as a function of pH, and it decreases with increasing the pH value [133].

Accordingly, the potential of the cathodic reaction (oxygen reduction) also decreases with pH according to equation 4.10. Since the potentials of the anodic and cathodic reactions both decrease with pH, the corrosion potential will decrease with pH, as the corrosion potential is somewhere between the thermodynamic potentials of the anodic and cathodic reactions.

In the case of solutions with pH below 4, as indicated in section 4.2, the oxide scale breaks down and reactions (4.3) and (4.4) occur simultaneously in the presence of dissolved oxygen, and as a result, the corrosion potential shifts to lower values.

The solutions that have pH of 10 or above showed the lowest corrosion rate. This is most likely due to the formation of a protective oxide film such as $FeAl_2O_4.TaO_2$ and Fe_3O_4 as predicted by Eh – pH diagram in Figure 4.3. It has to be noted that in all the above-mentioned steady state potential vs. pH cases, only the thermodynamics of the reactions were considered, as the Eh – pH diagram does not include the kinetics of the reactions, which limits the use of this diagram. However, in this discussion, this diagram was considered because it shows a clear relationship between the potential and pH, even without the consideration of the reaction kinetics.

A relationship between the corrosion rate and pH is illustrated in Figure 4.34. In all the temperatures, the highest corrosion rates were recorded in acidic solutions that have a pH of 3. In contrast, the lowest corrosion rates were recorded in alkaline solutions that have a pH of 10. As previously observed, the increase in temperature resulted in increasing the corrosion rate.

Figures 4.35 – 4.38 show micrographs of NCAT SMA that was tested in 0.6 M NaCl solution with different levels of pH at different temperatures. The observation in the micrographs is consistent with the electrochemical testing findings. NCAT samples that were tested in solutions having a pH of 3 show the most pitting and corrosion compared to the rest of the tested samples, and the severe corrosion appears to etch the alloy. The best corrosion resistance was observed in the NCAT samples that were tested in solutions having a pH of 10. Corrosion in and around the grain boundaries characterized with precipitates was mostly observed in the samples that were tested in solutions having a pH of 6 and 3 at RT and 40 ^{o}C, indicating that the alloy suffered intergranular corrosion (IGC) in these solutions. Visual inspection of the tested samples shows increased pitting and pits sizes as the temperature increased. More pitting is noticed in the samples that were tested in solutions with a pH of 3, especially at 80 ^{o}C. The size of the corroded area was

found to be larger for samples exposed to higher temperature. Samples tested in solutions with a pH of 10 showed the least amount of corrosion and pitting at all temperatures.

Table 4.9. The steady state potentials and equilibrium potentials calculated from the iron Eh-pH diagram in water at RT.

Solution	pH	Eh Steady State (E calomel) (V)		Eh Hydrogen Electrode (V)	Eh Oxygen Electrode (V)
0.6 M NaCl pH 6.0	6.0	- 0.145	(- 0.386)	-0.355	0.875
0.6 M NaCl pH 10.0	10.0	- 0.179	(- 0.420)	-0.591	0.639
0.5 M NaOH	12.8	- 0.213	(- 0.454)	-0.756	0.473

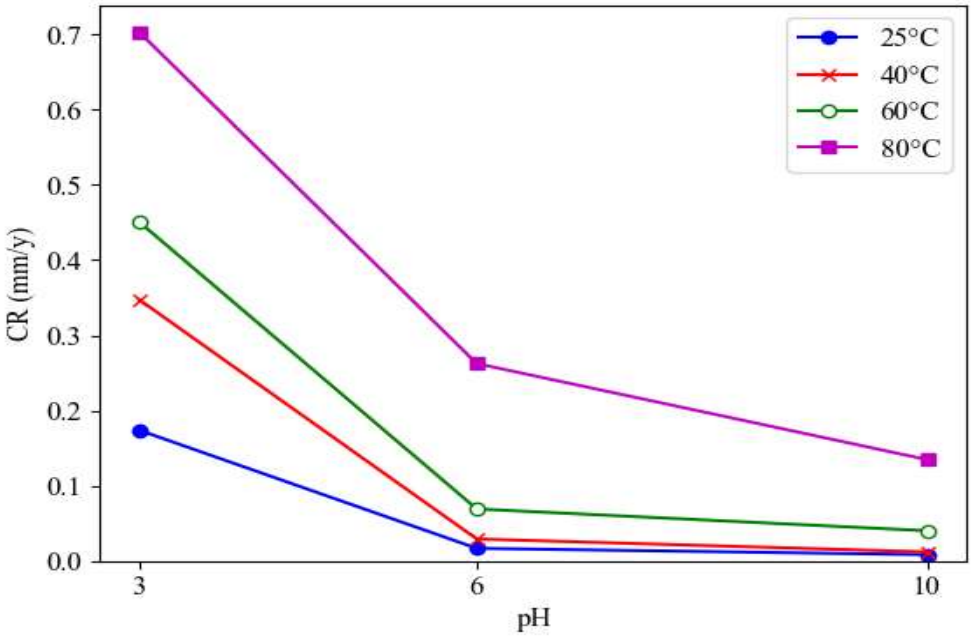

Figure 4.34. The effect of solution pH on corrosion rate of aged NCAT in 0.6 M NaCl solutions tested at different temperatures. High corrosion rates are found in solutions with a pH of 3 at all temperatures.

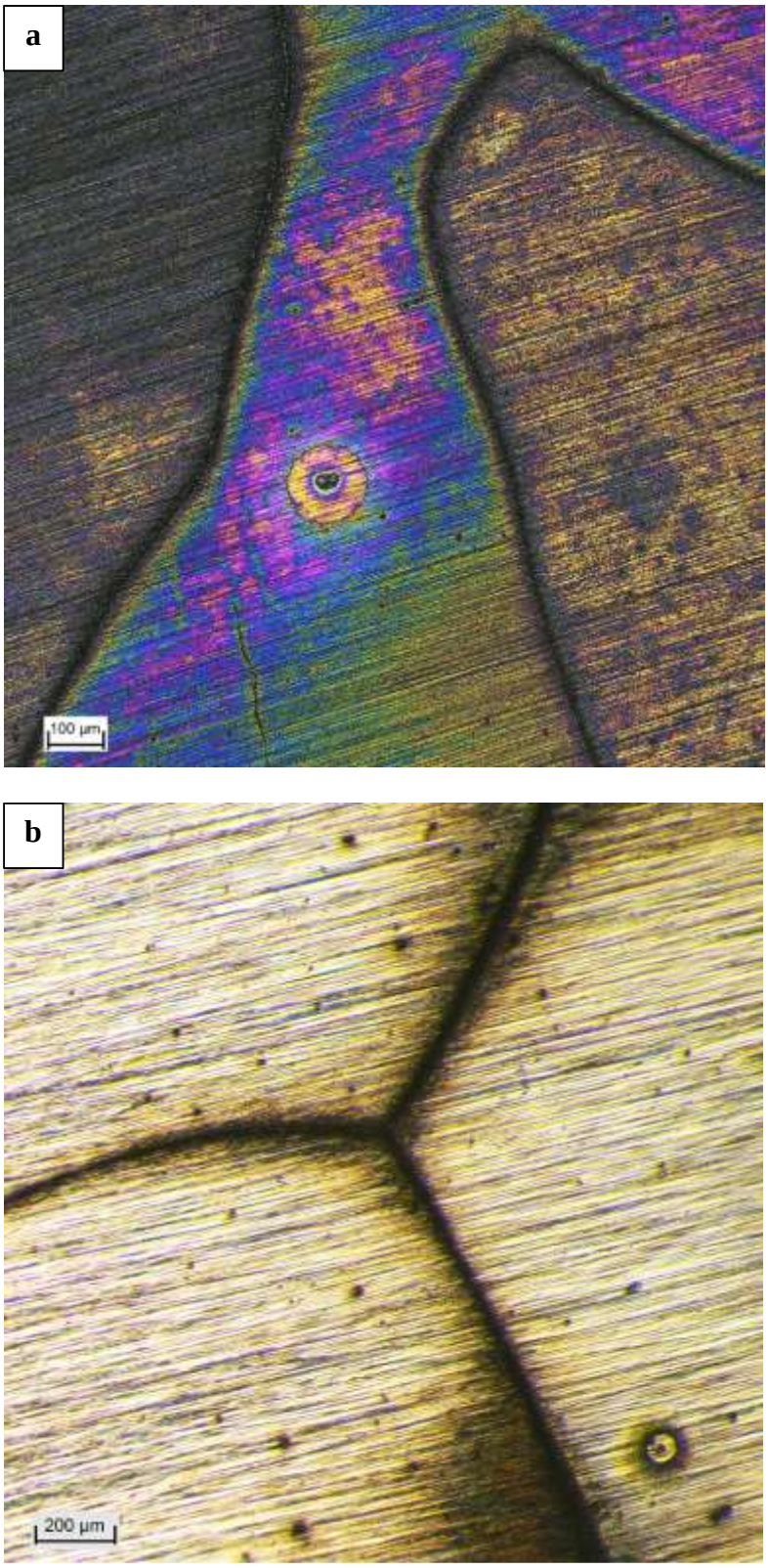

Figure 4.35. Micrographs obtained for aged NCAT after potentiodynamic polarization in a 0.6 M NaCl solution at RT and (a) pH 3, (b) pH 6, and (c) pH (10). High corrosion attack is observed in the solution with a pH of 3.

Figure 4.35. Continued.

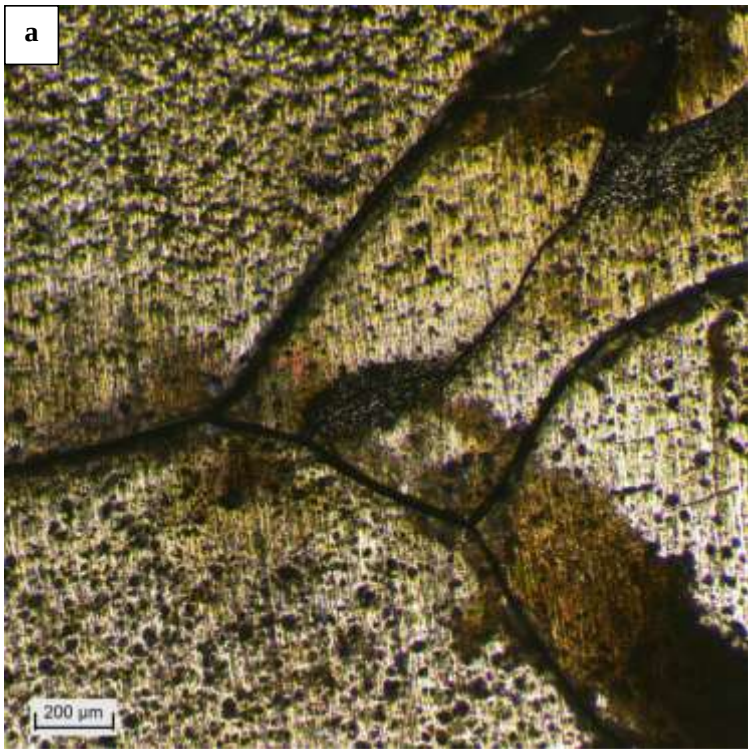

Figure 4.36. Micrographs obtained for aged NCAT SMA that was subjected to potentiodynamic polarization in a 0.6 M NaCl solution at 40°C and (a) pH 3, (b) pH 6, and (c) pH (10). Samples tested in solutions with a pH 3 show appreciable corrosion around the grain boundaries. IGC is evident in samples tested at this temperature in solutions with pH 6 and pH 3.

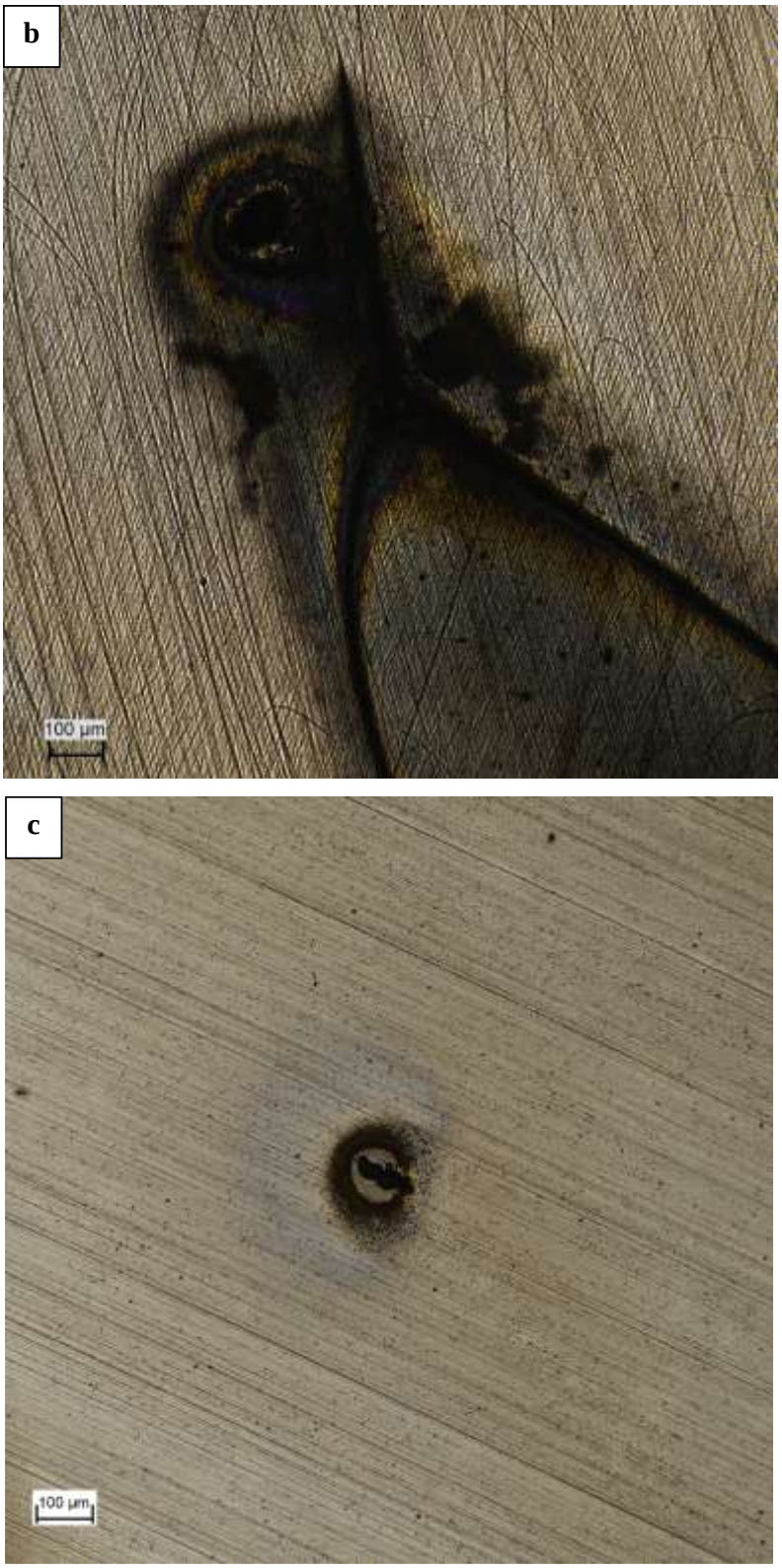

Figure 4.36. Continued.

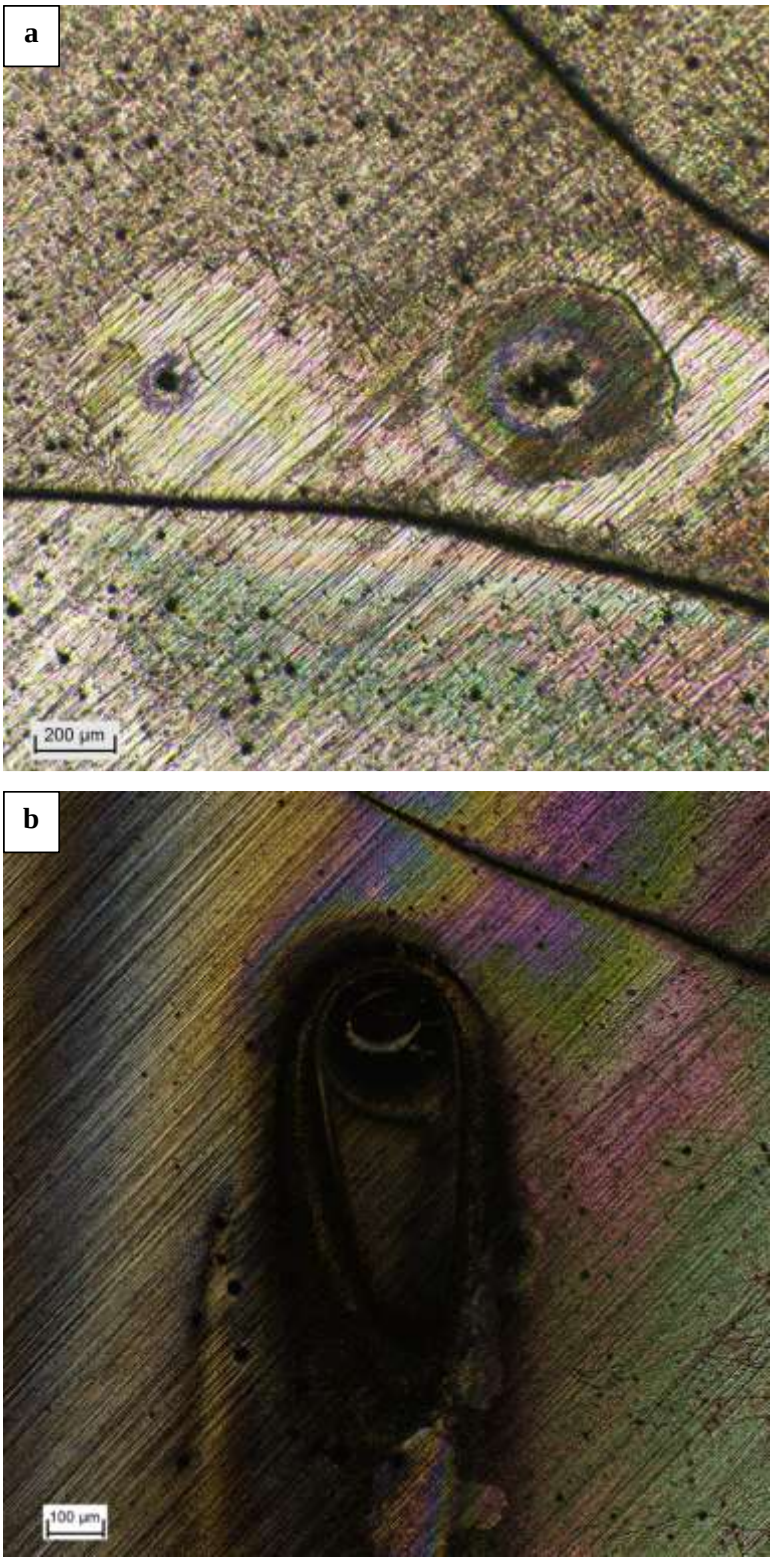

Figure 4.37. Micrograph obtained for aged NCAT SMA subjected to potentiodynamic polarization in a 0.6 M NaCl solution at 60^{o}C and (a) pH 3, (b) pH 6, and (c) pH (10). The severity of corrosion is more and the pitting size is bigger at this temperature compared to lower temperatures.

Figure 4.37. Continued.

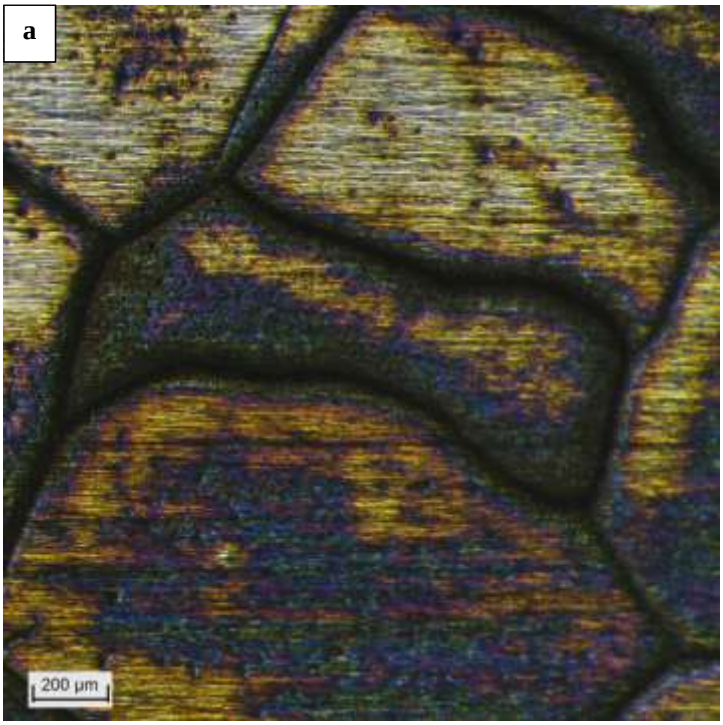

Figure 4.38. Micrographs obtained for aged NCAT SMA subjected to potentiodynamic polarization in a 0.6 M NaCl solution at 80°C and (a) pH 3, (b) pH 6, and (c) pH (10). Larger corroded area and more pitting are observed compared to specimens tested at lower temperatures. Specimens that were tested in solutions with a pH of 3 were the most affected by corrosion.

Figure 4.38. Continued.

4.7 Comparison of Corrosion of Solution Treated and Aged NCAT SMA in 0.6 M NaCl Solution at Different Temperatures and pH

In this section, the electrochemical corrosion properties obtained for solution treated NCAT alloy in 0.6 M NaCl solutions at different temperatures and pH with those of aged NCAT alloy under the same test conditions. All electrochemical tests were conducted in 0.6 M NaCl solutions at four different temperatures (RT, 40 °C, 60 °C and 80 °C), and three different pH values (3, 6, 10).

A comparison between the open circuit potentials obtained for solution treated and aged NCAT alloys in 0.6 M NaCl solution with different pH at different temperatures, is shown in Figure 4.39, while Figure 4.40 compares their potentiodynamic polarization curves. Table 4.10 summarizes the electrochemical corrosion parameters obtained for the alloys in the solution.

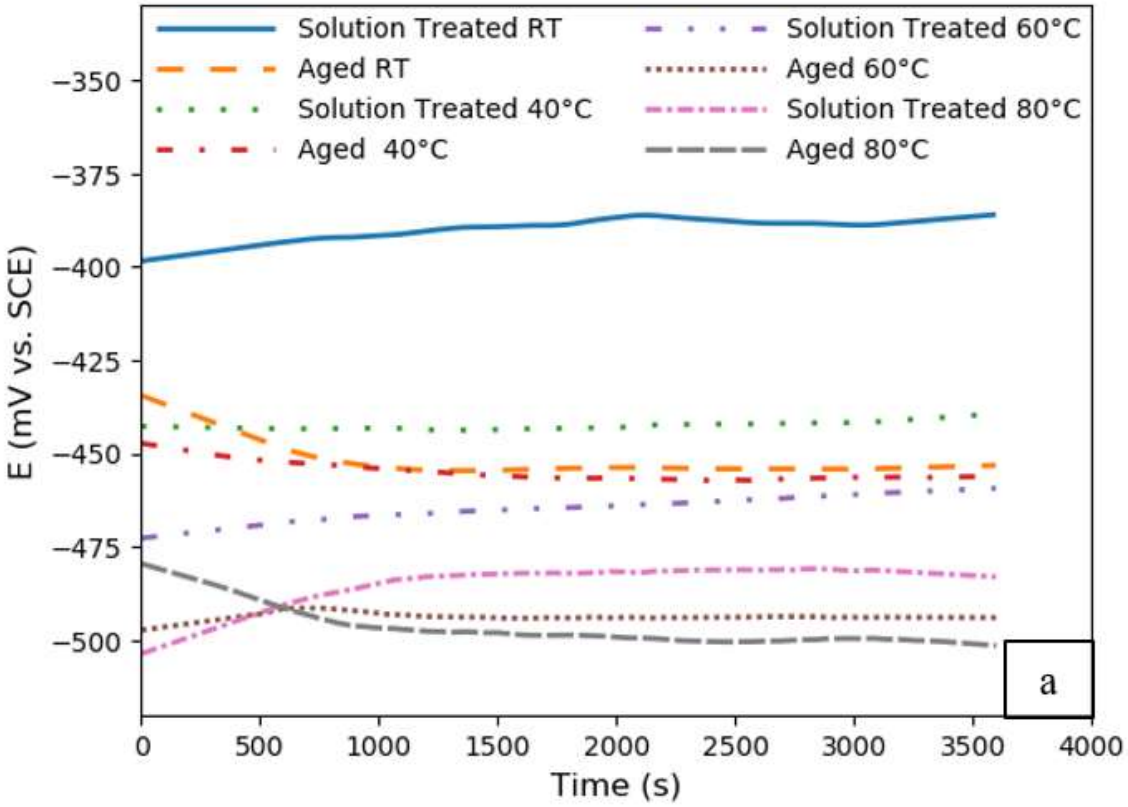

Figure 4.39. Typical open circuit potential obtained for solution treated and aged NCAT alloy in a 0.6 M NaCl solution with a pH of (a) 3, (b) 6, and (c) 10 measured at different temperatures. The lowest open circuit potential is observed for solutions having a pH of 3 and temperature of 80 °C.

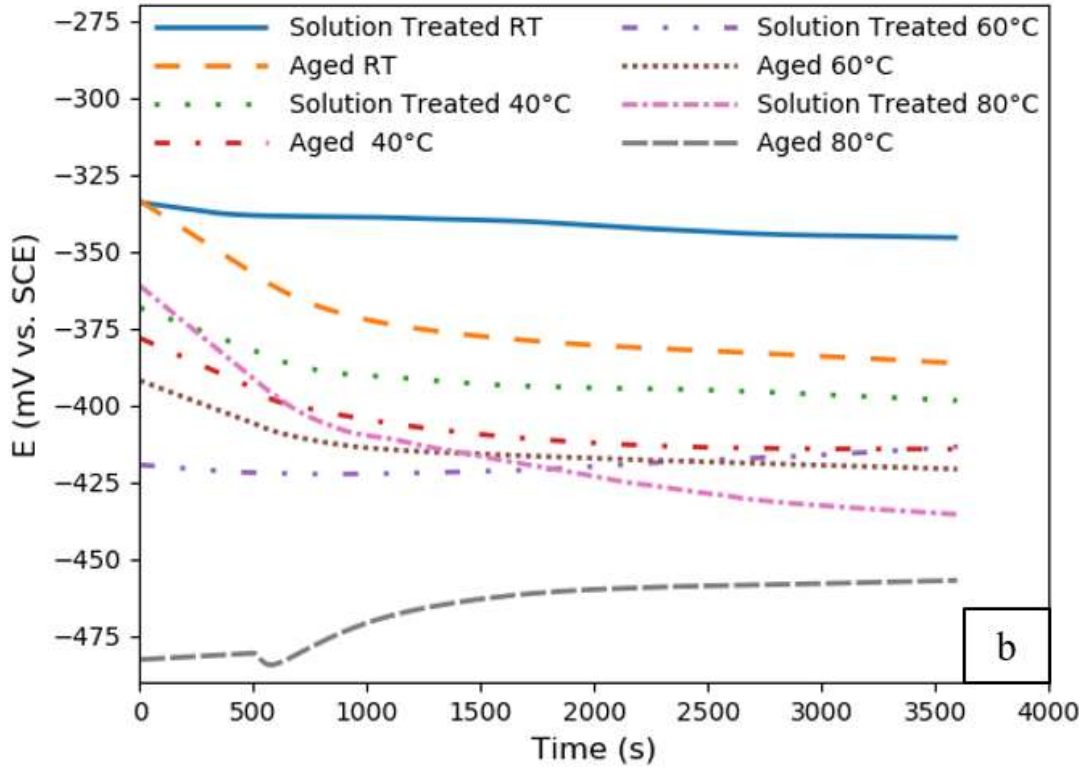

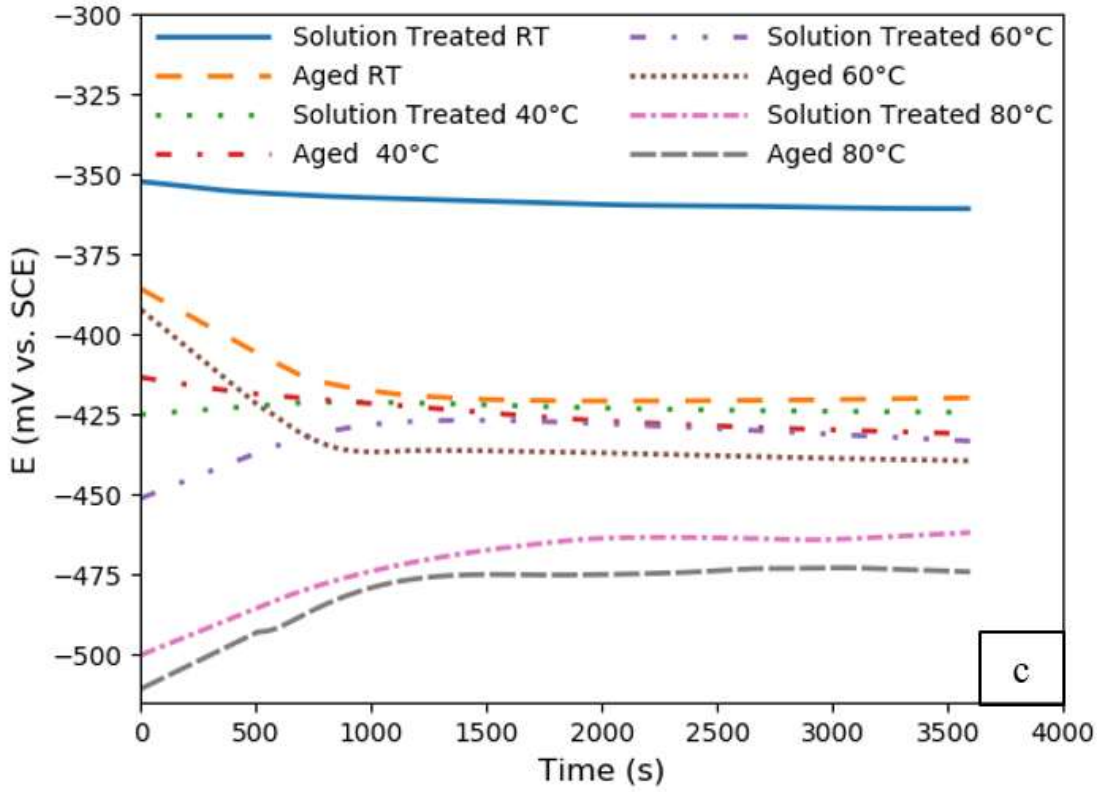

Figure 4.39. Continued.

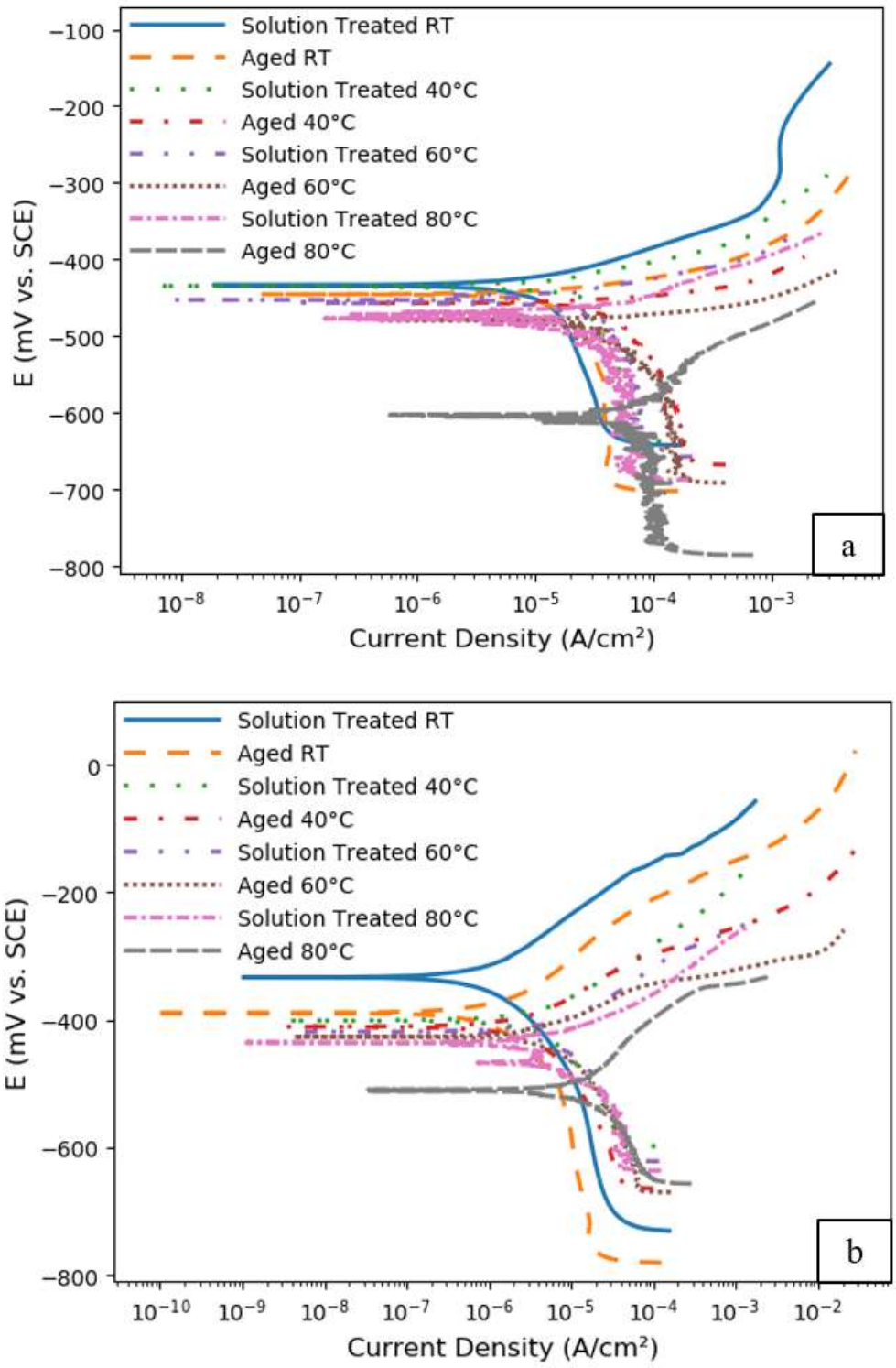

Figure 4.40. Potentiodynamic polarization curves obtained for solution treated and aged NCAT alloys in a 0.6 M NaCl solution with a pH of (a) 3, (b) 6, and (c) 10 measured at different temperatures. The highest current density values are observed in solutions with pH of 3, and the lowest values are found in solutions with a pH of 10. The corrosion current density is greater in all solutions at higher temperatures.

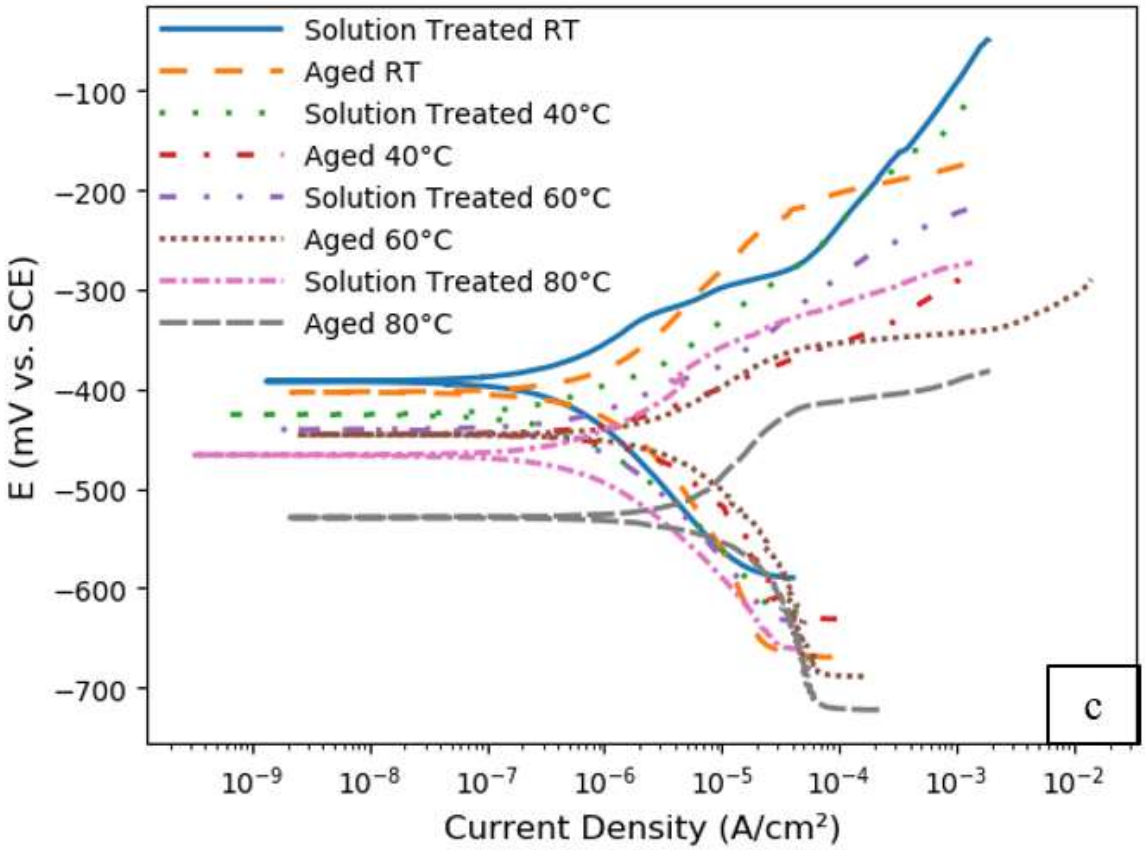

Figure 4.40. Continued.

From Figures 4.39-4.40 and Table 4.10, it is evident that both alloys display similar characteristics in 0.6 M NaCl solution. The open circuit and corrosion potentials became more negative and the corrosion current density increased with increasing temperature. Their corrosion rates increased with temperature regardless of the pH of the solution. The highest corrosion rate values and the lowest open circuit and corrosion potentials values were recorded at 80 ^{o}C in solutions with a pH of 3. Always aged NCAT alloy has lower open circuit and corrosion potentials and higher corrosion rates compared to the solution treated NCAT alloy in the same test conditions. This shows once again that the aging heat treatment resulted in reducing the corrosion resistance of the alloy in 0.6 M NaCl solution regardless of the solution temperature or pH. Figure 4.41 shows optical micrographs of solution treated NCAT and aged NCAT alloys that were tested at 40 ^{o}C in 0.6 M NaCl solution having a pH of 3. The aged NCAT alloy shows more pitting and larger corroded area compared to the solution treated NCAT alloy. The corrosion of aged NCAT is in the form of IGC, while the corrosion of the solution treated NCAT is in the form of pitting, and no

IGC can be observed. Appendix D shows more micrographs of solution treated NCAT specimens that were tested in 0.6 M NaCl solution at different temperatures and different solution pH. The corrosion of solution treated NCAT is characterized with relatively larger pits compared to the pits in the aged NCAT. This can also be observed in Figures D1– D3 in Appendix D.

An Arrhenius plot for the corrosion of solution treated NCAT and aged NCAT alloys in 0.6 M NaCl solution at different temperatures is shown in Figure 4.42. The thermodynamic parameters extracted from analysis of Figure 4.42 are summarized in Table 4.11. The curves that were generated from testing in solutions having pH of 3 and 10 in Figure 4.42 show clear linear relationship, thus indicating that only one process controlled the kinetics of the electrochemical reactions. The Arrhenius curves for the aged NCAT alloy show steeper slopes compared to those of solution treated NCAT alloy for all pH values. The steeper the slope of the curves, the greater the dependence of the corrosion rate on temperature and the higher the activation energy values. The values of activation energy obtained for solution treated NCAT alloy are lower than those obtained for the aged alloy. The higher the activation energy values, the more difficult it is to begin the corrosion process. This means that it is easier to start the corrosion process in the solution treated NCAT alloy compared to its aged counterpart. This could be due to the presence of γ phase precipitates in the aged alloy matrix, which hinders the progress of the corrosion in the alloy matrix. However, the presence of β phase precipitates in the grain boundaries weakens them, and results in progressing the corrosion in the aged NCAT in the grain boundaries, which eventually reduces the corrosion resistance of the alloy and results in more damage than is the case of solution treated NCAT.

Table 10. Electrochemical parameters obtained for solution treated NCAT and aged NCAT SMA in 0.6 M NaCl solution with three different levels of pH at four different temperatures.

Alloy	Temp. °C	pH	E_{oc}[1] mV	E_{corr}[1] mV	i_{corr} µA/cm²	β_a[1] V/decade	β_c[1] V/decade	R_p Ω.cm²	CR mm/y
Solution Treated NCAT	RT	6	-346	-334	1.75	0.06	-0.16	$1.05x10^4$	0.013
(SD)[2]			(±10.9)	(±35.4)	(±0.33)	(±0.02)	(±0.06)	($±5.8x10^3$)	(±0.002)
Solution Treated NCAT	RT	10	-361	-392	0.44	0.08	-0.12	$4.5x10^4$	0.003
(SD)[2]			(±5.9)	(±3.6)	(±0.13)	(±0.08)	(±0.006)	($±3.9x10^3$)	(±0.0009)
Solution Treated NCAT	RT	3	-384	-433	13.6	0.05	-0.37	$1.5x10^3$	0.101
(SD)[2]			(±31.2)	(±41.9)	(±3.90)	(±0.005)	(±0.09)	(±539.2)	(±0.03)
Solution Treated NCAT	40	6	-399	-400	5.80	0.09	-0.21	$4.4x10^3$	0.043
(SD)[2]			(±23.5)	(±26.4)	(±0.23)	(±0.02)	(±0.009)	(±294.5)	(±0.0005)
Solution Treated NCAT	40	10	-424	-426	0.71	0.08	-0.11	$3.5x10^4$	0.005
(SD)[2]			(±37.8)	(±42.2)	(±0.12)	(±0.03)	(±0.0005)	($±9.0x10^3$)	(±0.001)
Solution Treated NCAT	40	3	-438	-434	26.6	0.04	-0.36	614.1	0.198
(SD)[2]			(±13.9)	(±27.2)	(±0.30)	(±0.03)	(±0.06)	(±495.2)	(±0.002)
Solution Treated NCAT	60	6	-414	-418	10.3	0.09	-0.24	$3.1x10^3$	0.077
(SD)[2]			(±32.4)	(±21.0)	(±0.07)	(±0.03)	(±0.05)	(±656.3)	(±0.003)
Solution Treated NCAT	60	10	-433	-440	1.06	0.07	-0.13	$2.1x10^4$	0.008
(SD)[2]			(±49.7)	(±66.0)	(±0.14)	(±0.03)	(±0.06)	($±1.1x10^4$)	(±0.001)
Solution Treated NCAT	60	3	-459	-452	29.9	0.043	-0.25	481.6	0.222
(SD)[2]			(±11.1)	(±4.9)	(±2.90)	(±0.001)	(±0.09)	(±83.8)	(±0.02)
Solution Treated NCAT	80	6	-437	-436	14.1	0.09	-0.30	$2.6x10^3$	0.105
(SD)[2]			(±38.1)	(±23.8)	(±1.21)	(±0.007)	(±0.07)	(±647.2)	(±0.003)
Solution Treated NCAT	80	10	-462	-466	1.69	0.12	-0.15	$2.8x10^4$	0.013
(SD)[2]			(±55.6)	(±88.4)	(±0.42)	(±0.05)	(±0.05)	($±1.4x10^4$)	(±0.003)
Solution Treated NCAT	80	3	-488	-478	41.7	0.06	-0.42	342.3	0.31
(SD)[2]			(±40.7)	(±37.7)	(±0.16)	(±0.001)	(±0.07)	(±196.4)	(±0.001)

[1] All the potential values are measured vs. SCE. [2] Standard deviation (SD) values.

Table 4.10. Continued.

Alloy	Temp. °C	pH	E_{oc}[1] mV	E_{corr}[1] mV	i_{corr} µA/cm²	β_a[1] V/decade	β_c[1] V/decade	R_p Ω.cm²	CR mm/y
Aged NCAT (SD)[2]	RT	6	-386 (±16.4)	-389 (±13.5)	2.26 (±0.35)	0.12 (±0.01)	-0.22 (±0.03)	$1.6x10^4$ (±303.5)	0.017 (±0.002)
Aged NCAT (SD)[2]	RT	10	-420 (±33.4)	-403 (±48.6)	1.12 (±0.92)	0.13 (±0.06)	-0.16 (±0.02)	$2.4x10^4$ ($\pm2.5x10^4$)	0.008 (±0.007)
Aged NCAT (SD)[2]	RT	3	-453 (±13.8)	-446 (±20.1)	23.28 (±1.05)	0.03 (±0.02)	-0.53 (±0.04)	959.6 (±263.4)	0.174 (±0.008)
Aged NCAT (SD)[2]	40	6	-415 (±14.9)	-411 (±17.0)	3.91 (±0.81)	0.09 (±0.02)	-0.19 (±0.05)	$6.1x10^3$ ($\pm1.9x10^3$)	0.029 (±0.006)
Aged NCAT (SD)[2]	40	10	-431 (±27.6)	-445 (±48.8)	1.6 (±1.74)	0.06 (±0.03)	-0.09 (±0.03)	$8.7x10^3$ ($\pm1.8x10^3$)	0.012 (±0.01)
Aged NCAT (SD)[2]	40	3	-455 (±9.2)	-458 (±3.3)	46.5 (±7.11)	0.02 (±0.02)	-0.24 (±0.15)	331.5 (±152.7)	0.348 (±0.05)
Aged NCAT (SD)[2]	60	6	-421 (±31.6)	-426 (±9.4)	9.25 (±4.70)	0.09 (±0.02)	-0.23 (±0.03)	$3.8x10^3$ ($\pm1.5x10^3$)	0.069 (±0.03)
Aged NCAT (SD)[2]	60	10	-439 (±44.9)	-446 (±60.2)	5.38 (±5.50)	0.11 (±0.01)	-0.17 (±0.01)	$6.1x10^3$ ($\pm2.3x10^3$)	0.04 (±0.04)
Aged NCAT (SD)[2]	60	3	-492 (±11.8)	-480 (±14.2)	60.4 (±3.50)	0.023 (±0.02)	-0.322 (±0.082)	208.6 (±53.2)	0.451 (±0.026)
Aged NCAT (SD)[2]	80	6	-457 (±33.8)	-511 (±36.1)	35.13 (±10.90)	0.26 (±0.08)	-0.27 (±0.07)	$1.2x10^3$ (±624.01)	0.263 (±0.08)
Aged NCAT (SD)[2]	80	10	-473 (±41.8)	-528 (±79.3)	18.03 (±1.40)	0.32 (±0.12)	-0.25 (±0.07)	$2.9x10^3$ (±488.1)	0.135 (±0.01)
Aged NCAT (SD)[2]	80	3	-536 (±64.4)	-604 (±91.5)	94.2 (±2.20)	0.116 (±0.03)	-0.207 (±0.377)	207.0 (±483.1)	0.704 (±0.017)

[1] All the potential values are measured vs. SCE. [2] Standard deviation (SD) values.

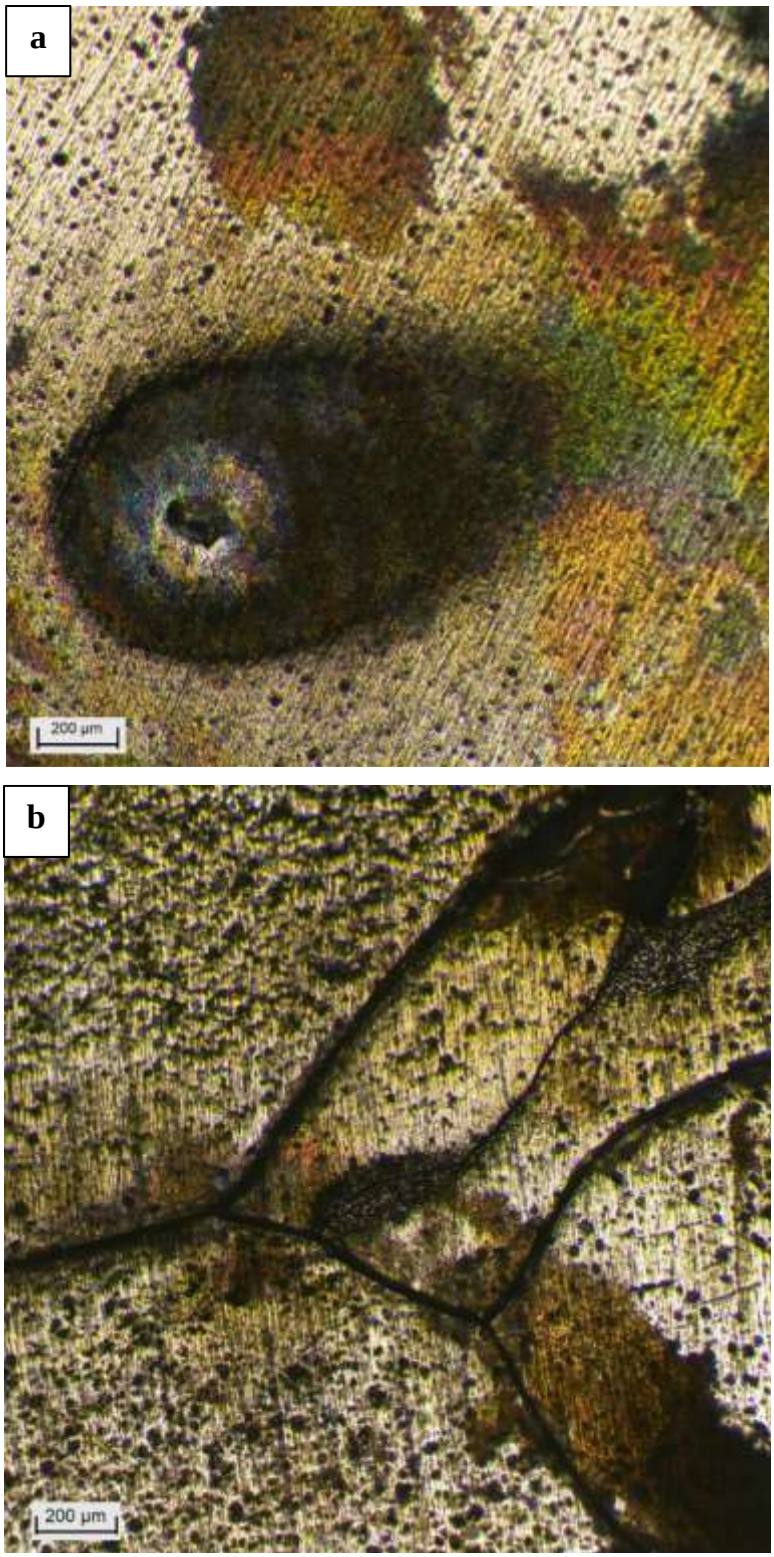

Figure 4.41. Micrographs obtained for (a) solution treated NCAT SMA and (b) aged NCAT SMA that were subjected to potentiodynamic polarization test at 40°C in a 0.6 M NaCl solution with a pH of 3. Increased pitting and larger corroded area are observed in the aged NCAT compared to the solution treated NCAT. IGC is also observed in aged NCAT.

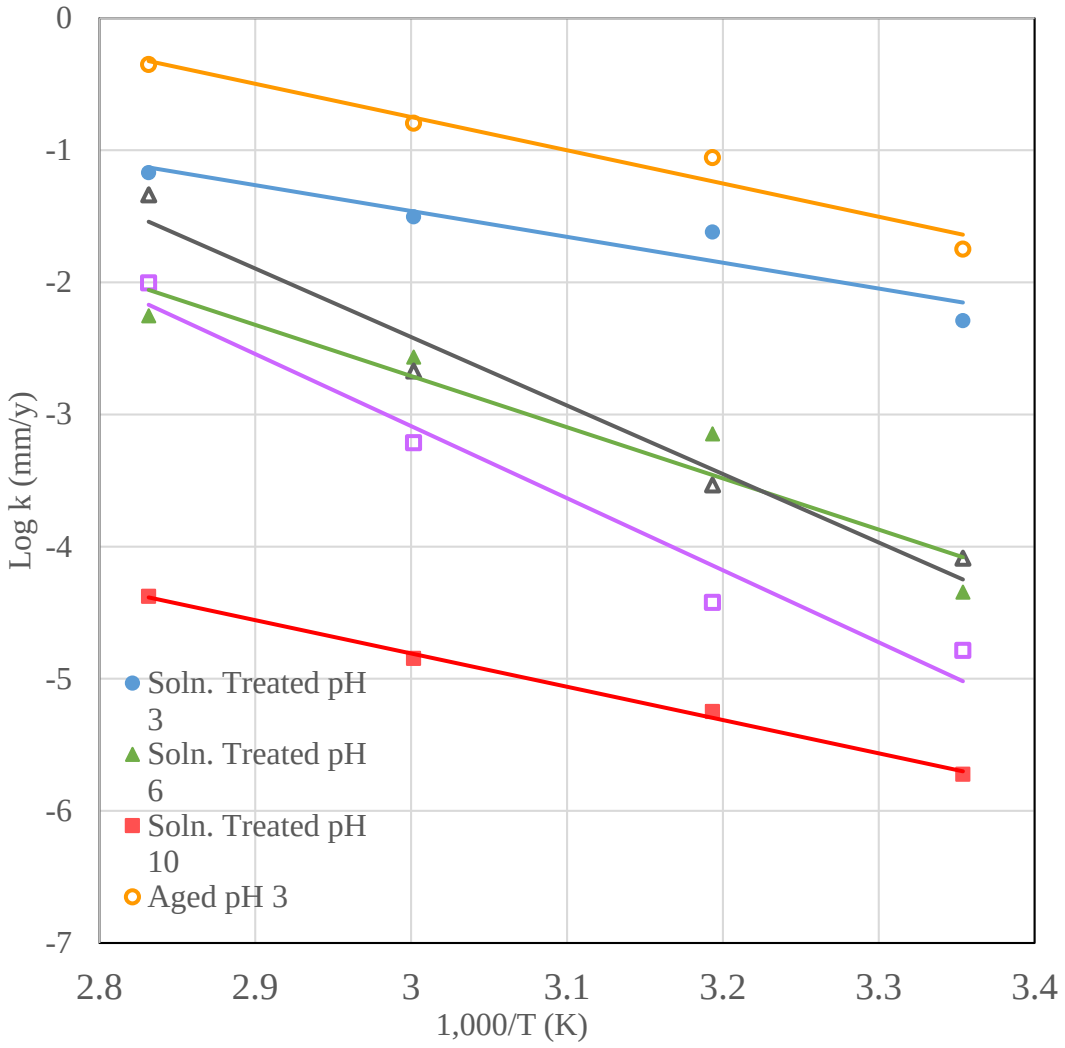

Figure 4.42. Arrhenius plots obtained for solution treated NCAT alloy compared with those of aged NCAT alloy in 0.6 M NaCl solution with three differnet pH, showing the effect of temperature on the corrosion rate of the alloys.

Table 4.11. Arrhenius parameters determined from the Arrhenius plot in Figure 4.42 for corrosion of solution treated and aged NCAT alloys in 0.6 M NaCl solution with different pH.

Parameter	**Solution Treated NCAT Alloy**		
	pH 3	pH 6	pH 10
Activation Energy (kJ / mole)	16.3	32.2	21.0
Constant A (mm / y. mole)	82.4	80,543.4	1.236

Parameter	**Aged NCAT Alloy**		
	pH 3	pH 6	pH 10
Activation Energy (kJ / mole)	21.0	43.1	45.3
Constant A (mm / y. mole)	893.6	485,645.2	715,879.6

Figure 4.43 presents the open circuit potentials obtained at four different temperatures for the two tested alloys in three 0.6 M NaCl solution having pH of 3, 6, and 10. The potentiodynamic polarization curves obtained for the alloy under the same test conditions are illustrated in Figure 4.44. The electrochemical parameters determined from the potentiodynamic polarization scans and linear polarization resistance experiments are provided in Table 4.10.

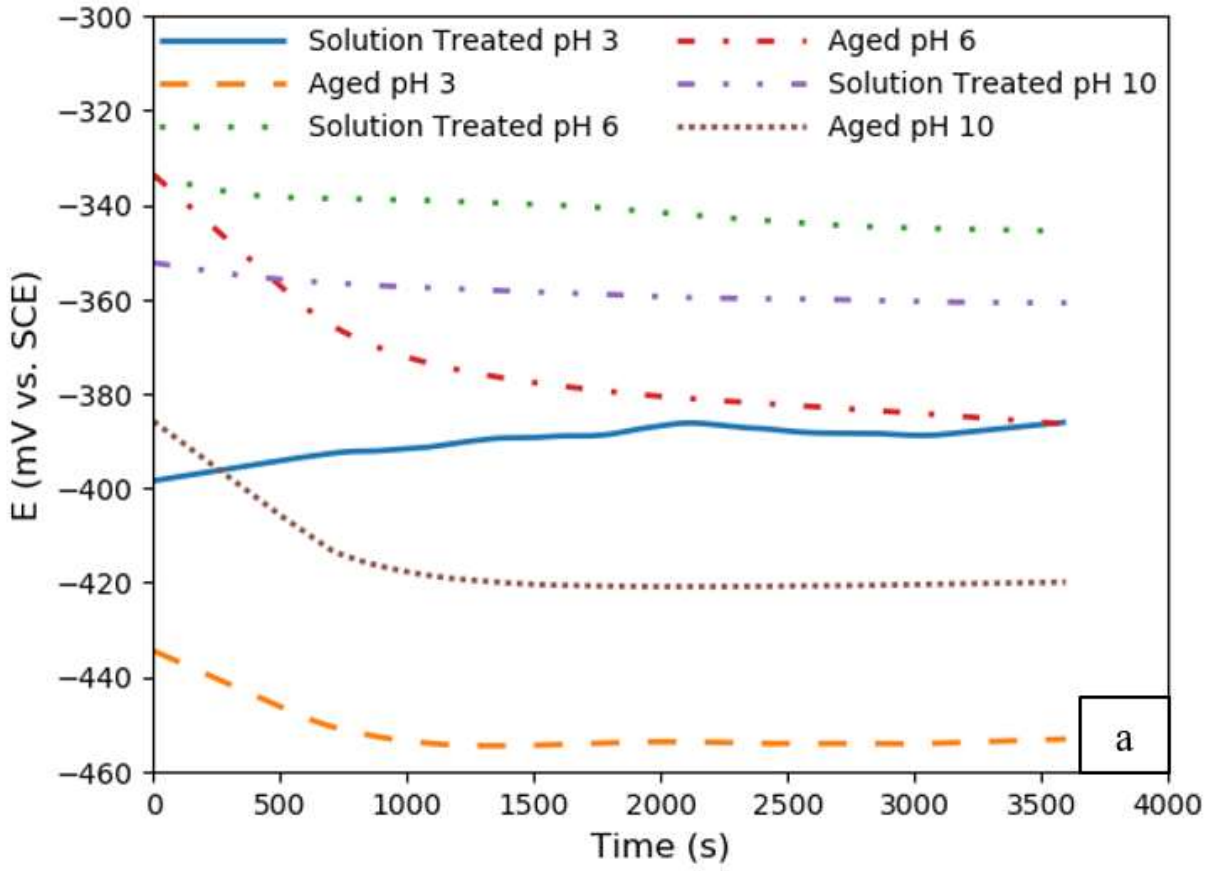

Figure 4.43. Typical open circuit potential curves obtained for solution treated NCAT and aged NCAT alloys in 0.6 M NaCl solution with different pH at: (a) RT, (b) 40 °C, (c) 60 °C, and (d) 80 °C. Open circuit potential shifted to negative values at high temperatures. The lowest values of open circuit potential are observed in the aged NCAT alloy and in solutions having a pH of 3.

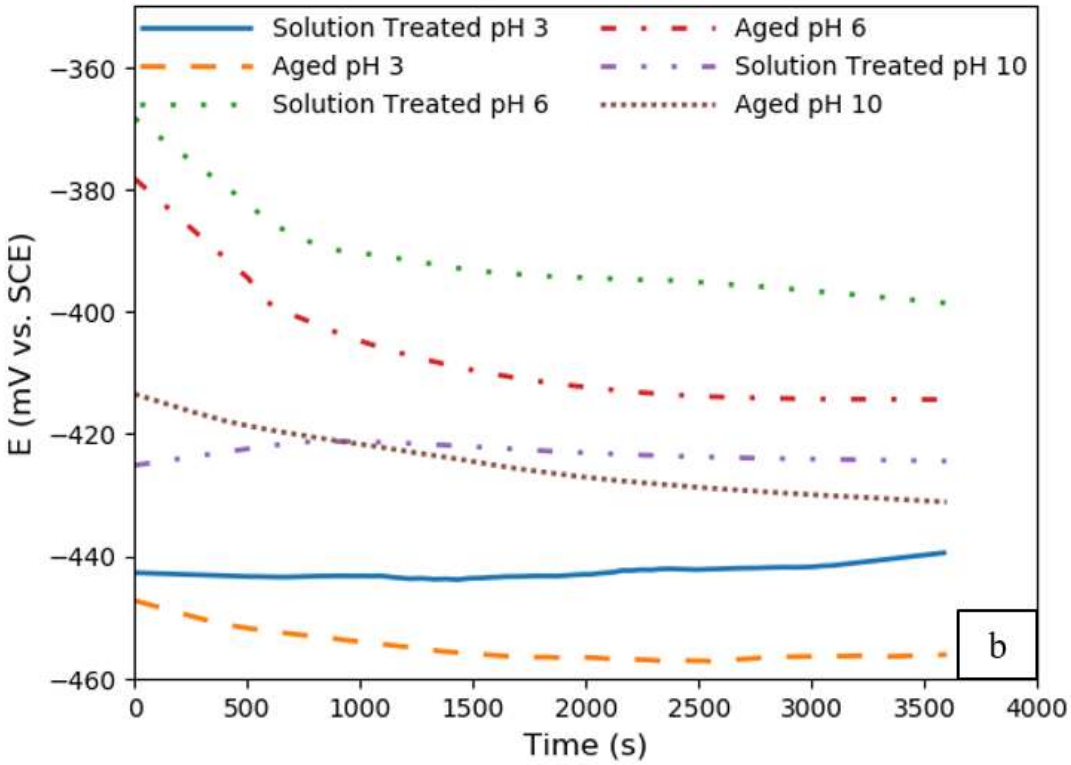

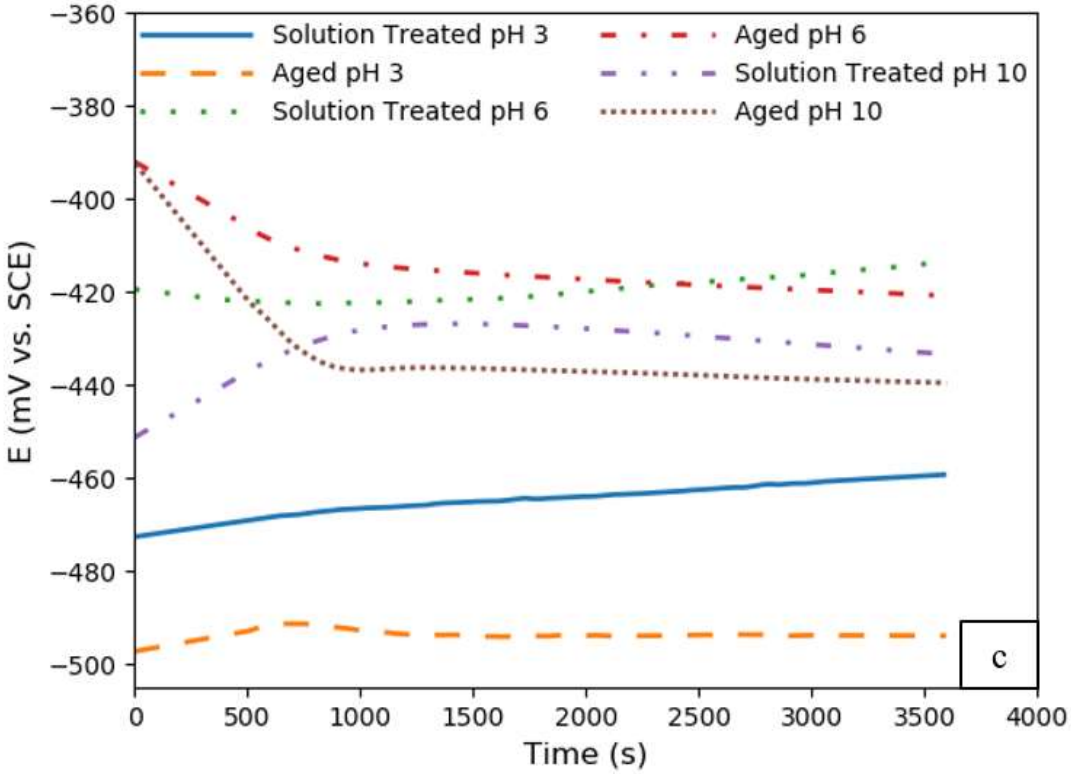

Figure 4.43. Continued.

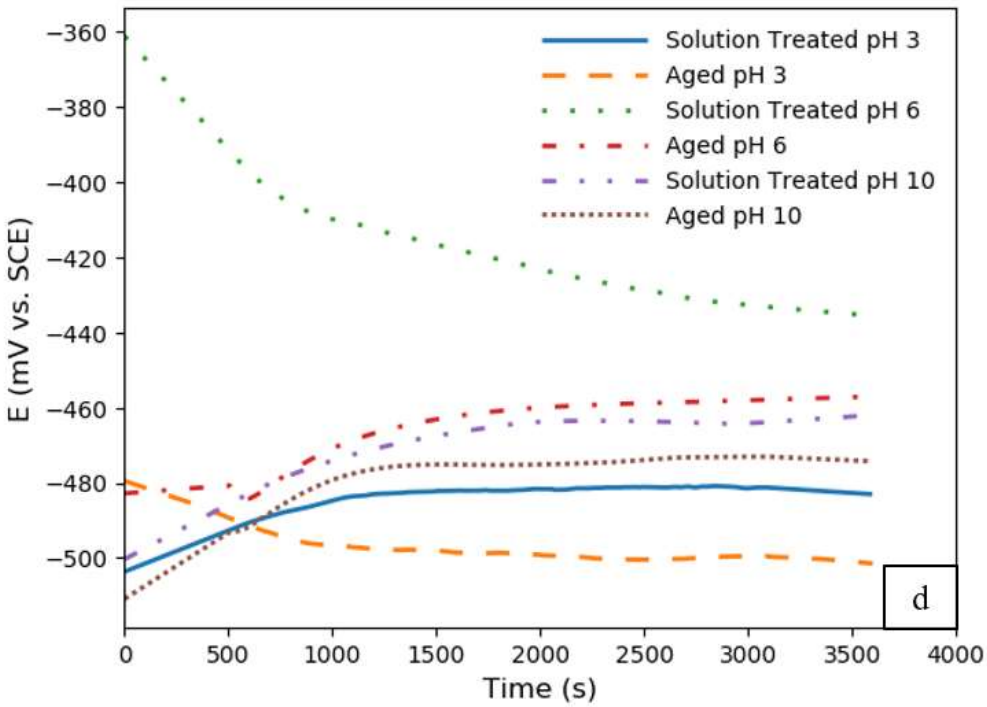

Figure 4.43. Continued.

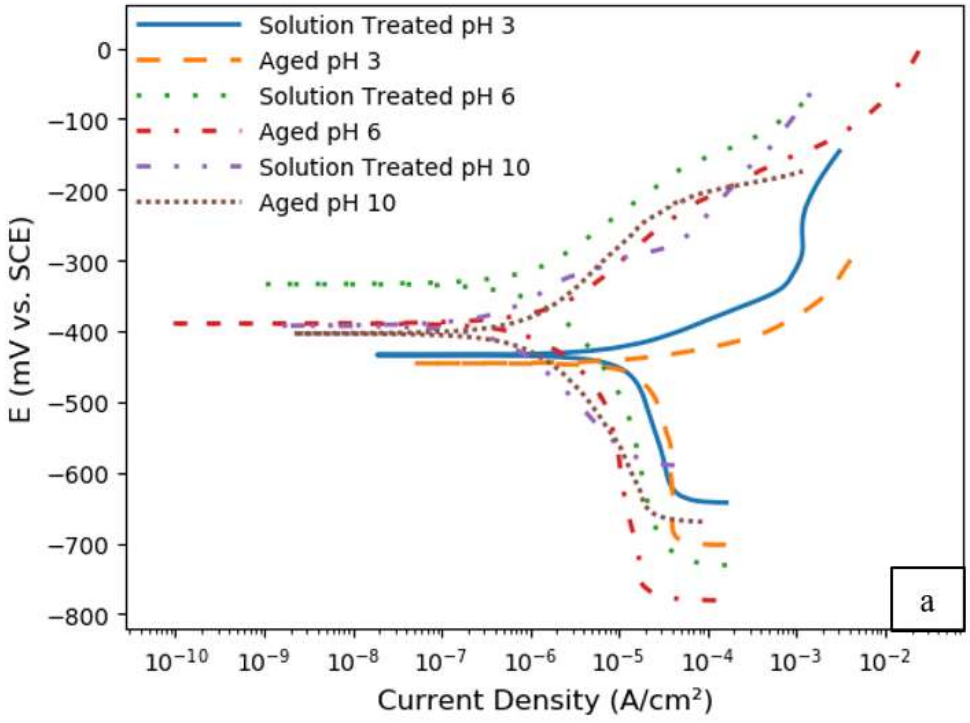

Figure 4.44. Typical potentiodynamic polarization curves obtained for solution heat treated NCAT and aged NCAT alloys in 0.6 M NaCl solution with different pH at: (a) RT, (b) 40 °C, (c) 60 °C, and (d) 80 °C. Solution treated NCAT alloy shows lower current density compared to the aged NCAT alloy. The lowest values are observed in samples tested in solutions with a pH of 10.

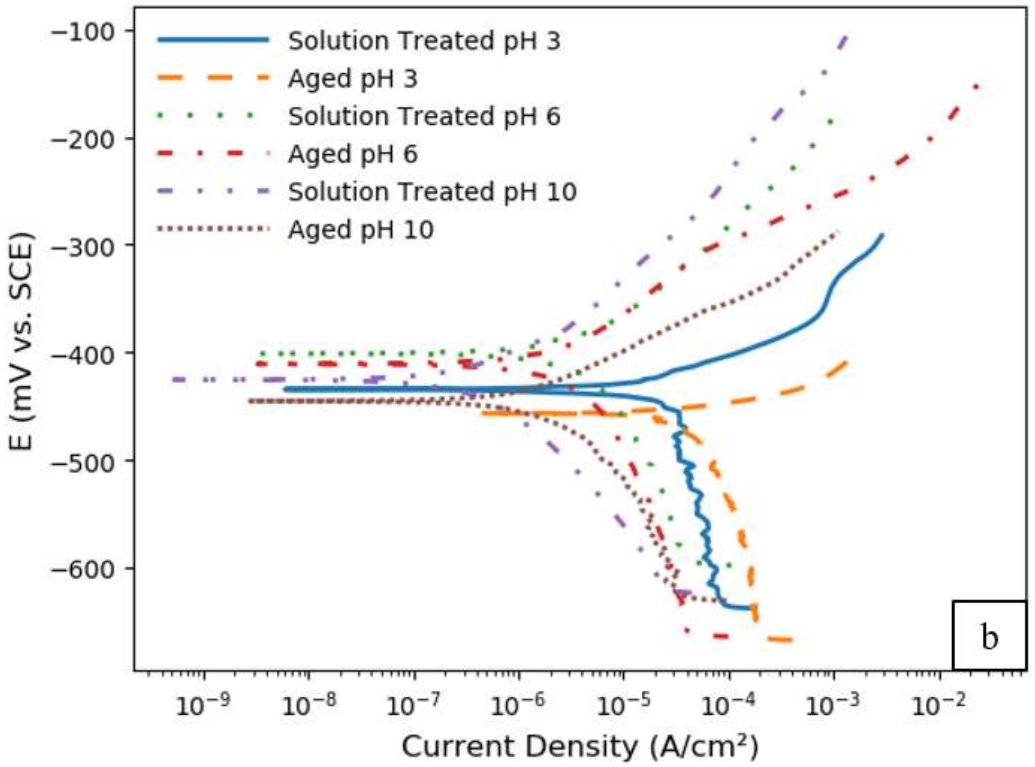

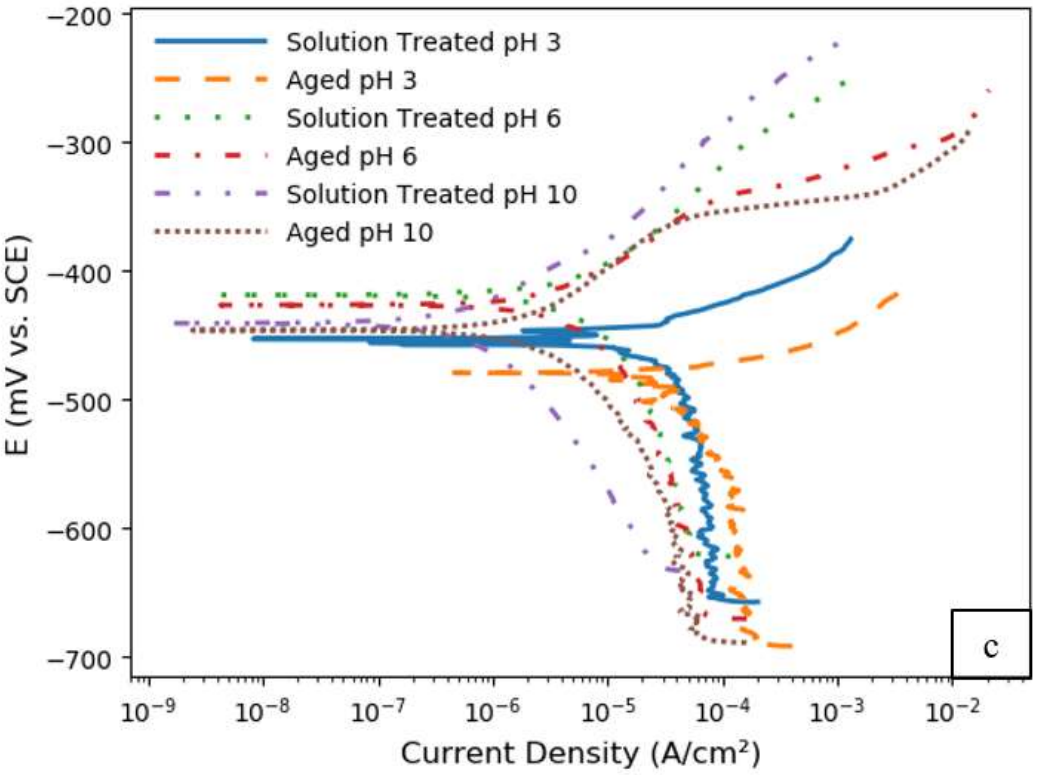

Figure 4.44. Continued.

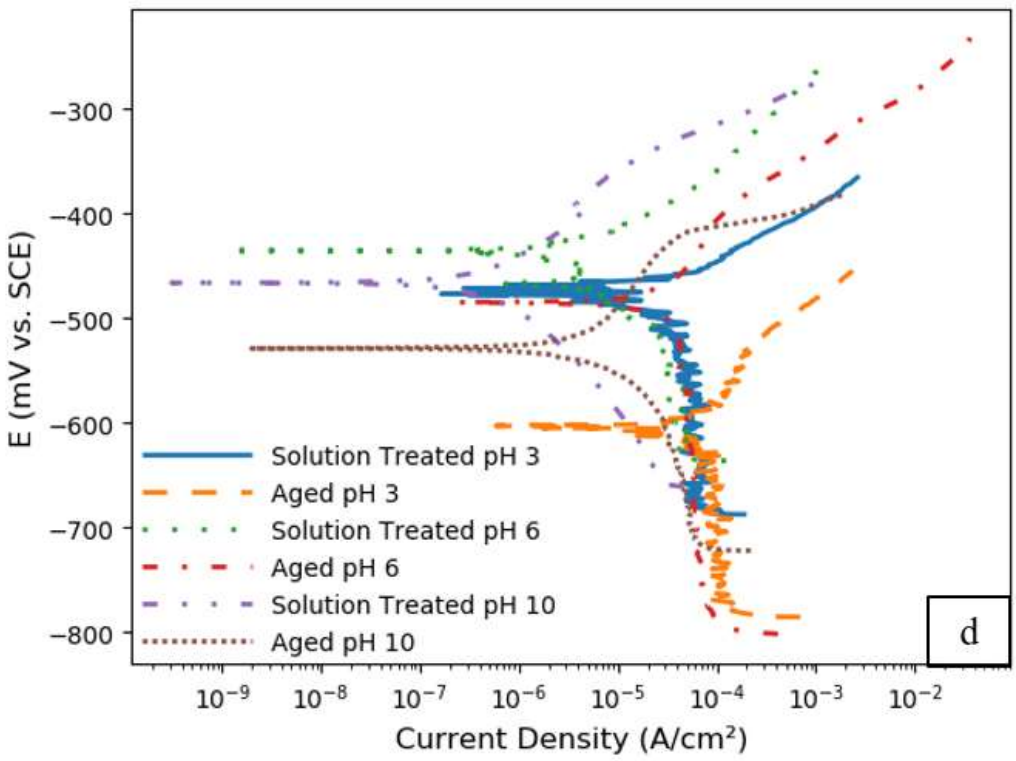

Figure 4.44. Continued.

Figure 4.43, Figure 4.44, and Table 4.10 show that the open circuit potential and corrosion potential of the two heat treated alloys are shifted to more negative values as the solution becomes more alkaline (pH 10) or more acidic (pH 3). The lowest values were observed in the solutions that are having a pH level of 3 and were tested at 80 ^{o}C. The corrosion current density, and subsequently the corrosion rate values, are greater in solutions having a pH of 3, and lower in solutions having a pH of 10. As previously observed, the higher temperature enhanced the corrosion and shifted the open circuit potential to negative values and the corrosion rate to greater values. In all the testing conditions, solution treated NCAT alloy showed higher corrosion resistance and more positive open circuit potential values than the aged NCAT alloy in the 0.6 M NaCl solution.

A relationship between the corrosion rate and solution pH of the two heat treated alloys is illustrated in Figure 4.45, where it is clear that the greater the acidity of the 0.6 M NaCl solution, the higher the corrosion rates and vice versa. The discussion of the results in section 4.6.2 applies to this section. The aging treatment was shown to result in lower open circuit potentials and higher corrosion rates, compared to the solution treatment of the alloy. As previously discussed, it is

believed that the grain boundary precipitates that are formed during the aging heat treatment are responsible for reducing the corrosion resistance of the alloy by forming preferred sites for pitting in the alloy matrix and causing IGC in the grain boundaries. Optical micrographs of the corroded solution treated NCAT that were subject to potentiodynamic polarization scans in 0.6 M NaCl solution at different temperatures and different pH are illustrated in Figures D1– D3 in Appendix D. The images correlate with the electrochemical testing findings, where a smaller number of pits and smaller corroded area were observed in the solution treated NCAT compared to the aged NCAT.

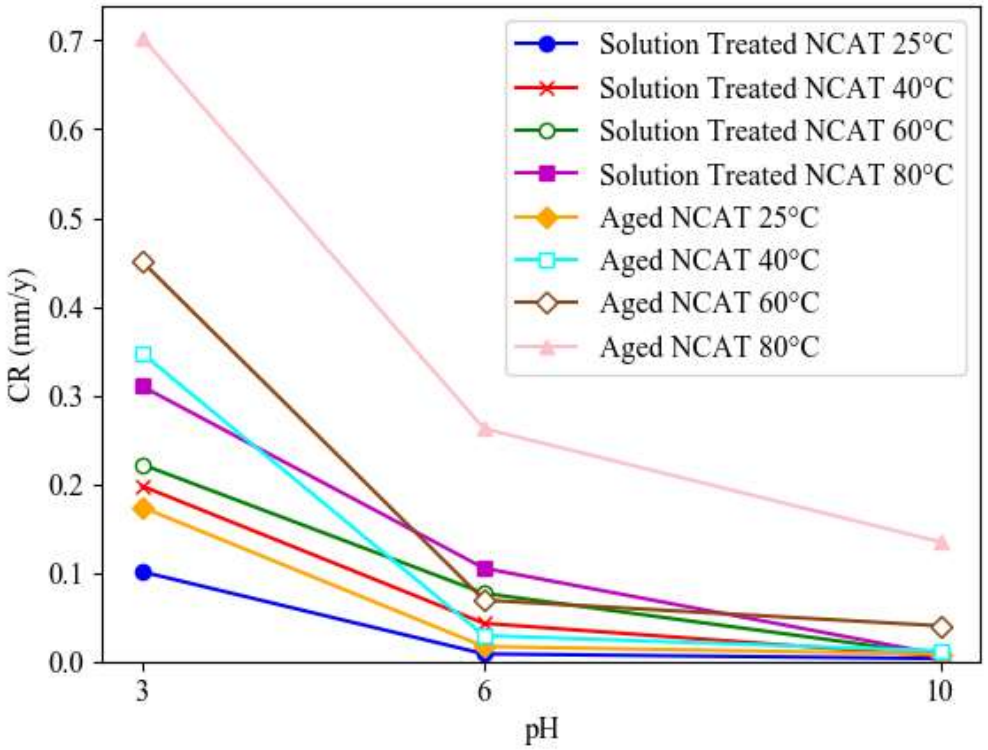

Figure 4.45. The effect of solution pH on the corrosion rate of solution treated NCAT and aged NCAT in 0.6 M NaCl solutions tested at different temperatures. Higher corrosion rates are observed in all the solutions with a pH of 3 at the higher temperatures, with the aged NCAT alloy showing more corrosion compared to the solution treated NCAT alloy.

In summary, the aging heat treatment reduced the corrosion resistance of the alloy. The temperature and pH have an impact on the corrosion properties of both the solution treated NCAT and aged NCAT. The higher temperature resulted in greater corrosion rates and lower open circuit potential. The pH has a different impact. The corrosion rate was greater in the acidic solution (pH

3), which was accompanied by a reduction in the corrosion potential. In contrast, the corrosion rate was lower at the higher pH of 10. This is most likely due to the formation of a protective oxide film on the surface of the alloy.

The effect of temperature and pH on corrosion rate (CR) and open circuit potential (E_{OC}) of solution treated NCAT alloy and aged NCAT alloy, is shown as contour plots in Figures 4.46 and Figure 4.47, respectively. As can be seen from Figure 4.46, the corrosion rate of solution treated NCAT alloy is consistently lower than that of aged NCAT alloy in 0.6 M NaCl solution with different pH at all test temperatures. For both alloys, the corrosion rate increased with increasing temperature and decreasing pH. Solution treated NCAT alloy at pH levels of ~ $5.3 \geq pH \leq 10$ shows a corrosion rate < 0.05 mm/y. At these levels of pH, the temperature does not seem to have a notable effect on the corrosion rate of the alloy. In contrast, in acidic solutions (≤ pH 5.1), the temperature clearly influences the corrosion rate. Greater corrosion rates are observed in the alloy at higher temperatures. The aged NCAT alloy, on the other hand, demonstrates double the corrosion rates (≤0.1 mm/y) only in a very limited range of pH ($9 \geq pH \leq 10$) as can be seen in Figure 4.46 (b). In pH levels ≤ 8.9, the higher temperature notably raises the corrosion rates.

The open circuit potential of both solution treated and aged NCAT alloys shifts to more negative value at higher temperatures, as seen in Figure 4.47. This indicates an increase in the corrosion activity of the alloy at these temperatures. The pH, on the other hand, has a different impact on the solution treated NCAT and aged NCAT. In both, the lower solution pH and higher solution pH resulted in very similar open circuit potential values compared to the pH values that are ~ 6. In solution treated NCAT, for example, the open circuit potential values of -400 mV vs. (SCE) are found in solutions with $3 \geq pH \leq 10$ in ~ $42\ ^{o}C \leq temp \geq 25\ ^{o}C$, while the same open circuit potential in aged NCAT is recorded in a lower pH range of ~ $5.3 \geq pH \leq 7.6$ and at lower temperature range of ~ $32\ ^{o}C \leq temp \geq 25\ ^{o}C$. The open circuit potential of aged NCAT alloy is consistently more negative than that of solution treated NCAT alloy in 0.6 M NaCl solution with different pH at all test temperatures. The contour plots illustrate the limitations on the use of aged NCAT alloy in 0.6 NaCl solutions compared to solution treated NCAT alloy.

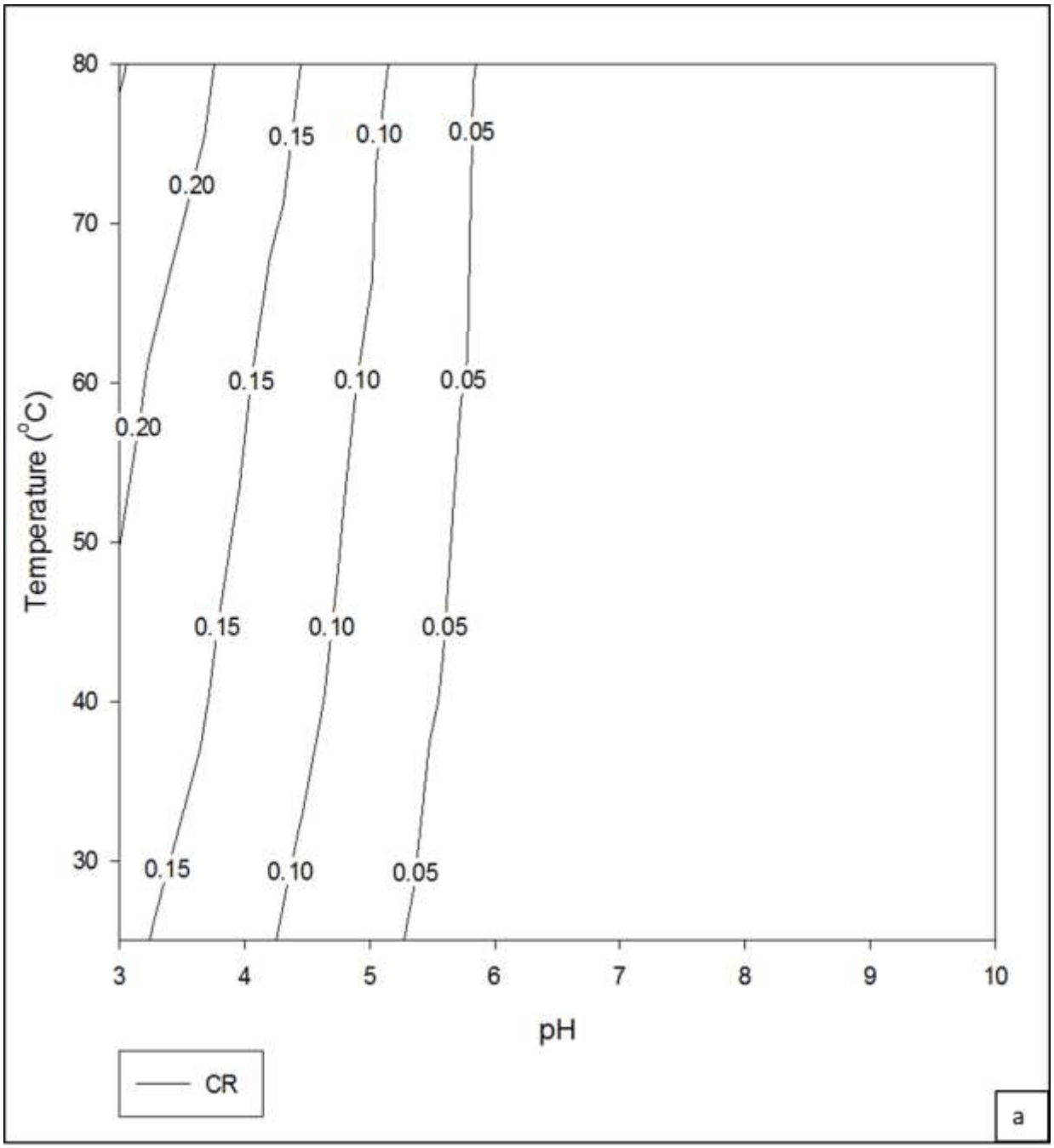

Figure 4.46. Contour plots for (a) solution treated NCAT alloy and (b) aged NCAT alloy showing the effects of pH and temperature on their corrosion rate in mm/y. Lower corrosion rates are observed at alkaline solutions and at lower temperatures. Aged NCAT alloy exhibit higher corrosion rates compared to solution treated NCAT alloy.

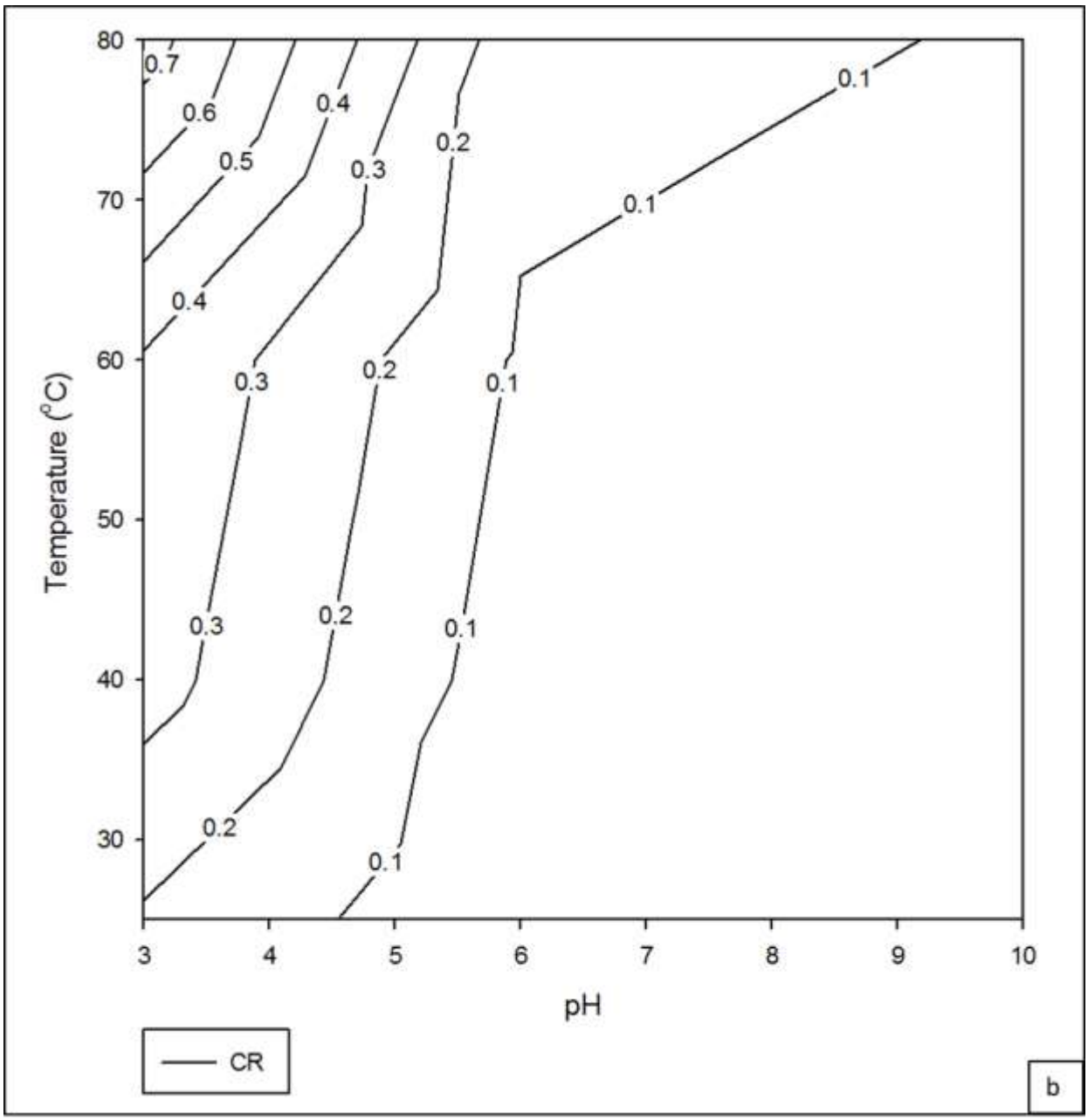

Figure 4.46. Continued.

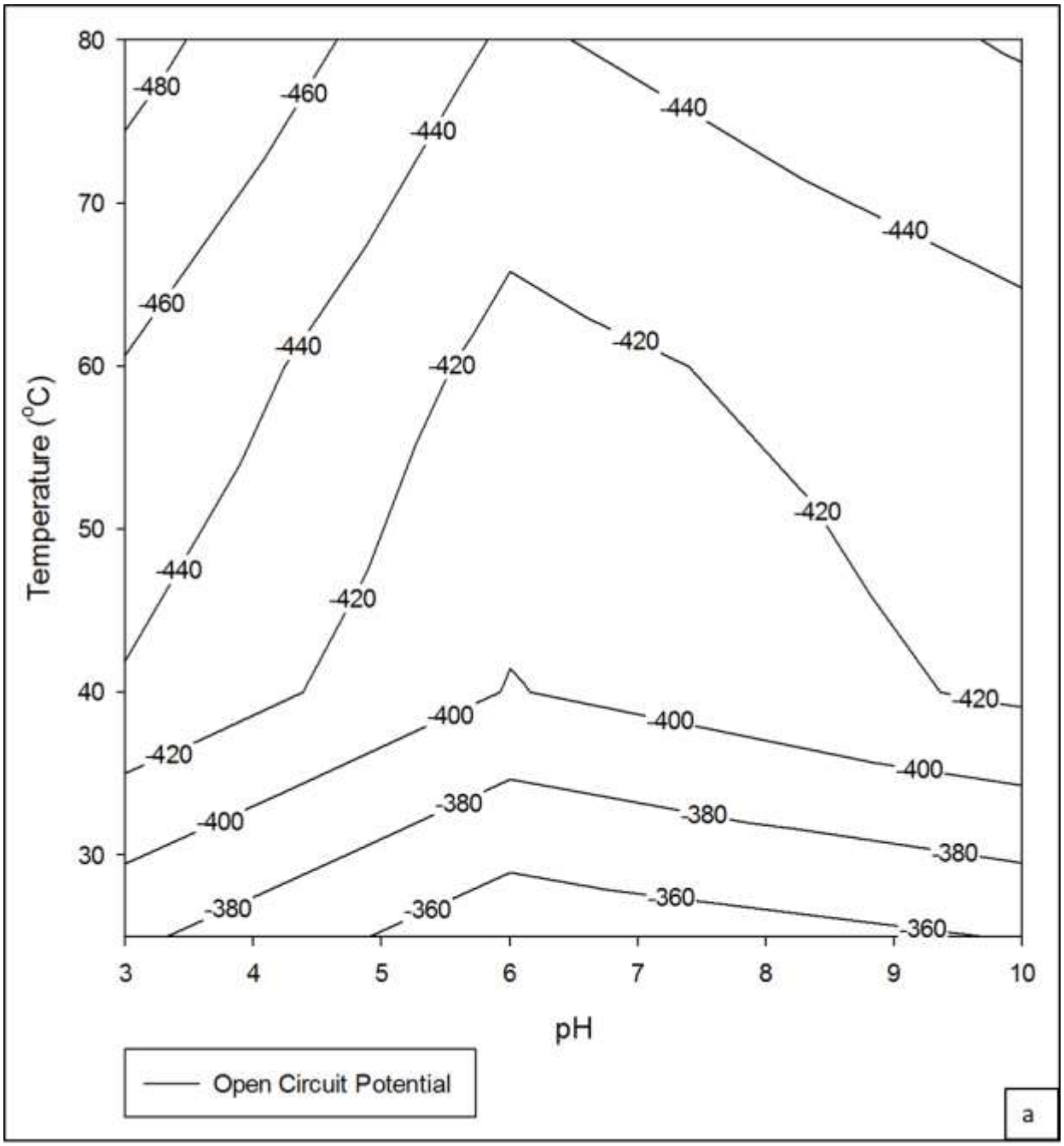

Figure 4.47. Contour plots for (a) solution treated NCAT alloy and (b) aged NCAT alloy showing the effects of pH and temperature on their open circuit potential (E_{oc}) in mV vs. (SCE). Acidic solutions and alkaline solutions were observed to have negative E_{oc} values compared to basic solutions (pH 6), and the higher temperatures of the solutions appear to shift E_{oc} to more negative values. Solution treated NCAT alloys show more positive E_{oc} values compared to aged NCAT alloy.

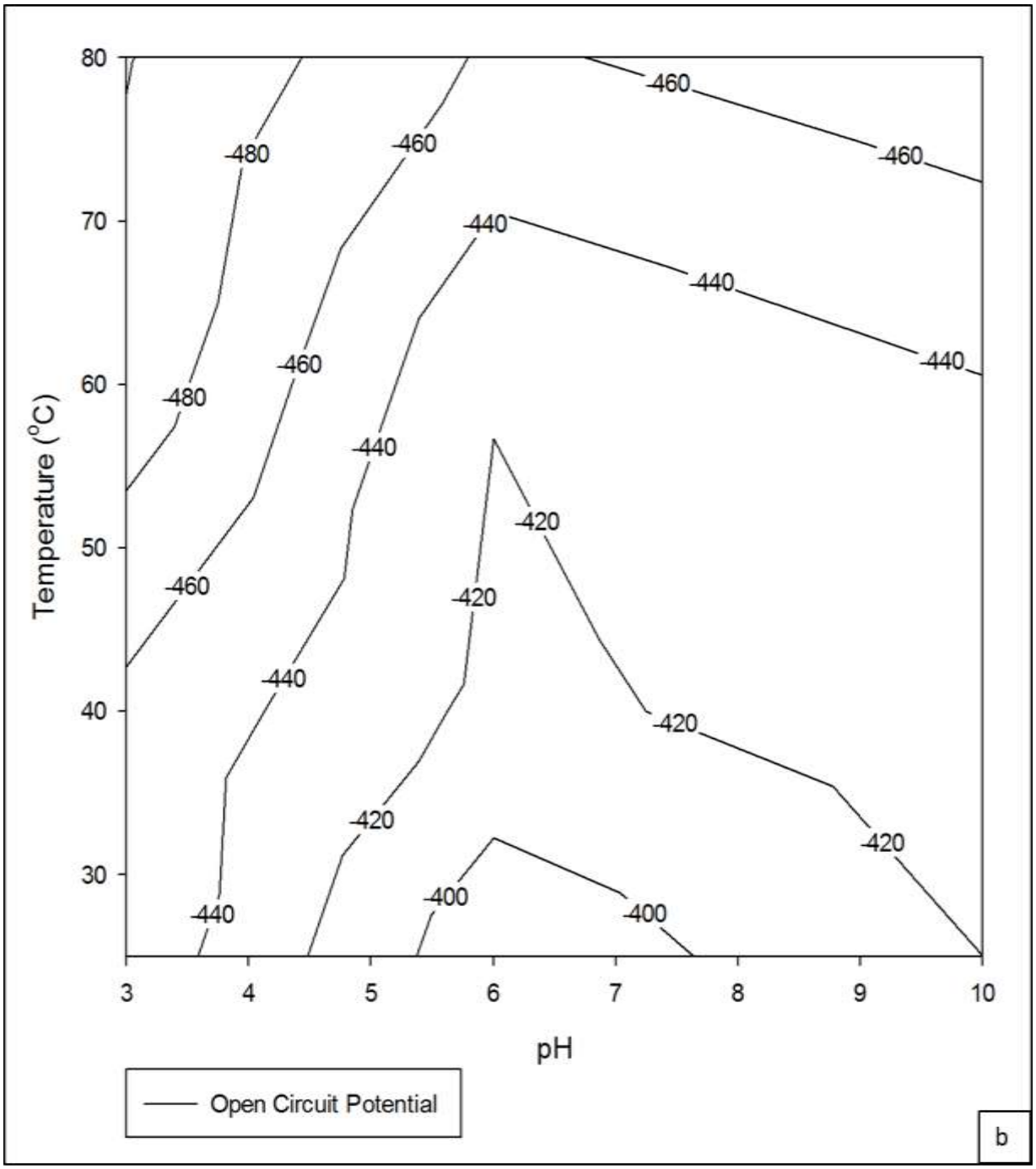

Figure 4.47. Continued

4.8 Galvanic Corrosion of NCAT SMA in a 0.6 M NaCl Solution at Different Temperatures

The shape memory effect and superelasticity characteristics of NCAT alloy is drawing a lot of attention, and is making it a candidate material for pipe couplers. This made it necessary to investigate the galvanic corrosion behaviour of the alloy when coupled with other commercial alloys. In this section, the results of experiments carried out to understand the galvanic corrosion behaviour of aged NCAT alloy are presented. The effect of coupling the alloy to four commercial alloys ((i) UNS G10180 (1018), (ii) UNS S30400 (304), (iii) UNS S31603 (316L), and (iv) UNS S32750 (2750)) in a 0.6 M NaCl solution at three different temperatures (RT, 40 ^{o}C, and 60 ^{o}C) was investigated.

The open circuit potential curves obtained for aged NCAT SMA and four commercial alloys in 0.6 M NaCl solution at RT and 60 ^{o}C are represented in Figure 4.48. The open circuit potential of NCAT is more positive when compared to the open circuit potential of alloy 1018 at RT and 60 ^{o}C. This indicates that NCAT is less active than alloy 1018 in the solution, and that alloy 1018 will act as an anode in the galvanic coupling. The rest of the alloys have positive open circuit potential when compared to NCAT at both RT and 60 ^{o}C. Therefore, NCAT was designated as the anode, when coupled with any of these stainless steel alloys. The open circuit potential of all the alloys is lower at 60 ^{o}C.

The potentiodynamic polarization curves of NCAT, and the four commercial alloys in a 0.6 M NaCl solution at RT and 60 ^{o}C, are represented in Figure 4.49. As previously discussed, NCAT does not show any passivation in 0.6 M NaCl solution. The corrosion behaviour of the alloy in both RT and 60 ^{o}C is that of general dissolution with localized attack (pitting). The corrosion attack was concentrated at the grain boundaries that were characterized with precipitates resulting in IGC, and pitting was found in the area adjacent to these grain boundaries (see section 4.3). Similar to NCAT SMA, 1018 carbon steel does not show any passivation in the test solution, whereas the stainless steel alloys show evidence of formation of protective oxide film in the solution as illustrated in Figure 4.49 at both RT and 60 ^{o}C, indicating that these alloys have better corrosion resistance than both NCAT and 1018 at the 0.6 M NaCl solution. The different electrochemical parameters determined from the plots in Figure 4.48 and Figure 4.49 are given in Table 4.12.

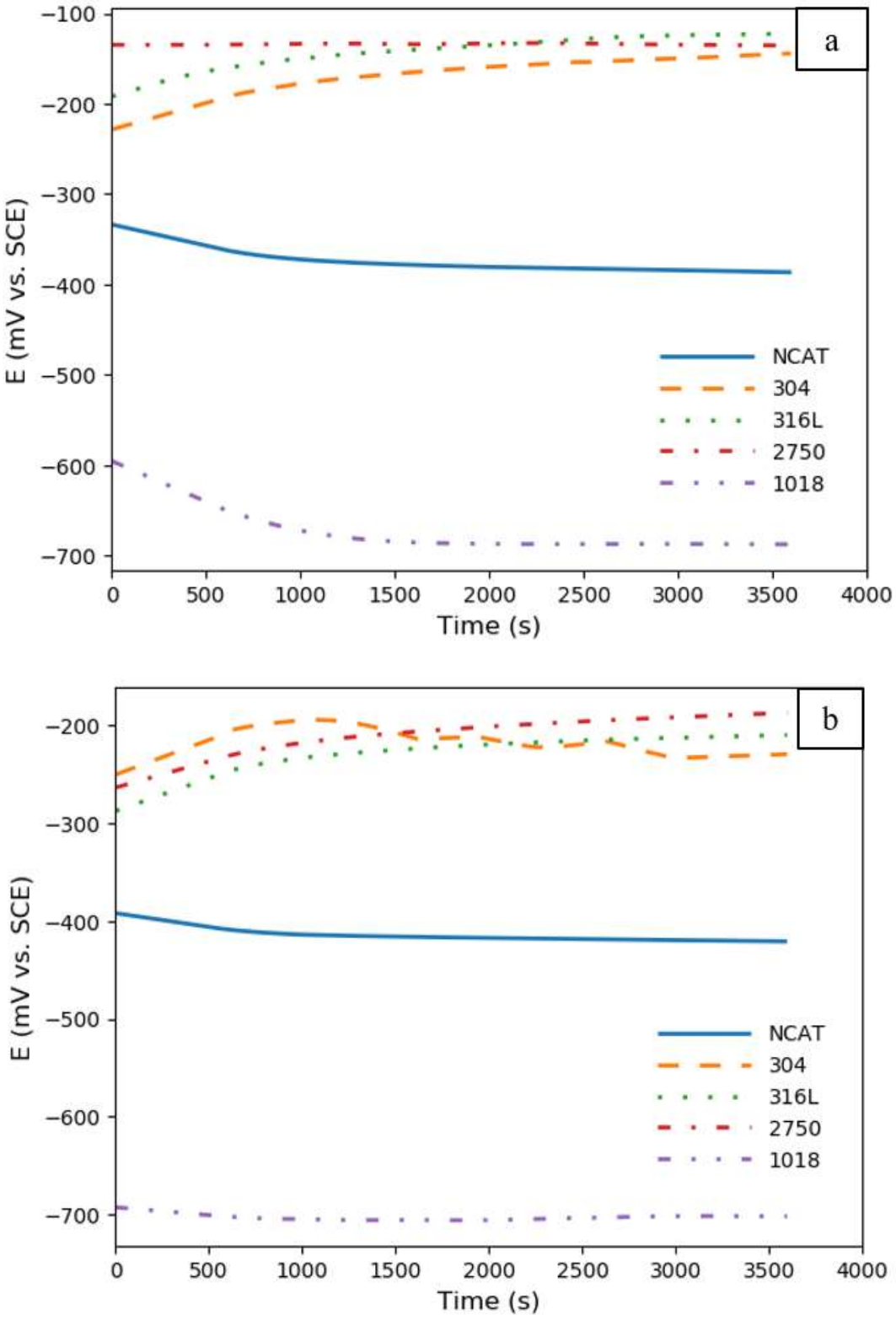

Figure 4.48. Typical open circuit potential measurement of uncoupled NCAT SMA compared to commercial alloys in 0.6 M NaCl at (a) RT and (b) 60 ºC. The open circuit potential of NCAT SMA is more negative than the other commercial alloys, except for 1018 carbon steel.

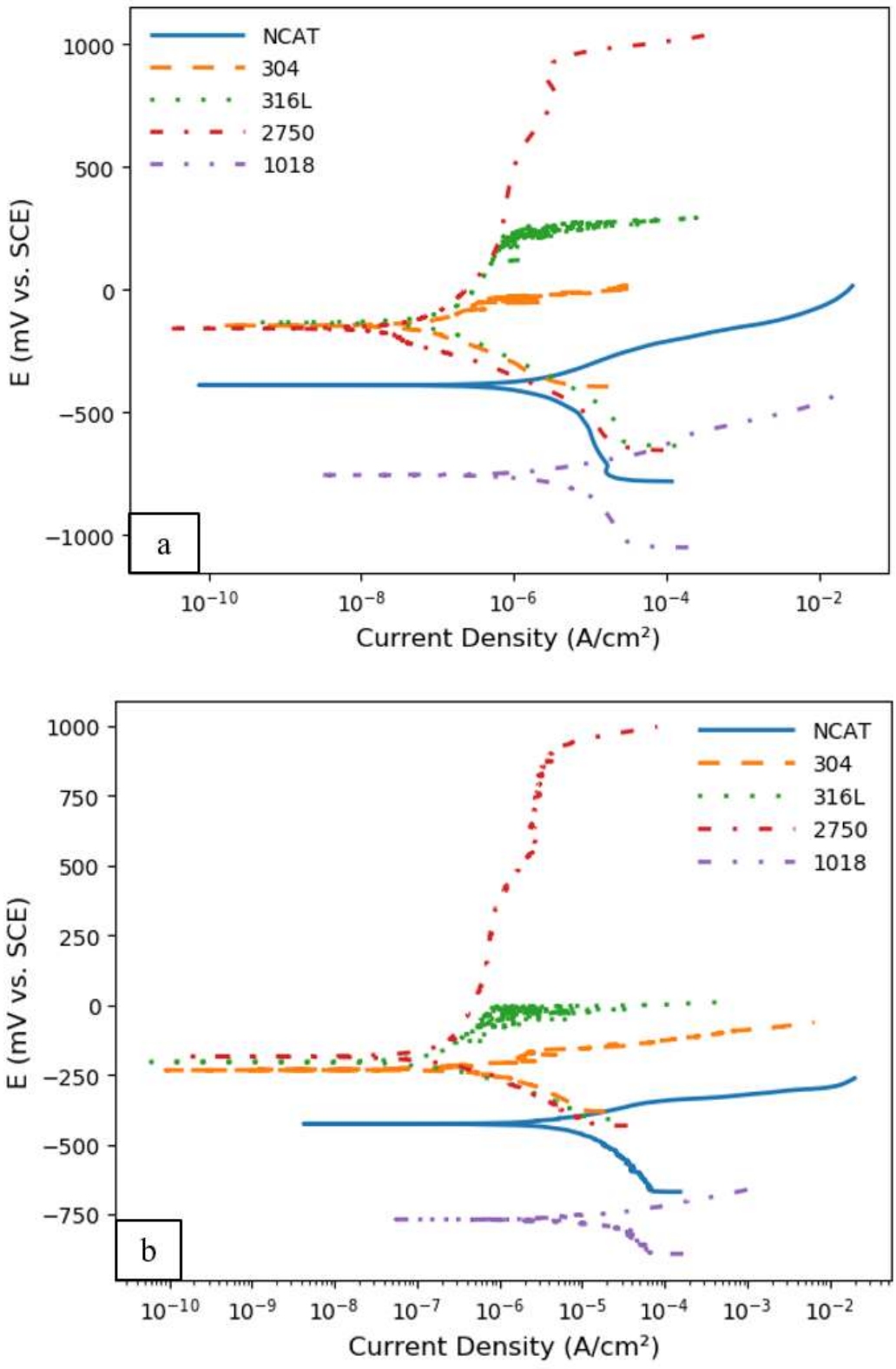

Figure 4.49. Typical potentiodynamic polarization curves of NCAT SMA and various commercial alloys in 0.6 M NaCl solution at (a) RT and (b) 60 ºC. NCAT and 1018 carbon steel have higher current density compared to the rest of the alloys, with 1018 having the highest value.

Table 4.12. Electrochemical parameters obtained for NCAT alloy and the commercial alloys in 0.6 M NaCl solution at RT and 60 °C.

Alloy	Temp. °C	E_{oc}[1] mV	E_{corr}[1] mV	i_{corr} µA/cm²	β_a[1] V/decade	β_c[1] V/decade	R_p Ω.cm²	CR mm/y
NCAT	RT	-386	-389	2.26	0.12	-0.22	$1.6x10^4$	0.017
(SD)[2]		(±16.4)	(±13.5)	(±0.35)	(±0.01)	(±0.03)	(±303.5)	($\pm 2x10^{-3}$)
NCAT	60	-421	-426	9.25	0.09	-0.23	$3.8x10^3$	0.069
(SD)[2]		(±31.6)	(±9.4)	(±4.70)	(±0.02)	(±0.03)	($\pm 1.5x10^3$)	(±0.03)
304	RT	-145	-146	0.13	0.11	-0.21	$2.9x10^5$	0.0007
(SD)[2]		(±1.7)	(±3.5)	(±0.02)	(±0.06)	(±0.03)	($\pm 8.3x10^4$)	($\pm 1x10^{-4}$)
304	60	-232	-234	0.83	0.08	-0.11	$2.7x10^4$	0.004
(SD)[2]		(±15.0)	(±13.4)	(±0.14)	(±0.02)	(±0.01)	($\pm 6.3x10^3$)	($\pm 7x10^{-4}$)
316L	RT	-123	-133	0.12	0.39	-0.16	$3.1x10^5$	0.0007
(SD)[2]		(±15.7)	(±16.4)	(±0.03)	(±0.03)	(±0.02)	($\pm 8.1x10^4$)	($\pm 2x10^{-4}$)
316L	60	-210	-205	0.13	0.18	-0.09	$1.6x10^5$	0.0008
(SD)[2]		(±6.5)	(±5.7)	(±0.05)	(±0.004)	(±0.007)	($\pm 1.3x10^4$)	($\pm 3x10^{-4}$)
2750	RT	-130	-129	0.07	0.22	-0.15	$4.3x10^5$	0.0005
(SD)[2]		(±9.1)	(±13.2)	(±0.01)	(±0.01)	(±0.02)	($\pm 2.1x10^5$)	($\pm 8x10^{-5}$)
2750	60	-187	-186	0.17	0.45	-0.10	$1.9x10^5$	0.001
(SD)[2]		(±2.1)	(±0.35)	(±0.07)	(±0.08)	(±0.02)	($\pm 2.2x10^4$)	(±0.0005)
1018	RT	-689	-651	8.80	0.05	-0.4	$2.3x10^3$	0.071
(SD)[2]		(±12.0)	(±19.9)	(±1.09)	(±0.005)	(±0.09)	(±660.8)	($\pm 8x10^{-3}$)
1018	60	-699	-703	23.8	0.04	-0.22	479.6	0.178
(SD)[2]		(±1.0)	(±11.0)	(±4.0)	(±0.005)	(±0.05)	(±163.4)	(±0.04)

[1] All the potential values are measured vs. SCE. [2] Standard deviation (SD) values.

4.8.1 Galvanic Potential and Galvanic Current Density Measurements

Results of measurements of galvanic current density (i_g) and galvanic potential (E_g) of aged NCAT alloy coupled with the commercial alloys in 0.6 M NaCl solution at RT, 40 °C, and 60 °C are shown in Figures 4.50 and 4.51, respectively. Figures 4.52 – 4.54 show the optical images obtained from each tested couple. As can be seen from Figures 4.50 and 4.51, the galvanic current density is greater while the galvanic potential is lower at higher temperatures. Similar behaviour was reported for other galvanic couples [143-145]. In general, the galvanic current density values for the couples were high initially and decreased over time. The values of galvanic current density for all stainless steel couples (304, 316L and 2750) at RT are relatively low when compared to the values of galvanic current density when aged NCAT alloy was coupled with alloy 1018. This indicates that alloy 1018 was more active in the electrolyte than NCAT.

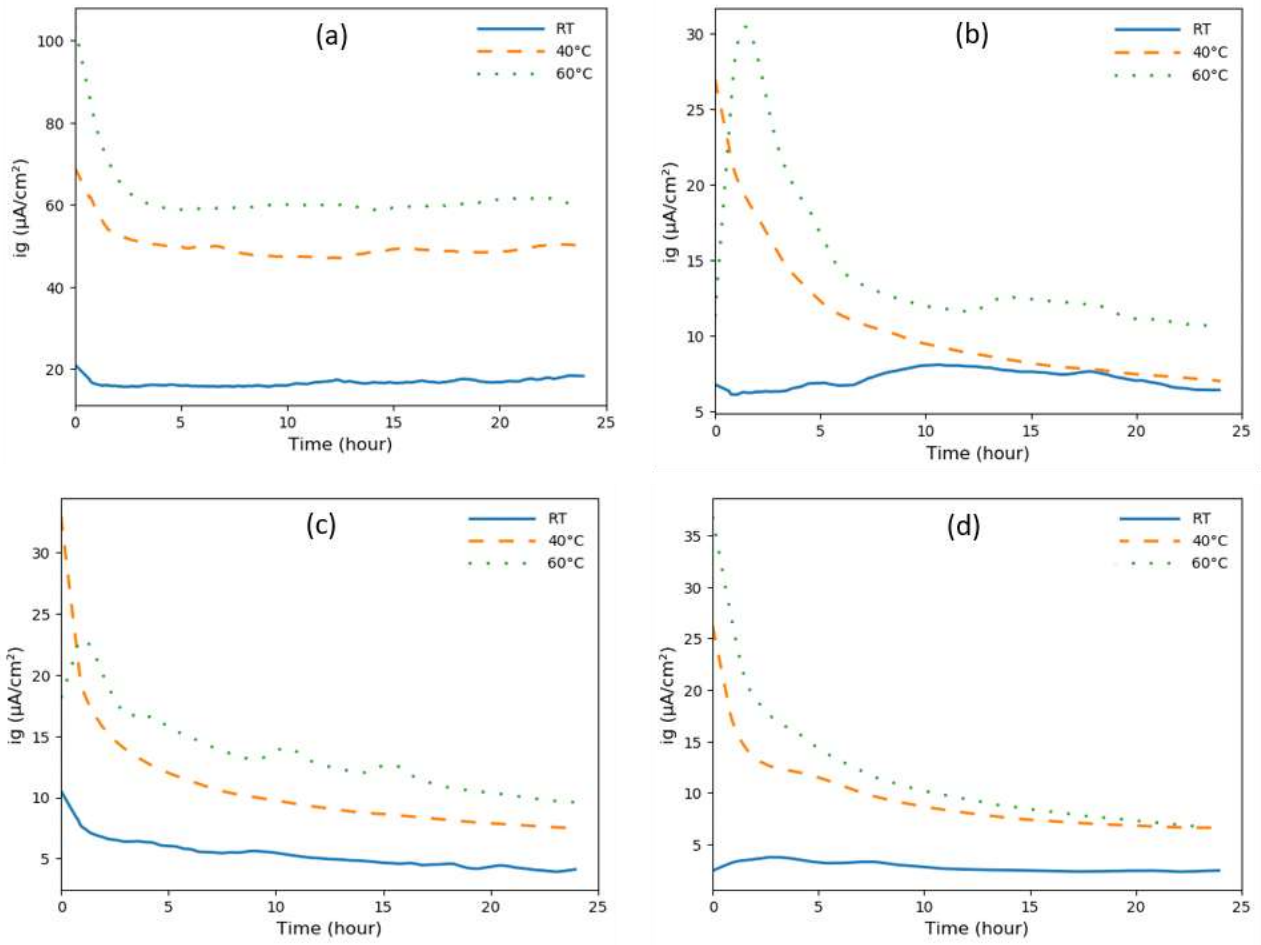

Figure 4.50. Galvanic current densities of NCAT alloy coupled with (a) 1018 carbon steel, (b) 304 stainless steel, (c) 316L stainless steel, and (d) 2750 duplex stainless steel in 0.6 M NaCl solution at a pH of 6 tested at different temperatures. Higher galvanic current density values were observed at higher temperatures.

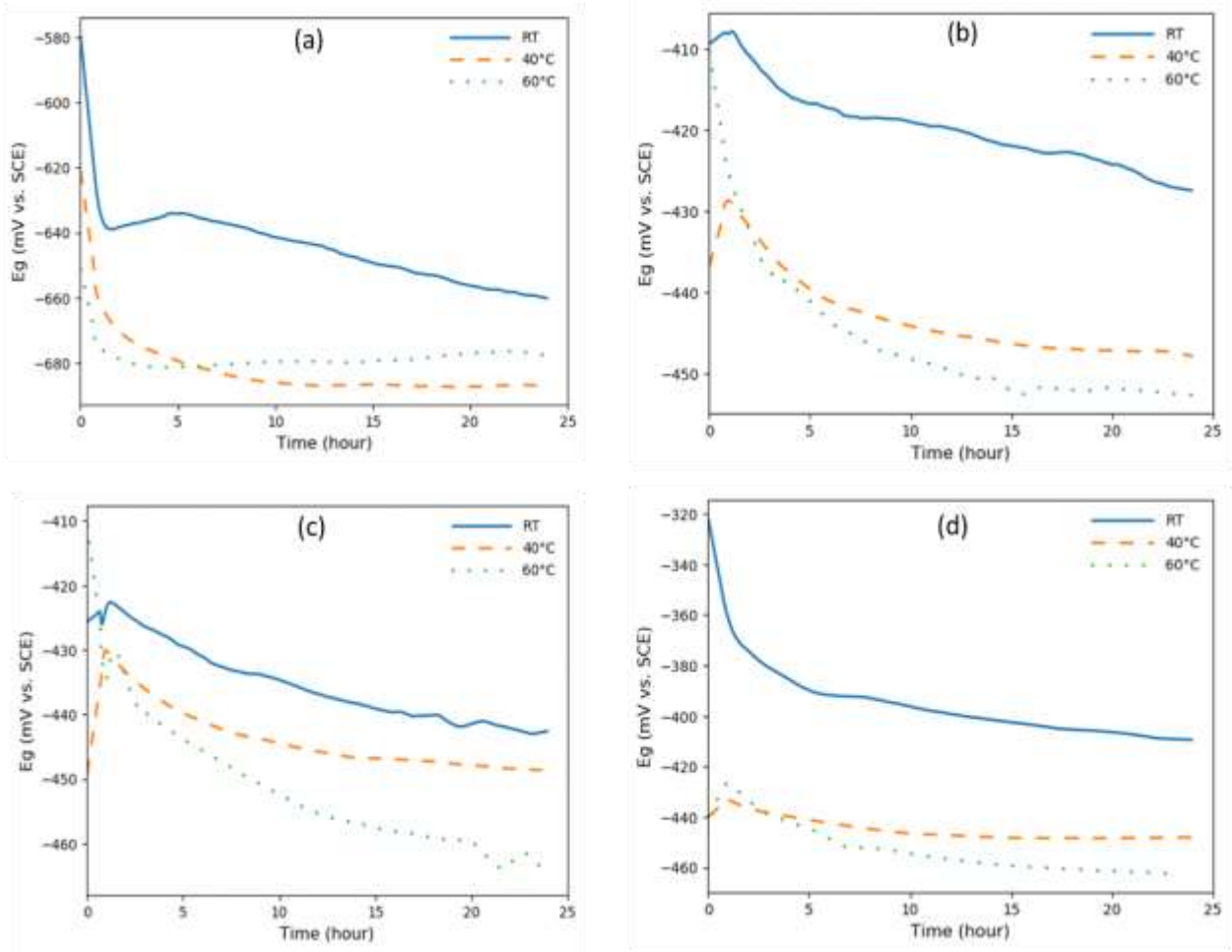

Figure 4.51. Galvanic potential of NCAT coupled with (a) 1018 carbon steel, (b) 304 stainless steel, (c) 316L stainless steel, and (d) 2750 duplex stainless steel in 0.6 M NaCl solution at a pH of 6 tested at three different temperatures. The higher temperature resulted in lower galvanic potential values.

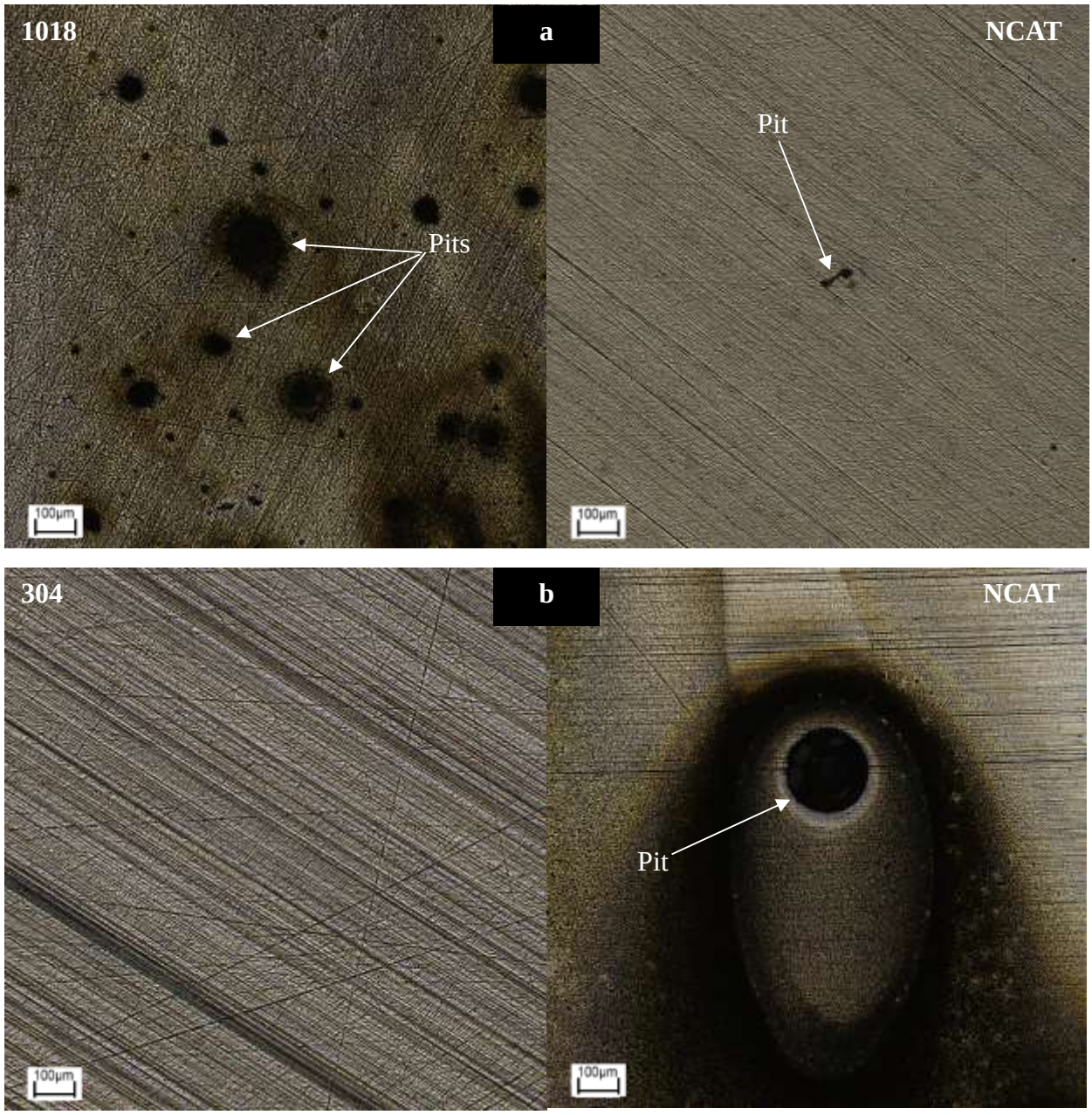

Figure 4.52. Optical micrographs of exposed surfaces of galvanic couples involving aged NCAT alloy with: (a) alloy 1018, (b) alloy 304, (c) alloy 316L, and (d) alloy 2750 after 24 hours of galvanic coupling under full immersion in 0.6 M NaCl solution at RT. NCAT acted as a cathode when coupled with alloy 1018 and as an anode when coupled with the rest of the alloys, where it suffered from pitting and more corrosion than the stainless steel alloys.

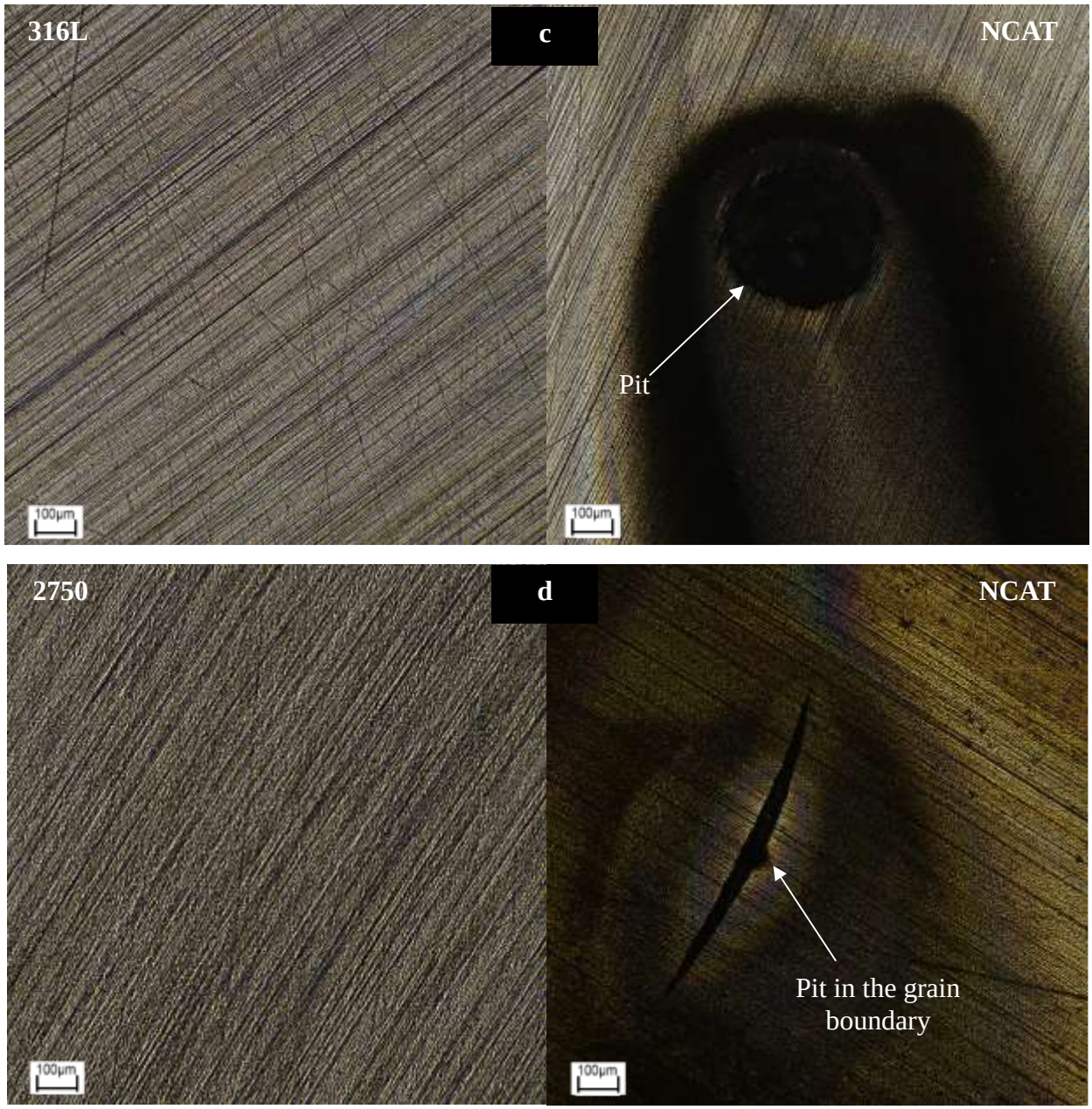

Figure 4.52. Continued.

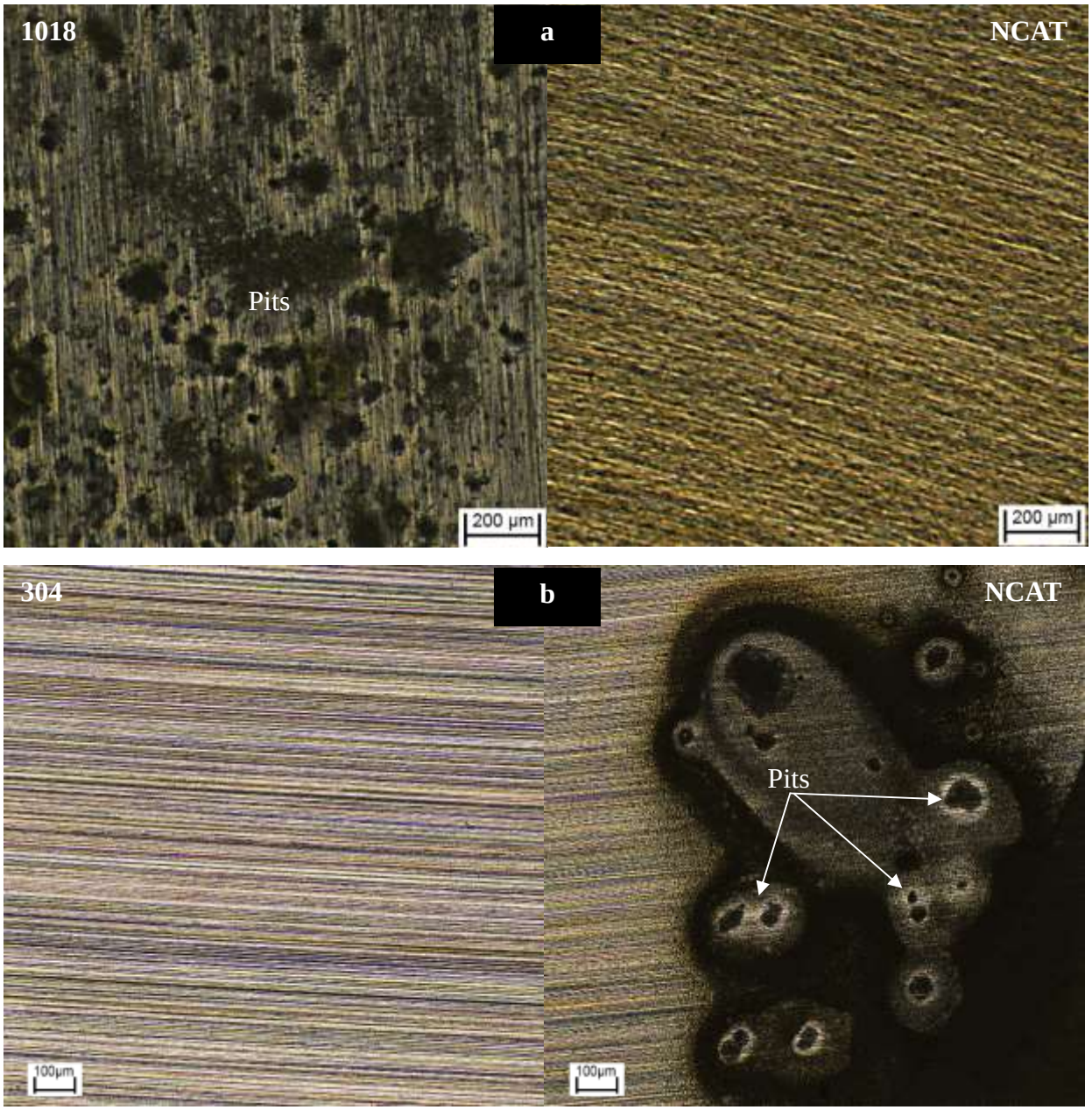

Figure 4.53. Optical micrographs of exposed surfaces of galvanic couples involving aged NCAT alloy with: (a) alloy1018, (b) alloy 304, (c) alloy 316L, and (d) alloy 2750 after 24 hours of galvanic coupling under full immersion in 0.6 M NaCl solution at 40 °C. Bigger pits and larger corroded area are observed at this temperature compared to RT.

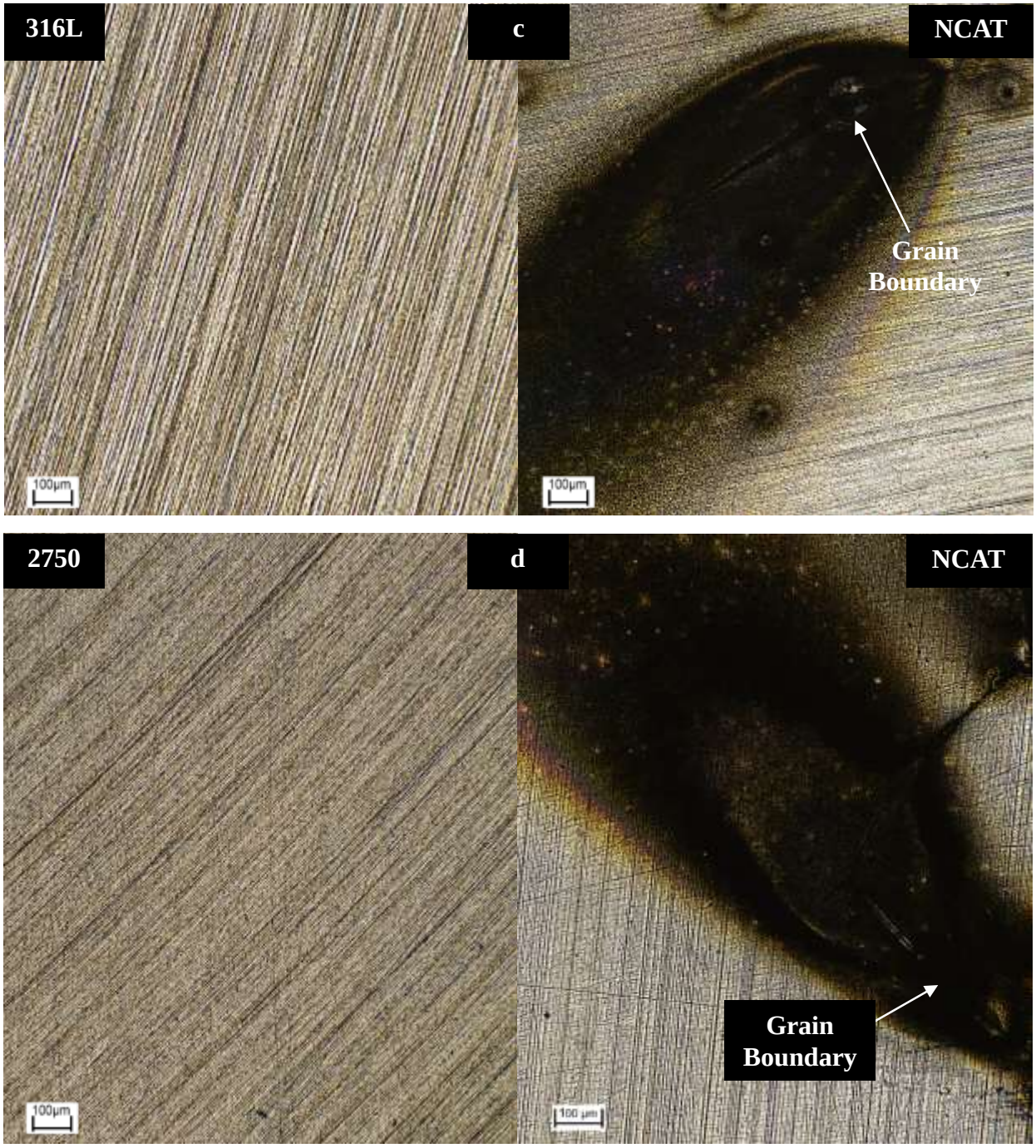

Figure 4.53. Continued.

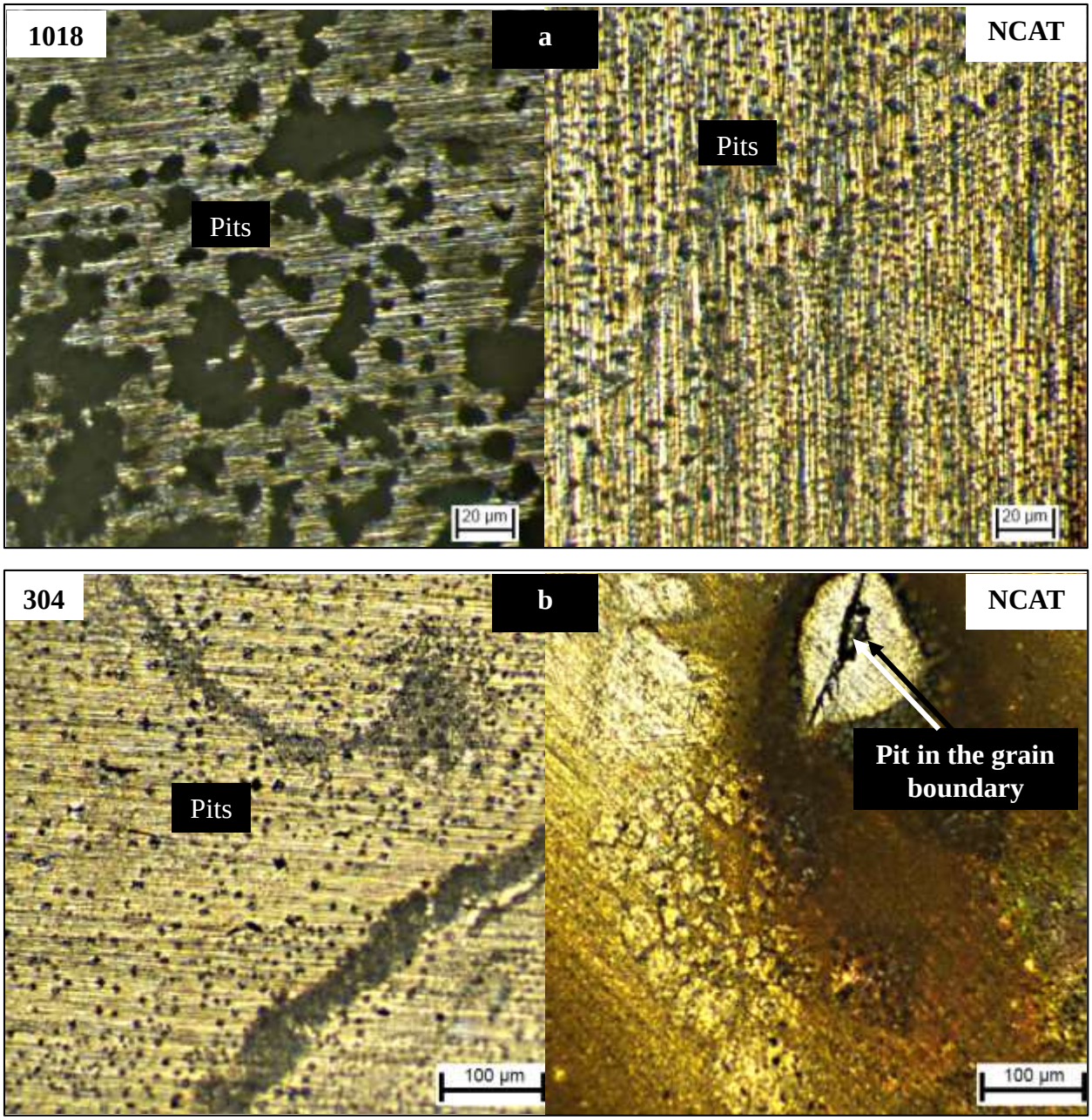

Figure 4.54. Optical micrographs of exposed surfaces of galvanic couples involving aged NCAT alloy with: (a) alloy1018, (b) alloy 304, (c) alloy 316L, and (d) alloy 2750 after 24 hours of galvanic coupling under full immersion in 0.6 M NaCl solution at 60 °C. All the alloys showed pitting and corrosion at this temperature. NCAT showed high corrosion in the couplings with stainless steel alloys, compared to the coupling with alloy 1018.

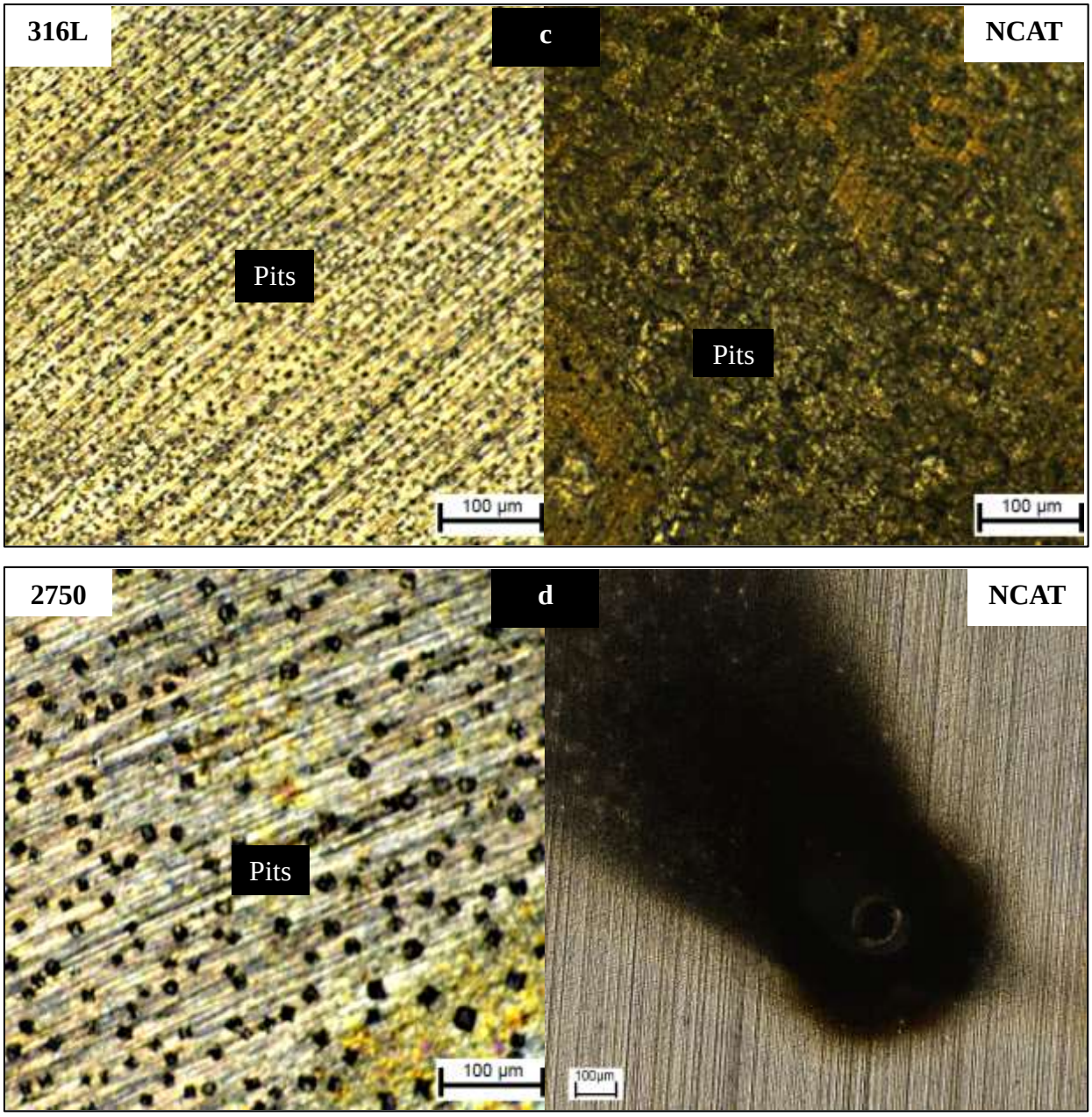

Figure 4.54. Continued.

Since NCAT alloy acted as a cathode when coupled with 1018 carbon steel and as an anode when coupled with the stainless steel alloys, the discussion in this part was divided into two sections: (i) NCAT coupling with stainless steels, and (ii) NCAT coupling with carbon steel. The effect of the coupling in each group is discussed.

4.8.1 NCAT Coupling with Stainless Steels (alloy 304, 316L and 2750)

As can be seen from Figures 4.52 – 4.54, NCAT alloy suffered severe pitting corrosion when coupled to stainless steels. At higher temperatures, the pitting attack became more severe, and the corrosion area became larger than at RT. It was assumed that reduction reactions on the anode are very small [142]. Therefore, the cathodic current was neglected, and only the galvanic current was considered when calculating the galvanic current density.

It is noted that at RT and 40 ^{o}C, no corrosion was detected in the cathodes (stainless steel alloys) as can be seen in Figures 4.52 and 4.53. However, they pitted at 60 ^{o}C as shown in Figure 4.54. This pitting is attributed to the breakdown of the passive protective films on the surfaces of the stainless steels. Pitting was reported at 60 ^{o}C in 304 and 316L austenitic stainless steels [143-145]. The high temperature is believed to boost the breakdown of the protective film. Li *et al.* [140] found the passive film on stainless steels to become more porous and less protective at higher temperatures.

A small fluctuation in the measured current density is seen in the coupling with the austenitic stainless steels (304 and 316L), especially at 60 ^{o}C (see Figure 4.50). Tian *et al.* [144] reported small current transient fluctuations before a stable pit appears. Each of these current transients reflects the formation, growth and repassivation of a metastable pit [144]. Metastable pit growth was found to occur below the pitting potential [146]. Pistrorius [147] stated that all stable pits go through metastable growth stage before stabilizing. It appears that during the first hour of the galvanic corrosion test at 60 ^{o}C, the current density increased considerably, probably due to the initiation of metastable pits, followed by the growth of these pits. After a certain time, the pits growth slowed down as they became stable pits and, as a result, the galvanic current density began to drop gradually [133, 140, 146-150]. The drop of galvanic current density took ~ 4 h, and ~ 1.5 h in the coupling with alloy 304 and 316L, respectively. The galvanic current density eventually stabilized after ~ 20 h and ~ 16.5 h in these couplings (304 and 316L, respectively). Evidence of the corrosion and pitting of 304 and 316L during coupling at 60 ^{o}C can be seen in Figure 4.56 (b and c), where alloy 304 displays larger corroded area when compared to alloy 316L.

Coupling NCAT to alloy 2750 showed very close values of galvanic current density of ~ 7.5 µA/cm^2 near the end of the test at 40 ^{o}C and 60 ^{o}C, when a steady state was reached. This indicates that at 40 ^{o}C and 60 ^{o}C, galvanic corrosion of the alloy was very similar. The micrographs of the couples in Figures 4.53 (d) and 4.54 (d) show no observable pits in alloy 2750 at 40 ^{o}C,

while at 60 ^{o}C, a substantial number of pits can be seen. Upon comparing the micrographs of NCAT alloy coupled to alloy 2750 at 40 ^{o}C and 60 ^{o}C in the same figures, it can be seen that large-sized pits developed in NCAT alloy. This indicates that the galvanic corrosion of NCAT when coupled to alloy 2750 was the main driver for the change in galvanic current density for the couple.

The galvanic potential measurements presented in Figure 4.51 show lower galvanic potentials at higher temperatures. Examination of Figure 4.51 reveals that it was difficult to reach a steady state potential when NCAT alloy was coupled with alloy 316L and alloy 304. According to Mizuno [151], at the start of any galvanic coupling, a transient high potential takes place as a result of the high polarizability of the surface of an initially passive anode (in this case NCAT). This transient is often sufficient to initiate localized corrosion on the surface and allow it to spread [151]. The localized corrosion and pitting can be seen in NCAT SMA coupled with the stainless steels in the micrographs in Figures 4.52 – 4.54. Relatively large pits are observed in these figures. The pits are mostly generated in the grain boundaries that are characterized by precipitates and in the surrounding area. The fluctuation in the coupling current density and potential possibly resulted from the ongoing change in the area fraction of the pitting sites during the galvanic corrosion testing, which in turn affects the polarization characteristics of the anodes.

In the coupling with stainless steels, the mean value of galvanic potential measurements is more negative than one would expect from the open circuit potential and polarization curves of NCAT and these alloys (Figures 4.48 and 4.49). The values are very close to the corrosion potential of an uncoupled NCAT. This indicates that almost all of the anodic reaction took place on NCAT alloy. Since NCAT alloy suffers from intergranular corrosion in the 0.6 M NaCl solution, it is difficult to apply the mixed potential theory on the coupling with NCAT in this solution. Furthermore, it appears from Figure 4.51 that the galvanic potential varied with time, and even after 24 h, a steady-state galvanic potential was not reached in some couplings with stainless steels. These negative values could be due either to a slowing in the kinetic or to an activation of anode kinetics relative to the behaviours illustrated in Figure 4.49 of freshly polished surfaces.

4.8.2.2 NCAT Coupling with Carbon Steel (1018)

As previously stated, when coupled with alloy 1018, NCAT acted as a cathode relative to 1018. The galvanic coupling resulted in shifting the potential of NCAT to more negative values. Similar to couplings with stainless steels, the higher temperatures resulted in greater galvanic current

density, lower galvanic potential, and an increase in the extent of localized corrosion (pitting corrosion) in the anode, as can be seen in Figures 4.52 – 4.54. The coupling with 1018 at RT does not result in a substantial corrosion of the NCAT SMA, but 1018 carbon steel appears to have severe pitting all over the alloy matrix. At RT, the open circuit potential of NCAT is -386 mV vs. (SCE) compared to -689 mV vs. (SCE) for alloy 1018 (see Table 4.13). This large difference in potential causes the severe corrosion and pitting of alloy 1018 when coupled with NCAT SMA.

Figure 4.55 shows SEM micrographs of NCAT alloy coupled with alloy 1018 (a) and coupled with alloy 304 (b) after longer period of galvanic coupling of 75 hours at RT. The longer galvanic coupling period was selected to allow corrosion, pitting initiation and growth to take place on the surface of the tested alloys. It also provided enough time for the galvanic current density and potential to stabilize in the case of the coupling with alloy 304 as can be seen in Figure 4.56. Higher galvanic current density and lower galvanic potential were recorded in the coupling with 1018 when compared to that of the coupling with 304. This means that 1018 experienced more galvanic corrosion in the electrolyte when coupled with NCAT compared to NCAT when coupled with alloy 304. This, as previously mentioned, is due to the large difference between the open circuit potential of alloy 1018 and NCAT SMA compared to the potential difference between NCAT and alloy 304. Furthermore, an appreciable level of fluctuation in galvanic current density and some variation in galvanic potential in the coupling with alloy 1018 was observed every 10 h and 20 h, respectively. The observed fluctuation is an indication that the anode suffered extensive localized corrosion that is characterized by pitting. It also suggests that, over time, there was a discernable change in the area where pitting took place. This, in turn, affected the polarization characteristics of alloy 1018 [142]. Pitting of alloy 1018 in the coupling with NCAT can be seen in the SEM micrographs in Figure 4.55 (a), where a large area of localized corrosion that is characterized by pitting is observed in alloy 1018. NCAT SMA, on the other hand did not show any appreciable corrosion and pitting in Figure 4.55 (a). In contrast, after coupling with alloy 304, NCAT SMA showed remarkable pitting (Figure 4.55 (b)).

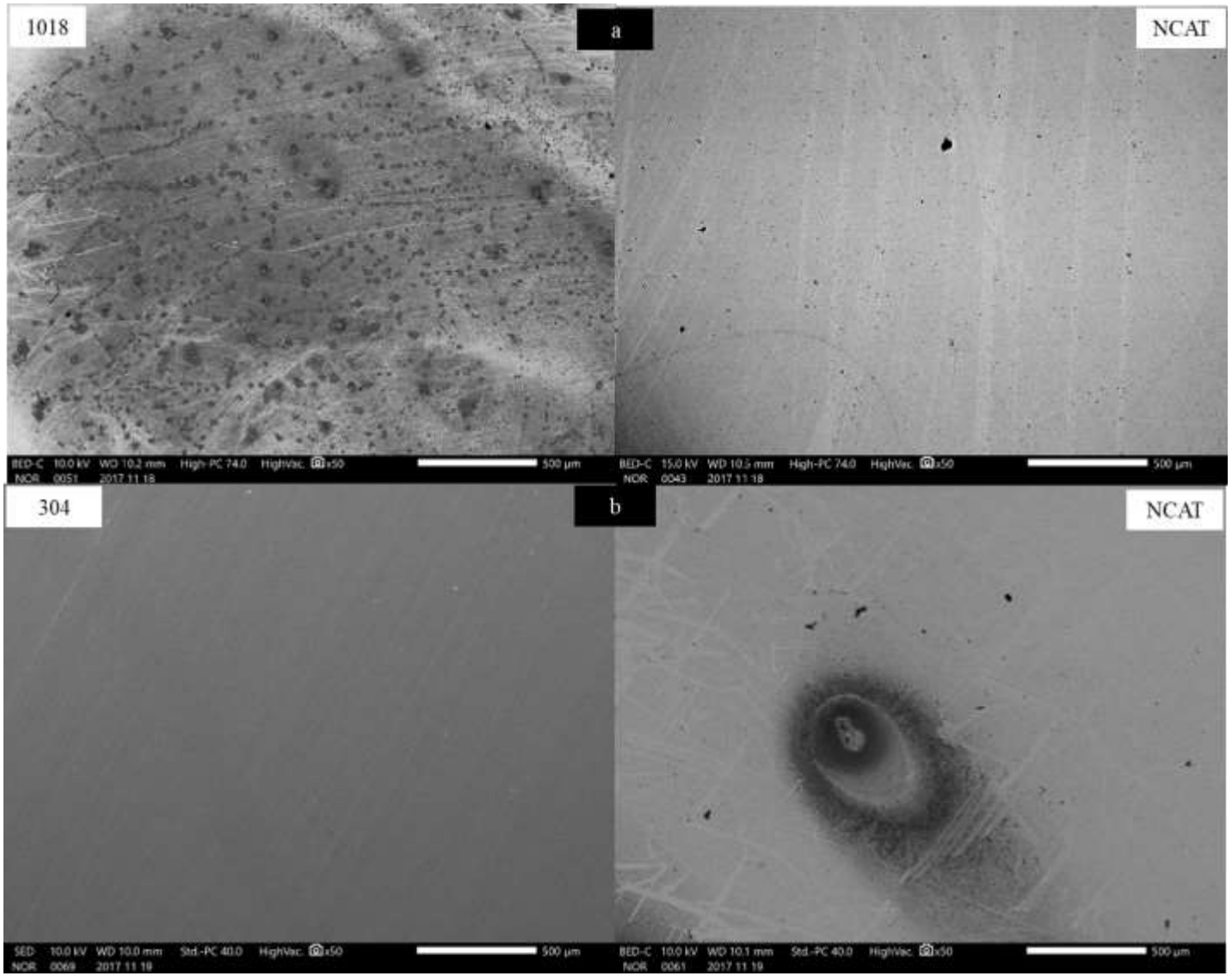

Figure 4.55. SEM micrographs at 50X of galvanic couples involving aged NCAT alloy with: (a) alloy 1018 and (b) alloy 304 after 75 hours of galvanic coupling under full immersion in 0.6 M NaCl solution at RT. Severe pitting is observed in 1018 when coupled with NCAT and a large pit is seen in NCAT when coupled with alloy 304.

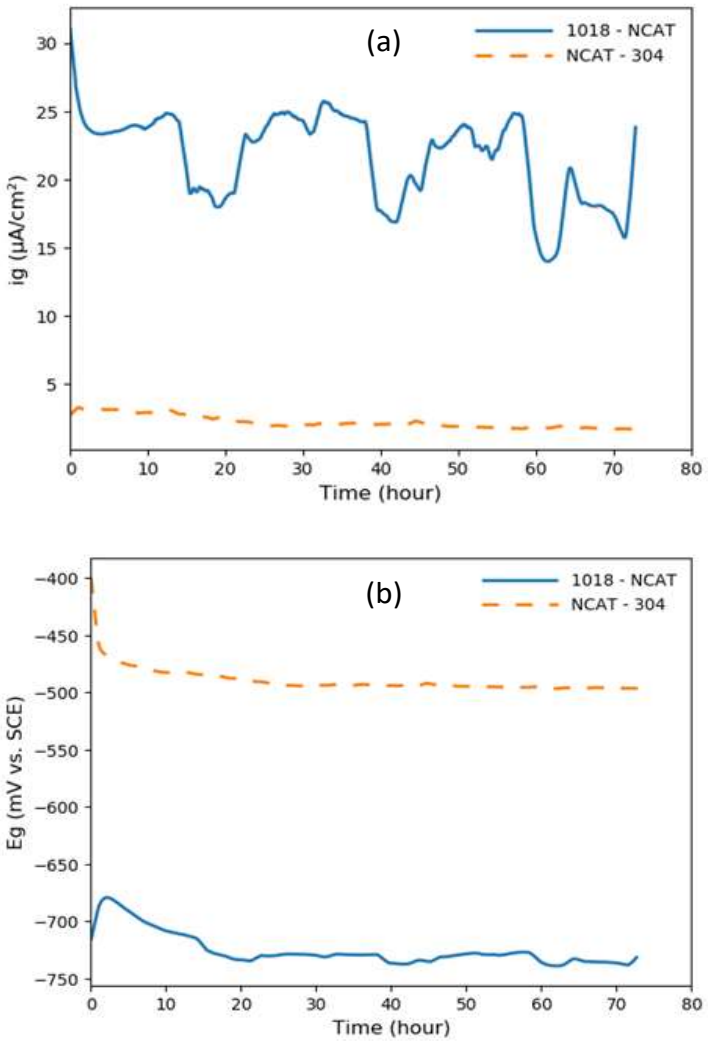

Figure 4.56. (a) Galvanic current densities, and (b) galvanic potentials of NCAT after 75 hours of galvanic coupling with alloy 1018 and alloy 304 in 0.6 M NaCl solution at RT. The coupling with alloy 1018 resulted in higher galvanic current density, and lower galvanic potential. The longer period of coupling allowed the galvanic current density and potential to stabilize in the coupling with alloy 304.

4.8.2 Statistical Analysis of the Galvanic Current Density and Galvanic Potential Data

In this section, a statistical analysis of the electrochemical noise was carried out using the galvanic current density and galvanic potential data that were acquired during the 24 h ZRA tests for couples between NCAT alloy and four commercial alloys. This statistical analysis is used to determine the type of corrosion attack due to the galvanic coupling (localized and/or uniform). The mean values of the galvanic current density (i_{gm}) and those of standard deviation of galvanic current density (σ_{ig}) were calculated. In addition, mean value of the galvanic potential (E_{gm}) and

standard deviation of galvanic potential values (σ_{Eg}) were determined for each couple for each hour of testing. Figures 4.57 and 4.58 show the plots of galvanic current density and galvanic potential, respectively, obtained for each couple at three different temperatures (RT, 40 ^{o}C, and 60 ^{o}C). The error bars are respectively the standard deviation of galvanic current density values (σ_{ig}) and standard deviation of galvanic potential values (σ_{Eg}). It can be seen that higher galvanic current density and standard deviation of galvanic current density were obtained at higher temperatures. Pistorius [147] reported the increase of standard deviation of electrochemical current to be associated with higher rate of nucleation of metastable pits [147]. This indicates that the higher temperatures are associated with the nucleation of these metastable pits in the galvanic couplings.

The standard deviations for corrosion potentials of the couples with 304 and 316L are greater at the higher temperatures, while the mean value of the galvanic potential is more negative at higher temperatures. Legat [152] and Mansfeld [153] found the high values of standard deviation of electrochemical potential to be associated with passivity or localized corrosion rather than corrosion rates. Unmistakably, localized corrosion in the form of pitting of NCAT alloy was dominant during galvanic coupling, and its rate is higher at higher temperature.

The mean current density values were used to calculate the localisation index (LI), which is used to differentiate between localized and uniform corrosion attacks [142]. LI was determined using equation (4.12)

$$\mathrm{LI} = \frac{\sigma \mathrm{i}}{\mathrm{irms}} \tag{4.12}$$

where i_{rms} is the root square mean of the galvanic current density. According to the authors in Ref. 142, LI values up to 0.01 are indicators of uniform corrosion; LI values between 0.01 and 0.1 represent mixed corrosion system; and LI values between 0.1 and 1.0 are associated with localized corrosion.

Although there is an argument that the use of a single statistical index to identify the corrosion mechanism may not be reliable [154], the use of the LI indicator in this study is utilizing the galvanic corrosion test results, and will only be used to provide confirmation to the findings that were obtained by the galvanic corrosion testing. The calculated LI values for the test couples at three temperatures are summarized in Table 4.13. The results show that the corrosion mechanism in aged NCAT alloy in 0.6 M NaCl solution is localized corrosion in the couples with stainless

steels, except for the couple with alloy 304 at RT, where the LI value of 0.094 indicated a mixed corrosion mechanism. The latter is not consistent with the test results and observations after the galvanic corrosion test, where mostly pitting was observed in all the couples with stainless steels. This proves the limitation of the use of this statistical index. One should note that the LI value was very close to the localized corrosion limit for localized corrosion. The couple with alloy1018 showed mixed corrosion mechanism at RT and 40 °C, which is expected from the micrographs of the alloy (Figures 4.52 and 4.53), where pitting and corrosion of the alloy matrix is obvious. At 60 ^{o}C, the LI values for all the couples indicated localized corrosion. This is consistent with the optical micrographs shown in Figure 4.54 and the galvanic current density and galvanic potential measurement analysis in section 4.8.2. Therefore, the results of the statistical analysis of the galvanic current density data are mostly consistent with the galvanic corrosion test results, where localized corrosion took place at the anodes during the coupling, and its rate probability increased with temperature. Future studies that investigate the influence of factors that affect the galvanic corrosion behaviour such as solution concentration and surface condition are recommended. In addition, a study of the galvanic corrosion in atmospheric conditions will be very beneficial if NCAT alloy is going to be used as a pipe coupler.

Table 4.13. Localisation index (LI) calculated from the results of the galvanic corrosion test.

Anode	Cathode	Temp (^{o}C)	Mean Current density (µA/cm^2)	σ_i	i_{rms}	LI	Type of Corrosion
NCAT	304	RT	7.174	0.599	6.426	0.094	Mixed
NCAT	316L	RT	5.296	1.144	4.096	0.279	Localized
NCAT	2750	RT	2.816	0.448	2.471	0.181	Localized
1018	NCAT	RT	16.743	0.843	18.346	0.046	Mixed
NCAT	304	40	10.511	4.129	7.036	0.587	Localized
NCAT	316L	40	10.619	4.054	7.512	0.540	Localized
NCAT	2750	40	9.343	3.382	6.626	0.510	Localized
1018	NCAT	40	49.869	3.468	50.234	0.069	Mixed
NCAT	304	60	14.383	5.009	10.638	0.471	Localized
NCAT	316L	60	13.503	3.238	11.490	0.282	Localized
NCAT	2750	60	10.694	5.133	6.103	0.841	Localized
1018	NCAT	60	61.927	6.841	59.183	0.116	Localized

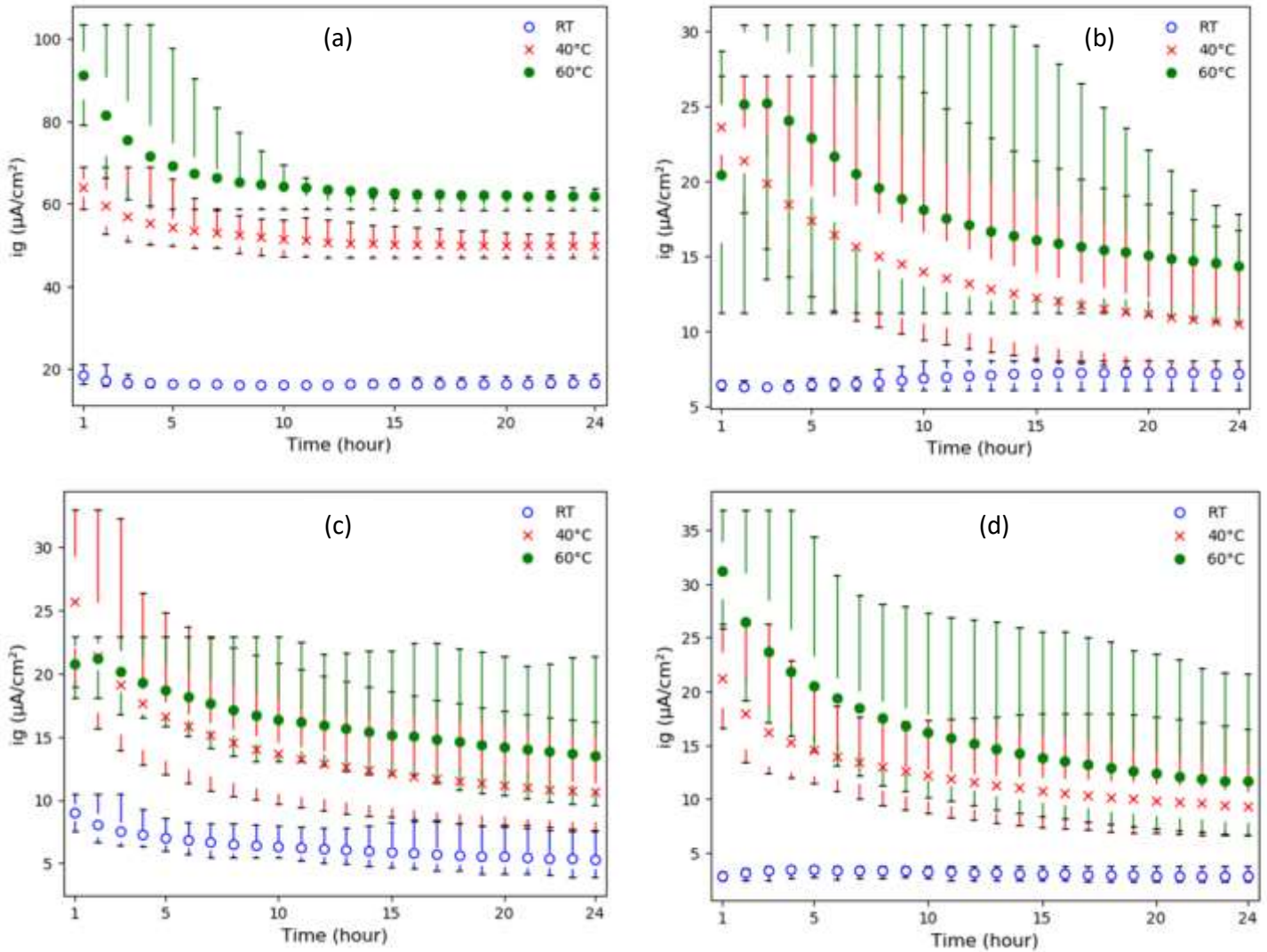

Figure 4.57. Mean values of galvanic current density obtained for galvanic couples of aged NCAT alloy with (a) 1018, (b) 304, (c) 316L, and (d) 2750 during each hour of the galvanic test at RT, 40 °C, and 60 °C. The error bars denote the standard deviations of the mean values.

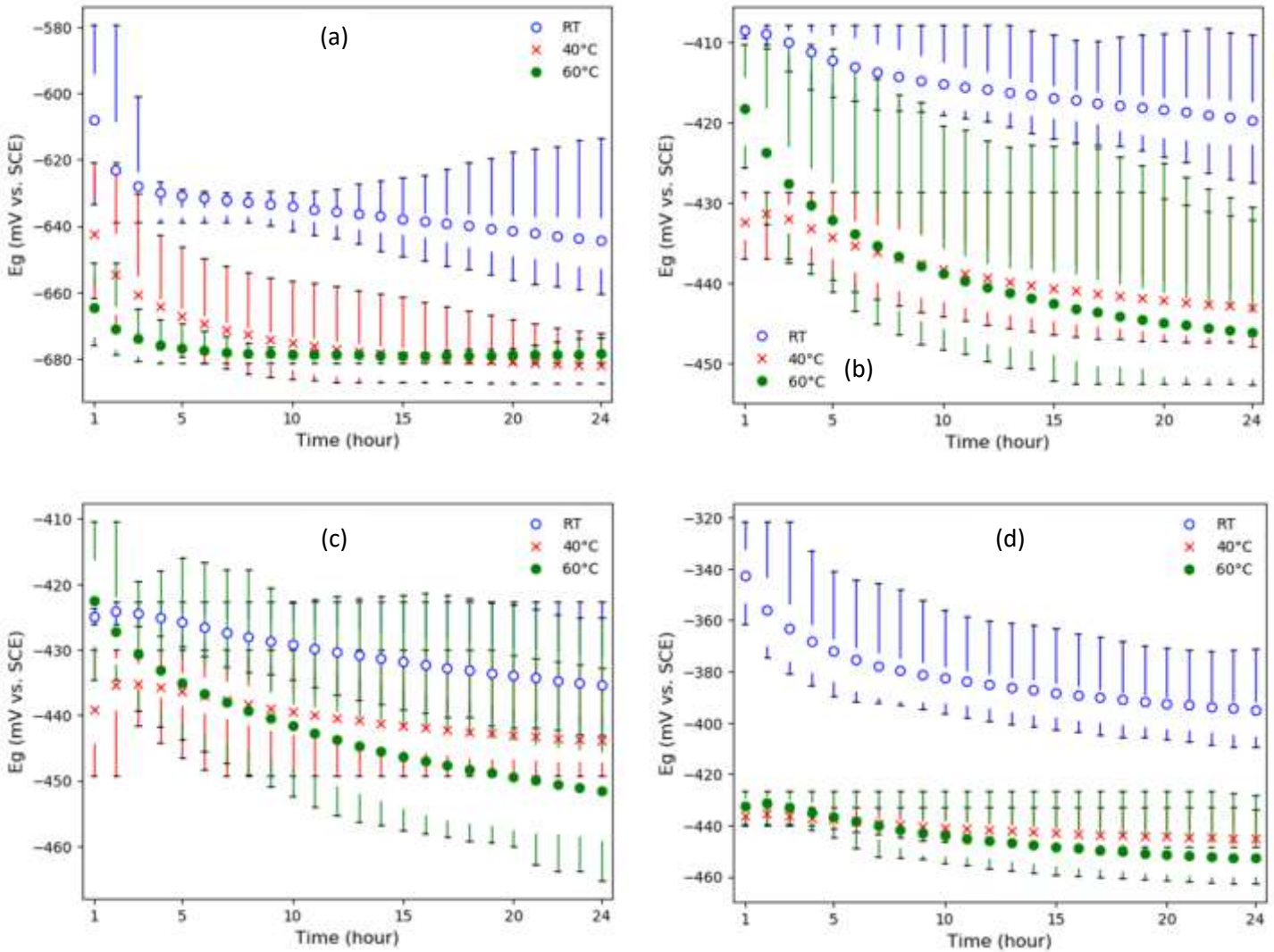

Figure 4.58. Mean values of galvanic potential obtained for galvanic couples of aged NCAT alloy with (a) 1018, (b) 304, (c) 316L, and (d) 2750 during each hour of the galvanic test at RT, 40 ºC, and 60 ºC. The error bars denote the standard deviations of the mean values

5. OVERALL SUMMARY AND CONCLUSIONS

5.1 Summary

This corrosion properties of a newly developed Fe-Ni-Co-Al-Ta shape memory alloy (NCAT SMA) are investigated in this research study to determine the suitability of NCAT SMA for industrial applications in corrosive environments. The alloy was tested in three different corrosion media (0.6 M NaCl, 0.5 M NaOH, and 0.5 M H_2SO_4 solutions) using electrochemical corrosion testing techniques. The results of testing in 0.6 m NaCl solution were compared with those of four commercially available alloys. The effects of heat treatment, solution pH and temperature were also investigated. In addition, the galvanic corrosion behaviour of the NCAT SMA, when coupled to four commercial alloys in a 0.6 M NaCl solution, was studied at three different temperatures. Thjs research study has three main objectives:

The first objective was to determine the forms of corrosion and corrosion properties of NCAT alloy in 0.6 M NaCl solution under different conditions of temperature and pH, and to compare its corrosion properties with four commercial alloys.

The second objective was to determine the galvanic corrosion properties of NCAT alloy when coupled to commercial alloys in 0.6 M NaCl solution at three different temperatures.

The third objective was to study the effect of heat treatment on microstructure and corrosion properties of the alloy. It also included determining the effect of the heat treatment on the corrosion properties of the alloy in 0.6 M NaCl, 0.5 M H_2SO_4, and 0.5 M NaOH.

5.2 Conclusions

On the basis of the experiments and results presented in Chapter 3 and Chapter 4, respectively, the following conclusions are made:

1. NCAT SMA does not passivate in 0.6 M NaCl solution. It has an open circuit potential of -386 mV (vs. SCE), which is higher than that of 1018 carbon steel, but lower than those of 304, 316L, and 2750 stainless steels. At 80 ^oC, NCAT showed high corrosion rate and low open circuit potential compared to other test temperatures.

2. When NCAT was tested in 0.6 M NaCl solution having a pH of 3, its corrosion resistance was low compared to solutions of pH 6. The best corrosion resistance of the alloy was recorded in solutions having a pH of 10.

3. NCAT acted as a cathode when coupled to 1018 carbon steel and as an anode when coupled to stainless steel, where it suffered localized corrosion in the form of pitting. Increasing the test temperature increased the galvanic corrosion of the galvanic couples.

4. Heat treatment caused β phase to precipitate in the grain boundaries, resulting in an elemental chemical segregation in the alloy and caused intergranular corrosion of the alloy in 0.6 M NaCl solution.

5. NCAT showed better corrosion resistance in 0.5 M NaOH compared to 0.6 M NaCl solution. When tested in 0.5 M H_2SO_4, the recorded corrosion rate for NCAT SMA was significantly higher than the corrosion rate recorded for the alloy in the other solutions. The solution treated NCAT showed better corrosion resistance in all the solutions compared to the aged NCAT SMA.

5.3 Recommendations for Future Work

Although a significant number of experiments were conducted to (a) determine the corrosion mechanisms, (b) document the corrosion properties of NCAT SMA in different corrosive media and different conditions, and (c) characterize the corroded surfaces, a gap in the corrosion research of this alloy still exists. Thus, additional future research studies are suggested below:

(1) Aged NCAT alloy suffered intergranular corrosion when tested in 0.6 M NaCl solution. Determining the effect of chloride ions (mainly their concentration in this solution) on the susceptibility of the alloy to intergranular corrosion, and studying the alloy's corrosion behaviour in other chloride containing solutions such as hydrochloric acid, would provide data that could be used to determine the limits for chloride concentrations that cause intergranular corrosion of the alloy.

(2) The aging heat treatment resulted in decreasing the corrosion resistance of NCAT SMA, especially in 0.6 M NaCl solution, by forming grain boundary precipitates. Investigating methods to reduce the formation of grain boundary precipitates would have a significant impact on the use of NCAT SMA in marine and chloride-containing environments. This includes performing electrochemical tests on NCATB SMA, where B has been added to NCAT alloy in order to supress the β precipitates formation in the grain boundaries. Another way to reduce the formation of these grain boundary precipitates is by optimizing

the aging heat treatment. A study of the effect of increasing the aging time on the corrosion rate and open circuit potential of the alloy is recommended.

(3) A study investigating the susceptibility of the alloy to chloride stress corrosion cracking (CSCC) in 0.6 M NaCl solution at RT, and determining the effect of the grain boundary precipitates on the susceptibility of the alloy to CSCC, would be interesting and useful. In order to carry out this test, a production of larger-sized samples would be required, and the use of the slow strain rate test recommended.

(4) The weight loss test could provide reliable information on the corrosion rate of NCAT SMA over a long period of time, and could enable the formation of thicker corrosion product on the surface of the alloy, which could be characterized. This test should be performed mainly in 0.6 M NaCl solution.

(5) Because the alloy's corrosion is in the form of pitting, especially in NaCl and H_2SO_4 solutions, characterization of the pits — which includes measuring the depth of pits using a profilometer, and determining the critical pitting temperature of the alloy using the critical pitting temperature test — would provide valuable information that is needed when selecting the alloy for industrial applications.

REFERENCES

[1] M. Colic, R. Rudolf, D. Stamenkovic, I. Anzel, D. Vucevic, M. Jenko, V. Lazic, G. Lojen. Relationship between microstructure, cytotoxicity and corrosion properties of a Cu-Al-Ni shape memory alloy, *Acta Biomater.* 6 (2010) 308-317.

[2] F. Barrie, Effects of constrained aging on the shape memory response of Nickel rich NiTi shape memory alloys, *M. Sc. Thesis*, TAMU, (2009) 1-4.

[3] J. Wang, N. Li, G. Rao, E. Han, W. Ke, Stress corrosion cracking of NiTi in artificial saliva, *Dent. Mater.* 23 (2006) 133-136.

[4] J. de Salazar, A. Soria, M. I. Barrena, Corrosion behaviour of Cu-based shape memory alloys, diffusion bonded. *J. Alloys Compd.* 387 (2005) 109-114.

[5] J. Wan, X. Huang, S. Chen, T. Y. Hsu, Effect of Nitrogen addition on shape memory characteristics of Fe-Mn-Si-Cr alloy, *Mater. Trans.* 34 (2002) 920-925.

[6] W. Cai, X. Meng, L. Zhao, Recent development of TiNi-based shape memory alloys, *Curr. Opin. Solid Stat. Mater. Sci.* 9 (2005) 296-297.

[7] O. Adiguzel, Smart materials and martensite microstructures in copper based shape memory alloys, *J. Mater. Proc. Tech.* 185 (2007) 120-124.

[8] K. Ullakko, P. G. Yakovenko, V. G. Gavriljuk, New developments in actuator materials as reflected in magnetically controlled shape memory alloys and high-strength shape memory steels, *SPIE* 2715 (1996) 42-50.

[9] A. Sato, E. Chishima, K. Soma, T. Mori, Shape memory effect in $\gamma \rightleftarrows \epsilon$ transformation in Fe-30Mn-1Si alloy single crystals, *Acta metal.* 30 (1982) 1177-1180.

[10] S. Kajiwara. Characteristic features of shape memory effect and related transformation behavior in Fe-based alloys, *Mat. Sci. Eng.* A273-275 (1999) 67-88.

[11] Y.H. Wen, W.L. Xie, N. Li, D. Li. Remarkable difference between effects of carbon contents on recovery strain and recovery stress in Fe-Mn-Si-Cr-Ni-C alloys, *Mater. Sci. Eng.* A 457 (2007) 334-337.

[12] J. C. Li, X. X. Lu, Q. Jiang. Shape memory effects in an Fe14Mn6Si9Cr5Ni alloy for joining pipe, *ISIJ Int*. 40 (2000) 1124-1126.

[13] U. Allenstein, Y. Ma, A. Arabi-Hashemi, M. Zink, S.G. Mayr, Fe-Pd based ferromagnetic shape memory actuators for medical applications: Biocompatibility, effect of surface roughness and protein coatings, *Acta Biomatet.* 9 (2013) 5845-5853.

[14] W. J. Lee, B. Weber, G. Feltrin, C. Czaderski, M. Motavalli, C. Leinenbach. Stress recovery behaviour of an Fe–Mn– Si–Cr–Ni–VC shape memory alloy used for prestressing, *Smart Mater. Struct.* 22 (2013) 1-9.

[15] A. Cladera, B. Weber, C. Leinenbach, C. Czaderski, M. Shahverdi, M. Motavalli, Iron-based shape memory alloys for civil engineering structures: An overview, *Construct. Build. Mater*. 63 (2014) 281-293.

[16] K. Ando, T. Omori, I. Ohnuma, R. Kainuma, K. Ishida, Ferromagnetic to weak-magnetic transition accompanied by bcc to fcc transformation in Fe–Mn–Al alloy, *Appl. Phys. Lett.* 95 (2009) 212504, 1-4.

[17] Y. Tanaka, Y. Himuro, R. Kainuma, Y. Sutou, T. Omori, K. Ishida, Ferrous polycrystalline shape-memory alloy showing huge superelasticity, *Sci.* 327 (2010) 1488-1490.

[18] T. Omori, S. Abe, Y. Tanaka, D. Y. Lee, K. Ishida, R. Kainuma, Thermoelastic martensitic transformation and superelasticity Fe-Ni-Co-Al-Nb-B polycrystalline alloy, *Scr. Mater.* 69 (2013) 812-815.

[19] Y. Geng, D. Lee, X. Xu, M. Nagasako, M. Jin, X. Jin, T. Omori, R. Kainuma, Coherency of ordered ϒ’ precipitates and thermoelastic martensitic transformation in FeNiCoAlTaB alloy, *J. Alloys Compd.* 628 (2015) 287-292.

[20] T. Maki, K. Kobayashi, M. Minato, I. Tamura, Thermoelastic martensite in an ausaged Fe-Ni-Ti-Co alloy, *Scr. Metall.* 18 (1984) 1105-1109.

[21] V. V. Kokorin, Yu. I. Samsonov, V. A. Cherneko, O. M. Shevchenko, Superelasticity in Fe-Ni-Co-Ti alloy, *Phys. Met. Metall.* 67 (1989) 202-204.

[22] J. Ma, B. Kockar, a. Evirgen, I. Karaman, Z.P. Luo, Y.I. Chumlyakov, Shape memory behavior and tension-compression asymmetry of a FeNiCoAlTa single-crystalline shape memory alloy, *Acta Mater.* 60 (2012) 2186-2195.

[23] I.V. Kireeva, Yu.I. Chumlyakov, V.A. Kirillov, I. Karaman, E. Cesari, Orientation and temperature dependence of superelasticity caused by reversible γ-α' martensitic transformations in FeNiCoAlTa single crystals, *Tech. Phys. Lett.* 37 (2011) 487-490.

[24] A. Evirgen, J. Ma, I. Karaman, Z.P. Luo, Y.I. Chumlyakov, Effect of aging on the superelastic response of a single crystalline FeNiCoAlTa shape memory alloy, *Scr. Metar.* 67 (2012) 475-478.

[25] Y.I. Chumlyakov, I.V. Kireeva, I.V. Kretinina, K.S. Keinikh, O.A. Kuts, V.A. Kirillov, I. Karaman, H. Maier, Shape memory effect and superelasticity in the [001] single crystals of a FeNiCoAlTa alloy with ϒ-α'-thermoelastic martensitic transformations, *Russ. Phys. J.* 56 (2013) 920-929.

[26] P. Kroob, M.J. Holzweissig, T. Niendorf, C. Somsen, M. Schaper, Y.I. Chumlyakov, H.J. Maier, Thermal cycling behavior of an aged FeNiCoAlTa single-crystal shape memory alloy, *Scr. Mater.* 81 (2014) 28-31.

[27] P. Kroob, C. Somsen, T. Niendorf, M. Schaper, I. Karaman, Y. Chumlyakov, G. Eggeler, H.J. Maier, Cyclic degradation mechanisms in aged FeniCoAlTa shape memory single crystals, *Act. Mater.* 79 (2014) 126-137.

[28] A. Ölander, An electrochemical investigation of solid cadmium-gold alloys, *J. Am. Chem. Soc*. 54 (1932) 3819-3833.

[29] W. J. Buehler, J. V. Gilfrich, R. C. Wiley, Effects of low-temperature phase changes on the mechanical properties of alloys near composition TiNi, *Journal of Applied Physics*. 34 (1963) 1475-1477.

[30] D. C. Lagoudas, Shape memory alloys: Modeling and engineering applications, Springer (2008) USA.

[31] K. Otsuka, X. Ren, Physical metallurgy of Ti–Ni-based shape memory alloys, *Prog. Mater. Sci*. 50 (2005) 511-678.

[32] S. Kajiwara, D. Liu, T. Kikuchi, N. Shinya, Remarkable improvement of shape memory effect in Fe-Mn-Si based shape memory alloys by producing NbC precipitates, *Scri. Mater.* 44 (2001) 2809-2814.

[33] T. Maki, I. Otsuka, C.M. Wayman, Ferrous shape memory alloys, *Shape Mem. Mater. Cambridge University Press* (1998) 117-132.

[34] T. Duerig, A. Pelton, d. Stockel, An overview of nitinol medical applications, *Mater. Sci. Eng*. A 273-275 (1999) 149-160.

[35] J. Guilemany, J. Fernandez, Relationships between structure and hardness developed during the high temperature ageing of a smart Cu-based alloy, *J. Mater. Sci.* 31 (1996) 4981-4984.

[36] K. Otsuka, X. Ren, Recent developments in the research of shape memory alloys, *Intermet.* 7 (1999) 525-526.

[37] M. Chentouf, M. Bouabdallah, J. Gachon, E. Patoor, A. Sari, Microstructural and thermodynamic study of hypoeutectoidal Cu–Al–Ni shape memory alloys, *J. Alloys Compd*. 470 (2009) 507-513.

[38] H. C. Lin, K. M. Lin, C. S. Lin, T. M. Ouyang, The Corrosion behavior of Fe-based shape memory alloys, *Corros. Sci.* 44 (2002) 2013-2026.

[39] Z. Dong, S. Kajiwara, T. Kikuchi, N. Shinya. High-corrosion-resistance Fe-Mn-Si-based alloys exhibiting nearly perfect shape memory effects, *SPIE*, 5387 (2004) 294-300.

[40] H. Peng, Y. Wen, B. Ye, N. Li, Influence of ageing after pre-deformation on shape memory effect in a FeMnSiCrNiC alloy with 13 wt% Cr content, *Mater. Sci. Eng*, A504 (2009) 36-39.

[41] O. Soderberg, X.W. Liu, P.G. Yakovenko, K. Ullakko, V.K. Lindroos, Corrosion behaviour of Fe-Mn-Si based shape memory steels trained by cold rolling, *Mater. Sci. Eng. A***.** 273-275 (1999) 543-548.

[42] A. Charfi, T. Bouraoui, M. Feki, C. Bradai, B. Normand. Surface treatment and corrosion behaviour of Fe–32Mn–6Si shape memory alloy, *C. R. Chimie*. 12 (2009) 270-275.

[43] F. Terwinghe, J. Celis, J. Roos, Stress corrosion susceptibility of beta aluminium brasses-II, *Br. Corros. J.* 19 (1984) 115-119.

[44] D. Z. Liu, D. F. Wang, W. Y. Ji, W. X. Liu, Study of Fe-Mn-Si-Re alloy pipe coupling, *2nd Int. Conf. on Shape Mem. Superelast. Tech., SMST-97* (1997) 329-334.

[45] B. C. Maji, C. M. Das, M. Krishnan, R. K. Ray, The corrosion behaviour of Fe-15Mn-7Si-9Cr-5Ni shape memory alloy, *Corros. Sci.* 48 (2006) 937-949.

[46] H. Bao-quan, B. Pei-kang, D. Zhi-zhong, C. Jun, Effect of Cu addition on corrosion resistance and shape memory effect of Fe-14Mn-5Si-9Cr-5Ni Alloy, *Trans. Nonfr. Metal. Soc. China*. 19 (2009) 149-153.

[47] Q. Sun, R. Matsui, K. Takeda, E. A. Pieczyska, Advances in shape memory materials, Springer (2017) Switzerland.

[48] J. Pena, F. Gil, J. Guilemany, Effect of microstructure on dry sliding wear behaviour in CuZnAl shape memory alloys, *Acta Mater.* 50 (2002) 3115-3124.

[49] J. Fernandez, X. Zhang, J. Guilemany, A one-cycle training technique for copper-based shape memory alloys, *J. Mater. Proc. Tech.* 139 (2003) 117-119.

[50] T. Omori, K. Watanabe, R. Y. Umetsu, R. Kainuma, K. Ishida, Martensitic transformation and magnetic field-induced strain in Fe–Mn–Ga shape memory alloy, *App. Phys. Lett*. 95 (2009) 082508, 1-3.

[51] W. Zhu, E.K. Liu, L. Feng, X.D. Tang, J.L. Chen, G.H. Wu, H.Y. Liu, F.B. Meng, H.Z. Luo, Magnetic-field-induced transformation in FeMnGa alloys, *Appl. Phys. Let*. 95 (2009) 222512, 1-3.

[52] T. Omori, K. Ando, M. Okano, X. Xu, Y. Tanaka, I. Ohnuma, R. Kainuma, K. Ishida, Superelastic effect in polycrystalline ferrous alloys, Sci. 333 (2011) 68-72.

[53] Y. N. Koval, G. E. Monastyrsky, Reversible martensite transformation and shape memory effect in Fe-Ni-Nb alloys, *Sc. Matell. Mater*. 28 (1993) 41-46.

[54] S. Kajiwara, Nearly perfect shape memory effect in Fe-Ni-C alloys, *Trans. Jpn. Inst. Met.* 26 (1985) 595-596.

[55] Yu. I. Chumlyakov, I. V. Kireeva, E. Yu. Panchenko, E. G. Zakharova, V. A. Kirillov, S. P. Efimenko, H. Sehitoglu, Shape memory effects in FeNiCoTi single crystals undergoing $\gamma \leftrightarrow \alpha'$ thermoelastic martensitic transformations, *Dokl. Phys.* 94 (2004) 74-50.

[56] S. Kobayashi, Y. Ohgoe, K. Ozeki, K. Sato, T. Sumiya, K. Hirakuri, H. Aoki, Diamond-like carbon coatings on orthodontic archwires. *Diamond Relat. Mater.* 14 (2005) 1094-1097.

[57] D. C. Lagoudas, Shape memory alloys: modeling and engineering applications, *Springer* (2010) USA.

[58] M. Leary, S. Huang, T. Ataalla, A. Baxter, A. Subic, Design of shape memory alloy actuators for direct power by an automotive battery, *Mater. Desig*. 43 (2013) 460-466.

[59] J. Mohd Jani, S. Huang, M. Leary, A. Subic, Analysis of convective heat transfer coefficient on shape memory alloy actuator under various ambient temperatures with finite difference method, *Appl. Mech. Mater*. 736 (2015) 127-133.

[60] J. Mohd Jani, S. Huang, M. Leary, A. Subic, Numerical modeling of shape memory alloy linear actuators, *Compu. Mech.* 56 (2015) 443-461.

[61] L. Medawar, P. Rocher, J. Hornez, M. Traisnel, J. Breme, H. Hildebrand, Electrochemical and cytocompatibility assessment of NiTiNOL memory shape alloy for orthodontic use, *Biomolec. Eng.* 19 (2002) 153-159.

[62] P. Rocher, L. El Medawar, J. Hornez, M. Traisnel, J. Breme, H. Hildebrand, Biocorrosion and cytocompatibility assessment of NiTi shape memory alloys, *Scri. Mater.* 50 (2004) 255-260.

[63] D. Starosvetsky, I. Gotman, Corrosion behavior of titanium nitride coated Ni-Ti shape memory surgical alloy, *Biomater.* 22 (2001) 1853-1858.

[64] G. Rondelli, B. Vicentini, Effect of copper on the localized corrosion resistance of Ni-Ti shape memory alloy, *Biomater.* 23 (2002) 639-643.

[65] G. Rondelli, Corrosion resistance tests on NiTi shape memory alloy, *Biomater.* 17 (1996) 2003-2007.

[66] W. J. Lee, R. Partovi-Nia, T. Suter, C. Leinenbach, Electrochemical characterization and corrosion behavior of an Fe-Mn-Si shape memory alloy in simulated concrete pore solutions, *Mater. Corro*. 67 (2016) 839-846.

[67] L. Janke, C. Czaderski, M. Motavalli, J. Ruth, Applications of shape memory alloys in civil engineering structures - Overview, limits and new ideas, materials and structures, *Mater. Struct*. 38 (2005) 578-592.

[68] E. Choi, Y. S. Chung, J. H. Choi, H. T. Kim, H. Lee, The confining effectiveness of NiTiNb and NiTi SMA wire jackets for concrete, *Smart. Mater. Struct.* 19 (2010) 035024, 1-8.

[69] A. K. Maji, I. Negret, Smart prestressing with shape memory alloy, *J. Eng. Mech*. 124 (1998) 1121, 1-8.

[70] C. Czaderski, B. Hahnebach, M. Motavalli, RC beam with variable stiffness and strength, *Constr. Build. Mater*. 20 (2006) 824-833.

[71] T. Sohmura, R. Oshima, F. E. Fujita, Thermoelastic FCC-FCT martensitic transformation in Fe-Pd alloy, *Scr. Metall.* 14 (1980) 855-856.

[72] T. Iwamoto, K. Fujita, An experimental study on rate-sensitive tensile deformation behaviour of Fe-based shape memory alloy, *MATEC Web of Conferences*. 33 (2015) 04003, 1-6.

[73] K. Tsuzaki, M. Ikegami, Y.Tomota, T. Maki, Effect of transformation cycling on the ε martensitic transformation in Fe-Mn alloys, *ISIJ*. 30 (1990) 666-669.

[74] B. Jiang, X. Qi, W. Zhou, Z. Xi, T. Hsu, The effect of nitrogen on shape memory effect in Fe-Mn-Si alloys, *Scri. Metall. Mater.* 34 (1996) 1437-1441.

[75] H. Otsuka, H. Yamada, T. Maruyama, H. Tanahashi, S. Matsuda, M. Murakami, Effects of Alloying Additions on Fe-Mn-Si Shape Memory Alloys, *ISIJ Int.* 30 (1990) 674-679.

[76] S. Kajiwara, D. Liu, T. Kikuchi, N. Shinya, Development of Fe–Mn–Si based shape memory alloys with no necessity of 'training', *J. Phys. IV France* 11 (2001) 199-204.

[77] A. Baruj, S. Kajiwara, T. Kikuchi, N. Shinya, Effect of pre-deformation of austenite on shape memory properties in Fe-Mn-Si based alloys containing Nb and C, *Mater. Trans.* 43 (2002) 585-588.

[78] A. Baruj, T. Kikuchi, S. Kajiwara, N. Shinya, Improvement of shape memory properties of NbC containing Fe–Mn–Si based shape memory alloys by simple thermomechanical treatments, *J. Mater. Sci. Eng.* A378 (2004) 333-336.

[79] A. Baruj, T. Kikuchi, S. Kajiwara, TEM observation of the internal structures in NbC containing Fe–Mn–Si-based shape memory alloys subjected to pre-deformation above room temperature, *J. Mater. Sci. Eng.* A378 (2004) 337-342.

[80] A. Baruj, T. Kikuchi, S. Kajiwara, N. Shinya, Improved shape memory properties and internal structures in Fe-Mn-Si-based alloys containing Nb and C, *J. Phys. IV France* 112 (2003) 373-376.

[81] Z. Dong, S. Kajiwara, T. Kikuchi, T. Sawaguchi, Effect of pre-deformation at room temperature on shape memory properties of stainless type Fe–15Mn–5Si–9Cr–5Ni–(0.5–1.5)NbC alloys, *Acta Mater.* 53 (2005) 4009-4018.

[82] N. Stanford, D. Dunne, H. Li, Re-examination of the effect of NbC precipitation on shape memory in Fe–Mn–Si-based alloys, *Scri. Mater.* 58 (2008) 583-586.

[83] Y.H. Wen, L.R. Xiong, N. Li, W. Zhang, Remarkable improvement of shape memory effect in an Fe-Mn-Si-Cr-Ni-C alloy through controlling precipitation direction of Cr23C6, *Mater. Sci. Eng.* A 474 (2008) 60-63.

[84] Z.Z. Dong, U.E. Klotz, C. Leinenbach, A. Bergamini, C. Czaderski, M. Motavalli, A novel Fe-Mn-Si shape memory alloy with improved shape recovery properties by VC precipitation, *Adv. Eng. Mater*. 11 (2009) 40-44.

[85] H. Kubo, K. Nakamura, S. Farjami, T. Maruyama, Characterization of Fe-Mn-Si-Cr shape memory alloys containing VN precipitates, *Mater. Sci. Eng. A*. 378 (2004) 343-348.

[86] S. Farjami, K. Hiraga, H. Kubo, Crystallography and elastic energy analysis of VN precipitates in Fe-Mn-Si-Cr shape memory alloys, *Acta mater*. 53 (2005) 419-431.

[87] B. C. Maji, M. Krishnan, M. Sujata, Gouthama, R. K. Ray, Effect of Co Addition on the Microstructure, Martensitic Transformation and Shape Memory Behavior of Fe-Mn-Si Alloys, *Metall. And Mater. Trans. A*. 44A (2013) 172-185.

[88] K. M. Lin, J. H. Chen, C. C. Lin, C. H. Liu, H. C. Lin, Optimization of shape-memory effect in Fe-Mn-Si-Cr-Re shape-memory alloys, *Jr. Mater. Eng. Perform*. 23 (2014) 2327-2332.

[89] W. Zhou, B. Jiang, X. Qi, T. Hsu, The influence of rare earth element on shape memory effect in Fe-Mn-Si alloys, *Scripta Metall. Mater.* 39 (1998) 1483-1487.

[90] V.V. Bliznuk, V.G. Gavriljuk, B.D. Shanina, A.A. Konchits, S.P. Kolesnik, Effect of Nitrogen and Carbon on electron exchange and shape memory in a Fe-Mn-Si base shape memory alloy, *Acta Mater.* 51 (2003) 6095-6103.

[91] M. Koyama, T. Sawaguchi, K. Tsuzaki, Microstructure characteristics and its effect on mechanical and shape memory properties in a Fe-17Mn-8Si-0.3C alloy, *Jr. Alloy. Compd*. 15 (2013) 15-19.

[92] B. C. Maji, M. Krishnan, Role of Si in improving the shape recovery of FeMnSiCrNi shape memory alloys, *Phy. Proced.* 10 (2010) 111-116.

[93] R. A. Shakoor, F. A. Khalid, K. Kang, Role of samarium addition on the shape memory behavior of Iron based alloys, *Mat. Sci. Eng. A* 528 (2011) 2299-2302.

[94] H. Sehitoglu, C. Efstathiou, H. J. Maier, Y. Chumlyakov, Magnetization, shape memory and hysteresis behavior of single and polycrystalline FeNiCoTi, *J. Magn. & Magn. Mater*. 292 (2005) 89-99.

[95] H. Sehitoglu, C. Efstathiou, H. J. Maier, Y. Chumlyakov, Hysteresis and deformation mechanisms of transforming FeNiCoTi, *Mech. Mater.* 38 (2006) 538-550.

[96] H. Sehitoglu, I. Karaman, X. Y. Zhang, Y. Chumlyakov, H. J. Maier, Deformation of FeNiCoTi shape memory single crystals, *Script. Mater*. 44 (2001) 779-784.

[97] Y. Liu, Z. Dong, L. Yu, Y. Liu, H. Li, Influence of aging on shape memory effect and corrosion resistance of a new Fe-Mn-Si-based alloy, *Jr Mater. Resear.* 30 (2015).179-185.

[98] K. Yamauchi, *I. Ohkata, K. Tsuchiya, S. Miyazaki,* Shape memory and superelastic alloys, *Woodhead Publishing Limited* (2011) USA.

[99] Y. Furuya, N. H. Hagood, P. Kimura, T. Watanabe, Shape memory effect and magnetostriction in rapidly solidified Fe-29.6 at %Pd alloy, *Mater. Trans.* 39 (1998) 1248-1254.

[100] R. Desroches, B. J. Smith, Shape memory alloys in seismic resistant design and retrofit: A critical review of their potential and limitations, *Earthq Eng.* 8 (2004) 415-492.

[101] I. Karaman, B. Basaran, H. E. Karaca, A. I. Karsilayan, Y. I. Chumlyakov, Energy harvesting using martensite variant reorientation mechanism in a NiMnGa magnetic shape memory alloy, *App. Phys. Lett*. 90 (2007) 172505, 1-3.

[102] I. V. Kireeva, Yu. I. Chumlyakov, V. A. Kirillov, I. V. Kretinina, Yu. N. Danil'son, I. Karaman, E. Cesari, Thermoelastic ϒ – α'-martensitic transformations in FeNiCoAlTa aging single crystals, *Russ. Phys. Jour*. 53 (2011) 1103-1106.

[103] J. Ma, B.C. Hornbuckle, I. Karaman, G.B. Thompson, Z.P. Luo, Y.I. Chumlyakov, The effect of nano-precipitates on superelastic properties of FeNiCoAlTa shape memory alloy single crystals, *Acta Mater*. 61 (2013) 3445-3455.

[104] J. Ma, I. Karaman, Materials science: Expanding the repertoire of shape memory alloys, *Science*. 327 (2010) 1468-1469.

[105] Y. Geng, M. Jin, W. Ren, W. Zhang, X. Jin, Effects of aging treatment on martensitic transformation of Fe-Ni-Co-Al-Ta-B alloys, *J. Alloys Compd*. 577 (2013) S631-S365.

[106] P. Kroob, T. Niendorf, I. Karaman, Y. Chumlyakov, H. J. Maier, Cyclic deformation behavior of aged FeNiCoAlTa single crystals, *Funct Mater Lett*. 5 (2012)1250045, 1- 4.

[107] Y. I. Chumlyakov, I. V. Kireeva, E. Y. Panchenko, V. A. Kirillov, E. E. Timofeeva, I. V. Kretinina, Y. N. Danilson, I. Karaman, H. Maier, E. Cesari, Thermoelastic martensitic transformations in single crystals with disperse particles, *Russ. Phys. J*. 54 (2012) 937-950.

[108] C. Efstathiou, H. Sehitoglu, A. J. W. Johnson, R. F. Hamilton, H. J. Maier, Y. Chumlyakov, Large reduction in critical stress in Co–Ni–Al upon repeated transformation, *Scr. Mater.* 51 (2004) 979-985.

[109] T. Niendorf, J. Dadda, J. Lackmann, J. A. Monroe, I. Karaman, E. Panchenko, H. E. Karaca, H. J. Maier, Tension-compression asymmetry in Co49Ni21Ga30 high-temperature shape memory alloy single crystals, *Mater. Sci. Forum*. 738-739 (2013) 82-86.

[110] H. H. Uhlig, Corrosion and corrosion control; An introduction to corrosion science and engineering, Wiley (2008) USA.

[111] X. X. Wang, L. C. Zhao, The effect of thermal-mechanical training on the formation of stress-induced ε martensite in an Fe-Mn-Si-Ni-Co alloy, *Scri. Metal. Mater.* 26 (1992) 1451-1455.

[112] J.C. Li, W. Zheng, Q. Jiang, Stacking fault energy of Iron-base shape memory alloys, *Mater. Lett.* 38 (1999) 275-277.

[113] X. Huang, S. Chen, T. Y. Hsu, X. Zuyao, Corrosion behavior of Fe25Mn6Si5Cr shape memory alloys modified with rare earth in a NaCl solution, *Jr. Mat. Sci.* 39 (2004) 6857-6859.

[114] Y. S. Zhang, X. M. Zhu, Electrochemical polarization and passive film analysis of austenitic Fe–Mn–Al steels in aqueous solutions, *Corros. Sci*. 41 (1999) 1817-1833.

[115] Y. S. Zhang, X. M. Zhu, M. Liu, R. X. Che, Effects of anodic passivation on the constitution, stability and resistance to corrosion of passive film formed on an Fe-24Mn-4Al-5Cr alloy, *Appl. Surf. Sci*. 222 (2004) 89-101.

[116] H. Li, D. Dunne, New corrosion resistant Iron-based shape memory alloys, *ISIJ Int*. 37 (1997) 605-609.

[117] Y. Zhang, X. Zhu, S. Zhong, Effect of alloying elements on the electrochemical polarization behavior and passive film of Fe–Mn base alloys in various aqueous solutions, *Corros. Sci.* 46 (2004) 853-876.

[118] Y. Moriya, H. Kimura, S. Ishizaki, S. Hashizume, S. Suzuki, H. Suzuki, T. Sampei, Properties of Fe-Cr-Ni-Mn-Si (-Co) shape memory alloys, *J. Phys IV* 1 (1991) C4, 443-437.

[119] H. Fukai, S. Suzuki, N. Masashi, S. Hanada, T. Maruyama, H. Kubo, Y. Waseda, Improvement of oxidation resistance of an Fe–Mn–Si–Cr shape memory alloy by annealing under vacuum, *Mater. Trans*. 46 (2005) 1745-1748.

[120] S. N. Balo, F. Yakuphanolgu, The effects of Cr on isothermal oxidation behavior of Fe-30Mn-6Si alloy, *Thermo. Acta*. 560 (2013) 43-46.

[121] H. Otsuka, H. Yamada, H. Tanahashi and T. Maruyama, Shape memory effect in Fe-Mn-Si-Cr-Ni polycrystalline alloys, *Mater. Sci. Forum*. 56-58 (1990) 655-659.

[122] K. Ullakko, P. Jakovenko, V. Gavriljuk, High-strength shape memory steels alloyed with nitrogen, *Scri. Mater.* 35 (1996) 473-478.

[123] H. Otsuka, M. Murakami, S. Matsuda, Effects of alloying additions on Fe-Mn-Si shape memory alloys, *ISIJ Int.* 30 (1990) 674-679.

[124] C. A. Della Rovere, J. H. Alano, J. Otubo, S. E. Kuri, Corrosion behaviour of shape memory stainless steel in acid media, *Jr. of Alloys Comp.* 509 (2011) 5376-5380.

[125] C. A. Della Rovere, J. H. Alano, R. Silva, P. A. P. Nascente, J. Otubo, S. E. Kuri, Characterization of passive films on shape memory stainless steels, *Corros. Sci*. 57 (2012) 154-161.

[126] C. A. Della Rovere, J. H. Alano, R. Silva, P. A. P. Nascente, J. Otubo, S. E. Kuri, Influence of alloying elements on the corrosion properties of shape memory stainless steels, *Mater. Chem. Phys*. 133 (2012) 668-673.

[127] T. Nishimura, Structure of the passive film formed on Fe-Mn-Si-Cr-Ni shape memory alloy after wet and dry corrosion test, *Mater. Trans.* 55 (2014) 871-876.

[128] T. Nishimura, Nano structure of the rust formed on an Iron-based shape memory alloy (Fe-Mn-Si-Cr) in a high chloride environment. *ISIJ Int*. 54 (2014) 1913-1919.

[129] ASTM G59-97, Standard test method for conducting potentiodynamic polarization resistance measurements, *ASTM Int.* (2014).

[130] ASTM G5-14, Standard reference test method for making potentiodynamic anodic polarization measurements, *ASTM Int.* (2014).

[131] ASTM F3044-14, Standard test method for evaluating the potential for galvanic corrosion for medical implants, *ASTM Int.* (2014).

[132] ASTM E3-11, Standard guide for preparation of metallographic specimens, *ASTM Int*. (2017).

[133] D. A. Jones, Principles and Prevention of Corrosion, *Prentice Hall* (1996) USA.

[134] S. Heino, Role of Mo and W during sensitization of superaustenitic stainless steel–crystallography and composition of precipitates, *Metall. Mater. Trans.* 31A (2000) 1893-2904.

[135] D.M.E. Villanueva, F.C.P. Junior, R.L. Plaut, A.F. Padilha, Comparative study on sigma-phase precipitation of three types of stainless steels: austenistic, superferritic and duplex, *Mater. Sci. Technol*. 22 (2006) 1098-1104.

[136] S. X. Lin, W. K. Bao, J. Gao, J. B. Wang, Intergranular corrosion of austenitic stainless steel, *Appl. Mech. and Mater*. 229-231 (2012) 14-17.

[137] J. Qian, C. Chen, H. Yu, F. Liu, H. Yang, Z. Zhang, The influence and the mechanism of the precipitate/austenite interfacial C-enrichment on the intergranular corrosion sensitivity in 310S stainless steel, *Corros. Sci*. 111 (2016) 352-361.

[138] B. I. Onyeachu, E. E. Oguzie, D. I. Njoku and I. Ukaga, The electrochemical characteristics of an ultra–fine grain γ/-Ni3Al coating in 3.5% NaCl solution, *IJST* 3 (2014) 728-735.

[139] C. Trepanier, A. Pelton, Effect of temperature and pH on the corrosion resistance of passivated nitinol and stainless steel, *Proc. Int. Conf. Shape Memory and Superelastic Tech*. (2004) 361-366.

[140] H. Li, Z. Jiang, H. Feng, S. Zhang, P. Han, W. Zhang, G. Li, G. Fan, Effect of temperature on the corrosion behaviour of super austenitic stainless steel S32654 in polluted phosphoric acid, *Int. J. Elect. Sci*. 10 (2015) 4832-4848.

[141] S. A. Bradford, Corrosion Control, *CASTI* and *ASM Int*. (2004) Canada.

[142] E. Blasco-Tamarit, A. Igual-Munoz, J. Garcia Anton, Effect of temperature on the galvanic corrosion of high alloyed austenitic stainless steel in its welded and non-welded conditions in LiBr solutions, *Corros. Sci.* 49 (2007) 4472-4490.

[143] N. J. Laycock, R. C. Newman, Temperature dependence of pitting potentials for austenitic stainless steels above their critical pitting temperature, *Corros. Sci.* 40 (1998) 887-902.

[144] W. Tian, N. Du, S. Li, S, Chen, Q. Wu, Metastable pitting corrosion of 304 stainless steel in 3.5% NaCl solution, *Corros. Sci*. 85 (2014) 372-379.

[145] Y. T. Sun, J. M. Wang, Y. M. Jiang, J. Li, A comparative study on potentiodynamic and potentiostatic critical pitting temperature of austenitic stainless steels, *Mat. Corros.* 69 (2018) 44-52.

[146] P. C. Pristrorius, G. T. Burstein, Growth of corrosion pits on stainless steel in chloride solution containing dilute sulphate, *Corros. Sci.* 33 (1992), 1885-1897.

[147] P. C. Pristrorius, The effect of some fundamental aspects of the pitting corrosion of stainless steel on electrochemical noise measurements, Electrochemical noise measurements for corrosion applications, *ASTM STP*. 1227 (1996) 343-358.

[148] C. Wang, J. Wu, Q. Li, Analysis of the temperature influence on galvanic corrosion and mathematical model, *J. Theo. Appl. Info. Tech*. 47 (2013) 712-717.

[149] E. Blasco-Tamarit, D. M. Garcia-Garcia, J. Garcoa-Anton, A. Guenbour, Study of the effect of temperature on the galvanic corrosion between alloy 31 base metal and its weld in polluted phosphoric acid, *Int. J. Electr. Sci*. 6 (2011) 6244-6260.

[150] G. O. Ilevbare, G. T. Burstein, The role of alloyed molybdenum in the inhibition of pitting corrosion in stainless steels, *Corros. Sci*. 43 (2001) 485-513.

[151] D. Mizuno, R. G. Kelly, Galvanically induced intergranular corrosion of AA5083-H131 under atmospheric exposure conditions: part 1-experimental characterization, *Corros.* 69 (2013) 580-592.

[152] Legat, C. Zevnik, The electrochemical noise of mild and stainless steel in various water solutions, *Corros. Sci.* 35 (1993) 1661-1666.

[153] F. Mansfeld, H. Xiao, Electrochemical noise and impedance analysis of iron in chloride media, Electrochemical noise measurement for corrosion application, *ASTM STP*. 1277 (1996) 59-78.

[154] F. Mansfeld, Z. Sun, Technical note: Localized index obtained from electrochemical noise analysis, *Corros.* 55 (1999) 915-918.

[155] NACE IMPACT, International Measures of Prevention, Application, and Economics of Corrosion Technology Study, *NACE Int.* (2016).

[156] M. G. Fontana, Corrosion Engineering, *McGraw-Hill* (1986) Singapore.

APPENDIX A. Basics of Corrosion Engineering

This section provides an introduction to the concept of corrosion engineering and its basics.

A.1 Corrosion Definition

Corrosion is the degradation of a material by chemical and / or electrochemical reaction with its environment [133]. In 2013, a study by the National Association of Corrosion Engineering (NACE) reported the global cost of corrosion to be around US$2.5 trillion [155]. This is equivalent to 3.4% of the global Gross Domestic Product (GDP) [155]. The study also determined that a saving of between 15% and 35% of the cost of corrosion could be achieved when using corrosion control practices [155].

A.2 Electrochemical Aspects of Corrosion

The electrochemical nature of corrosion can be illustrated by the attack on iron by aqueous solutions, which leads to the formation of rust. This is an electrochemical process that requires the presence of an electrolyte (water) and oxygen, at which hydrated oxides such as $Fe(OH)_3$, $FeO(OH)$ and $Fe_2O_3.H_2O$ are formed on the iron's surface. This process is illustrated in Figure A.1 and the electrochemical reactions are described below.

When water comes into contact with iron-based SMA, in the presence of oxygen, iron will be dissolved (oxidize), and an anodic reaction takes place as follows [156].

$$Fe \longrightarrow Fe^{2+} + 2e^- \qquad (A.1)$$

A cathodic reduction reaction takes place at the same time, at which the resulted electrons from reaction (2 – 1) are consumed. The cathodic reduction reaction changes with the change in solution pH.

(i) In solutions with pH below 4 (acidic water), the oxide scale on the iron surface is soluble and the corrosion rate increases (due to the presence of H^+ that is reduced by the following reaction), which leads to hydrogen gas evolution.

$$2H^+ + 2e^- \longrightarrow H_2 \qquad (A.2)$$

Dissolved oxygen can easily access the surface, when the oxide scale breaks down, which further increases the corrosion rate. Dissolved oxygen is cathodically reduced by:

$$O_2 + 4H^+ + 4e^- \longrightarrow H_2O \qquad (A.3)$$

(ii) As the iron corrodes, more hydrogen ions will be consumed, and as a result the pH will rise. In a pH range of 4 –10, a loose, porous ferrous oxide scale is formed on the surface [133]. The corrosion rate in this case is controlled by uniform diffusion of dissolved oxygen and is nearly constant [133]. Oxygen is reduced by the following reaction:

$$O_2 + 2H_2O + 4e^- \longrightarrow 4OH^- \qquad (A.4)$$

The resulting hydroxide ions (OH^-) react with the iron ions to produce insoluble iron (II) hydroxide.

$$Fe^{2+} + 2OH^- \longrightarrow Fe(OH)_2 \qquad (A.5)$$

Another reaction, involving iron (II) ions, hydrogen ions and oxygen, takes place to produce iron (III) ions.

$$4Fe^{2+} + 4H^+ + O_2 \longrightarrow Fe^{3+} + 2H_2O \qquad (A.6)$$

The produced iron (III) ions from the above reaction react with hydroxide ions to produce iron (III) hydroxide as follows:

$$Fe^{3+} + 3OH^- \longrightarrow Fe(OH)_3 \qquad (A.7)$$

$Fe(OH)_3$ eventually transforms into $Fe_2O_3.H_2O$, which is the common red-brown rust.

A.3 Polarization

During the cathodic reaction (*A*.2), when enough electrons are available, excess electrons accumulate at the metal-solution interface, resulting in more negative potential at the metal surface. This negative potential change is called cathodic polarization, at which the reaction is not fast enough to accommodate all the available electrons [133].

Likewise, the electrons that are liberated by reaction (*A*.1) cause a deficiency of electrons in the metal, and result in a positive potential change that is called anodic polarization, which is associated with a slow liberation of electrons by the surface reaction [133].

A.4 Activation Polarization

When one or some of the steps of the electrochemical reaction at the metal-electrolyte interface control the rate of the reaction, activation polarization arises. One example of this is the hydrogen-evolution reaction on iron-based SMA as per reaction (*A*.2). This reaction involves three steps [133]. Each one of these steps can control the rate of the reaction and result in activation polarization.

3. The first step involves the reaction of H^+ with an electron released from the iron-based SMA to form an adsorbed hydrogen atom (H_{ads}).

$$H^+ + e^- \longrightarrow H_{ads} \qquad (A.8)$$

3. The second step involves the reaction of two adsorbed hydrogen atoms to form a hydrogen molecule (H_2).

$$H_{ads} + H_{ads} \longrightarrow H_2 \qquad (A.9)$$

4. The third step involves the combination of sufficient molecules to form a hydrogen bubble on the surface.

In media that contains a high concentration of active species, activation polarization usually controls the rate of the reaction.

A.5 Concentration Polarization

In concentration polarization, the electrochemical reaction is controlled by the diffusion in the electrolyte. This often occurs when the concentration of the reducible species is small. In the case of the hydrogen evolution, at high reaction rates, reduction reactions deplete the solution of the dissolved hydrogen ions. In this case, the reduction reaction rate will be controlled by the diffusion of hydrogen ions to the metal surface [156].

The effect of environmental factors differs with each type of polarization that controls the reduction reaction. For example, if the velocity or agitation of the corrosive medium is increased, the reaction rate will increase only if the reaction was controlled by concentration polarization. If the reaction is controlled by activation polarization, agitation will not influence the reaction rate [156].

A.6 Passivity

Passivity can be defined as the loss of chemical reactivity of metals and alloys under specific environmental conditions [156]. To quantitatively describe the passivity of a metal or an alloy, a relationship between the potential of a corroded metal/alloy and the corrosion rate is established (see Figure A.2). In this figure, the behaviour of a metal or an alloy is divided into three main regions: active, passive, and transpassive. A description of the electrochemical behaviour in each region is provided below [156].

(i) Active Region:

When a metal or an alloy is immersed in an aqueous solution, a steady state potential will be reached on the surface of the metal/alloy. This potential is known as the open circuit potential (OCP) or corrosion potential. When the oxidizing power of the solution increases, the anodic reaction rate (corrosion rate) generally increases. Anodic polarization is the driving force for corrosion by the anodic reaction and results in increasing the surface potential of the metal/alloy.

(ii) Passive Region

When a critical potential (E_p) is reached, a thin protective oxide film is formed on the metal/alloy's surface. It acts as a barrier to the anodic dissolution reaction and, as a result, the corrosion rate starts to decrease, even though the driving force for corrosion is high.

(iii) Transpassive Region

The protective oxide film is only stable over a range of oxidizing power (potential). As the concentration of the oxidizer increases, the protective film breaks down, and the corrosion rate starts to increase again with an increase in oxidizing power.

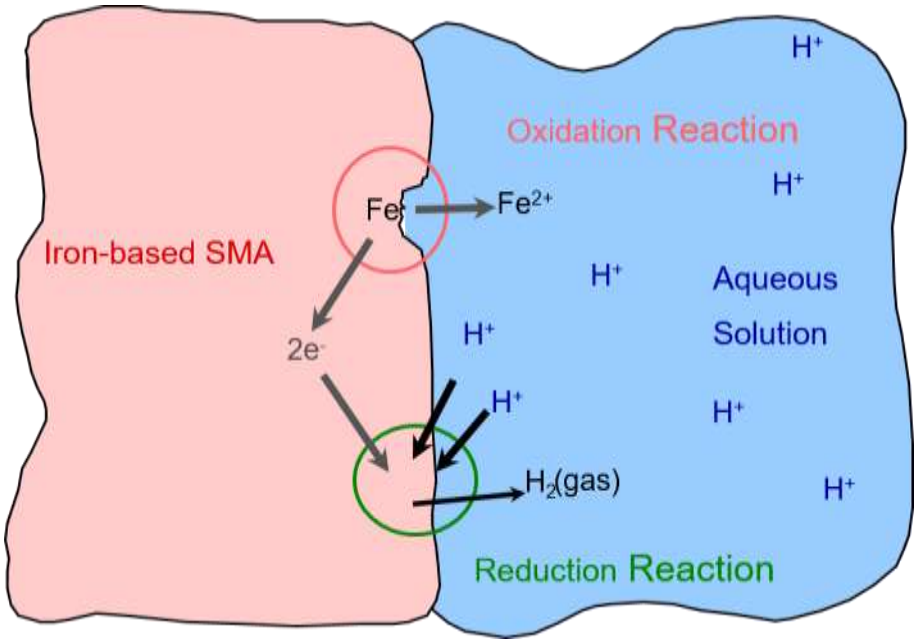

Figure A.1. Schematic diagram showing the corrosion of iron-based SMA in an aqueous solution. Iron breaks down into iron ions (Fe^{2+}) and electrons (e^-).The electrons are consumed by the reduction of H^+ to H_2.

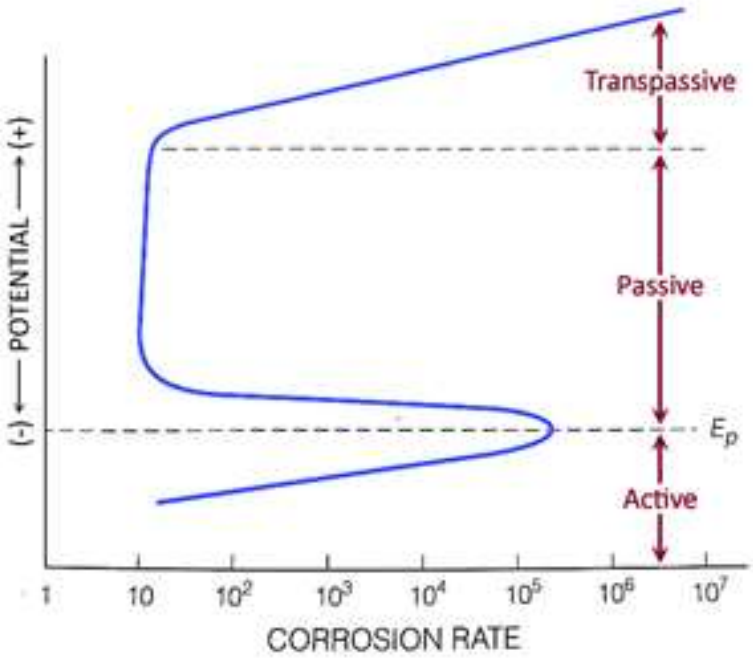

Figure A.2. Corrosion electrochemical behaviour of an active-passive metal as a function of solution oxidizing power (electrode potential).

APPENDIX B. Micrographs of Aged NCAT SMA Etched Using Different Etchants

Several etching solutions were tried on NCAT2 SMA to reveal the grains and grain boundary precipitates. In this appendix, micrographs of NCAT2 SMA etched using three different etchants are illustrated in Figures B.1 – B.3.

Figure B.1. The microstructure of aged NCAT using an etchant composed of 15 g sodium bisulfate + 10 g potassium meta-bisulfate + distilled water, where it was very difficult to reveal the grain boundary precipitates.

Figure B.2. The microstructure of aged NCAT etched using 10% nitric acid etchant showing the β grain boundary precipitates. The grains and grain boundary precipitates are over-etched.

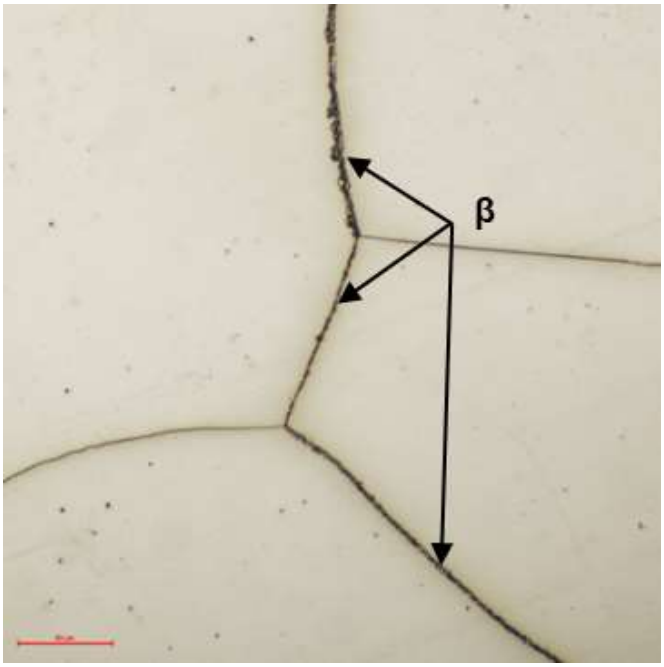

Figure B.3. The microstructure of aged NCAT using a 6% nitric acid etchant. B grain boundary precipitates are very obvious and the grains are not over-etched. This etchant gave the best results.

An invention and innovation report for the use of the etchant in Figure B.3 to reveal grain boundary precipitates in NCAT SMA was submitted to the University of Saskatchewan Innovation Enterprise Office. A copy of the first page of the report is provided in Figure B.4.

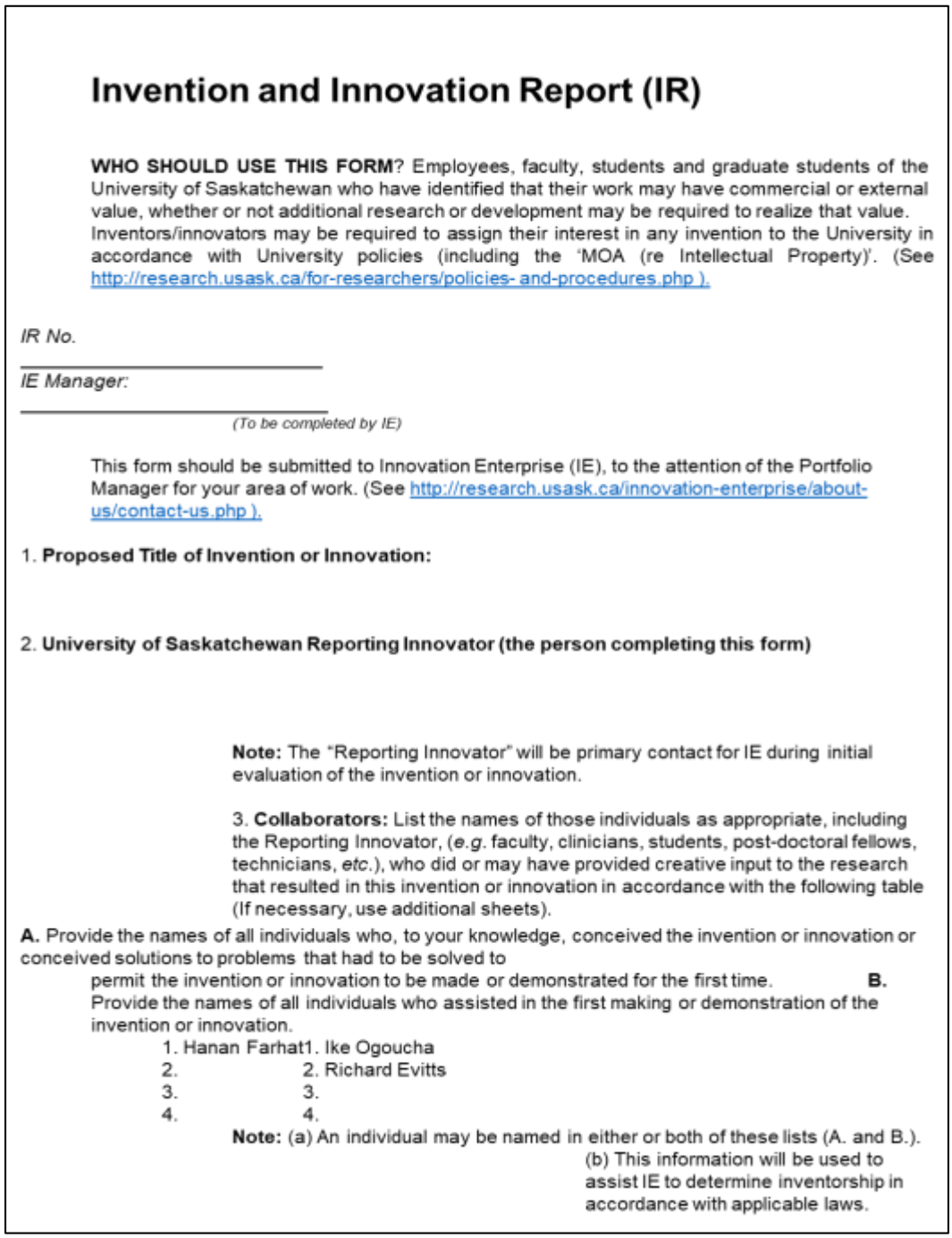

Invention and Innovation Report (IR)

WHO SHOULD USE THIS FORM? Employees, faculty, students and graduate students of the University of Saskatchewan who have identified that their work may have commercial or external value, whether or not additional research or development may be required to realize that value. Inventors/innovators may be required to assign their interest in any invention to the University in accordance with University policies (including the 'MOA (re Intellectual Property)'. (See http://research.usask.ca/for-researchers/policies- and-procedures.php).

IR No.

_____

IE Manager:

_____

(To be completed by IE)

This form should be submitted to Innovation Enterprise (IE), to the attention of the Portfolio Manager for your area of work. (See http://research.usask.ca/innovation-enterprise/about-us/contact-us.php).

1. **Proposed Title of Invention or Innovation:**

2. **University of Saskatchewan Reporting Innovator (the person completing this form)**

Note: The "Reporting Innovator" will be primary contact for IE during initial evaluation of the invention or innovation.

3. **Collaborators:** List the names of those individuals as appropriate, including the Reporting Innovator, (*e.g.* faculty, clinicians, students, post-doctoral fellows, technicians, *etc.*), who did or may have provided creative input to the research that resulted in this invention or innovation in accordance with the following table (If necessary, use additional sheets).

A. Provide the names of all individuals who, to your knowledge, conceived the invention or innovation or conceived solutions to problems that had to be solved to permit the invention or innovation to be made or demonstrated for the first time. **B.** Provide the names of all individuals who assisted in the first making or demonstration of the invention or innovation.

1. Hanan Farhat	1. Ike Ogoucha
2.	2. Richard Evitts
3.	3.
4.	4.

Note: (a) An individual may be named in either or both of these lists (A. and B.).
(b) This information will be used to assist IE to determine inventorship in accordance with applicable laws.

Figure B.4. The first page of the invention and innovation report for the etching solution for NCAT SMA.

APPENDIX C. Optical Micrographs of Heat Treated NCAT SMAs Tested at Different Solutions

In this section, micrographs of NCAT samples that were solution heat treated NCAT and aged NCAT are presented in (Figures C.1 – C.6. All the samples have been subjected to potentiodynamic polarization tests. The tests were conducted in three different solutions (0.6 M Nacl, 0.5 M NaOH and 0.5 M H_2SO_4). All the images were acquired at 5X magnification.

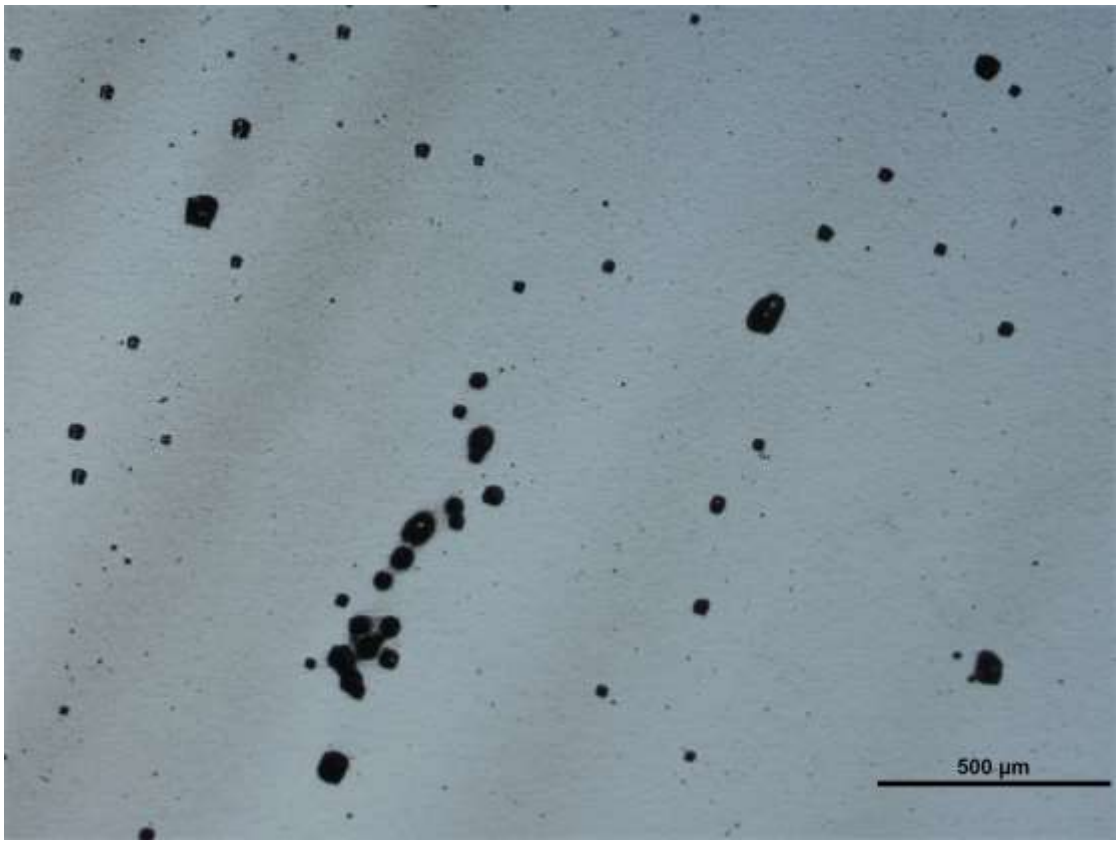

Figure C.1. Micrograph of solution treated NCAT alloy that was subject to potentiodynamic polarization test in 0.6 M NaCl solution at 25 ^{o}C showing pitting in the alloy matrix.

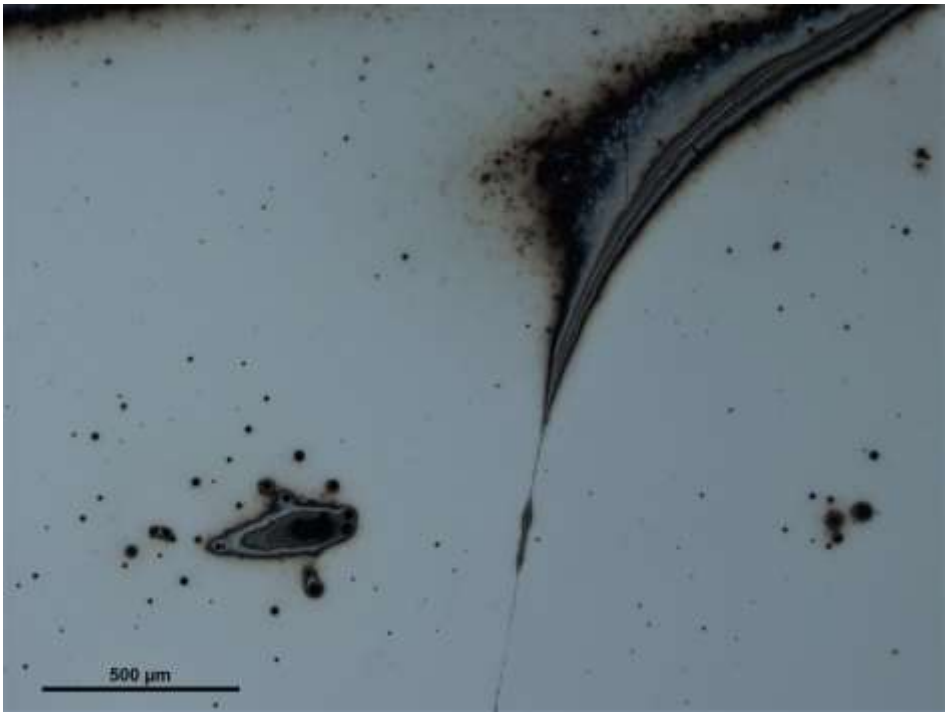

Figure C.2. Micrograph of aged NCAT alloy that was subject to potentiodynamic polarization in 0.6M NaCl solution at 25 ^{o}C showing IGC and pitting near the grain boundaries that have precipitates.

Figure C.3. Micrograph of solution treated NCAT alloy that was subject to potentiodynamic polarization test in 0.5 M NaOH solution at 25 ^{o}C showing no signs of corrosion.

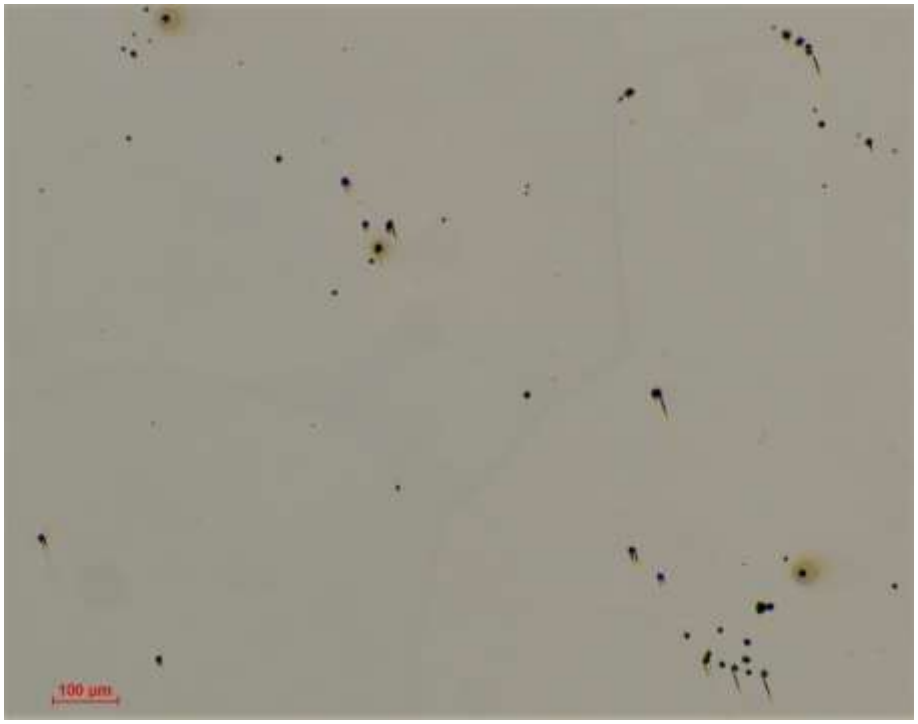

Figure C.4. Micrograph of aged NCAT alloy that was subject to potentiodynamic polarization in 0.5 M NaOH solution at 25 ^{o}C showing small pits distributed in the alloy matrix.

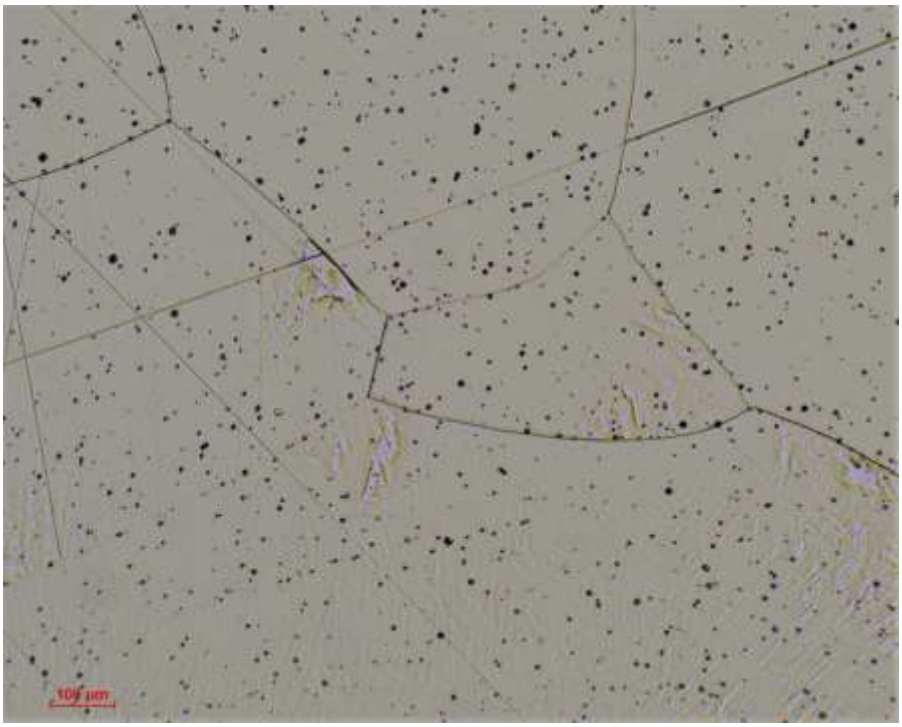

Figure C.5. Micrograph of solution treated NCAT alloy that was subject to potentiodynamic polarization test in 0.5 M H_2SO_4 solution at 25 ^{o}C showing pitting all over the alloy matrix.

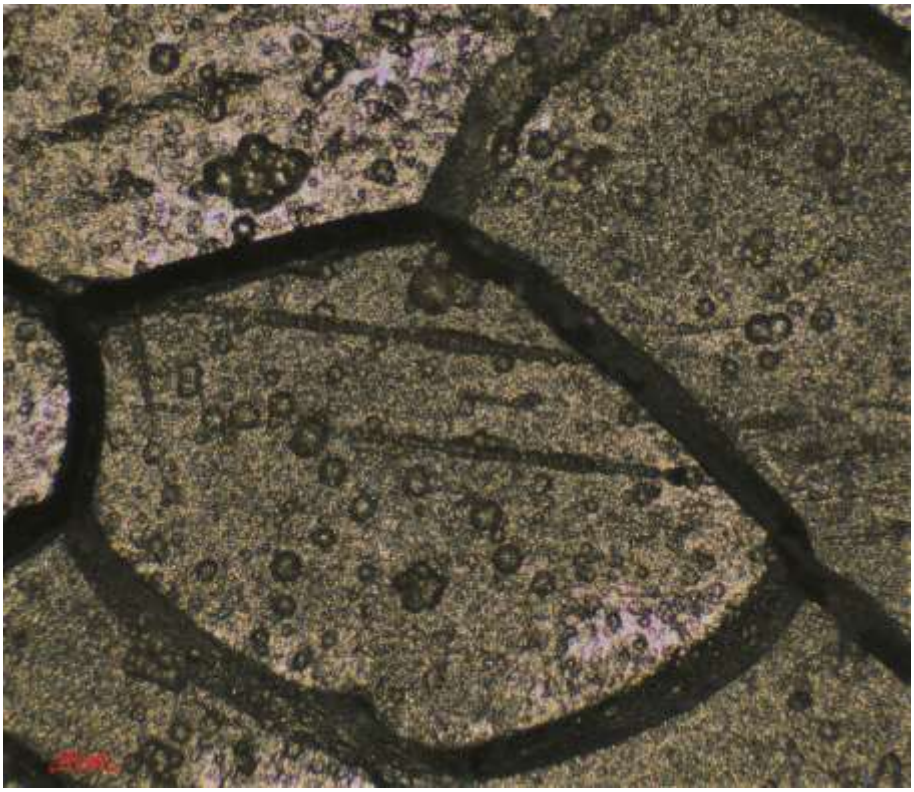

Figure C.6. Micrograph of aged NCAT alloy that was subject to potentiodynamic polarization in 0.5 M H_2SO_4 solution at 25 ^oC showing large pits distributed all over the alloy matrix and corrosion in the grain boundaries. The acid solution appears to etch the alloy and attack the grains and grain boundaries. No signs of IGC were observed.

APPENDIX D. Optical Micrographs of Solution Treated NCAT Alloy Tested at Different Temperatures and Different pH

Micrographs of solution treated NCAT SMA that was subjected to potentiodynamic polarization tests in 0.6 M NaCl solution at four different temperatures (RT, 40 ^{o}C, 60 ^{o}C, and 80 ^{o}C) in solution with different levels of pH (3, 6, and 9) are illustrated in Figures D.1 – D.3. The higher temperature resulted in larger number of pits, and bigger pit and corrosion area size. Different coloured corrosion scales were observed at the high temperatures, mainly 80 ^{o}C. Samples that were tested in solutions with a pH of 10 show smaller size of pits and corroded area, while samples that were tested in solutions with a pH of 3 show a considerably higher number of pits, and bigger pit sizes and corroded area.

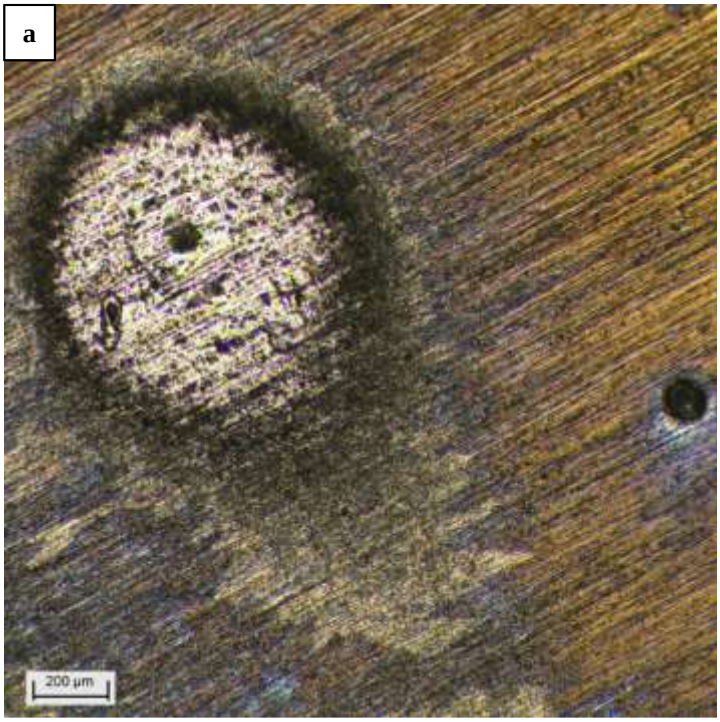

Figure D.1. Micrographs of solution treated NCAT after potentiodynamic polarization test in a 0.6 M NaCl solution that has a pH of 3 at (a) RT, (b) 40 ^{o}C, (c) 60 ^{o}C, and (d) 80 ^{o}C showing larger area that is covered by corrosion scale at the higher temperature.

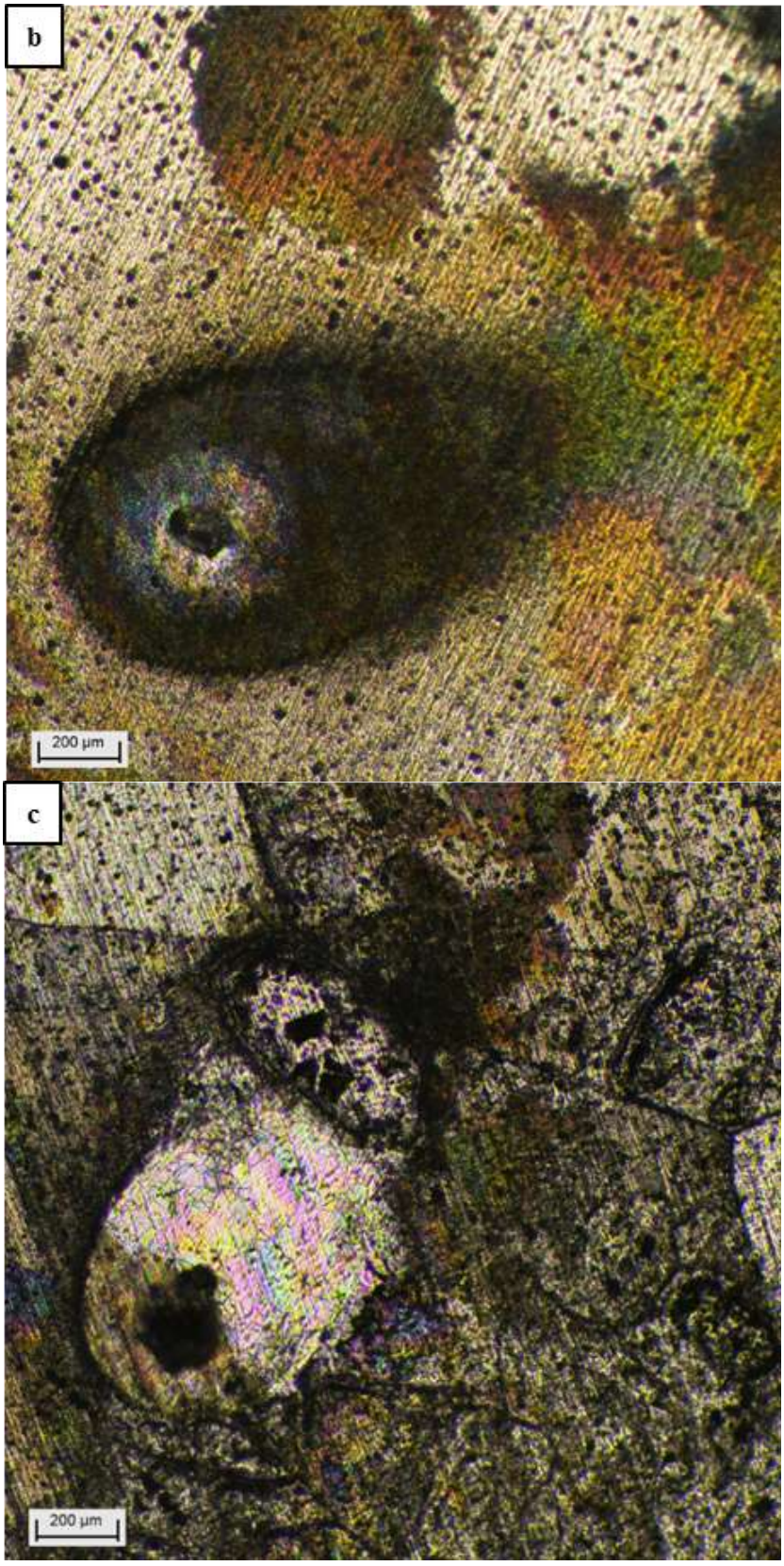

Figure D.1. Continued.

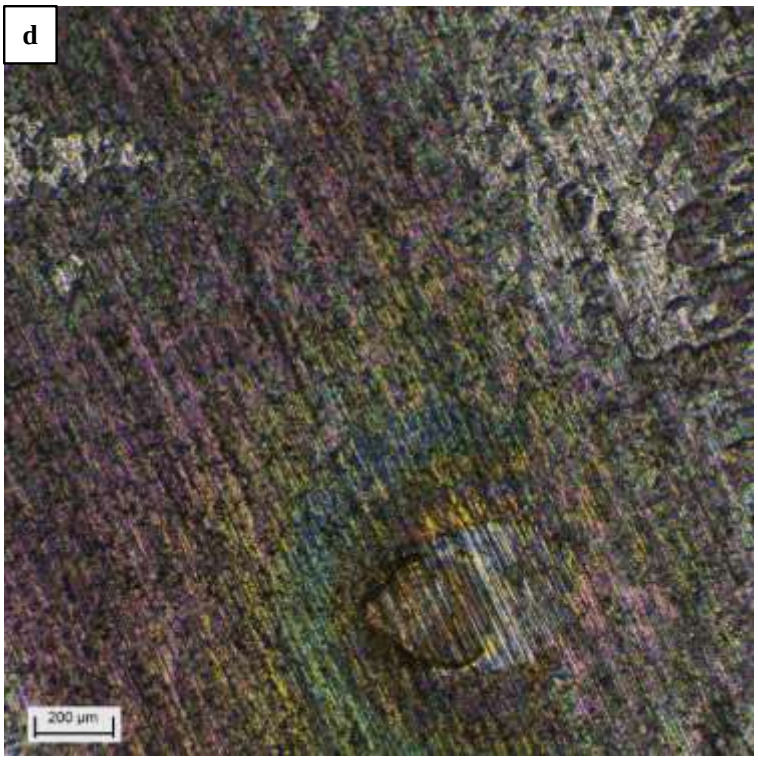

Figure D.1. Continued.

Figure D.2. Micrographs of solution treated NCAT after potentiodynamic polarization test in a 0.6 M NaCl solution that has a pH of 6 at (a) RT, (b) 40 ^{o}C, (c) 60 ^{o}C, and (d) 80 ^{o}C. Larger pit size and corroded area are observed at higher temperatures.

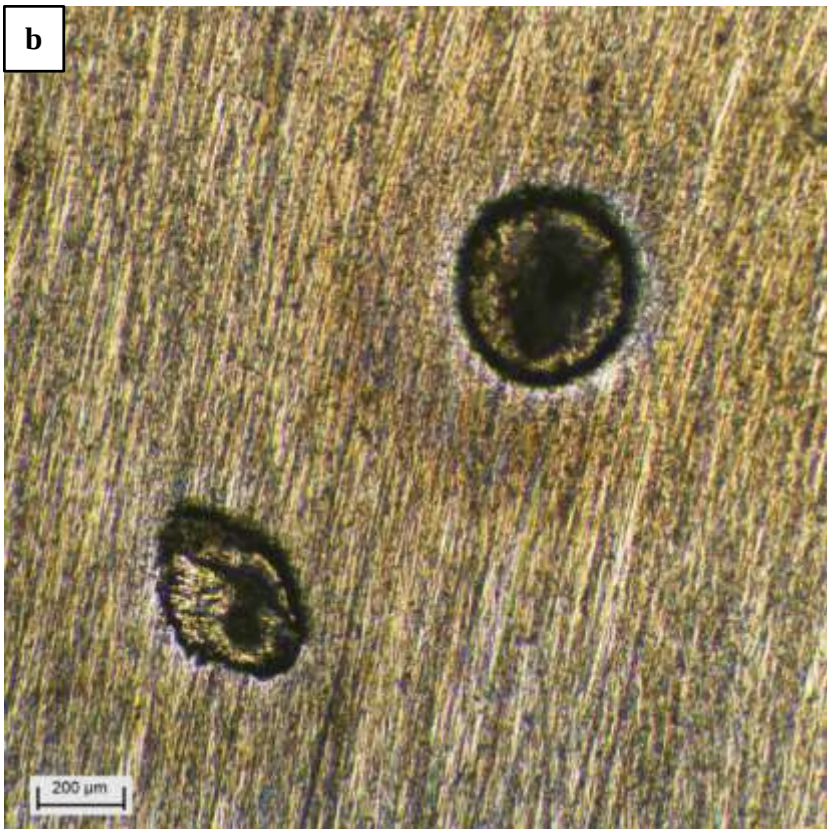

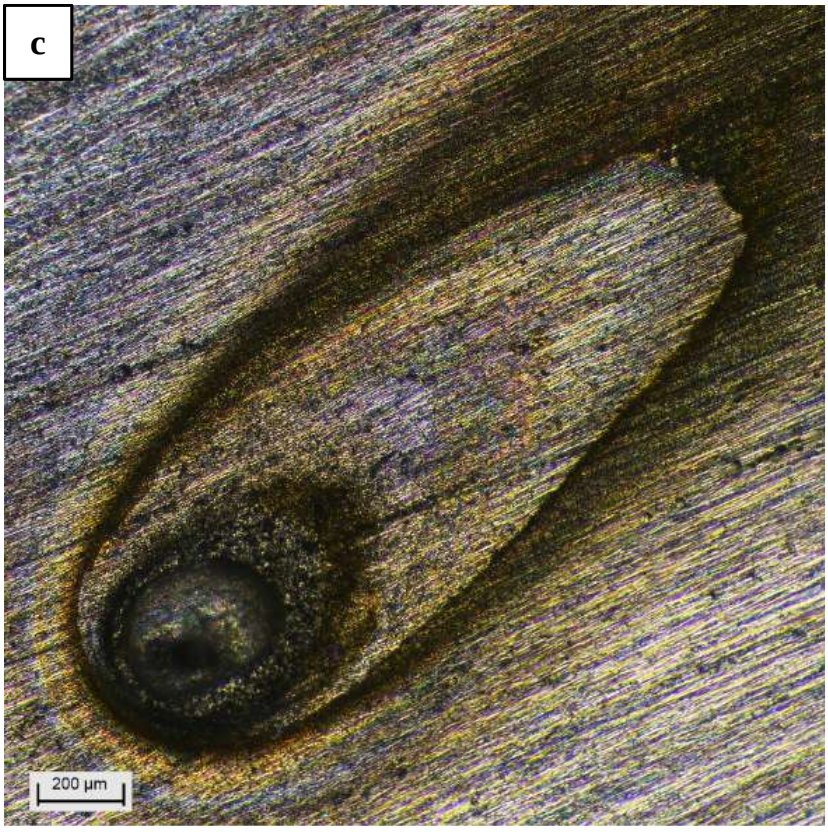

Figure D.2. Continued.

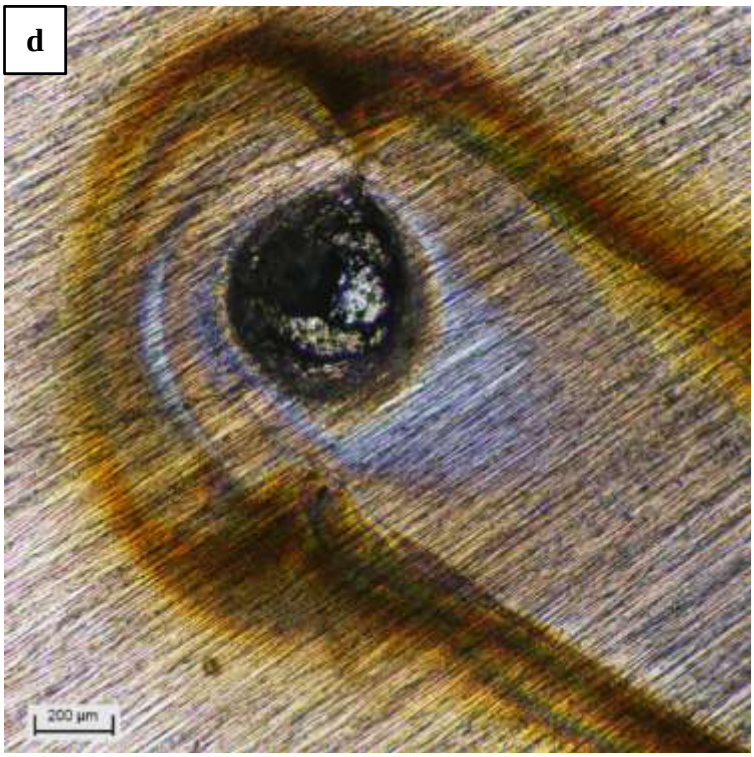

Figure D.2. Continued.

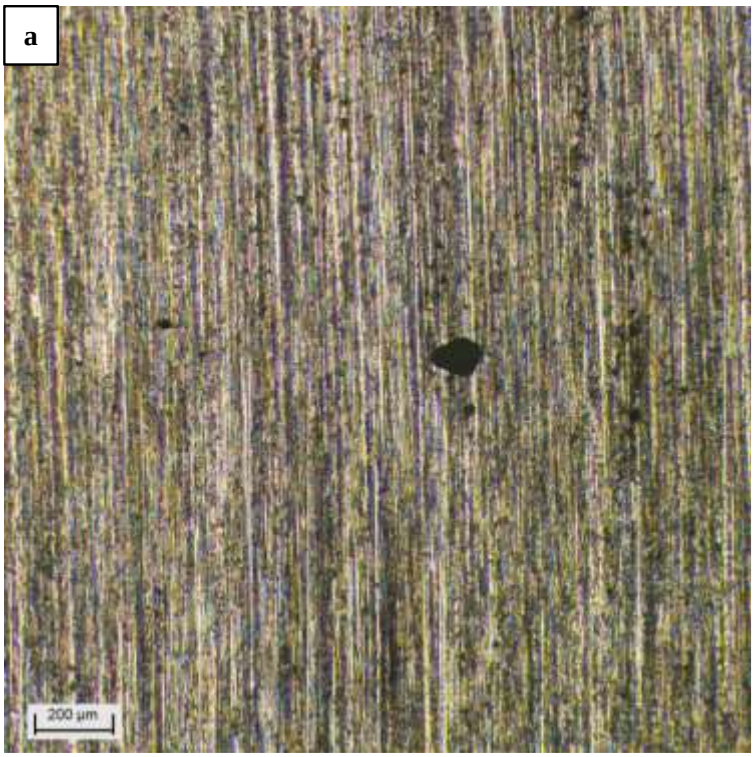

Figure D.3. Micrographs of solution treated NCAT after potentiodynamic polarization test in a 0.6 M NaCl solution that has a pH of 10 at (a) RT, (b) 40 ºC, (c) 60 ºC, and (d) 80 ºC. This solution showed remarkably smaller pit size and corroded area, compared to the other solutions.

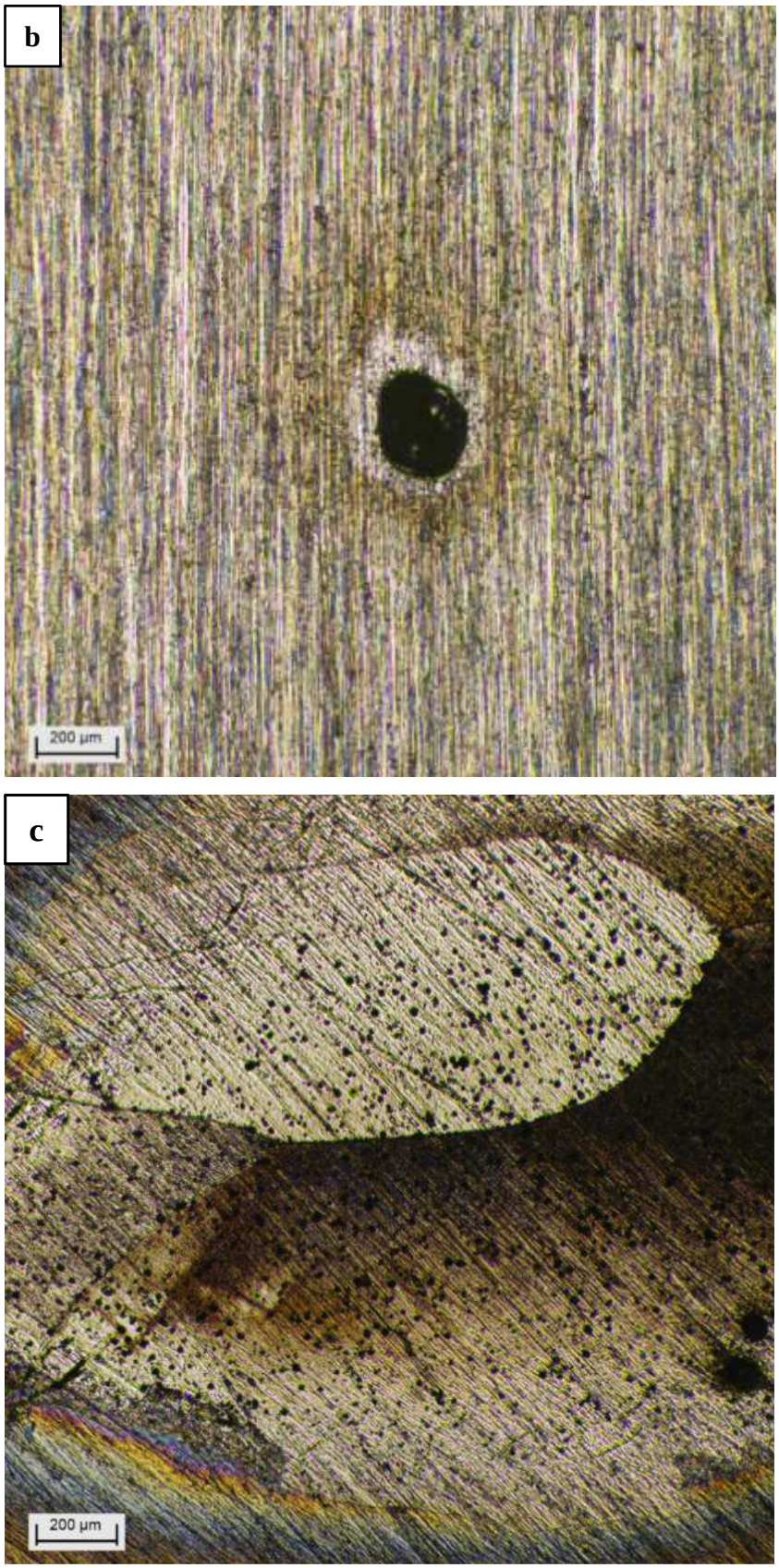

Figure D.3. Continued.

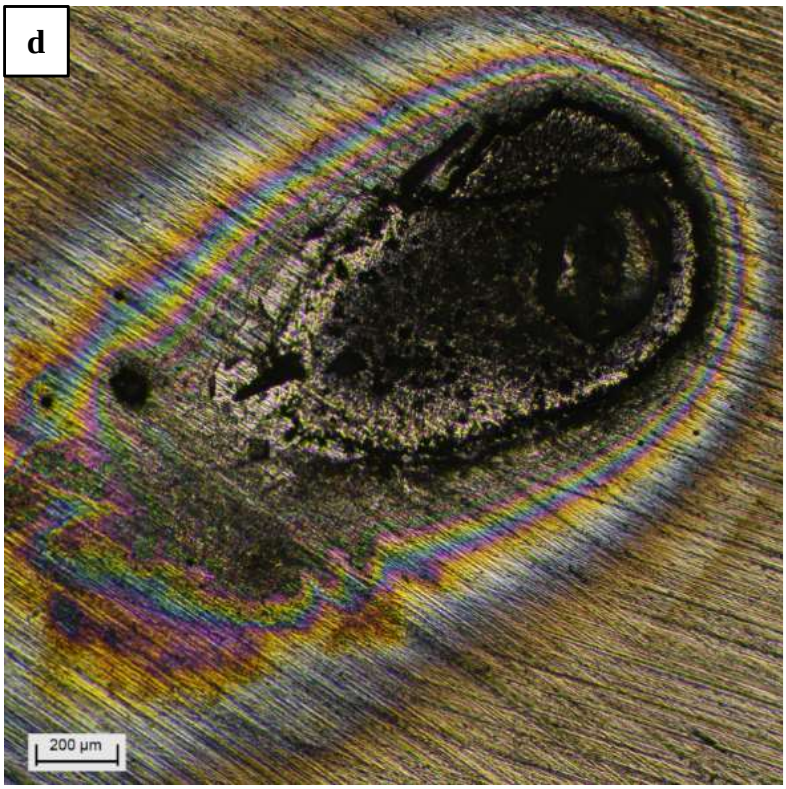

Figure D.3. Continued.